Imperial College London
Department of Mechanical Engineering

# Fracture of particle-modified epoxies: Effect of test rate and temperature

Wing Lam Tsang

November 2, 2017

Supervised by Dr Ambrose Taylor

Submitted in fulfilment of the requirements for the degree of
Doctor of Philosophy in Mechanical Engineering of Imperial College London
and the Diploma of Imperial College London

## Declaration of Originality

I declare that this thesis is my own work and all other materials from others are referenced appropriately. This thesis has not been submitted to any other universities or institutions for any degrees.

Wing Lam Tsang

## Copyright Declaration

The copyright of this thesis rests with the author and is made available under a Creative Commons Attribution Non-Commercial No Derivatives licence. Researchers are free to copy, distribute or transmit the thesis on the condition that they attribute it, that they do not use it for commercial purposes and that they do not alter, transform or build upon it. For any reuse or redistribution, researchers must make clear to others the licence terms of this work.

# Abstract

This study compares the effect on the fracture energy of epoxy from addition of different weight % of particles, at both quasi-static and high test rates (up to 1 m/s). Silica and core-shell rubber (CSR) particles, and the hybrid of both (from 0.5 weight % to the maximum concentration of 25.4 weight %) are used. Tapered double cantilever beam (TDCB) and single-edge notch bending (SENB) specimens were used for measurement of the fracture energy, $G_c$.

The silica and CSR formulations were then compared with ceramic microsphere and PES formulations. The toughening mechanisms involved were confirmed by fracture surface images obtained from field emission gun scanning electron microscopy (FEG-SEM). Most of the specimens from all formulations show debonding and void growth is also expected in silica due to the relatively high fracture energy found. As the CSRs were made up from small CSR particles, mostly localised deformations were found, with some debonding of small CSR particles. In ceramic microsphere and PES specimens, fracture energy improvement was small, and the amount of improvement was similar. PES modified epoxy shows different structures at different wt% as they were dissolved before mixing with the epoxy. Some brittle particles tear off were found in low wt%, while some local phase inversions were found in high wt%. The main mechanisms in PES specimens were particle pull out, bridging and debonding.

The experimental results were compared with simulation results using the finite element analysis software 'Abaqus' and analytical models. When compared to experimental results, analytical models predicted the modulus and fracture energy of each formulation according, predictions agreed with experimental results, while different predictions were found from FE model.

# Contents

# List of Tables

# List of Figures

# Chapter 1

# Introduction

## 1.1 Introduction

Epoxy is a thermoset polymer, which is highly crosslinked and brittle. In service, epoxy will experience cyclic loading, impact or other stresses and hence brittleness would highly affect its lifetime. Hence there is a need to toughen epoxy for use in engineering applications, such as the bonding of joints in the automotive industry, the use of epoxy as a matrix in fibre composites and the use of adhesives for repairing of components. This project principally uses silica nanoparticles, core-shell rubber (CSR) particles and hybrids of both particle types, to investigate the toughening effect of epoxy with different weight % of nanoparticles at both quasi-static and high test rates. The work will investigate the synergistic toughening effects of combining silica nanoparticles with micron-sized rubber particles.

There are two main aspects in study: the effect of different weight % of nanoparticles added, and the effect of different test rate (i.e. quasi-static and high rate). Silica particles will be added in at concentrations of 0.5, 1, 2, 3, 5, 10, 15 and 20 weight %, and at the maximum possible concentration (25.4 weight %). CSR particles will be added in at the same weight percentages, but up to a maximum of 10 weight %. In previous work [1–3] , the effects of different weight % of silica have been investigated with relatively large weight percentages of nanoparticles (of 10 weight % and above, e.g. by Hsieh et al. [2] and Mohammed et al. [4]) but not with small weight percentages. It has been suggested that small percentages of silica nanoparticles are more effective at toughening epoxy than large weight percentages, but this has not yet been investigated. Hence this study will provide more information about the effect of small percentages of silica. This effect can be shown and explained by comparing the fracture energy, $G_c$, against the weight % of silica nanoparticles. The toughening mechanisms have been identified as shear yielding in the epoxy plus debonding of the particles followed by

void growth of the epoxy. The results would be expected to show a positive increase in toughness as the percentage of nanoparticles increases, and a plateau at the maximum point. However, only about 15% of the silica nanoparticles have been observed to debond at high wt% [2]. The small weight % of silica particles added in could have a greater effect on the overall curve, as a higher % of the silica particles may be able to undergo debonding and void growth than at high weight % of silica particles, and hence a steeper increase in $G_c$ vs wt% than observed in the literature, such as from Hsieh et al. [2], at small weight% may be expected.

For the effect of test rate, this study will start with a quasi-static rate, and then investigate the toughness at higher test rate. The increased rate is expected to produce an increase in brittleness, and hence a reduction in the fracture energy. The hard silica particles are expected to show less of a reduction of toughness with increasing test rate when compared to the soft rubber particles. This is because rubber is viscoelastic and will become harder to cavitate at high test rates, but silica is a ceramic and hence is not sensitive to changes in the test rate. The increased test rate is equivalent to a reduced temperature, so the high rate data may be compared to low temperature fracture data. A fracture mechanics approach will be used to characterise the toughness of the epoxy. To understand the mechanisms responsible for the measured changes in properties, analytical and finite element modelling can be performed. It has been shown that the modulus of particle modified epoxies can be predicted from the modulus of the particles and of the epoxy using the Halpin-Tsai, Nielsen or Mori-Tanaka models [5]. The toughness can be predicted using the Huang and Kinloch model [2], which was modified by Hsieh et al. [3]. This model predicts the toughening effect from each mechanism which is identified from microscopy, and hence the fracture energy of the particle modified epoxy can be predicted. The fracture energy properties were inputted into a FE model, resultant force for fracture was recorded and compared to the experimental values.

A synergistic toughening effect has been observed in previous work for silica and rubber particles. However, other combinations of particles are frequently used in epoxies, e.g. CSR, carboxyl-terminated butadiene acrylonitrile (CTBN) and carbon nanotubes with silica.

Thus for further comparison, other particles of ceramic microspheres and polyethersulfone (PES) are used. The ceramic microsphere used is a medium size of microsphere in the series of products, they have a relatively small particle size (13 $\mu$m) when compared to most of the particles used in this study, except for silica (20 nm). They are expected to show similar mechanisms to silica, as debonding is the main failure mechanism for

ceramic microspheres. SEM imaging results confirmed these failure mechanisms found for ceramic microsphere, allowing a comparison between toughening using nanometre particles (silica) and micrometre particles (ceramic microspheres). The PES particles are dissolved into a solvent before mixing into epoxy, and then phase separates during curing. The wt% used was only up to 10 wt% so the microstructure is expected to be PES particles in an epoxy matrix. However, there were very different fracture surfaces found with different wt% of PES, mainly due to the problems of dissolving the PES particles.

The aims of this work were to investigate the effects of these particles on the microstructure and properties of epoxy, and to identify any synergistic toughening effects. The toughening mechanisms will be identified, and the fracture energy predicted using modelling. The model predictions will be compared to the experimental data.

## 1.2 Structure of thesis

This thesis is mainly structured by the different methods of testing and the materials used, as well as by the sequence of the testing methods, (e.g. quasi static method first, then the high rate and low temperature tests are introduced.) Starting with a literature review and introducing the materials used, this study then explores the measurement of the fracture energies of these materials, with discussion of the fracture mechanisms and some modelling work. The contents of each Chapter are as follows:

Chapter 2: This literature review discusses the properties of epoxy as an adhesive, and the particles used to toughen epoxies. The principles of fracture mechanics, the different geometries used for testing fracture properties and the different types of crack growth during fracture are presented. The toughening mechanisms which increase the fracture energy are also introduced.

Chapter 3: This chapter provides information on the epoxy and the other materials used in this study (silica nanoparticles, core-shell rubber particles, ceramic microsphere and polyethersulfone), their properties, the weight % used and the formulations used in mixing. Some known properties of the materials from previous studies are also included in this chapter.

Chapter 4: This describes the quasi-static tapered double cantilever beam (TDCB) testing, using silica, CSR and silica / CSR hybrid formulations. This chapter describes the manufacture and testing of the TDCBs, and the method of calculating the fracture energy and crack information. The results of quasi-static rate TDCB tests are presented, considering stick-slip and stable crack propagation separately.

Chapter 5: The use of high rate TDCB tests and the data reduction strategy are discussed. The high rate TDCB set up and the analysis method are described. High rate TDCB results are shown and the fracture types are determined here.

Chapter 6: Single edge notch bend (SENB) testing on bulk samples was performed as there were uncertainties in TDCB fracture energies due to the presence of interfacial failure. The use of single-edge notch three-point bending, how the tests were done, specimen preparation, the different test conditions (quasi-static, high rate and low temperature) and fracture energy results are presented for the silica, CSR and silica / CSR hybrid formulations.

Chapter 7: A short chapter presents the comparison between the fracture energies of the silica and CSR modified epoxies measured using SENB and TDCB tests at quasi-static test rate. It summarises the fracture energy findings, and compares the results from the different test geometries.

Chapter 8: The analytical models of Halpin-Tsai and Huang and Kinloch are used to predict the modulus and fracture energy of the silica, CSR and silica / CSR hybrid formulations. The Halpin-Tsai model estimates the Young's modulus of the material and the Huang and Kinloch model estimates the fracture energy of material. There were three cases in the Huang and Kinloch model: Shear band yielding only, plastic void growth of 15% of particles and 100% of plastic void growth. All the combinations are analysed and compared with the experimental findings.

Chapter 9: Scanning electron microscopy (SEM) imaging was performed to identify the fracture and toughening mechanisms, to explain the changes in the measured fracture energies. This chapter describes the SEM conditions used, and shows a selection of SEM images. The effect of the wt% of particles is discussed for all formulations. The effects of high rate and low temperature also presented.

Chapter 10: Finite element modelling of the TDCB and SENB tests was performed with the use of experimental data. Details about the model, for example the boundary conditions used, element sizes used, cohesive layer used and the cohesive zone properties are discussed. All the formulations and test conditions are modelled and their results are explained in this chapter.

Chapter 11: The ceramic microsphere and PES materials were used in the later stage of the study to provide an all round comparison of particles used in epoxy toughening. Hence their results were compared in the later section of the thesis. For the experimental parts, the results of tensile, DMA, low rate SENB and low temperature SENB tests are presented. For the modelling part, the analytical models of the modulus and fracture energy are described in this chapter.

Chapter 12: The conclusions summarise the main findings from the results and comment on the use of different particles in the toughening of epoxy.

Chapter 13: The future work chapter discusses how further work could improve understanding or accuracy. There are a few different directions of studies proposed for the future work, mainly focusing on the use of different experimental studies and different approaches in FE model building.

# Chapter 2

# Literature review

## 2.1 Epoxy adhesives

### 2.1.1 Introduction

There is a long history in the use of adhesives in industry. There are many advantages in using adhesives; one big advantage is the reduction of cost. There is also an improvement in product appearance, and an improvement in stress distribution and corrosion resistance, these factors enhance the design possibilities [6]. However, there are also drawbacks, for example adhesive bonding requires surface pretreatment of the substrates, it cannot join thick metallic components effectively, non-destructive testing methods are not applicable and it lowers the upper-service temperature [6].

In order to minimize these drawbacks, investigations into adhesive properties have been ongoing. To help the understanding and assessment of adhesive joints, finite element analysis (FEA) and fracture mechanics approaches are often used. These approaches can be used to predict service life and improve joint properties under different environments [6].

Due to the brittleness of adhesives, they are often modified by particles to improve their toughness without changing their glass transition temperature, $T_g$ [7]. However, some of the toughening mechanisms such as particle bridging, crack pinning and deflection are not applicable for nanoscale particles, as the particles are smaller than the crack opening displacement [7, 8]. Therefore the size of the particles used is one of the most important parameters in toughening epoxy. There is a higher critical stress for debonding for smaller particles, hence a reduced amount of debonding would be expected. These toughening mechanisms can be investigated by scanning electron microscopy (SEM). Transmission electron microscopy (TEM) and transmission optical microscopy (TOM) [7] can be used to assess the dispersion of the particles. Agglomeration of the particles can reduce the toughness of the polymer, and will increase the viscosity of the uncured

resin which may lead to processing difficulties [3]. There can be a large increase in toughness of the modified epoxy due to the toughening mechanisms described below, and the increased toughness is also maintained when the epoxy is used in fibre composites [3]. The toughness of the modified epoxy depends on the amount of crosslinking of the epoxy, the type of particles used, the particles' size and their concentration [3].

### 2.1.2 Rubber-toughened epoxy

There has been a long history in the use of rubber particles in the toughening of epoxy. It is established that the larger the rubber particles, the higher the stress concentrations [9] and hence a higher amount of localised deformation. There are two principal types of rubber-toughened epoxy: carboxyl-terminated butadiene-acrylonitrile (CTBN) rubber and core-shell rubber (CSR) particles are commonly used. Carboxyl-terminated butadiene-acrylonitrile (CTBN) rubbers are rubbers containing butadiene and acrylonitrile as copolymers [10, 11]. They are added as a liquid rubber which dissolves in the epoxy resin and phase-separates to form particles during curing of the epoxy. Examples of different extents are amino-terminated-acrylonitrile (ATBN) and vinyl-terminated butadiene-acrylonitrile (VTBN).

There are two requirements for the CTBN rubber to be added to the epoxy: 1. the rubber must be able to dissolve in the epoxy resin and then be able to precipitate out during curing, and 2. the rubber must be able to react with the epoxide group to ensure good interfacial bonding between the particle and the epoxy. The particle size or diameter, d, of the CTBN rubber particles depends on the curing cycle, volume fraction, $V_p$, and concentration of the butadiene and acrylonitrile in the rubber. Larger rubber particles would be formed when a slow curing process is used. When the amount of rubber added increases, their diameter and volume fraction would increase [12–14]. At high concentrations phase inversion can occur, where the rubber becomes the matrix with epoxy particles inside [15]. The rubber would stay in a dispersed phase when its concentration is less than 20 wt% [16]. As a consequence, the addition of 10-20 wt% of rubber particles provides the optimum toughening effect [16].

Hybrids can be formed by the addition of other particles to the rubber-toughened epoxy. Phase separation can be reduced with the addition of silica nanoparticles [16]. Lee et al. [15] found that silica nanoparticles enhanced the toughness of the rubber-modified epoxy though the silica nanoparticles agglomerated [15].

Core-shell rubber (CSR) particles are pre-formed rubber particles with a soft core and a hard outer shell. The glassy polymeric shell can prevent the rubber particles

aggregating and deforming during processing [17]. The CSR structure can be designed according to different factors (such as the chemical components of the matrix). Multilayer structures are very commonly used [11]. The particles are performed, so the diameter is not dependent on the curing process, unlike CTBN.

The major toughening mechanisms for rubber particles are localized plastic shear yielding and particle cavitation [17] followed by plastic void growth, these are discussed in Section 2.4. The toughening mechanism in rubber toughening is due to the change in yield shear stress at the crack tip, which reduces the stress concentration of the region and enhances optimal shear banding. In order for this mechanism to occur, the stress fields near particles need to be overlapped and so the spaces between them are critical [18].

### 2.1.3 Silica-toughened epoxy

It has been established that the addition of silica ($SiO_2$) nanoparticles can increase the toughness of epoxy [4, 8]. A sol-gel process is used to produce these silica nanoparticles, as liquid sol is transformed into a solid gel phase. The increase in the wt% of silica particles has shown a positive increase in toughness of the epoxy. By investigating different particle diameters (240 nm to 1.56 $\mu$m) and volume fractions (0 to 0.35), Adachi et al. [19] found that the increase in volume fraction and the decrease in particle size of silica can greatly increase the fracture toughness of silica-modified epoxy [19]. There were also studies about the effect of bimodal silica particle sizes, where significant improvements in toughness were also found with the use of a mixture of particle sizes [20]. However the different sizes of silica particles used have not shown a significant effect on the modulus [21], which depends principally on the volume fraction. When adhesion is low at the interfaces between the silica particles and the epoxy, there would be more debonding of particles, and this leads to more plastic void growth [8, 19, 22]. Shear banding and void growth are the major toughening mechanisms in silica nanoparticle-modified epoxy [21].

The toughening mechanisms in silica-modified epoxy are similar to other particles, but there is no crack pinning [4, 19], discussed in Section 2.4.3, because the particle diameter is less than the crack-opening displacement. Work on silica nanoparticle-modified epoxy performed by Hsieh et al. [19] has shown that some of the common fracture mechanisms (crack pinning, crack deflection and immobilised polymer around particles) can be discounted for silica nanoparticles. The major mechanism there was plastic deformation of epoxy. This means that the particles debonded from the matrix,

there were highly localised stress concentrated regions, which caused plastic deformation of the epoxy.

There have also been studies of addition of both rubber and silica particles and they have shown a good toughening effect [23]. It is because these two types of particles provide a good balance of modulus and toughness [24]. A synergy effect was found, giving a significant increase in toughness, from studies by Hsieh et al. [3] and Manjunatha et al. [24], with the use of a combination of silica and CTBN particles. With the use of block copolymers or CSR with silica particles, synergy effect in terms of toughness was also found in the study by Chen et al. [5, 25].

### 2.1.4 Polyethersulfone-toughened epoxy

As toughening epoxy using thermoplastic does not affect its $T_g$, when there is complete phase separation, there have been many investigations into toughening of epoxy resins with thermoplastics, such as commercial polyethersulfone (PES).
There are a few criteria in order for a thermoplastic to achieve high toughness in epoxy, including [26]:
1. Thermoplastic backbone: which provides good thermal stability, must be soluble in epoxy and phase separate when cured.
2. Morphology: co-continuous / phase inverted morphology provides the optimum toughness.
3. Reactive endgroups: might not be necessary, but can be an advantage.
4. Crosslink density: thermoplastics are found to be more effective in increasing crosslink density of particles modified epoxy, when compared with using CSR in particles modified epoxy.
5. Molecular weight: increased molecular weight can increase the toughness of the system, but can also depend on the practical use requirements.

To sum up, high toughness is achievable given that the PES phase is present with good thermal stability from the thermoplastic backbone and the epoxy used has a high crosslink density [26]. However, a high crosslink density and molecular weight are not necessary, as these factors would vary for different applications. The morphology has an important factor in the toughness of the PES modified epoxy, there are three phases found when different wt% of particles are added, see Figure 2.1:
At low wt%: Particles of PES in an epoxy matrix.
At medium wt%: The co-continuous (CC) structure, where both phases are continuous

and interpenetrate each other, usually formed when the viscosities are equal.
At large wt%: Phase inversion with epoxy particles in a PES matrix.

The co-continuous structure has been found to have the optimum toughness [26, 27] due to the lack of adhesion in a single phase structure (Figure 2.2).

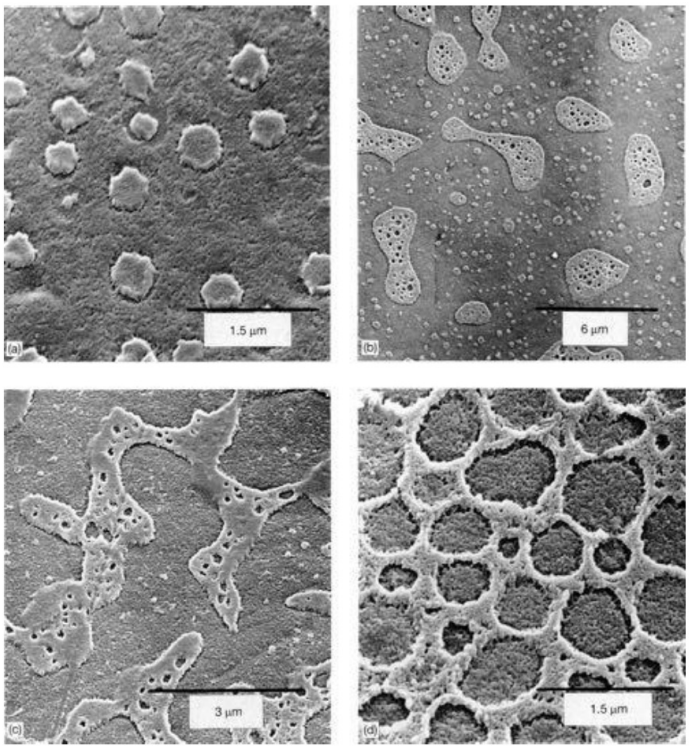


Figure 2.1: Different phases of PES in epoxy: a) Particulate, b) Transition between particulate and co-continuous, c) Co-continuous and d) Phase-inverted microstructure [28]

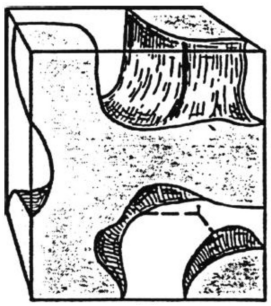

Figure 2.2: Co-continuous phase [17]

PES particles are suitable in many other applications, for example as a coating in

solvents, use in films and hollow-fibre membranes. The use of PES is well established, but not under brittle failure (such as low temperature testing and high rate effect using DMA). Therefore, this study would concentrate on comparing the established results with tests under low temperature conditions. More brittle failure and a small increase in fracture energy would be expected, but the failure mechanisms were expected to be similar to the other rigid particles used.

### 2.1.5 Ceramic microsphere-toughened epoxy

Ceramic microspheres are commonly used as an additive in applications such as paint, however, their use in epoxy as a toughening agent by industry is not common. This might be due to the complexity in the different phases formed, for example due to aggregation of spheres and interaction with CTBN or PES phases. Hence, more studies about the use of ceramic microsphere in epoxy are desired in the future.

### 2.1.6 Phase separation

For PES or CTBN modified epoxies, where the toughening phase is initially dissolved in the epoxy, there is phase separation during curing, but it may not be completed. When phase separation occurs, rubber would aggregate into micron-sized spherical particles and the addition of silica particles would reduce phase separation, and it was found by Lee et al. [15] that the silica particles added in can enhance the toughness.

The amount of phase separation can be calculated by the Fox equation, using the glass transition temperatures of the two phases. The amount of rubber that did not phase separate will reduce the measured $T_g$ of the formulation, and can be calculated by using [28]:

$$\frac{1}{T_g} = \frac{W_{ep}}{T_{g,e}} + \frac{W_r}{T_{g,r}} \tag{2.1}$$

where W = weight fraction, Subscripts: ep = epoxy, r = rubber and $T_g$ = glass transition temperature.

## 2.2 Fracture mechanics

### 2.2.1 Introduction

Linear elastic fracture mechanics (LEFM) is used in considering the fracture circumstances in epoxy polymers as they show a linear elastic response with plasticity confined

to only a small zone at the crack tip. At the crack tip, there are different directions of stresses; therefore, there would be different modes of loading, which could cause a crack to grow. All the three modes of loading (mode I, mode II and mode III) would occur at the crack tip, see Figure 2.3 [16], but mode I is the most critical one as it has the lowest energy and hence the most likely to cause fracture.

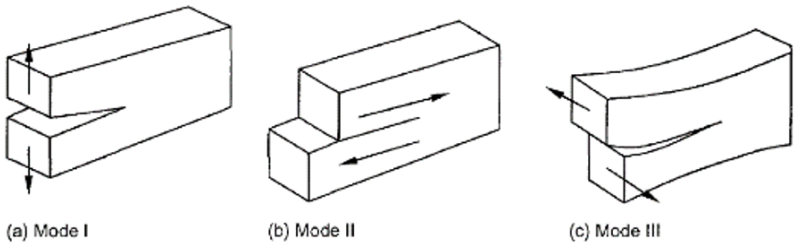


Figure 2.3: The different modes of loading for fracture [26]

### 2.2.2 Fracture energy

There are two approaches to calculate the fracture toughness, one is based on energy while the other considers the stress intensity of the crack [11].
1) Energy approach: Fracture occurs when sufficient energy is released from the stress field to cause growth of the crack, and the energy criterion is [28]:

$$\frac{1}{B}\frac{dU}{da} \geq G_c \tag{2.2}$$

where B = width of crack front, U = potential energy of the loaded specimen, a = crack length and the critical parameter is the fracture energy (critical strain energy release rate), $G_c$. For bulk linear elastic behaviour away from the crack tip, $G_c$ is given by [28]:

$$G_c = \frac{P_c^2}{2B}\frac{dC}{da} \tag{2.3}$$

where $P_c$ = load required for fracture (crack propagation), and C = compliance (displacement/load) of the specimen.
2) Stress intensity factor approach: The critical stress parameter is the critical stress intensity factor, $K_c$, which is expressed in a slightly different way under plane stress and plane strain [16]. To be conservative, the minimum value is desired, so plane strain conditions are considered in tests.

For plane stress (i.e. a thin sheet) [28]:

$$K_c^2 = EG_c \tag{2.4}$$

For plane strain:

$$K_c^2 = \frac{E}{1-v^2}G_c \tag{2.5}$$

where $E$ = Young's modulus and v = Poisson's ratio [16]. The correlation between $G_c$ and $K_c$ in plane strain is [29, 30]:

$$G_c = \frac{(1-v^2)K_c^2}{E} \tag{2.6}$$

### 2.2.3 Plastic zone size

The plane stress and plane strain conditions also have an effect on the plastic zone at the crack tip; the radius of the plastic zone at the crack tip, $r_y$, see Figure 2.4, can be calculated [29, 31].

For plane stress (i.e. a thin sheet):

$$r_y = \frac{1}{2\Pi}(K_c/\sigma_y)^2 \tag{2.7}$$

where $\sigma_y$ = uni-axial tensile yield stress and $K_c$ = stress intensity factor at the onset of crack growth.

For plane strain (i.e. a thick sheet):

$$r_y = \frac{1}{6\Pi}(K_c/\sigma_y)^2 \tag{2.8}$$

The crack opening displacement, $d_{crack}$ [16], (which is in the y direction) in plane strain is given by:

$$d_{crack} = \frac{K_c}{E\sigma_{yt}}(1-v^2) \tag{2.9}$$

where $K_c$ = stress intensity factor at the onset of crack growth, $\sigma_{yt}$ = tensile yield stress, E = Young's modulus and $v$ = Poisson's ratio [32]. All of these concepts are used in considering the right thickness of adhesive in a joint [33], which must be greater than $2r_y$ for the full toughness to be developed.

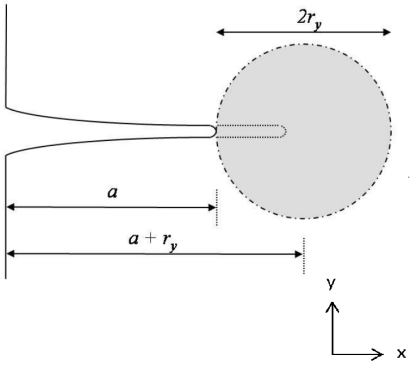


Figure 2.4: Plastic zone model [33]

### 2.2.4 Tapered double cantilever beam (TDCB)

The tapered double cantilever beam (TDCB) (see Figure 2.5) test and the double cantilever beam (DCB) test are LEFM methods that are commonly used in determining the fracture energy, $G_c$, of adhesive joints, because these methods can determine the fracture resistance of a crack to initiation, propagation and arrest.

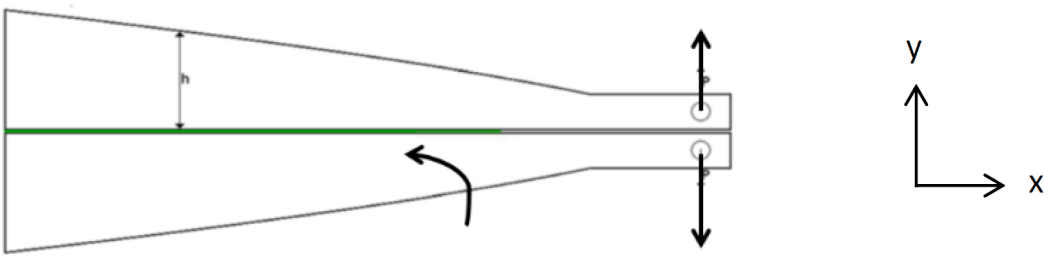


Figure 2.5: TDCB geometry [34]

Moreover, the R-curve (resistance-curve) of the adhesive fracture energy against crack length can also be found from the data obtained in the test, as the toughness may increase with crack length due to additional toughening mechanisms. Therefore, they are very useful in providing information about the fracture performance of the adhesive [31, 35].

The TDCB specimen is designed such that the fracture energy, calculated using Equation 2.10, is not dependent on the value of crack length, so the rate of change of compliance with crack length is constant [36]. The value of $G_c$ can be calculated using Equation 2.9. The relationship between compliance and crack length is kept constant

by varying the height of the specimen, see Figure 2.5, with the Equation [31, 35]:

$$\frac{dC}{da} = \frac{3a^2}{h^2} + \frac{1}{h} = m \tag{2.10}$$

where a = crack length, h = height of substrate beam at a crack length a, and m = specimen geometry factor (constant). Substituting the value of $\frac{dC}{da}$ into Equation 2.3 allows the fracture energy to be calculated.

Both TDCB and DCB specimens use the same principles in the test method (mode I, in-plane tensile), but TDCB is more stable as its shape reduces the stress concentration at the start of the crack, hence improving the accuracy of the results [31]. The TDCB is more suited to high rate tests as the failure load does not depend on the crack length, and hence the crack length does not need to be measured, thus simplifying the test method.

There are two main categories of failure types for adhesive joints. (i) cohesive and (ii) adhesive/interfacial failure. Cohesive failure is when failure happens within the adhesive layer, see Figure 2.6. This occurs when the interface strength is high [37][36]. Adnan et al. [37] showed that cohesive failure can occur under tensile loading or shear loading, where adhesive deformed through cavitation and bulk shear [37].

Adhesive or interfacial failure is when failure is in-between the adhesive and substrate [38], due to the presence of low interfacial strength [37], see Figure 2.6. Aluminium alloy has a relatively high yield stress, so a plastic zone cannot be formed there and the measured fracture energy will be much lower than the cohesive value. Therefore the fracture energy measured would be that of the adhesive/substrate interface, but not of the adhesive itself.

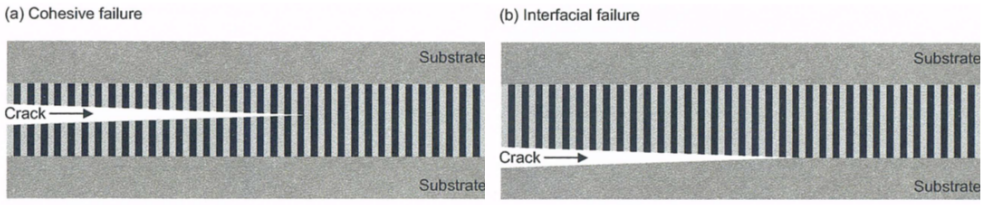


Figure 2.6: Failure modes diagram a) cohesive, and b) interfacial failure [15]

### 2.2.5 Types of crack growth

Crack growth in the TDCB test is not always in a stable manner. There are three types of crack growth (see Figure 2.7). The brittle and stable type was termed Type C [15],

where the brittle adhesive would usually have high yield stress, little plasticity and the crack would be sharp. This is a typical of epoxy adhesives, especially at high test rate and low temperatures. Smooth, featureless surfaces can be observed with continuous crack propagation [16]. Type B is stick-slip failure, which is unstable crack growth, it produces a significant pattern (where initiation and arrest points can be seen) on the load against displacement curve, it is brittle but has not got as high yield stress as Type C. Type A is stable ductile crack growth, where the adhesive has high ductility and a rough or torn fracture surface is produced. The fracture behaviour links to the testing temperature, as the adhesive usually has a low yield stress, leading to high crack-tip plasticity and blunting which cause the ductile failure and stable crack growth.

When the test rate is increased, there is less crack tip blunting [33]. Less load is required to propagate the crack than to initiate it and hence stick-slip failure occurs. When the temperature is low and the loading rate is high, crack initiation only needs a minimum yielding at the crack tip; therefore the crack is sharp and results in a low stress intensity factor. It is the same when there is a very high crack tip strain rate with very short deceleration times at arrest points [32].

When the temperature is high, the yield stress reduces and plastic flow could be increased resulting in more crack tip yielding. This results in a larger stress intensity factor [32] and hence Type A crack growth occurs. The transition between the types of crack growth depends on the temperature and usually a clear state of transition occurs, where the changes in characteristics of the points are very significant [32, 33]. Figure 2.7 shows the three different fracture types, which are extended to four types of crack growth under high rate testing (see Section 2.3) [39].

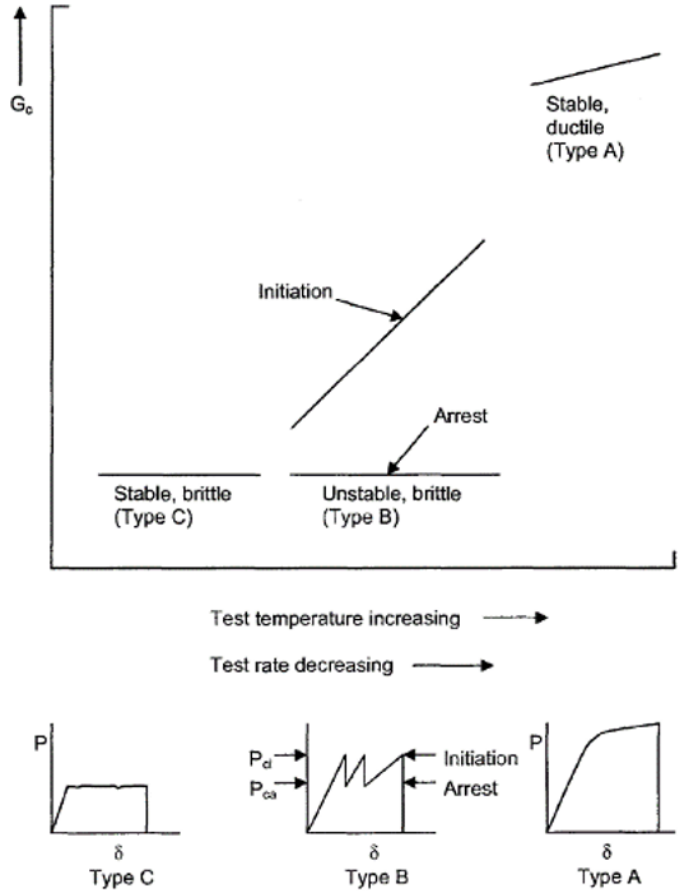


Figure 2.7: Graphic representation of fracture types under different testing conditions [15]

### 2.2.6 Single-edge notch bending (SENB)

Single-edge notch bending (SENB) tests are used with bulk materials rather than adhesive joints, and measure the fracture energy, $G_c$, and fracture toughness, $K_c$, of the material. SENB testing can be performed under both quasi-static and high rates. However, there are dynamic effects under high rate that can cause large oscillations in the results graphs. The use of damping and a displacement method can ensure that this is usually not a problem. According to the ISO 13586 standard [30], SENB specimens (see Figures 2.8 and 2.9) should be 6 mm thick, 12 mm in width and 60 mm in length, with at least 6 replicate tests for each formulation.

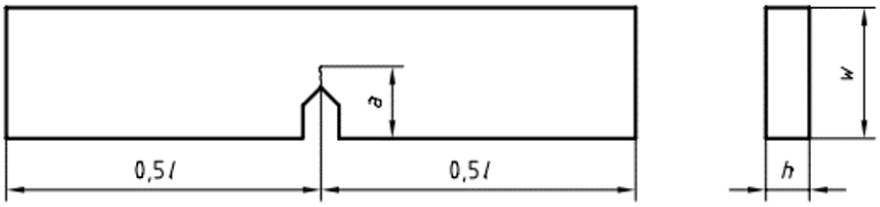


Figure 2.8: Single-edge notch bending (SENB) specimen [30]

Due to the conditions of high rate tests in this study, the linear elastic fracture mechanics (LEFM) method was used in determining the peak load from SENB testing (where the energy method would not be as accurate under high rate conditions of this material). The peak load values were then used to calculate the fracture toughness or critical stress intensity, $K_c$, and fracture energy, $G_c$. The fracture toughness, $K_c$, can be found by using [28, 40]:

$$K_c = \left(\frac{P_c}{B\sqrt{W}} f(x)\right) \tag{2.11}$$

where $P_c$ = the load at crack growth initiation (specified in the standard ISO 13586), B = thickness, W = width and

$$f(x) = 6\sqrt{x}\frac{1.99 - x(1-x)(2.15 - 3.93x + 2.7x^2)}{(1+2x)(1-x)^{\frac{3}{2}}} \tag{2.12}$$

$$x = \frac{a}{W} \tag{2.13}$$

The fracture energy can be calculated for the LEFM method [41] using:

$$G_c = \frac{((1-v^2)K_c^2)}{E} \tag{2.14}$$

where the Poisson's ratio v = 0.35 [41], and E = tensile Young's modulus. To make the results valid, there are two criteria which must be met [30]:

1. Size calibration:

$$B, a, (W-a) > 2.5\frac{K_c}{\equiv_\sigma yt} \tag{2.15}$$

2. Maximum fracture load, $P_{max}$:

$$\frac{P_{max}}{P_Q} < 1.1 \tag{2.16}$$

$P_Q$ is the load where the crack starts to grow at the start of test, and $P_{max}$ is the maximum load, which may happen towards the end of the test, as the specimen is about to break.

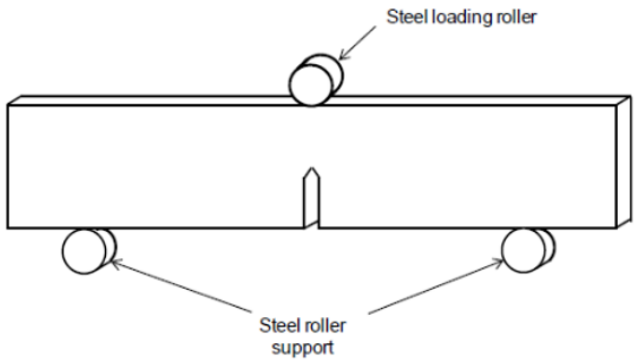


Figure 2.9: Single edge notch bending (SENB) test, loaded in three point bending [41]

## 2.3 High rate testing

### 2.3.1 Introduction

There are very limited studies on high rate testing of toughened epoxies due to the challenges involved, such as: 1. The more complicated failure mechanisms and dynamic effects in high rate can cause problems with accuracy of the analysis and the results; 2. The analysis needs to be chosen according to the type of fracture (stable propagation and stick-slip failure are analysed with different approaches), and 3. Due to the increase in

the kinetic energy in the high rate test, this energy must be accounted for in the results [42]. Therefore a data reduction strategy was developed by Blackman et al. [43] for accurate high rate data analysis. The data reduction strategy is summarised in the flow chart shown in Figure 2.10 [43]. This protocol was first used for DCB specimens using a frame-by-frame analysis of video approach. Four groups of fracture types were developed in the protocol, and more details are discussed in the high rate test experimental Section 5.1. This protocol enables the analysis of high rate results taking account of dynamic effects, hence the reliability of the data is assessed.

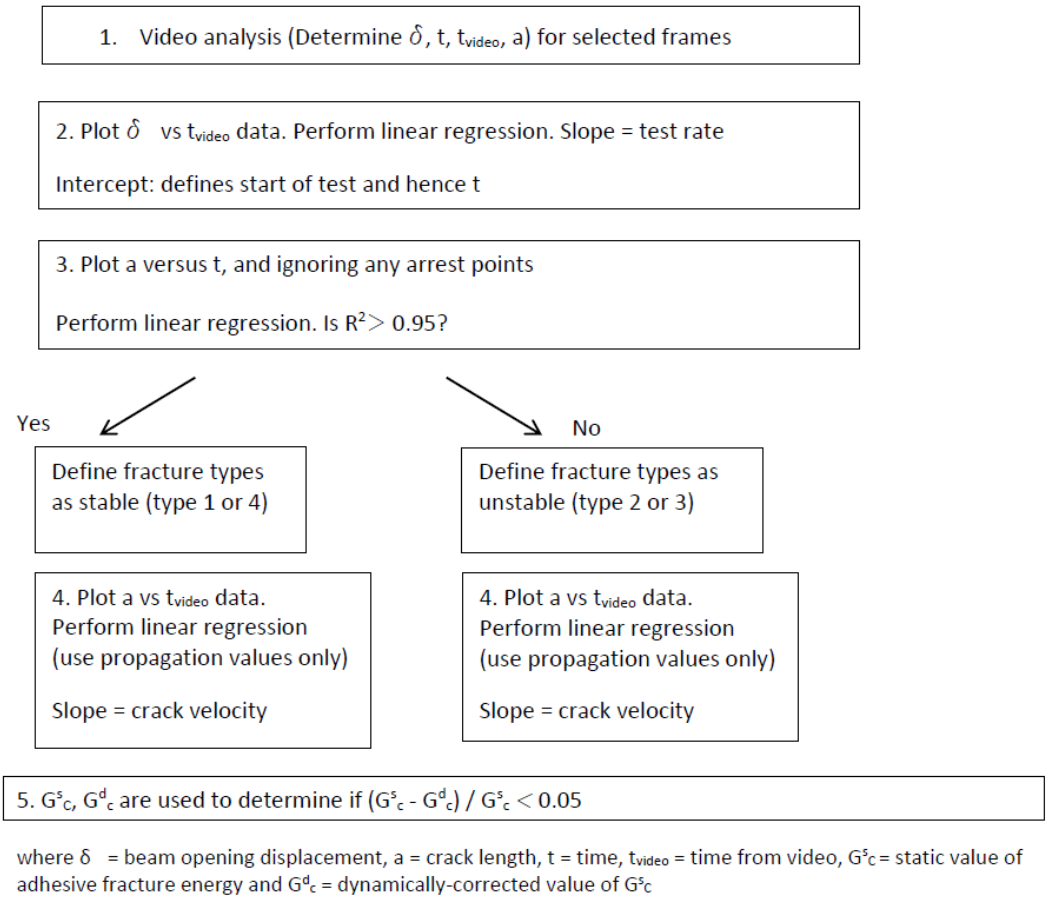


Figure 2.10: Flow chart for data reduction strategy of TDCB test [43]

There are several factors that can affect the high test rate results, and the main considerations are stated in Section 2.3.2.

### 2.3.2 Uncertainties

When measured load values were reliable it means that there were no significant dynamic effect that altered the values, so type 1 and 2 were considered to be reliable, see Figure 2.10. Other uncertainties were also taken into account of the reliability of the results, such as uncertainties from the instruments used and the analysis types. For example, it was reported that there was a 6 % uncertainty when analysing type 1 and 2, while there was a 4 % uncertainty in analysing type 3 and 4 [44]. Thus the uncertainties vary slightly when the different types of analysis were used, but are small.

It is expected that there would be more unstable crack growth when the rate of test increases. This was found by Blackman et al. [45], where at test rates higher than 8.3 x $10^{-5}$ m/s, unstable crack propagation occurs. It is found that the initiation and arrest points are difficult to distinguish when the rate is 1 m/s, this could be due to the decrease in crack-length distance between initiation and arrest points [46]. Identifying crack initiation and arrest points at rates higher than 10 m/s is impossible [47].

It is expected that when the test rate is high, the toughening mechanisms would become less effective, which means there would be less plastic deformation due to the lower energy dissipation at the crack tip as the yield stress will increase with test rate [44].

### 2.3.3 Geometry factor

The flexural rigidity of the specimen is highly related to the test geometry. The TDCB has a high flexural rigidity when compared to DCB, hence could provide more reliable results at both low and high rates. The larger size of the specimens also reduces the thermal shrinkage between substrate and adhesive layer, and as the data reduction strategy does not consider residual stresses, TDCB specimens have their advantage. However, this larger geometry can also bring more significant inertial effects that could lead to unstable crack growth [48]. The geometry factor is also affected by the toughness of the adhesive, the tougher the adhesive is, the less that it is affected by the inertial effects. Therefore, it is expected that TDCB specimens would provide more reliable results when compared to DCB specimens.

More about the data reduction method is described in the experimental part of this thesis in Section 5.3.

## 2.4 Toughening mechanisms

### 2.4.1 Introduction

There are different toughening mechanisms for different kinds of particles. For large particles, the main toughening mechanisms are pinning, deflection, debonding with void growth and shear yielding (i.e. shear bands). Pinning and deflection would not occur for small particles (nanometre-sized particles), as nanoparticles would be too small for these mechanisms to occur (as the diameter of the particle, $d_{particle}$, is a lot smaller than $d_{crack}$). Instead, the mechanisms for nanoparticles are debonding followed by void growth and shear yielding. This depends on the relationship between the diameter of a particle, $d_{particle}$ and crack opening displacement, $d_{crack}$, and more details are described in Section 2.4.3.

### 2.4.2 Shear bands and shear yielding

Shear banding is produced when there is a tensile stress applied to the polymer chains, and is caused by the orientation of polymer chains. It is plastic deformation due to shear force [29], which absorbs energy and hence increases toughness. It is a mechanism that involves localized inhomogeneous plastic deformation [33]. It occurs when there is a brittle fracture; it involves only little energy dissipation. But when there is a higher shear deformation around the crack tip, propagation of crack would become ductile. Therefore it would blunt the crack tip, and this leads to an increase in toughness of the material. When there is bulk yielding and fully ductile failure behaviour, shear yielding can be limited [33].

### 2.4.3 Crack pinning

The crack can be pinned when approaching particles, and so bows out between them. As the energy is proportional to the length of the crack front then extra energy is required, increasing the toughness. The crack then breaks away and moves forward from the particles, producing tails at the particles. This is due to the presence of rigid particles. Secondary cracks could be formed between particles if bow out is followed by crack pinning [40]. This would produce a new fracture surface and an increase in the length of crack front. The consequence of the formation of new surfaces is the increase in crack resistance, as the energy needed would be higher [40], see Figure 2.11. Crack pinning can only happen when the diameter of a particle, $d_{particle}$, is larger than the

crack opening displacement, $d_{crack}$, so will only occur with large particles (i.e. micron sized) [33].

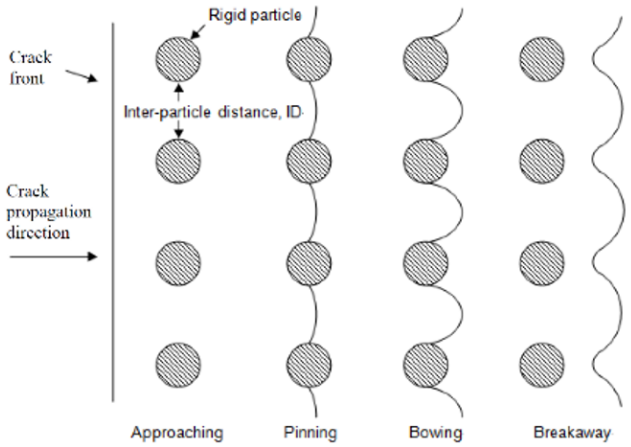


Figure 2.11: The process of crack pinning [29]

### 2.4.4 Crack deflection

When the crack is approaching a rigid particle, it is deflected around the particle, see Figure 2.12, as it cannot propagate through the particle which is tougher than the epoxy. This tilts the crack, so the local crack propagation is mixed mode (I/II) not pure mode I. Thus more energy is required, as mode II propagation crack requires more energy than mode I, increasing the measured toughness. There is usually an angle of where the crack tilts, and this would depend on the stress and the particles there. Crack deflection also causes a tail to be formed behind a particle. As for crack pinning, crack deflection requires that $d_{particle} > d_{crack}$ [33].

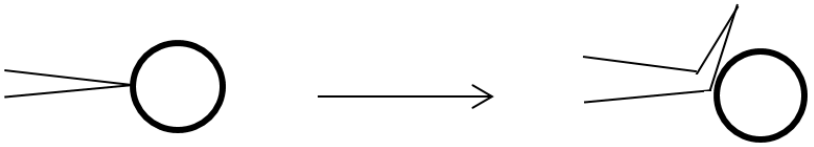

Figure 2.12: Crack deflection by a particle, after [33]

### 2.4.5 Cavitation

Cavitation is when the triaxial stresses in the plastic zone at the crack tip cause a soft particle to fail internally. This causes a void within the particle, see Figure 2.13. It

causes blunting of crack under the triaxial stress state [49]. It happens before the shear yielding or plastic void growth, cavitation does not give a significant toughening effect on its own, but plastic deformation involving enlarged voids, which require a higher surface and strain energy and hence increase energy dissipation [50], increase the toughness. It was found that there would be more initiation of cavitation for particles which had a higher Poisson's ratio [51] or a larger diameter [52].

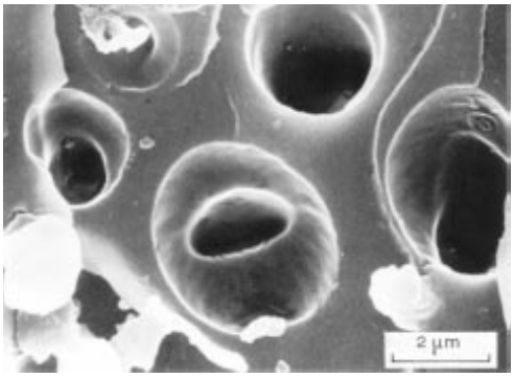


Figure 2.13: SEM image of cavitation of rubber particles [6]

### 2.4.6 Debonding

Debonding will occur when the interfacial adhesion between the particle and the epoxy is poor, so the particle becomes detached from the epoxy when under stress. Surface debonding involves only a small amount of energy being absorbed. However plastic deformation and void growth follow debonding, and these processes can absorb a significant amount of energy [29], see Figure 2.14.

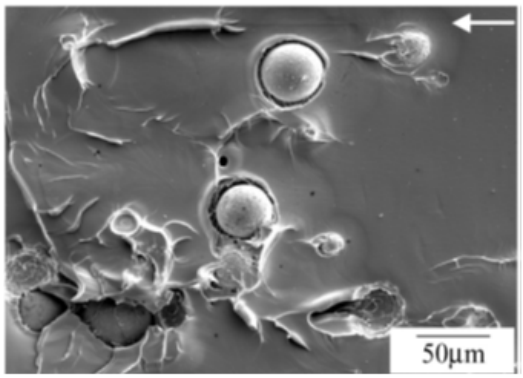


Figure 2.14: SEM image of debonding of glass particles [53]

### 2.4.7 Rubber bridging

Bridging occurs when rubber particles are stretched and a bridge is formed in-between the two fracture surfaces of a crack. It is only for large (micron sized) particles as smaller particles will fracture before the bridge is formed. Stretching of the rubber will require energy, but it is not a major mechanism and does not show any significant effect in rubber particle toughening as the particles are very soft [29], see Figure 2.15.

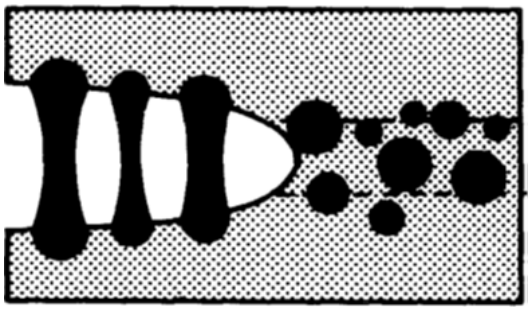

Figure 2.15: Rubber bridging model [54]

### 2.4.8 Plastic void growth

Figure 2.16 below shows the result of plastic void growth of a rubber modified epoxy. Debonding of hard particles or cavitation of soft particles relieves the constraint on the epoxy. The triaxial stress in the plastic zone at the crack tip causes the voids to grow and hence dissipates energy [55]. Plastic void growth has a great effect on the fracture energy measured. More regarding plastic void growth of rubber modified epoxy are discussed with the SEM images in the experimental results section in Chapter 9.

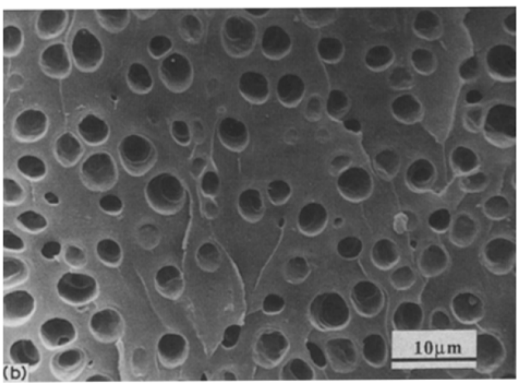


Figure 2.16: SEM showing plastic void growth of epoxy (tested at 40°C) [55]

### 2.4.9 Modelling toughening mechanisms

The toughness of the particle modified epoxy can be predicted using analytical models [2, 3]. In theory, there would be 100% cavitation and void growth for soft particles, or debonding and void growth for rigid particles. However, all of the mechanisms are affected by the particle distribution, particle size, volume fraction and stress field due to the neighbouring particles [56]. Therefore, not all of the particles can undergo the toughening mechanisms.

The percentage of voids is low when particles are too close, as the energy required for voiding would be too high [2]. However voids can be formed further away from a voided particle. According to this theory, when there is a large wt% of silica nanoparticles, there would only be 14.3 % of voids [2]. On the other hand, when particles are a long distance apart, 100% of voids can be achieved with silica.

For large ceramic particles such as glass, the proportion of particles which debond can vary from 0% to 100% depending on the strength of interfacial adhesion [57, 58].

For rubber particles, both CTBN and core-shell rubber, 100% of the particles cavitate, e.g. [3]. For both particles types (soft and silica), shear yielding is the main toughening mechanism, e.g. [3]. The total energy absorbed can be predicted analytically by:

$$G_c = G_{shear} + G_{DB+VG} + G_{unmodified} \tag{2.17}$$

where $G_c$ = fracture energy, $G_{shear}$ = fracture energy from shear-banding, $G_{DB+VG}$ = fracture energy from debonding and void growth and $G_{unmodified}$ = fracture energy of unmodified epoxy. Expressions for these terms have been derived by Huang and Kinloch [59] and Hsieh et al. [29].

## 2.5 Conclusions

Many aspects of the use of particles in modifying epoxy have been reviewed. A significant improvement in toughness has been found in most of the studies available. The level of improvement can be highly affected by the dispersion of the particles and the individual toughening mechanisms. Other factors that contribute to the properties of joints are such as surface treatment and adhesive thickness, because they would affect the failure type and crack growth type. Epoxy toughness can be quantified using a fracture mechanics approach, such as the energy approach using TDCB specimens. At quasi-static test rates the analysis is relatively straight forward. However, at high test rates the analysis depends on the specimen behaviour (e.g. type of crack growth) and

may be affected by dynamic effects. Therefore, fewer studies have been conducted using high rate, and more investigations and understanding of their toughening mechanisms are required for further improvement of the material, especially at high rate.

# Chapter 3

# Materials

## 3.1 Introduction

There were in total four types of particles used: silica nanoparticles, core shell rubber (CSR), polyethersulfone (PES) and alumino silicate ceramic particles. These represent the main classes of particles used to modify polymers, i.e. ceramic, rubber and thermoplastic. Hybrid formulations were also used, by combining soft polymeric particles with hard ceramic particles, as previous work has shown that this may lead to a synergistic toughening effect [4]. The particle sizes were chosen to give a large difference in diameter, e.g. 20 nm diameter silica and 38 to 106 $\mu$m diameter core shell rubber particles. The epoxy and the particles used are discussed in more detail in the sections below.

## 3.2 Epoxy polymer

The epoxy resin was Araldite LY 556 (Huntsman Advanced Materials, Belgium), which is a diglycidyl ether of bisphenol A (DGEBA) with an epoxy equivalent weight (EEW) of 185 g/mol and density of 1.175 g/ml [60]. As some of the nanoparticles are supplied in epoxy resin, the stoichiometric amounts of the epoxy for the silica, CSR, epoxy and hardener were found by using their equivalent weight.

The hardener was Albidur HE-600 (Nanoresins, Germany), which is an accelerated methylhexahydrophthalic acid anhydride with a density of 1.08 g/ml, and an anhydride equivalent weight (AEW) of 170 g/mol [61]. This was used at a stoichiometric ratio of 1:1.09 resin:hardener.

## 3.3 Silica nanoparticles

The silica nanoparticles were Nanopox F400 (Nanoresins, Germany), which is a masterbatch with 40 weight % of silica particles in DGEBA and a density of 1.4 g/ml [62]. These silica particles have a mean diameter of 20 nm, they are in the form of a colloidal silica sol. The silica has been surface-treated by the manufacturer to prevent agglomeration.

The nano-silica particles were added in at 0.5, 1, 2, 3, 5, 10, 15, 20 weight % and at the maximum concentration of 25.4 weight %. The results were expected to show a positive increase in toughness with increasing weight % of silica particles, followed by a plateau at the maximum point. However, the low weight % of the silica particles may show a steeper increase, as hinted at other work [13]. This outcome will be particularly linked to the mechanisms of fracture, especially variations in the percentage of silica particles which undergo debonding and void growth. The properties of silica-modified epoxy would be compared with CSR-modified and hybrid (silica and CSR) epoxies.

## 3.4 Core shell rubber

The core shell rubber was Paraloid EXL-2300G (Rohm and Haas, UK). The particles are supplied in powder form. They were sieved into three sizes: $>106$ $\mu$m, in-between 106 $\mu$m and 38 $\mu$m and $< 38$ $\mu$m. The size of in-between 106 $\mu$m and 38 $\mu$m were used in this work. Specimens with 0.5, 1, 2, 3, 5 and 10 weight % of CSR were made, as 10 weight % was the highest possible wt% for mixing CSR particles into epoxy, due to the increased viscosity.

## 3.5 CSR / silica hybrid

The hybrid formulations used the same wt% of silica nanoparticles and CSR mixed into the epoxy, e.g. 5 weight % of silica plus 5 weight % of CSR. A maximum of 10 weight % CSR and 10 weight % of silica was used, as this was the highest possible wt% which could be manufactured due to the high viscosity.

Synergy has been observed for the toughness of epoxy with micron size CTBN + nanosilica [63] but not with micron size CSR particles + nanosilica. The presence of a synergy effect in the CSR hybrid would be investigated, using CSR particles which are much larger than those used previously. The sieved CSR with particles sizes in-between 106 $\mu$m and 38 $\mu$m were used.

## 3.6 Polyethersulfone (PES)

PES (Polyethersulfone) is a thermoplastic, it is available as a heat resistant amorphous resin or in powder form. It has a high $T_g$ of $225^oC$ [64], and often the powder form is used for modifying epoxy to improve impact strength. The powder form used is the 5003P grade (SUMIKAEXCEL, Japan), which has the reduced viscosity of 0.5 cP, it has good adhesion properties because of the presence of the terminal hydroxyl group, ranging from 0.6 to 1.4 wt% of polymer repeating units [64]. Due to the properties of the blend, it is expected to have 3 phases when different wt% of PES is added:
At low wt%: Particles of PES in epoxy matrix.
At medium wt%: Co-continuous (CC) structure with one phase inside the other, usually formed when the viscosities are equal.
At high wt%: Phase inversion (PI) with particles of epoxy in a PES matrix.
Co-continuous phase and phase inversion were often observed in thermoplastic modified epoxies, such as the study from Chen et al. [27]. The co-continuous phase can in some cases have a better fracture resistance than the phase-inverted structure, due to the lack of adhesion between the epoxy and PES phases.
The % of PES particles used was 0, 2, 5 and 10 weight %
Hybrids (PES + silica) were also made, more details are shown in Section 3.7.

To mix the PES into the epoxy, the powder form PES was first dissolved in DGEBA before mixing with the silica masterbatch and hardener. After a few trials, it was found that the particles could be dissolved at about $145^oC$ overnight. An electric mixer was used throughout the whole process to ensure that the particles were evenly distributed.

## 3.7 PES / silica hybrid

The PES / silica hybrids, used 2, 5 and 10 weight % of each particle. Equal amounts of each were used, so the 2 wt% hybrid contains 2 wt% of PES and 2 wt% of silica. This combination has both large and small particles, hence it could enhance the toughening effect. Hybrid PES / silica with silica had not been studied previously, so this combination would provide some information on the hybrid effect of silica with thermoplastics, and whether a similar synergy is seen as with CTBN rubber.

## 3.8 Alumino silicate ceramic microsphere

The ceramic microsphere used were grade ceramic microsphere (3M, USA), and are white-coloured high-strength microsphere that are made of alkali alumino silicate ceramic. They have a size of 13 $\mu$m by volume, surface area of 5 $m^2/cm$ and true density of 2.4 g/$cm^3$ [65]. They are often used to reduce VOC levels, increase filler loadings, and improve hardness and abrasion resistance [66]. The wt% of ceramic microsphere particles added in to the epoxy was 2, 5 and 10 weight %.

Hybrid ceramic microsphere andcore shell rubber specimens were also produced, and are included in Section 3.9.

Ceramic microsphere are more commonly used as an additives in paint and coatings, to provide resistance to high temperature. Ceramic modified epoxy is also used as a coating for factory or warehouse floors to improve abrasion resistance. The microsphere were added to the DGEBA and mixed before the hardener was added.

## 3.9 Alumino silicate ceramic / CSR hybrid

Hybrids of alumino silicate ceramic microsphere and core shell rubber particles were used in 2, 5 and 10 weight % for comparison with other formulations. This combination is also one large type (CSR particles) and one small type of particles (ceramic particles), which will allow comparison with similar systems, such as the micron size CSR / nano-silica hybrid.

## 3.10 Conclusions

This Chapter has described the choices of particles used in toughening the epoxy specimens used. The properties of particles and the formulations used have been included. The toughening effects found from experimental results are expected to behave according to the particle properties described in this Chapter and the relevant toughening mechanisms. The next Chapter onwards discusses the testing methods used to investigate the fracture properties using TDCB tests.

# Chapter 4

# Tapered Double Cantilever Beam

## 4.1 Introduction

Tapered double cantilever beam (TDCB) specimens were prepared using an epoxy with a range of different concentrations of particles. This Chapter discusses the experimental details of preparing TDCB joints, the test method, and how the data were analysed. The experimental results of quasi-static rate TDCB tests using silica, CSR and silica / CSR hybrid formulations are presented.

## 4.2 Experimental

### 4.2.1 TDCB specimen preparation

Aluminium alloy substrates (grade EN AW 2014A) were used in preparing the TDCB specimens. The substrates were first cleaned with acetone, and grit-blasted with 180/220 mesh alumina grit using a compressed air pressure of 400 kPa. The surface was then cleaned with acetone again before chromic acid etch treatment. The substrates were placed in a 70$^o$C chromic-sulphuric acid bath for 10 minutes (composition of bath is 0.1 kg of copper sulphate, 3.87 kg of sodium dichromate, 0.06 kg of powdered aluminium, 7.2 litres of sulphuric acid (s.g. 1.84) and 40 litres of distilled water) [67]. They were then rinsed with tap water and placed in a tap water bath for 15 minutes. They were rinsed with distilled water and then dried in an oven at 90$^o$C for 5 minutes.

The epoxy resin and hardener were poured into a breaker, mixed using a mechanical stirrer at 60$^o$C for 15 minutes at 90 rpm, then degassed in a vacuum oven. The mixture was spread on the substrate using a spatula, ensuring that it covered the whole surface. A piece of polytetrafluoroethylene (PTFE) film (Aerovac, UK) of 60 mm long was placed at one end for creating a pre-crack, and a stainless steel wire of 0.4 mm diameter was

placed at each end of the substrate to provide a constant thickness of the adhesive layer of 0.4 mm.

A bonding jig (Figure 4.1) was used to align and clamp the substrates together. Three specimens were prepared each time; this can provide a higher consistency of the specimen conditions (as they would be prepared with the same jig). The jig was coated with release-agent Frekote 700-NC (Loctite, UK) to prevent the adhesive sticking to the jig and allowing removal of the specimens. The specimens were placed in the jig, and each of the two substrates were aligned. The jig was closed and the nuts were tightened to a torque of 11 Nm. The jig was placed in a fan oven, and the adhesive was cured, using the schedule described in Section 4.2.2 below

After curing the specimens were removed from the jig and the excess adhesive was removed using sandpaper. The joint was coloured using white correction fluid and a paper ruler marked in millimetres was secured under the bonding line to allow the crack length to be measured, see Figure 4.2.

Figure 4.1: TDCB bonding jig

Figure 4.2: TDCB specimens

### 4.2.2 Differential scanning calorimetry (DSC) tests

The completeness of curing was confirmed by measuring the glass transition temperature, $T_g$, of the specimens using differential scanning calorimetry (DSC) [44]. There were two different curing cycles used in the 1st and 2nd sets of control specimens to compare the $T_g$ of the specimens, and to ensure that the epoxy was fully cured even with the high thermal inertia of the substrates and the jig. The two curing cycles used were:
Control 1st three specimens: Preheat oven to 60°C, ramp at 1°C/min to 95°C, dwell for 1 hour, ramp at 1°C/min to 165°C, and dwell for 2 hours, ramp at 2°C/min to room temperature (20°C).
Control 2nd three specimens: Preheat oven to 60°C, Ramp at 1°C/min to 95°C, dwell for 3 hours, ramp at 1°C /min to 155°C and dwell for 5 hours, ramp at 2°C/min to room temperature (20°C).
As the oven does not have forced cooling, the specimens will cool slowly to room temperature.

DSC works by measuring the amount of heat energy needed to increase the temperature of the sample. An example of the second heating cycle is shown in Figure 4.3.

For the DSC measurements, 10 mg samples were used. Samples were taken from the TDCB joints using a knife, weighed and sealed into a pan. The procedure was to heat from 30$^o$C to 180$^o$C, at a rate of 10$^o$C/min, cool to 30$^o$C, heat from 30$^o$C to 180$^o$C. This

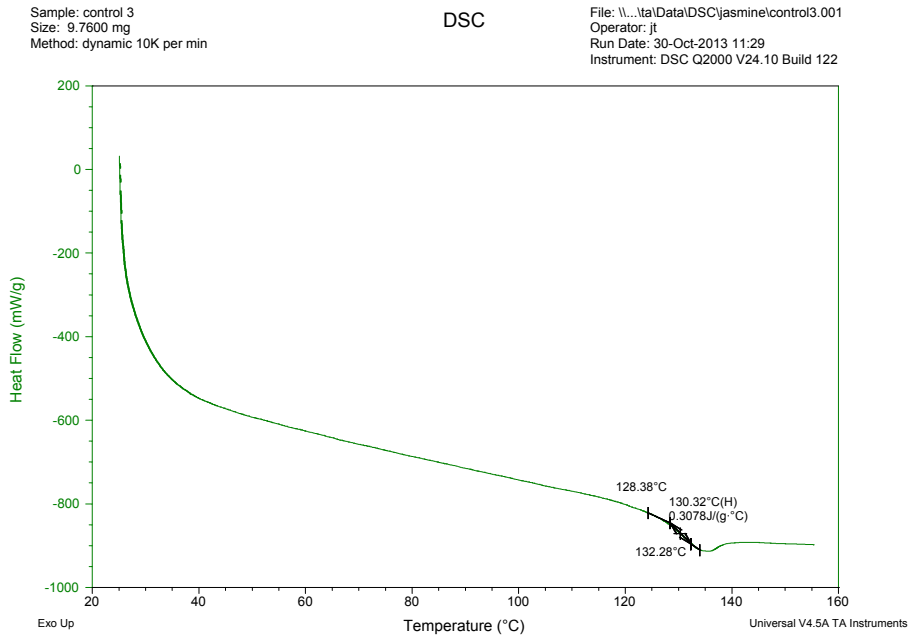


Figure 4.3: Second heating cycle in DSC showing calculation of $T_g$

first heating cycle erases the history of sample. The $T_g$ was obtained from the second heating cycle. The glass transition temperature, $T_g$, was found by using the slope before the dip. The final $T_g$ was the average of three repeats. $T_g$ measured was 133.2$^o$C for both curing cycles, which was in the expected range. Hsieh et al. [2] reported 143$^o$C ($\pm$2$^o$C) for the same anhydride-cured epoxy via DSC. Johnsen et al. [1] reported $T_g$ (DMA) is 10 to 18$^o$C higher than $T_g$ (DSC) and Mohammed et al. [4] reported a $T_g$ of 153$^o$C using DMA. The $T_g$ value can be slightly different when there is a different curing cycle used, as well as different specimen size. Therefore no adjustment is needed for the curing cycle used in all the other specimens. The curing cycle chosen for all the rest of specimens was the first one: Preheat at 60$^o$C, ramp at 1$^o$C/min to 95$^o$C, dwell for 1 hour, ramp at 1$^o$C/min to 165$^o$C, and dwell for 2 hours, ramp at 2$^o$C/min to room temperature (20$^o$C)

### 4.2.3 Quasi-static rate tests

The TDCB tests were performed using a tensile testing machine with a cross-head displacement rate of 0.1 mm/min, see Figure 4.4. The specimen is fixed with a load-cell of 5 kN, and the load and displacement were recorded by the testing machine. The

experiment was set up with a travelling microscope for measuring the crack length. The crack length was measured to a precision of 0.5 mm. The procedure is described in more detail below.

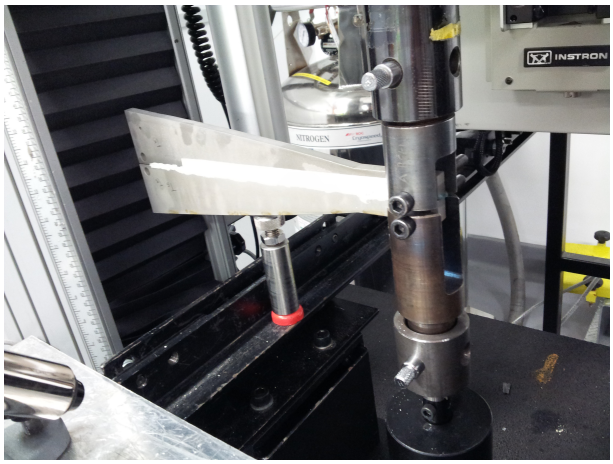


Figure 4.4: TDCB test set up for room temperature tests

### 4.2.4 Initial loading and re-loading

There were two loadings performed in each quasi-static TDCB test: 1. Initial loading (precracking) and 2. Re-loading (actual loading) [31]. During the initial loading at a constant cross-head rate of 0.1 mm/min, the test was stopped when the crack travelled beyond the end of the starter film, which would be the insert length ($a_0$) and started to propagate into the adhesive. This generates a sharp natural crack, as the starter film is relatively blunt and many give $G_c$ values that are high.

The specimen was then unloaded at a constant cross-head rate of 0.1 mm/min, and readings were taken at about every 0.1 mm of change of extension. This closed the crack up, the unloading curves should be able to go back to the origin, a slightly negative force when the extension was zero was acceptable, as there might be slight inaccuracy from reading or some interference between the fracture surfaces, but a large negative load value would be an indication of permanent deformation of the substrate and the test would not be valid. No permanent deformation of the substrates was found in any of the tests.

The specimen was reloaded at the same rate as the initial loading (0.1 mm/min). The first crack propagation would be the precrack value (NL, Visual and Max/5 wt%), as explained in Section 4.2.5 below. The crack length readings were taken until the

specimen was opened up completely or until there were enough data points. At least 15 readings are recommended by the protocol from Blackman et al. [48].

### 4.2.5 Initiation and propagation values

There were three types of initiation values, NL, Visual and Max/5 % and visual observation was used in this study [28]:
Non-linear (NL): There is a linear region at the beginning of the force versus displacement graph where the material can go back to its original shape with linear elastic deformation. NL is the point at which the elastic behaviour ends, and the force versus displacement data start to curve away from linear.
Visual observation (Vis): It is the first visible crack propagation.
5 % or Max: It is the maximum point from the curve (Max), or where a line of initial compliance +5 % cuts the graph (5 %). The value which occurs at the smaller displacement should be used.

All these initiation values were calculated, but the visual values will be used in this thesis. The height of the substrate was measured at 3 points (near both ends and at the middle) of the beam before and after bonding, in order to monitor the thickness of the adhesive layer. The thickness of epoxy was 0.4 mm as expected. The height of specimen is tapered such that a constant specimen geometry factor, m, is used.

$$\frac{3a^2}{h^2} + \frac{1}{h} = m \tag{4.1}$$

where a = crack length, m = 2 $mm^{-1}$, h = height of substrate beam at a crack length of a [28].

### 4.2.6 Determination of $G_c$ in TDCB

There are three methods for determining the value of $G_c$ : Experimental compliance method (ECM), simple beam theory (SBT) and corrected beam theory (CBT) [68]. Their equations are shown below. The use of ECM and CBT can provide more accurate results [31] than SBT, because of the simplifying assumptions that the SBT method makes.
Experimental compliance method (ECM):

$$G_c = \frac{P^2}{2B}\frac{dC}{da} \tag{4.2}$$

where P = critical load, B = width of specimen, and dC/da is obtained from the

slope of the graph of C against a (a = crack length, C = compliance).
Simple beam theory (SBT):

$$G_c = \frac{4P^2}{E_s B^2} m \tag{4.3}$$

Corrected beam theory (CBT):

$$G_c = \frac{4P^2 m}{E_s B^2} \left( 1 + 0.43 \left( \frac{3}{ma} \right)^{1/3} \right) \tag{4.4}$$

where $E_s$ is the flexural or tensile modulus of the substrate.

It has been shown that the CBT method is more accurate than the SBT method, because of the correction factors that are in the equations. The CBT method is also easier to apply when compared to the ECM method. It also produces less scatter because it is not dependent on measurements of the displacement ($\delta$). For the unmodified epoxy, control samples results from all three methods were studied, and details for the comparison are shown in Section 4.3.1.

## 4.3 Quasi-static TDCB results

### 4.3.1 Fracture energies

The three methods (simple beam theory, corrected beam theory and experimental compliance method) used to calculate the fracture energy values were expected to give similar values, and they did. Table 4.1 compares the $G_c$ values for the control (unmodified) epoxy for the three methods. Simple beam theory (SBT) usually gives a slightly lower value according to previous experience [31], and these data fit this observation.

There are two types of crack propagation - stable propagation and stick-slip, see Figure 4.8. These values cannot be averaged, and need to be considered separately, such as by comparing averaged initiation values etc. [31]. The data are expected to show an increase in the amount of stick-slip when the test rate is increased [43], as discussed in Section 5.1.

### 4.3.2 Control

Stick-slips with propagations were found for the control specimens, but mostly the TDCBs failed by stable crack propagation. Table 4.1 and Figure 4.5 show the control TDCB fracture energies from the SBT, CBT and ECM methods. Using the CBT

method, an average fracture energy of 80 $J/m^2$ was calculated. The fracture energies from the control specimens were lower or at the lowest end of results ( to 110 $J/m^2$) when compared to studies from Masania et al. [1, 69], but these results are realistic, as they are similar to the 77 $J/m^2$ found from Hsieh et al. [2].

The lower fracture energy values might be due to the thin layer of adhesive applied on the joint, and with relatively small standard deviations (within 10 %), the control results were considered to be very reliable for the epoxy material.

Figure 4.5 shows that the crack initiates at high $G_c$. When stick-slip crack propagation occurs, the crack propagates very quickly for a distance and then arrests. The following arrest points are at lower $G_c$ as there is insufficient energy for the crack to grow further. The crack length then stays constant, the applied load would increase until initiation starts again when the critical value of fracture energy is reached.

Table 4.1: TDCB fracture energy results for control epoxy

| Point [J/m$^2$] | $G_c$ (SBT) | $G_c$ (CBT) | $G_c$ (ECM) |
|---|---|---|---|
| Mean propagation | 73 | 80 | 111 |
| SD of propagation | 7 | 7 | 9 |
| Mean initiation | 81 | 89 | 123 |
| SD of initiation | 5 | 6 | 10 |
| Mean arrest | 56 | 62 | 83 |
| SD of arrest | 3 | 3 | 4 |

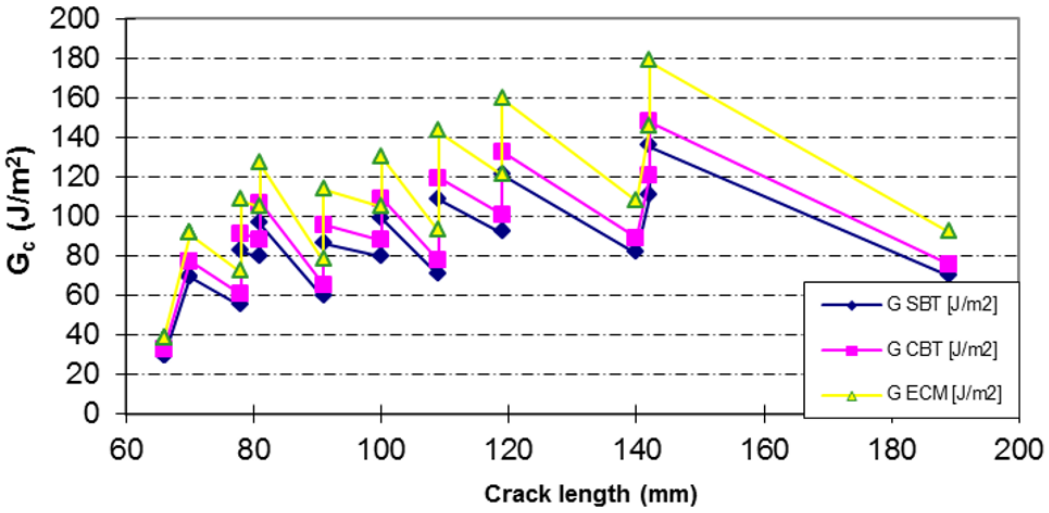


Figure 4.5: Fracture energy versus crack length for the control epoxy from TDCB specimen

### 4.3.3 Silica-modified epoxy

There was a mixture of stick-slip and stable crack propagations in the silica modified epoxy specimens. The addition of silica generally increased the toughness compared to the control epoxy, see Table 4.2. There was an increasing trend in mean $G_c$ from control to the addition of 2 weight % of silica, but when there was a higher amount of silica added, no pattern was formed and values were a lot lower than expected. There was interfacial failure, and no stick slips, in specimens with 10 and 15 weight % of silica.

According to the initiation data shown in Figure 4.6, there is a peak in the $G_c$ value with the addition of 2 weight % of silica, the $G_c$ value dropped after this point. This could be due to the presence of greater than 15% of debonding when a lower % of silica is added. It has been shown from previous studies [2, 70] that toughening using silica particles was due to debonding and void growth, but not all of the silica particles debond, typically 15% using the silica particles debond. However these authors only considered high wt% of silica, and would not have observed a peak at low wt%.

The % of debonding reduces when there is a higher % of silica added, because when particles are more concentrated, they would become too close to each other, so the energy needed for voiding would be higher [4], therefore these results are according to predictions. It is also found by Johnsen et al. [4] that there was a large increase in fracture energy when 13 wt% of silica nanoparticles were added in [4].

There were two lower values when 3 wt% and 15 wt% of silica particles were used,

these drops were not expected, they would be errors due to the use of specimens from different batches, as the graph is expected to show a clear trend. A plateau is expected after the peak, the relatively high weight % of silica particles would not show significant effects in toughening. At very high weight % of silica particles the toughness will decrease due to there being too little epoxy between the particles to absorb the maximum energy, this occurred for some of the silica specimens.

Table 4.2: Summary of fracture energies of silica modified epoxy calculated using the CBT method from TDCB specimens, mean and standard deviation shown

| Wt% of Silica | Initiation ($J/m^2$) | init-SD | Arrest ($J/m^2$) | arrest-SD | Propagation ($J/m^2$) | prop-SD | Hsieh-% | Hsieh-$G_c$ ($J/m^2$) |
|---|---|---|---|---|---|---|---|---|
| 0 | 88 | 6 | 62 | 3 | 80 | 7 | 0 | 102 |
| 0.5 | 95 | 3 | 67 | 5 | 76 | 3 | 4 | 122 |
| 1 | 142 | 5 | 87 | 4 | 129 | 5 | 8 | 149 |
| 2 | 158 | 1 | 73 | 1 | 123 | 9 | 11 | 169 |
| 3 | 116 | 9 | 102 | 8 | 134 | 6 | 15 | 190 |
| 5 | 70 | 1 | 64 | 1 | 113 | 20 | 20 | 220 |
| 10 | \ | \ | 84 | 1 | 163 | \ | \ | \ |
| 15 | 109 | 1 | \ | \ | 115 | \ | \ | \ |
| 20 | \ | \ | \ | \ | 141 | \ | \ | \ |
| 25.4 | \ | \ | \ | \ | 147 | \ | \ | \ |

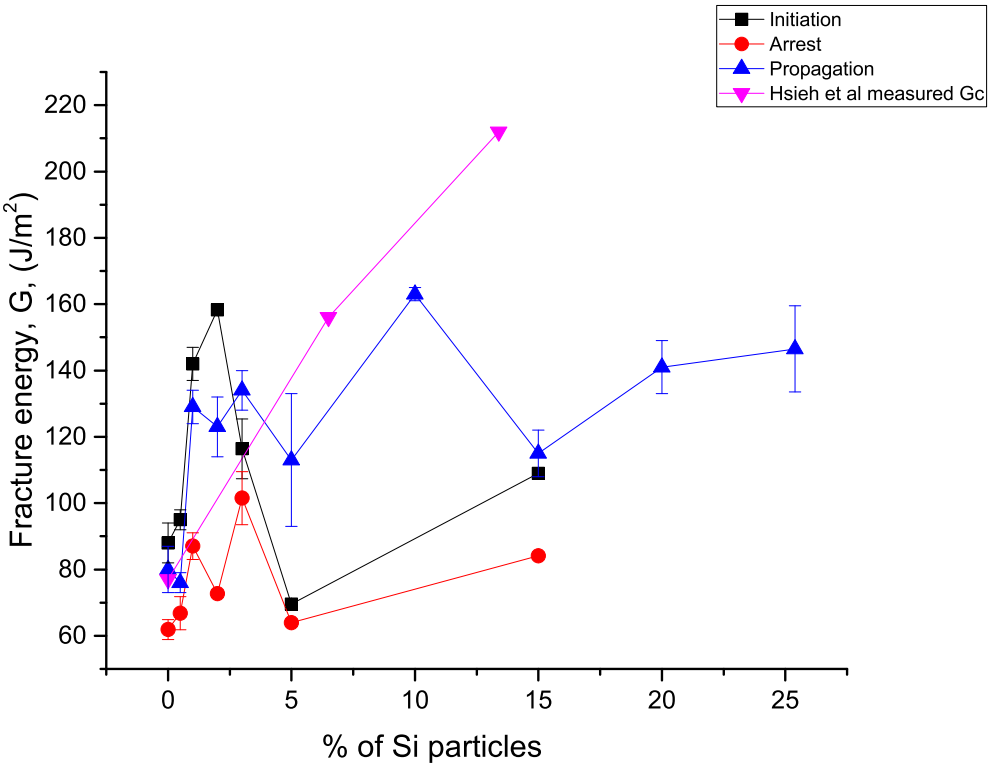


Figure 4.6: Fracture energy against percentage of silica from TDCB specimens (CBT) and model predictions from Hsieh et al. [42, 71]

### 4.3.4 CSR modified epoxy

It was found that the fracture energy of the CSR-modified epoxy was about double that of the silica-modified epoxy for all weight %. There is a general increase in toughness when the wt% of particles increases, the small drop in fracture toughness at 2 wt% of CSR when stick/slip failure occurred might be caused by clustering of particles that couldn't be mixed properly. Most regions of the CSR-modified TDCB beams showed cohesive failure, while some of the silica-modified beams had interfacial failure, which partly explains why there were remarkably larger $G_c$ values for the CSR modified specimens, see Table 4.3 and Figure 4.7. This indicated that the fracture energies of the silica-modified joints were not measured accurately due to the effect of interfacial failure. The cause of inaccuracy in the silica-modified TDCB specimens can also be due to the viscosity of the resin. The silica-modified epoxy had a low viscosity and some of the resin dropped down from the beams during making of the joints. It caused uneven filling of the bondline.

Table 4.3: Summary of fracture energies of CSR modified epoxy calculated using the CBT method from TDCB specimens, mean and standard deviation shown.

| % of CSR particles | Propagation ($J/m^2$) | Prop-SD | Initiation ($J/m^2$) | Init-SD | Arrest ($J/m^2$) | Arrest-SD |
|---|---|---|---|---|---|---|
| 0 | 80 | 7 | 88 | 6 | 62 | 3 |
| 0.5 | 121 | 13 | 149 | 15 | 90 | 11 |
| 1 | 179 | 9 | 211 | 14 | 156 | 14 |
| 2 | 218 | 0 | 165 | 5 | 11 | 13 |
| 10 | 300 | 126 | 599 | 284 | 182 | 15 |

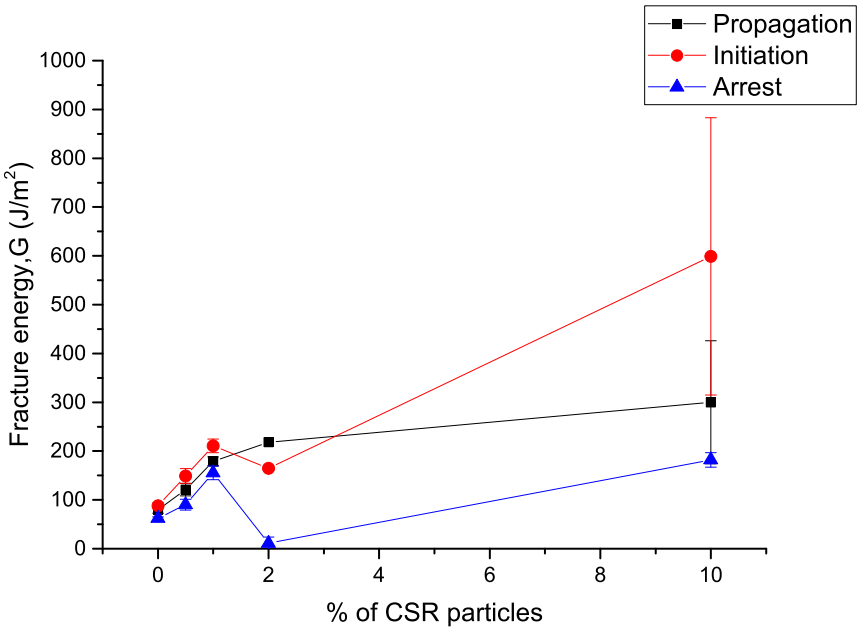


Figure 4.7: Fracture energy against percentage of particles for CSR-modified epoxy from TDCB specimens

Due to the presence of interfacial failure and stick-slips, silica / CSR hybrid specimens were tested using the SENB test geometry, which is included in Chapter 6.3.

### 4.3.5 Fracture surfaces

In unmodified epoxy, only cohesive failure was found, but there was an increasing amount of interfacial failure found when there was 1 and 2 weight % of silica added in. The amount of interfacial failure was reduced by changing the acid tank for refining the quality of the acid etch treatment. This showed that the surface treatment of the aluminium alloy highly affects the adhesive bonding and its failure. However, specimens with higher weight % of silica (from 3 weight % onwards) showed mainly interfacial failure with crack growth by stable crack propagation only. It could be due to the differences on the surface of beams used (new and recycled beams), this could cause variations in bonding of joints. Most of the regions in CSR modified specimens were cohesive failure, so the toughness values were reliable. Figure 4.8 shows the two failure types (interfacial and cohesive) and indicates the stick-slip region in the specimens.

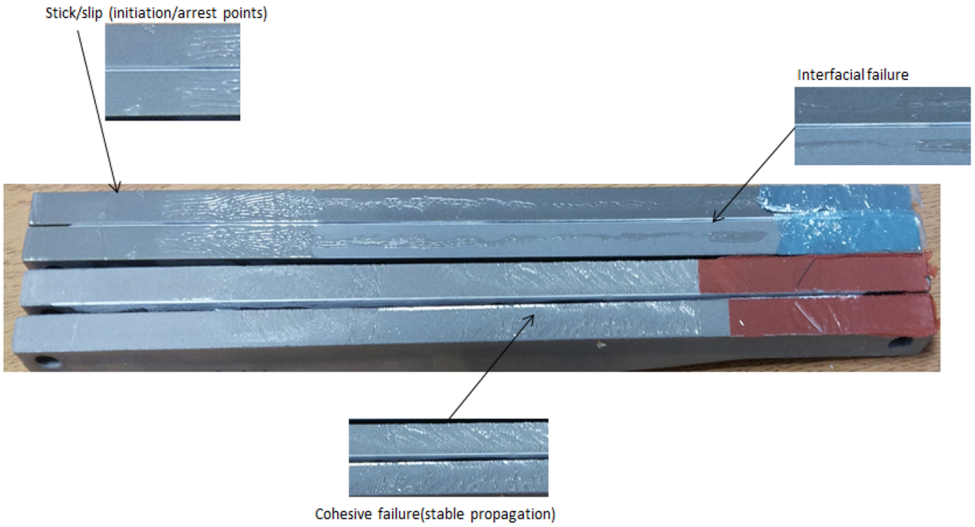


Figure 4.8: Fracture surfaces of silica modified TDCB specimens (crack propagation from right to left)

### 4.3.6 Conclusions

The use of the TDCB test provides fracture energy as well as crack behaviour information. The presence of stick-slips showed unstable crack growth and hence different fracture energy values are found compared to stable crack propagation. Stick-slips were found in most specimens, the use of new TDCB beams (not recycled) and new acid tank improved the adhesion of the joint, and produced less stick-slips and less interfacial failure, but there were still a significant amount of stick-slips present. Therefore, the fracture energy measurements of CSR / silica hybrids were made using SENB specimens, which is included in Chapter 6.3. Fracture surfaces with both interfacial failure and stick/slip area confirmed the results found. There were also some regions found to be lack of resin, hence producing different fracture surfaces shown in Figure 4.8. Most of the results showed an increase in fracture energy when the wt% of particles used increases (for both CSR and silica particles). Some $G_c$ values of silica modified specimens were very similar to those found from Hsieh et al. [3], others were within the same range of finding. The standard deviations were not high for most of the results, hence the results were reliable. TDCB tests under higher rates are discussed in the next chapter.

# Chapter 5

# High Rate Tapered Double Cantilever Beam

## 5.1 Introduction

High rate testing was performed with tapered double cantilever beam (TDCB) and single-edge notch three-point bending (SENB) samples. Silica, CSR and silica / CSR hybrid modified specimens were tested using high rate TDCB. The effects of high test rate on the fracture behaviour were investigated, such as if there is any fracture type transition when the test rate is increased. SENB high rate results provided additional information to clarify the results found from TDCB tests, as SENB uses bulk samples and so does not exhibit interfacial failure like TDCB. However, TDCB provided information for the propagation of the crack, not just initiation as for SENB. The results of the high rate TDCB tests are presented in this chapter, and those of the high rate SENB tests are presented in Chapter 6.3. After testing, the fracture surfaces were analysed using field emission gun scanning electron microscopy (FEGSEM) (more details in Chapter 9), to identify the toughening mechanisms and the percentage of silica nanoparticles which undergo debonding and void growth. The measured fracture energies will be compared with predictions from analytical models, such as those by Hsieh et al. [2, 3]. As high rate TDCB tests involve more analysis and with the limited storage of data from the camera, approximately four different concentrations of nanoparticles would be used for each high rate test, unlike the bulk specimens (where all formulations were tested in the SENB specimens).

## 5.2 TDCB high test rate set up

The experimental set up for high rate testing was similar to that at low rate, but instead of a travelling microscope being used to measure crack length, a high-speed

video camera was used to improve the accuracy of the crack length and displacement measurements. In the test set up, the upper side of the loading shackle was connected to a titanium lost motion device (LMD), which was then attached to the hydraulic ram of the testing machine. A linear variable displacement transformer (LVDT) was used to measure the position, and hence to calculate the velocity, of the hydraulic ram, see Figure 5.1. The lower side of the loading shackle was the stationary part of the set up; it was connected to a piezo-electric load cell (PCB 221B04, range of 4.48 kN, Sensitivity: 1124.1 mV/kN, rise time of 10 $\mu$s). A Phantom 3.1 high-speed camera (Vision Research, USA) was used. High-speed video (HSV) was used to measure the local displacement of the TDCB loading pins without significant dynamic oscillations which affect the LVDT, and hence improves accuracy.

The lost motion device (see Figure 5.2) was used to provide fast acceleration of the specimen during the high rate test; it was made up of a titanium rod with an aluminium 'cup and cone' contact unit. The 'cup and cone' gives a greater contact area enabling greater damping and a smoother acceteration of the specimen. The LMD has a movable extension rod, which allows the machine ran to accelerate before the specimen is picked up and helps to ensure constant speed before the movement reaches the specimen. The LMD was kept at its minimum weight to reduce inertial effects. Inertial effects were also minimised by attaching the components (load cell to the test specimen and to the stationary loading shackle) together as close as possible. This reduced oscillations caused by stress wave reflections and acceleration during the test. However, there might be bouncing effects and oscillations during the contact of the LMD, therefore rubber washers were used as damping between the surfaces of the cup and cone. Data was acquired via an Imatek system; the system was linked to the testing machine and computer, and synchronised all the data, so no manual adjustment was needed.

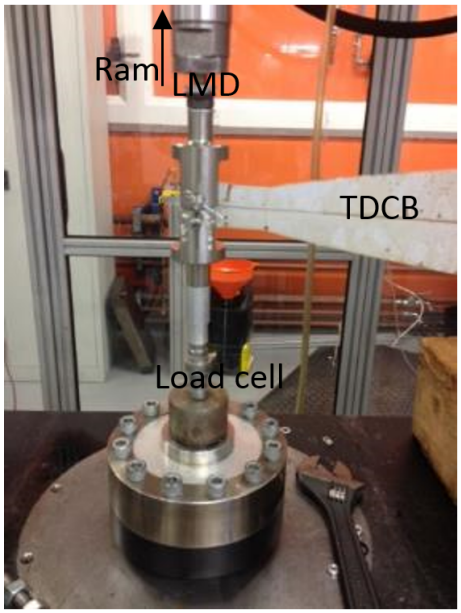


Figure 5.1: TDCB high rate test setup showing lost motion device (LMD) which allows rapid specimen acceleration [39]

Figure 5.2: TDCB high rate test setup showing high speed video camera [39]

For the high speed video (see Figure 5.3), the high framing rate used would reduce the amount of data that can be stored in the camera, as the camera has a limited memory. Therefore, images were cut to the 'letterbox' area, or reduced in image size. Figure 5.3 shows the 'letterbox' image shape used for high rate TDCB tests, which captures

the displacement of the two loading pins and the position of the crack tip. Different combinations of framing rate and picture resolution were used at different test rates. Hence the frame information was different for each test. The high speed photography was used to measure the crack length, from which the crack velocity could be calculated. No stress whitening was observed during the tests.

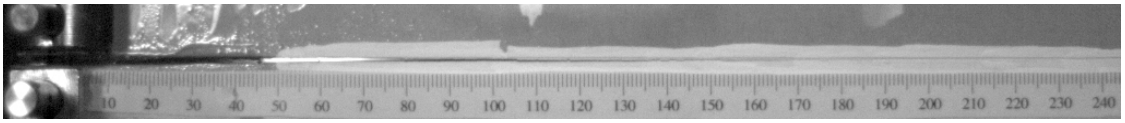


Figure 5.3: Example of high rate silica modified TDCB image. Crack propagation was from left to right

In order to see the effect of rate in fracture, it was intended that test rates of 0.1 m/s, 1 m/s and 10 m/s would be used. However, due to the increase in difficulty in recording the crack length at high rate, 10 m/s tests could not be performed.

## 5.3 High rate data reduction strategy

### 5.3.1 Fracture types

There are four fracture types identified by the data reduction strategy in [53], for the four different types of crack growth seen in the TDCB test:
Type 1: Slow, stable propagation
Type 2: Slow, unstable (stick-slip) propagation
Type 3: Fast, unstable (stick-slip) propagation
Type 4: Fast, stable propagation
There are different analysis methods required for the different types of crack growth, more about their analysis is discussed in Section 5.3.2.3.

### 5.3.2 Data analysis

#### 5.3.2.1 Video analysis

Measurements of displacement, crack length and time were taken from selected frames of the video, as shown in Figure 5.4.

Crack length (a): Crack length was measured manually from each of the video images, as there was white ink painted on the specimen, the crack was visible as a black line between the substrates of the adhesive joint. The crack tip was identified on the image,

and the crack length was read off the paper scale that was stuck onto the side of the specimen.

Load point displacement ($\delta$): The displacement was measured manually from each of the video images by recording the distance between the centres of the two pins when compared to their initial positions.

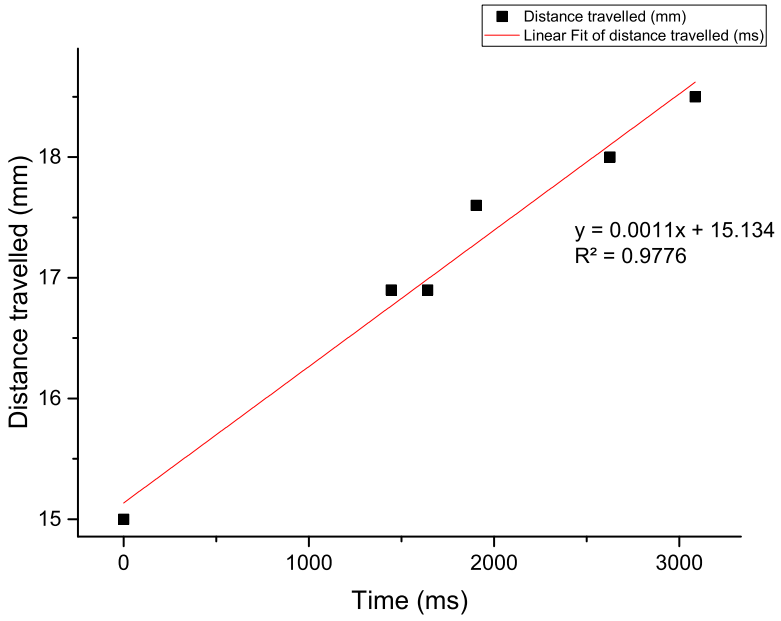


Figure 5.4: Distance between centres of pins against time graph for TDCB specimen (1 mm/s)

The numbers of pixels in the images were calibrated with the actual displacement in mm from the joint. This was performed by first measuring the distance between two selected points within the white ink painted region on the side of the specimen. The same points were selected in the software and then by using the pixel information from the camera software settings, the number of pixels within the selected region could be found as a reference for calibration. It is important to use a large distance between the two points used for the calibration, as the error from one pixel would be more significant within a short distance. The time of each image in the video was calculated from the framing rate and was used in the analysis.

#### 5.3.2.2 Plots

There are three plots used in this method: displacement (between loading pins) against time, load against time, and crack length against time (see Figure 5.5). Load and machine ram displacement data would be obtained from the oscilloscope or Imatek system. The Imatek system collates the readings from the testing machine and the oscilloscope, so that the different sets of data could be synchronised. Load data from the piezoelectric loadcell at low rate are reliable, but at high test rate there would be uncertainty in the load values due to dynamic effects (even with rubber washers there to minimise oscillations). Therefore the load values obtained from machine can only be used at low rate, or maybe at intermediate rates. Instead, displacement and crack length obtained from the video would be used to analyse the fracture at high rate.

Considering stable and stick-slip crack growth, propagation points and initiation points were plotted separately as they should be analysed separately [39], and the arrest points are not used. When the test rate is high, it is difficult to distinguish between stable and stick-slip propagation. Hence, to distinguish whether the cracks were stable or unstable, linear regression would be performed on the crack length versus time data, see Figure 5.5 for example, to calculate whether the regression coefficient $R^2 > 0.95$ [43]:

If $R^2$ is larger than 0.95, the fracture type would be defined as stable, where propagation values would be used to plot the linear regression line. Whether it is type 1 or 4 depends on whether the kinetic energy (KE) was significant.

If $R^2$ is smaller than 0.95, the fracture type would be stick-slip fracture, where initiation values would be used to plot the linear regression line. It would be defined as a type 2 or 3 fracture depending on whether the KE was significant.

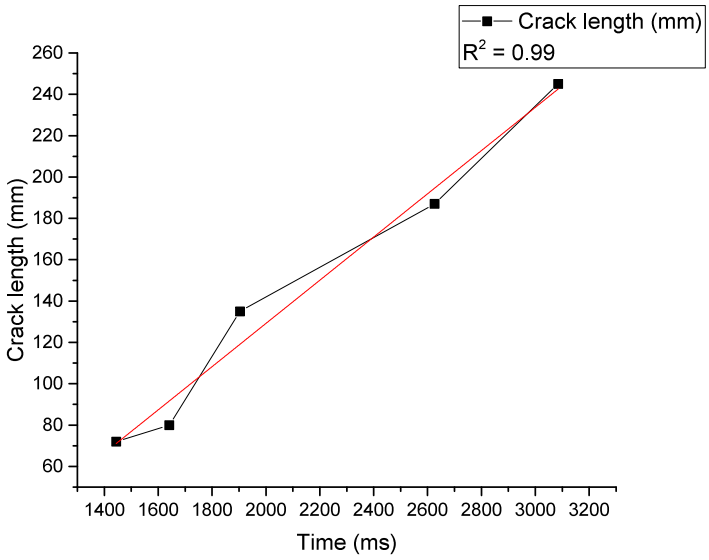


Figure 5.5: Crack length against time graph for TDCB specimen

#### 5.3.2.3 Calculation of $G_c$ values

The values of $G_c^s$ (static value of the adhesive fracture energy) and $G_c^d$ (dynamic value of the adhesive fracture energy) are used to determine whether the kinetic energy (KE) was significant. The KE would be considered significant when the fracture energy increases by more than 5 % of the quasi-static value due to the increase in test rate, i.e. when:

$$(G_c^s - G_c^d)/G_c^s < 0.05 \tag{5.1}$$

then the KE would not be significant. The fracture would be analysed as type 1 or 2 (depends on whether it is stable or unstable from the crack length against time plot mentioned above). Hence $G_c^s$ values would be reported. If

$$(G_c^s - G_c^d)/G_c^s \neq< 0.05 \tag{5.2}$$

then the KE would be significant, and the fracture would be analysed as type 3 or 4 (depends on if it is stable or unstable from the crack length against time plot mentioned above). Hence $G_c^d$ values would be reported. The equations used to calculate $G_c^s$ and $G_c^d$ for the TDCB specimens [48] are quoted below:

For type 1 fracture (slow, stable crack propagation), $G_c^s$ is reported. It is a CBT method that uses propagation values which is applied using:

$$G_c^s = \frac{4P^2 m}{EB^2}\left[1 + 0.43\left(\frac{3}{ma}\right)^{1/3}\right] \tag{5.3}$$

where $G_c^s$ = quasi-static value of the adhesive fracture energy, P = load, E = Young's modulus of substrate, B = width of test specimen, a = crack length and m = specimen geometry factor (m = 2 $mm^{-1}$ for the TDCB specimens used in present work) which is given by:

$$m = \frac{3a^2}{h^3} + \frac{1}{h} \tag{5.4}$$

where h = height of specimen substrate.

For type 2 fracture (slow, unstable (stick-slip) crack propagation). It is a CBT method that uses initiation values, which is applied using:

$$G_c^s = \frac{4P^2 m}{EB^2}\left[1 + 0.43\left(\frac{3}{ma}\right)^{1/3}\right] \tag{5.5}$$

For type 3 fracture (fast, unstable (stick-slip) crack propagation), the analysis only uses crack initiation values. The fracture energy is calculated using:

$$G_c^d = \frac{E}{4m}\left[\frac{\delta}{2a^*}\right]^2\left[1 + 0.43\left(\frac{3}{ma}\right)\right]^{1/3}\left[1 - 3\left(\frac{9}{22}\right)^3\left(\frac{a^*}{C_L t}\right)^2 mh(a^*)\right] \tag{5.6}$$

where $\delta$ = displacement between loading pins, t = time, a = crack length, h(a*) = height of beam at a distance a* from load line, where a* is the crack length at a specific height, and is given by

$$a^* = a + 0.64\left(\frac{3a^2}{m}\right)^{1/3} - \frac{2}{3}x_0 \tag{5.7}$$

where for TDCB specimens the initial crack length $x_0 = 50$ mm.

Also, $C_L$ = longitudinal wave speed, which is given by:

$$C_L = \frac{\sqrt{E}}{\rho_s} \tag{5.8}$$

where E = modulus of substrate and $\rho_s$ = density of substrate. For the aluminium alloy substrates used, these values are 70 x $10^9 Pa$ and 2700 $kg/m^3$ respectively [48].

For type 4 fracture (fast, stable crack propagation which only uses crack propagation

values, the fracture energy is calculated using):

$$G_c = G_c^d = G_c^s \left(1 - \frac{9}{11}\left(\frac{\dot{a}}{C_L}\right)^2 \left[1 + 0.43\left(\frac{3}{ma}\right)^{1/3}\right]^2 mh(a^*)\right) \tag{5.9}$$

where

$$G_c^s = \frac{E}{4m}\left[\frac{(V/2)}{\dot{a}}\right]^2 \left[1 + 0.43\left(\frac{3}{ma}\right)^{1/3}\right]^{-1} \tag{5.10}$$

where $\dot{a}^*$ = average crack velocity and V = velocity of loading applied to the TDCB arms from the machine.

Three specimens from each of the selected formulations were used for each test rate, intended to be 0.1, 1 and 10 m/s, but due to problems with analysing the results from the high speed video when test rate was high, the test rates used were changed, see Section 5.4 for more details.

The different rates of tests would provide insights into the effect of the rate of testing on the fracture behaviours.

## 5.4 High rate TDCB results

Trials with CSR 2 weight % specimens showed unstable crack growth at under 1 m/s, so analysis would be using the type 3 equation as the load from the machine is not reliable due to dynamic effects from the fast unstable crack growth. There were very different values of $G_c$ found at different points during crack growth, varying from 420 to 2748 $J/m^2$.

There is a limitation for the number of frames that can be recorded in the camera, this depends on the size of images recorded. As the whole ruler needed to be seen, the number of frames recorded was reduced accordingly. Due to the limitations with the number of frames used, the results could only be analysed when the rate used was not higher than 3 m/s. Test rates of 0.1, 1, 2 and 3 m/s were used. Average fracture energy values were calculated, as the crack points found were assumed to be propagations in this method. The value of $R^2$, the regression coefficient from the crack length against time plot, was calculated for each test. For all formulations, the values of $R^2$ were found to be smaller than 0.95, so they were stable crack propagations with type 1 or type 4. As all the data were analysed using the video, they are considered as type 4.

Figure 5.6 shows the average fracture energy at a test rate of 0.1 m/s. There were very similar trends found in all formulations. The CSR modified epoxy gave the highest

fracture energy values, followed by the silica / CSR hybrid and the silica modified epoxy gave the lowest values. Most of the standard deviations were small, so the results were reliable. Dynamic effects were not significant at the rate of 0.1 m/s.

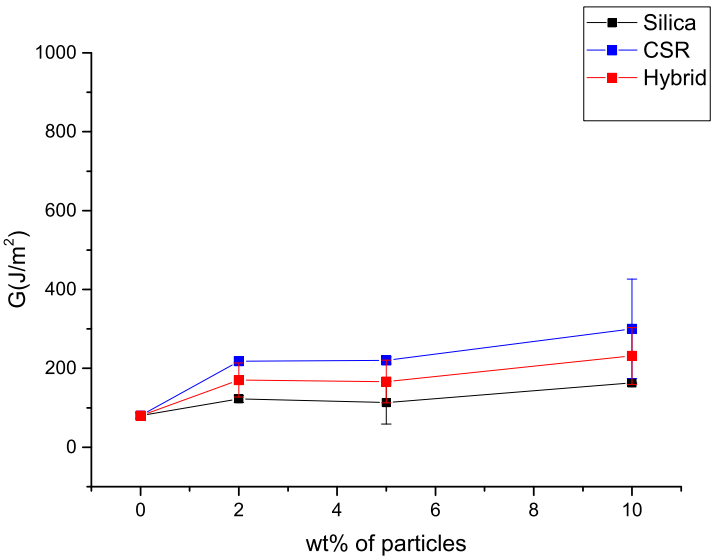


Figure 5.6: Average fracture energy from TDCB tests when rate is 0.1 m/s

Figure 5.7 shows the average fracture energy at a test rate of 1 m/s. There is an increase in fracture energy up to 5 wt%, and then a drop at 10 wt% for all formulations. This could be due to the uneven mixing of 10 wt% specimens as this concentration was high for CSR and silica / CSR hybrid formulations. For the silica specimens, 10 wt% was not a very high concentration; and because all the specimens showed this behaviour (the drop), this could be due to dynamic effects. Hybrid specimens showed higher fracture energy values for all the wt%, but most of the values found were similar for all formulations. There were high standard deviations found at 2 wt% for CSR and silica specimens, but their values showed a steady increase in fracture energy, so the results were still reasonable.

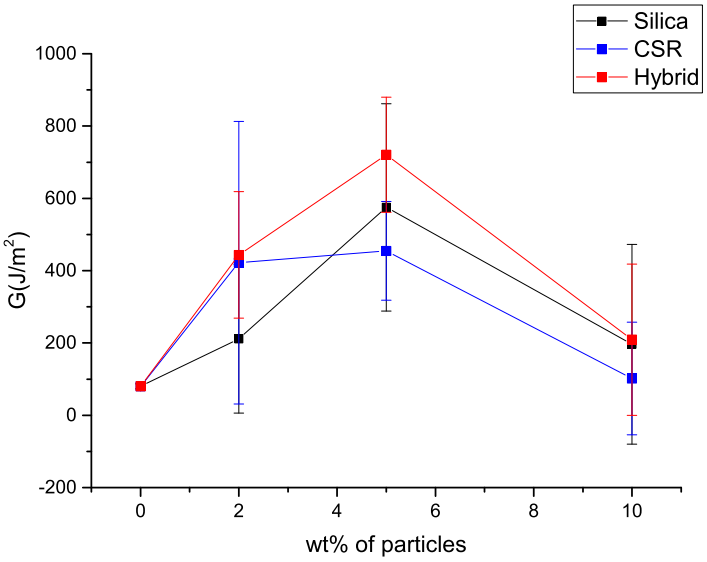


Figure 5.7: Average fracture energy from TDCB tests when rate is 1 m/s

Figure 5.8 shows the average fracture energy at a test rate of 2 m/s. There is a very similar pattern found at a rate of 2 m/s when compared to 1 m/s for CSR and silica / CSR hybrid modified specimens, there was a steady increase in fracture energy until 5 wt%, and a drop at 10 wt%. There were high standard deviations found at 2 wt% of CSR. The silica modified specimens showed a steady increase in fracture energy for all wt% when the wt% of particles increases. These results showed that dynamic effects were significant from rates at above 1 m/s.

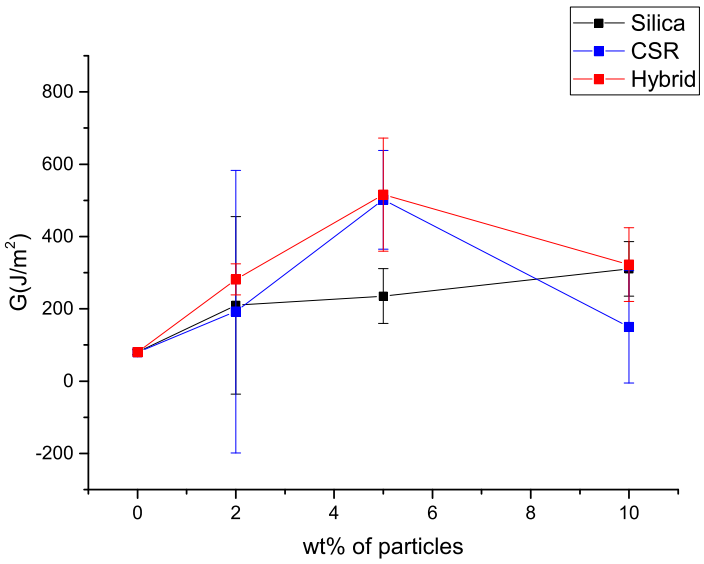


Figure 5.8: Average fracture energy from TDCB tests when rate is 2 m/s

Figure 5.9 shows the average fracture energy at a test rate of 3 m/s. There is an increase in fracture energy only at 2 wt% and then a steady decrease from 5 wt% to 10 wt% for all formulations. There were almost the same values found in silica and silica / CSR hybrids. The effect of different formulations was not very significant when compared to the rate effect at high test rates. CSR showed lower fracture energy values for all wt%, but the overall trend is the same. There were higher standard deviations found in all formulations, which could be due to the increase of dynamic effects that alters the results obtained. Any rate higher than 3 m/s could not be performed because a larger number of frames would be required in order to record the crack length from the images, than the camera was capable of recording.

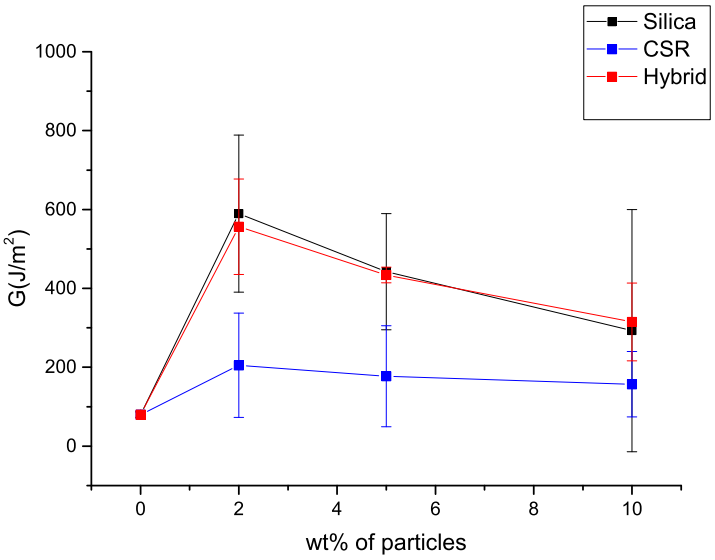


Figure 5.9: Average fracture energy from TDCB tests when rate is 3 m/s

Figures 5.10, 5.11 and 5.12 show the high rate TDCB results for the individual formulations at the different rates, these help to show the effect of different formulations when testing at high rate.

Figure 5.10 shows the high rate TDCB results from the silica modified specimens. There was a decrease in fracture energy for all wt% at a rate of 2 m/s, and their standard deviations were lower when compared to other test rates. There were very different results for different wt% at rates of 1 and 3 m/s, but there is no pattern of the higher the wt%, the higher the fracture energy. There are no trends found in these results. The range of results was highest at 3 m/s, this could be due to the increase in dynamic effects at 3 m/s, which matches the comparison at individual test rates. The below zero fracture energy found at 3 m/s was due to dynamic effects as zero fracture energy is not possible.

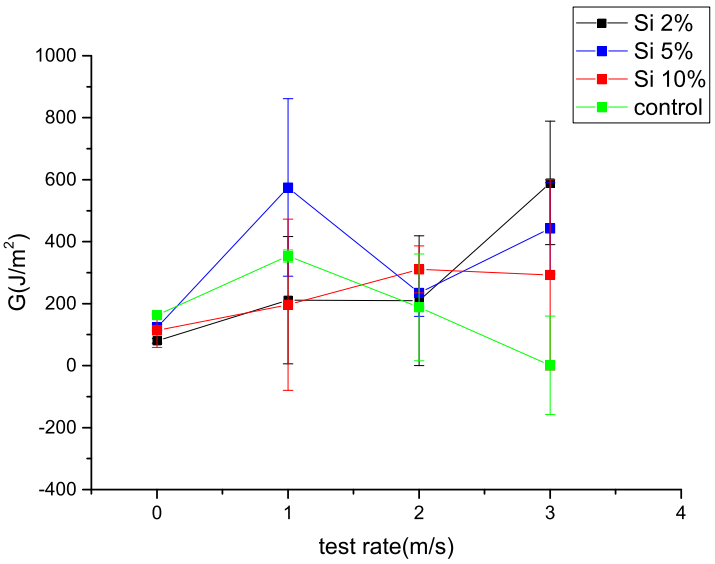


Figure 5.10: Average fracture energy of silica TDCB specimens at different rates

Figure 5.11 shows the high rate TDCB results from the CSR specimens. All the different wt% show different behaviour at the same test rate for all the results. The only similarity is the drop at rate of 3 m/s for all wt%, which is the same as the results found from the silica specimens. There were large standard deviations found at the rate of 1 m/s, which matches with the individual 2 m/s graph and silica results. Other standard deviations were slightly large, but these are in a similar range when compared to other results in this study. The effect of formulation at high rate was not significant for the CSR TDCB specimens.

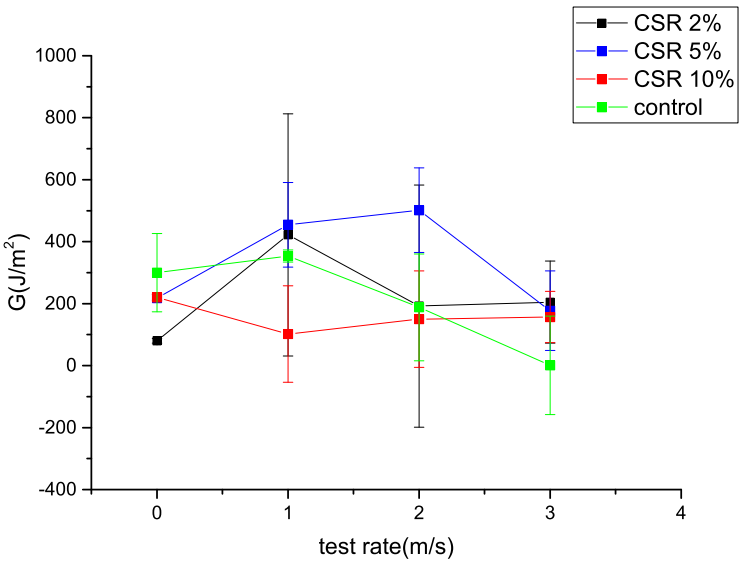


Figure 5.11: Average fracture energy of CSR TDCB specimens at different rates

Figure 5.12 shows the high rate TDCB results from silica / CSR hybrid specimens. There were a similar range of standard deviations found at all test rates, but they are all relatively large except for the quasi-static rate results. Hybrid modified specimens showed slightly higher fracture values than silica and CSR modified specimens for all 3 rates used, while silica and CSR modified specimens showed very similar results. The higher wt% of particles didn't always produce a higher fracture value, which is the same as in other formulations.

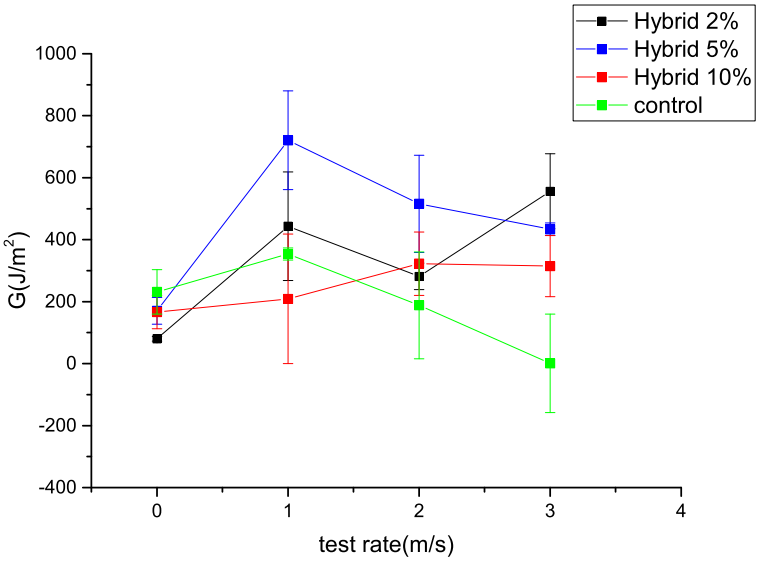


Figure 5.12: Average fracture energy of silica / CSR hybrid TDCB specimens at different rates

## 5.5 Conclusions

Silica, CSR and silica / CSR hybrid modified epoxy TDCB specimens were tested at rates of 0.1, 1, 2 and 3 m/s. There were no very clear patterns of the rate effect on the different formulations. The results did not show an increase in fracture energy when there is an increase in wt% of particles for all formulations. Most of the results showed a large range of values and relatively large standard deviations. This is more significant at the test rate of 3 m/s, this could be due to the increase in dynamic effects when the test rate increases.

There were difficulties in performing the high rate TDCB tests, including dynamic effects and difficulties in analysing data due to the limit of the number of frames that the camera can provide when the failure happens in a very short time. There were still results which could be found from test rates higher than quasi-static, and they provided some more information on the fracture behaviour of the materials used. However, improvement in the test method is needed, further investigations into the rate effect are covered in the high rate SENB tests Section 6.4.

# Chapter 6

# Single-Edge Notch Bending

## 6.1 Introduction

Due to the presence of interfacial failure, single-edge notch three-point bending (SENB) tests were performed after the tapered double cantilever beam (TDCB) tests for further investigations of the rate effect on the fracture properties of the particle toughened epoxies. In this Chapter, all of the SENB tests performed under different conditions will be discussed. These included quasi-static test rate, high rate (0.1 and 1 m/s) and low temperature (-40 and -80$^oC$) SENB tests. All the formulations are tested, silica, CSR and silica / CSR hybrids (with equal weight % of silica and CSR particles) and the results are compared in this Chapter.

As it is expected that ceramic microsphere and PES toughened epoxy would have slightly different failure mechanisms when compared to silica and CSR, so the SENB results from ceramic microparticles, PES, ceramic microparticles / CSR and PES / silica are included in Chapter 11, for separate comparison.

This Chapter starts with introducing the tensile testing, as the tensile modulus is required for the linear elastic fracture mechanics (LEFM) method used to calculate the fracture energy from the measured data for the SENB tests used in this study. More details about this LEFM method are included in Section 6.3.

## 6.2 Tensile tests

### 6.2.1 Introduction

Tensile tests on bulk samples provided the Young's modulus, E, of the materials for calculations of the fracture energy, $G_c$, when using the linear elastic fracture mechanics (LEFM) method in the SENB test. The tensile Young's modulus value was found

using the linear portion of the stress-strain curves. The tensile fracture stress was also calculated.

### 6.2.2 Tensile test specimen preparation

Tensile tests were performed using specimens with the type 1BA dumb-bell geometry (see Figure 6.1) according to ISO Standard 527 [72]. The plates were made in 3 mm thick vertical moulds, using the same procedure as used to manufacture the plates for the SENB specimens described in Section 6.3.2. Specimens were then manufactured by computer numerical control (CNC) milling from the cast plates.

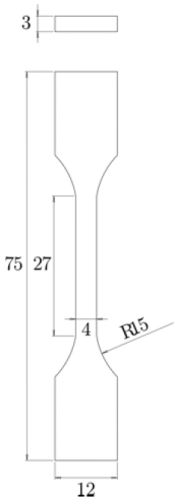


Figure 6.1: Tensile test geometry (dimensions in millimetres) [28]

### 6.2.3 Tensile test procedure

The tensile tests were performed at a test rate of 1 mm/min. Six replicate specimens were tested for each formulation. An Instron 2620-601 dynamic extensometer was attached to the specimen to measure the extension in the gauge length for providing accurate strain values. The mean and the standard deviation of the Young's modulus and fracture stress are reported in the Figures and Tables in Section 6.2.4.

The Young's modulus, E, was calculated by curve fitting of the slope of the stress versus strain curve. The modulus was calculated by using linear regression of the experimental data over an interval from a strain of 0.025% to 0.075%. The initial non-linear part (that comes before the linear part) due to the take-up of slack in the system of the

curve was removed, so that a correct strain can be found.

### 6.2.4 Tensile results

Figure 6.2 shows a typical tensile stress against strain curve for the control epoxy. A linear increase is initially seen, then the response curves towards the strain axis. There is no clear yield point visible, as the sample fails by brittle fracture before yield occurs in tension.

The tensile modulus results are shown in Figure 6.3 and Table 6.1 below. A Young's modulus for the control epoxy of 3.14 GPa (with a standard deviation of 0.1 GPa) was measured. This result is the same as that measured by Masania et al. [63].

Similar values of Young's modulus were measured for all specimens; most of the specimens have a modulus of about 3 GPa, and within an acceptable range of standard deviations. The modulus generally increased with the increased amount of particles added in. Addition of silica increased the Young's modulus approximately linearly to a maximum of 4.47 GPa at the addition of 25.4 wt% silica. This is because the Young's modulus of silica is 70 GPa, which is much greater than that of the epoxy. The addition of silica reduces the epoxy content in the specimens, and hence, the overall modulus increased.

The addition of CSR increased the Young's modulus up to 5 wt%, where a value of 3.90 GPa was measured, then there is a significant reduction in the modulus value at CSR 10 wt%, see Table 6.1, which is due to agglomeration of the particles. The high wt% has a different fracture surface when compared to the other wt%, more information can be found from SEM imaging as discussed in Chapter 9. Hence, the optimum % of CSR particles used was 5 wt%. It had been expected that the addition of CSR particles would reduce the Young's modulus of the specimens, because the rubber core will have a much lower modulus then that of the epoxy. However, the small increases in the modulus values indicate that the PMMA shell has a higher modulus compared to the epoxy and this causes the overall increase.

It is expected that the use of hybrid formulations would provide different modulus values when compared to using one particle only, but the hybrids did not show significant changes in their tensile properties compared to the addition of silica only, see Figure 6.3. The increases were within the experimental error, confirming that the addition of CSR only gives a relatively small increase in modulus due to the presence of the PMMA shells. The use of 10 wt% of CSR in the hybrid gave a decrease in the modulus, which is likely to be due to agglomeration as for the 10 wt% CSR only.

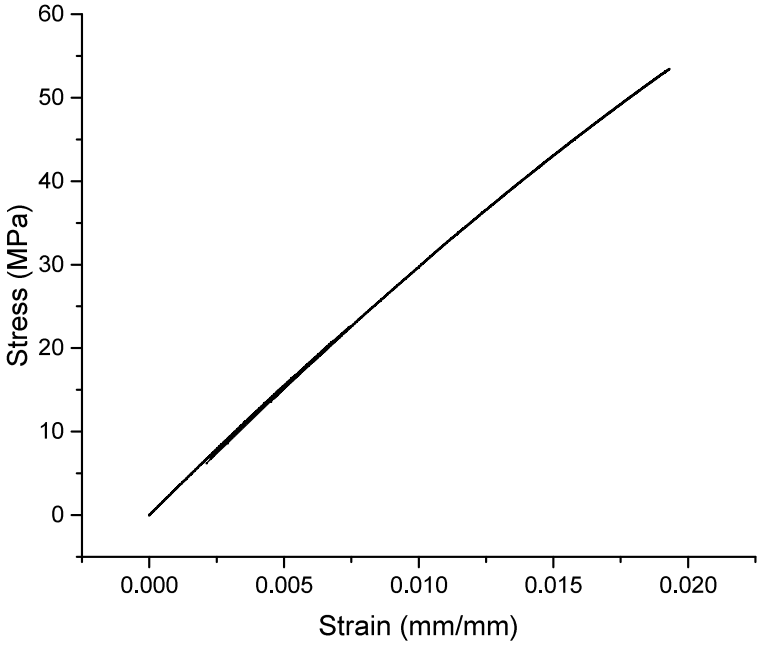


Figure 6.2: Tensile stress against strain curve example - control epoxy

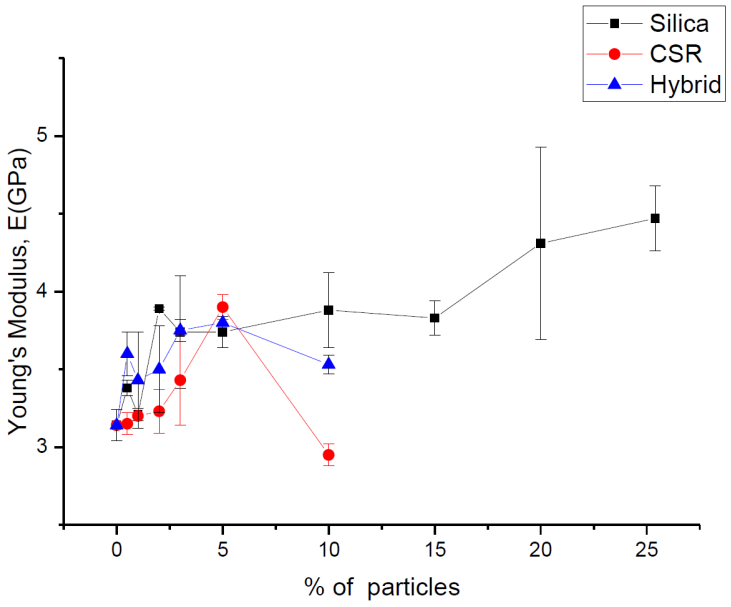


Figure 6.3: Tensile modulus results of particle-modified epoxy

Table 6.1: Tensile test results of particle-modified epoxy

| particles | Silica | | CSR | | Hybrid | |
|---|---|---|---|---|---|---|
| % of particles | Young's Modulus (GPa) | SD | Young's Modulus (GPa) | SD | Young's Modulus (GPa) | SD |
| 0 | 3.14 | 0.10 | 3.14 | 0.10 | 3.14 | 0.10 |
| 0.5 | 3.38 | 0.05 | 3.15 | 0.07 | 3.60 | 0.14 |
| 1 | 3.21 | 0.04 | 3.20 | 0.00 | 3.43 | 0.31 |
| 2 | 3.89 | 0.01 | 3.23 | 0.14 | 3.50 | 0.28 |
| 3 | 3.74 | 0.36 | 3.43 | 0.29 | 3.75 | 0.07 |
| 5 | 3.74 | 0.10 | 3.90 | 0.08 | 3.80 | 0.00 |
| 10 | 3.88 | 0.24 | 2.95 | 0.07 | 3.53 | 0.06 |
| 15 | 3.83 | 0.11 | | | | |
| 20 | 4.31 | 0.62 | | | | |
| 25.4 | 4.47 | 0.21 | | | | |

The fracture stress values were very similar for all specimens, and the measured values are shown in Table 6.2. There is generally a reduction in the fracture stress at high wt% of CSR, which is due to the agglomeration of the CSR particles.

Table 6.2: Fracture stress results of particle-modified epoxy

| particles | Silica | | CSR | | Hybrid | |
|---|---|---|---|---|---|---|
| % of particles | Fracture stress (MPa) | SD | Fracture stress (MPa) | SD | Fracture stress (MPa) | SD |
| 0 | 60 | 13 | 60 | 13 | 60 | 13 |
| 0.5 | 64 | 14 | 65 | 6 | 51 | 13 |
| 1 | 61 | 11 | 57 | 10 | 66 | 4 |
| 2 | 63 | 8 | 53 | 4 | 56 | 12 |
| 3 | 67 | 14 | 50 | 2 | 51 | 4 |
| 5 | 77 | 5 | 50 | 3 | 59 | 6 |
| 10 | 86 | 4 | 51 | 2 | 56 | 2 |
| 15 | 69 | 12 | | | | |
| 20 | 62 | 31 | | | | |
| 25.4 | 69 | 8 | | | | |

## 6.3 Quasi-static single-edge notch bending (SENB) tests

### 6.3.1 Introduction

Single-edge notch bending (SENB) tests were used to measure the fracture toughness, $K_c$, and fracture energy, $G_c$. These values were compared with the results from the TDCB tests.

The particle contents used are presented in Table 6.3 below. (There were twice the wt% of particles as seen in the table, e.g. 10 wt% hybrid = 10 wt% silica + 10 wt% CSR = 20 wt% of particles.) The wt% used were the same as the ones in the quasi-static TDCB tests. As the effect of addition of low wt% of particles was not clearly known in the literature, there were more low wt% formulations used for this study, for investigations of their toughening effects.

Table 6.3: Particle contents used in SENB specimens

| Silica | CSR | Hybrid | |
|---|---|---|---|
| % of Silica particles | % of CSR particles | % of Silica particles | % of CSR particles |
| 0 | 0 | 0 | 0 |
| 0.5 | 0.5 | 0.5 | 0.5 |
| 1 | 1 | 1 | 1 |
| 2 | 2 | 2 | 2 |
| 3 | 3 | 3 | 3 |
| 5 | 5 | 5 | 5 |
| 10 | 10 | 10 | 10 |
| 15 | | | |
| 20 | | | |
| 25.4 | | | |

### 6.3.2 Quasi-static specimen preparation

SENB specimens were machined from 6 mm thick cast plates. To cast the plates, first the steel vertical moulds were cleaned. Pieces of residual epoxy were cleaned off the mould using a razor blade. The moulds were then wiped with acetone and release agent (Frekote 700-NC, Henkel, UK) was coated on the surfaces. The moulds were clamped firmly and preheated to 60$^o$C in a fan oven. The epoxy resin, modifiers and hardener were stirred with an overhead mixer at 90 rpm and degassed at 60$^o$C in a vacuum oven. The epoxy was poured into the mould, and the mould was placed into the fan oven.

The curing cycle used was: Starting temperature at 60$^o$C, ramp at 1$^o$C/min to 95$^o$C, dwell for 1 hour, ramp at 1$^o$C/min to 165$^o$C and dwell for 2 hours, ramp 2$^o$C/min to room temperature (20$^o$C). Two bulk plates were made for each formulation, and were cut and polished into SENB specimens of 6 mm thickness, 12 mm in width and 60 mm in length according to the ISO 13586 standard [40]. Six specimens were made for each formulation for low rate testing, and three specimens for high rate testing. For each specimen, a 4 mm deep notch was machined and a natural crack was made by tapping the notch with a liquid nitrogen-chilled razor blade. The cracks produced need to be at least four times the length of the notch tip radius. Test specimens would be rejected

if crack length is 10% more than 6 mm. The specimen (see Figure 6.4) dimensions are specified to ensure plane strain conditions. The criteria are indicated below according to the Standard [40]:
thickness, $B > 2.5r$
crack length, $a > 2.5r$
ligament length, $(W - a) > 2.5r$
where $r = K_c^2/\sigma_y^2$
where $K_c$ = fracture toughness and $\sigma_y$ = tensile yield stress.

For the epoxy used in this thesis, the $K_c = 1.07$ MPa $m^{1/2}$, and the minimum fracture stress = 69.0 MPa, so $r = \frac{K_c^2}{\sigma_y^2} = 0.0002\ m$. This gives a minimum thickness of B = 0.0006 m = 0.6 mm. The specimens used are 6 mm thick, so this size requirement is readily met.

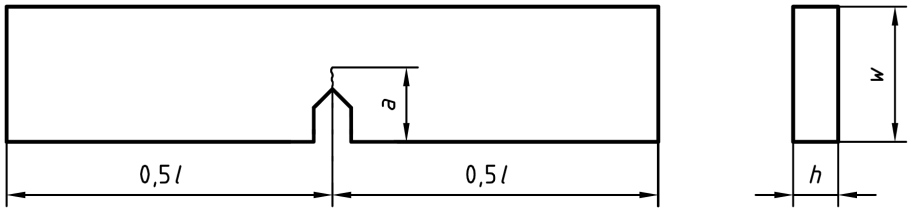


Figure 6.4: SENB specimen geometry according to the ISO Standard [40], where W is width, l is overall length, B is thickness and a is crack length.

### 6.3.3 Quasi-static SENB test procedure

SENB tests were performed at a constant displacement rate of 10 mm/min using an Instron 3369 universal testing machine. There are two methods of analysis which can be used according to ISO 13586 [40], energy method and LEFM method. The LEFM method is used in this study. This is because in the LEFM method, only the peak load is used in the calculation, so the oscillations from high rate SENB tests would not affect the results. While in the energy method, this would produce some effects in the results.

The fracture toughness, $K_c$, can be found by using [28, 40]:

$$K_c = (\frac{P_c}{B\sqrt{W}} f(x)) \tag{6.1}$$

where $P_c$ = the load at crack growth initiation (specified in the standard ISO 13586), B = thickness, W = width and

$$f(x) = 6\sqrt{x}\frac{1.99 - x(1-x)(2.15 - 3.93x + 2.7x^2)}{(1+2x)(1-x)^{\frac{3}{2}}} \tag{6.2}$$

where

$$x = \frac{a}{W} \tag{6.3}$$

and a = crack length.

The fracture energy can be calculated for the LEFM method [41] using:

$$G_c = \frac{((1-v^2)K_c^2)}{E} \tag{6.4}$$

where the Poisson's ratio v = 0.35 [41], and E = tensile Young's modulus

The SENB test setup is shown in Figure 6.5, and an extensometer is not needed to measure the displacement as only the maximum load (not the energy method) is used. An example of a force versus displacement graph is shown in Figure 6.6 below, where the maximum load at which the sample fracture occurs is indicated.

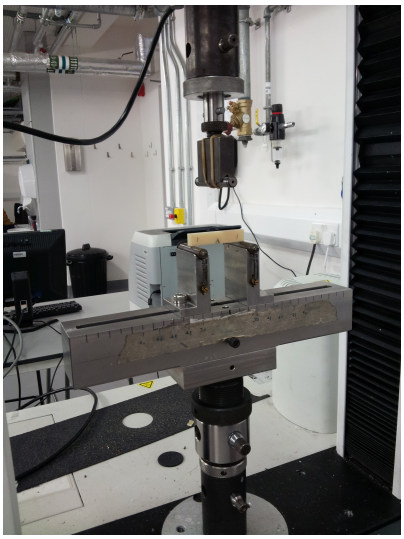

Figure 6.5: Quasi-static SENB test setup at room temperature

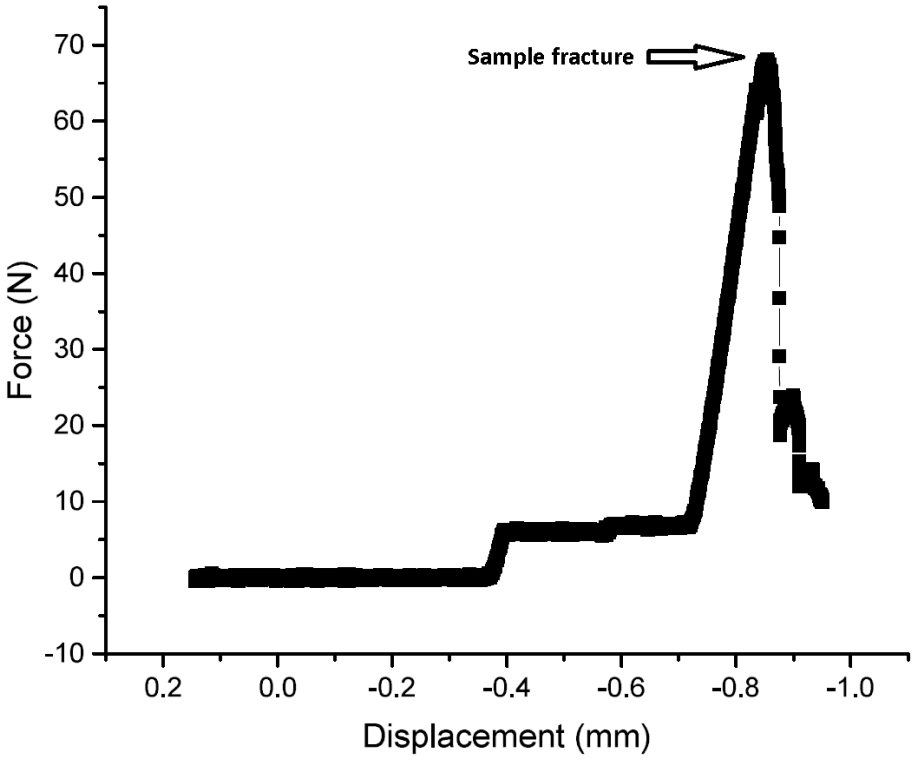


Figure 6.6: SENB force against displacement graph

### 6.3.4 Quasi-static test rate SENB results

For the control epoxy a fracture energy of $G_c = 68\ J/m^2$ was measured. This is slightly lower than the 77 $J/m^2$ found in literature [11], but lies within one standard deviation. As expected, there was an increasing trend of toughness when the wt% of particles added is increased. The addition of particles highly increased the toughness of the epoxy.

There was an approximately linear increase of fracture energy when the wt% of silica increases up to 15 wt%. The increase was most significant at 10 and 15 wt%. Then the fracture energy values stay at a similar level when the silica content increases to 20 and 25.4 wt%. For the silica-modified specimens, fracture energy increases to 223 $J/m^2$ when the % of silica added was the maximum of 25.4 weight % (see Figure 6.7 and Table 6.4) compared to the control epoxy.

There was a small increase in fracture energy when wt% of CSR particles added in increases, but then there was also a notable plateau when the wt% of CSR particles added was high, above 5 wt% of CSR. The increase in fracture energy values of the intermediate wt% of CSR were not significant, it could be because the big visible CSR particles were made up of small CSR particles, some of the big particles break into small particles during mixing. Therefore there is some regions that have the big CSR particles and some regions were covered with the very small CSR particles, which results in uneven distribution of particles.

The results of the addition of core shell rubber from a previous study can be compared with the Paraloid EXL CSR studied here. The previous work [11] used MX156 CSR particles with the same epoxy and curing agent as in this study.

The toughening effect was a lot lower when the CSR 10 wt% (108 $J/m^2$) data are compared to MX 156 9 wt% CSR (485 $J/m^2$) [11], this is partly due to the lower tensile modulus of 2.33 GPa measured by Giannakopoulos et al. [11], which results in a higher fracture energy value in the calculation, see Equation 6.5 below.

$$G_c = \frac{(1 - v^2)K_c^2}{E} \tag{6.5}$$

MX 156 has a diameter of 85 - 115 nm, while the Paraloid EXL CSR is about 36 $\mu$m in diameter. This showed the effect of particle size on the failure mechanisms, the use of smaller particles increases the toughening effect.

There was a steady increase in fracture energy when the wt% of hybrid particles added in increases, hybrid 10 wt% had the largest improvement in fracture energy. This formulation uses 10 wt% silica particles and 10 wt% of CSR particles. It was an

intermediate result, their fracture energy values were in between the CSR and the silica results or even worse, the synergy effect was not significant. This was due to uneven mixing of particles found in SEM images (see SEM imaging Chapter 9 for more) when there is a higher amount of particles added in. It was notable that saturation of particles occurred at 10 wt% in hybrid mixture, as particles were covering the whole surface. In the future, with the use of wt% in between 5 to 10 wt% could improve mixing of silica CSR hybrid specimen.

The quasi-static test results are compared to the high test rate results in Section 6.5.3.

The fracture energy values of the silica-modified specimens were found to be significantly larger than the CSR-modified ones, which agrees with the quasi-static TDCB results, where the addition of silica particles produced a larger increase in fracture energy than with the use of CSR particles for all wt%. The comparison of the different fracture energies measured from the TDCB and SENB tests is included in Chapter 7.

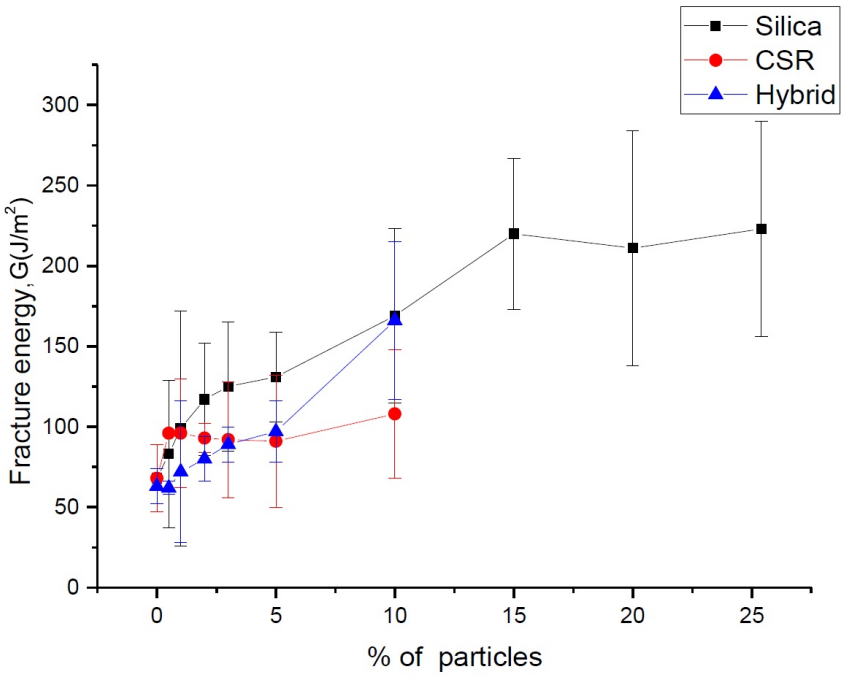


Figure 6.7: Fracture energy of modified epoxy from SENB tests at quasi-static test rate

Table 6.4: Fracture energy of modified epoxy from SENB tests at quasi-static test rate

| particles | Silica | | CSR | | Hybrid | |
|---|---|---|---|---|---|---|
| Wt % of particles | G (J/m$^2$) | SD | G (J/m$^2$) | SD | G (J/m$^2$) | SD |
| 0 | 68 | 21 | 68 | 21 | 63 | 11 |
| 0.5 | 83 | 46 | 96 | 1 | 62 | 4 |
| 1 | 99 | 73 | 96 | 34 | 72 | 44 |
| 2 | 117 | 35 | 93 | 9 | 80 | 14 |
| 3 | 125 | 40 | 92 | 36 | 89 | 11 |
| 5 | 131 | 28 | 91 | 41 | 97 | 19 |
| 10 | 169 | 54 | 108 | 40 | 166 | 49 |
| 15 | 220 | 47 | | | | |
| 20 | 211 | 73 | | | | |
| 25.4 | 223 | 67 | | | | |

## 6.4 High rate SENB tests

### 6.4.1 Introduction

High rate SENB tests were performed for comparison with the fracture energy values measured in the high rate TDCB tests. When compared to the high rate TDCB tests, the SENB test has a simpler setup, the procedure was less complicated and more direct in the method of obtaining the results. Unlike TDCB, SENB does not produce interfacial failure. Hence the results were expected to be more reliable than the results from the high rate TDCB tests. However, the same dynamic effects were also present in high rate SENB. More details about the comparison of fracture energies measured in SENB and TDCB tests are included in Section 6.5.

### 6.4.2 High rate SENB test procedure

High rate SENB tests (see Figure 6.8) were performed with the same high rate Instron as used for the high rate TDCB tests, using a piezoelectric loadcell type PCB 208 A03, which has a sensitivity of 10.19 mV/lb (or 10.10 mV/4.482 N). The test rates used initially were 0.1 m/s, 1 m/s and 5 m/s, with 100 mm of travel (80 mm for acceleration before hitting the sample and 20 mm for deceleration).

At high test rates, damping is often required to reduce the dynamic effects to ensure that the measured load is reliable; either grease or Blu-tak is typically used. The

Standard specifies that these oscillations must be within ±5% of the maximum load when the load is above half of the maximum value (see Figure 6.10). The peak load from load signal against time graph was used in calculating fracture energy (see Figure 6.9). There was no need to apply grease at the rate of 0.1 m/s as the data showed that dynamic effects were within the ±5% region. As grease could not provide sufficient damping at a rate of 1 m/s, a layer of 0.05 mm thick Blu-tak was applied as damping, this damping was sufficient for test rates up to and including 1 m/s.

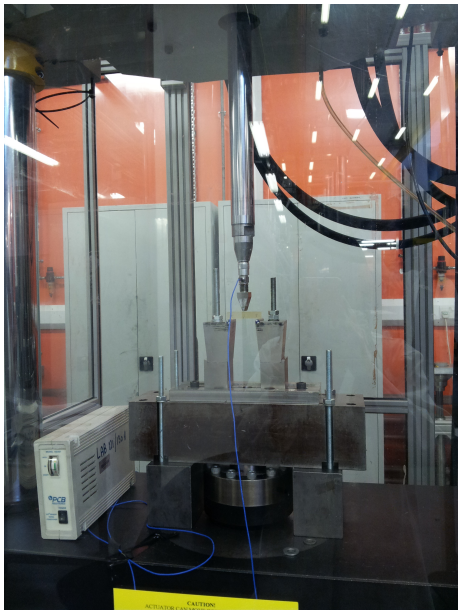

Figure 6.8: High rate SENB test setup

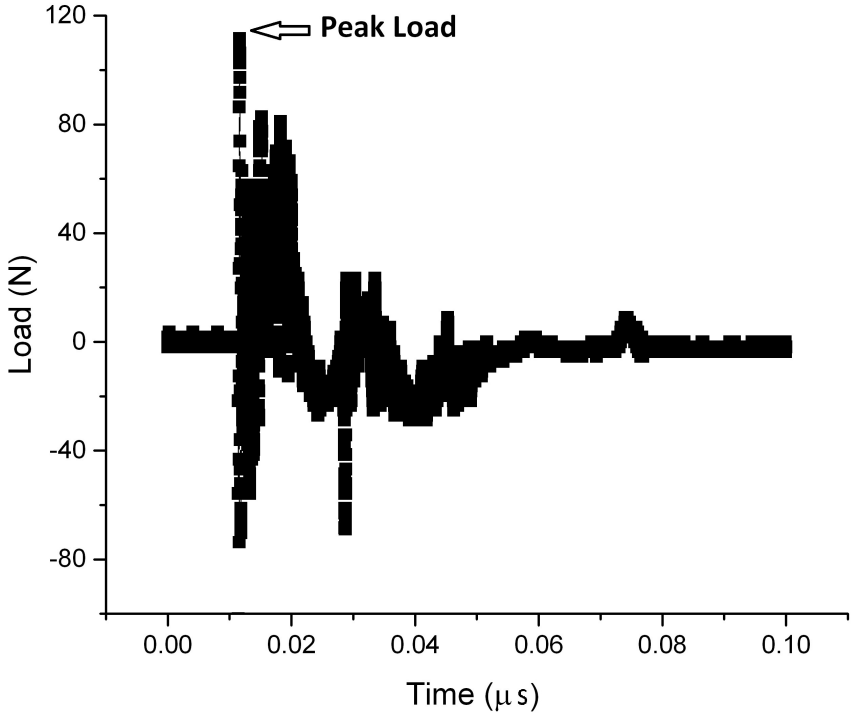


Figure 6.9: Load signal versus time graph example for SENB at a test rate of 1 m/s

When the rate was greater than 1 m/s, such as at 5 m/s, there were a large amount of oscillations even with significant damping applied to the specimen (Blu-tak of 0.1 mm thickness), and a thicker layer of Blu-tak did not make a difference. Therefore, test results from rates higher than 1 m/s were not reliable, and the formulations were not tested at 5 m/s. To improve the reliability of the results, investigations on testing specimens at lower temperatures were performed (more about the method is described in Section 6.5) as lower temperatures are equivalent to higher test rates.

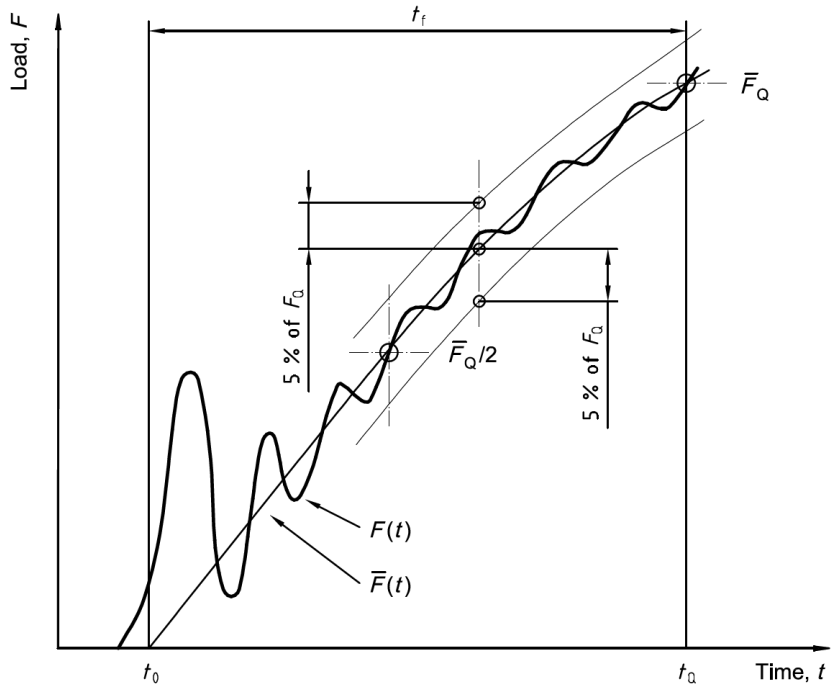


Figure 6.10: Force fluctuations in SENB fracture tests [40]

### 6.4.3 High rate SENB test results

#### 6.4.3.1 Silica-modified epoxy

Figure 6.11 and Table 6.5 show the fracture energies for SENB specimens of silica-modified epoxy tested at different test rates. There were some significant increases in the toughness for all wt% of silica when the rate of test was increased. Tests under quasi-static rate and 0.1 m/s showed similar results, the toughness values were not affected when the rate was changed but the values were relatively low. The increase in wt% at 1 m/s gave a steady increase in fracture energy up to 15 wt%. The highest values at 1 m/s were for 15 weight % of silica, which might be due the fact that when even higher

% of particles added, there is insufficient epoxy to increase the energy needed for void growth and shear yielding mechanisms. The literature reports that only some of the silica particles debond and lead to void growth of the epoxy matrix. Guild et al. [2] predicted that 14.3% of the silica particles would debond at high wt% of silica, which agrees with experimental measurements of 15% of the particles which debond [29]. The debonding of the silica particles will be discussed in the SEM fractography Chapter 9.

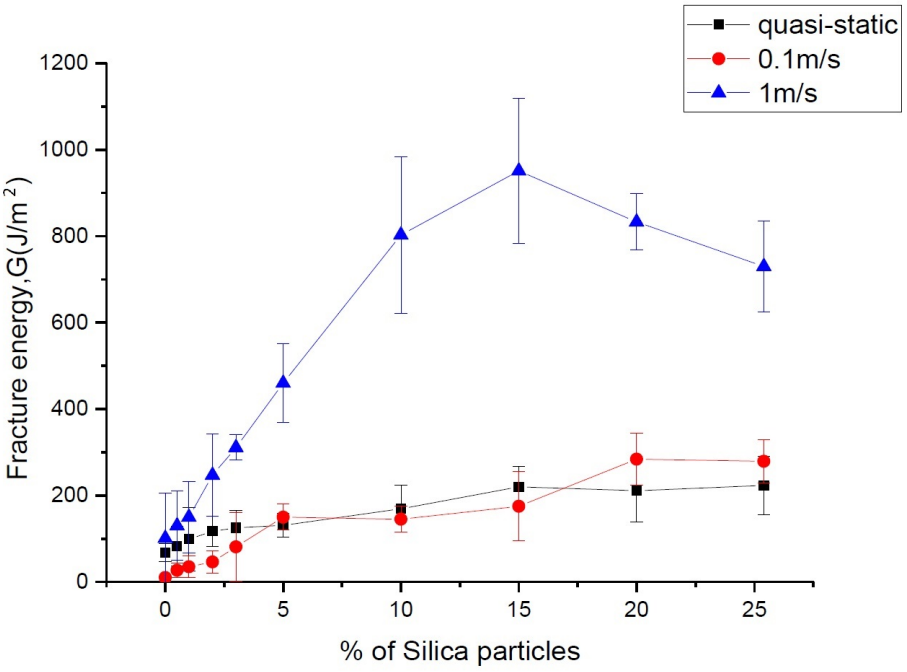


Figure 6.11: Fracture energy of silica-modified epoxy from SENB tests at different test rates

Table 6.5: Fracture energy of silica-modified epoxy at different rate

| Rate | quasi-static | | 0.1 m/s | | 1 m/s | |
|---|---|---|---|---|---|---|
| Wt% of Silica particles | G ($J/m^2$) | SD | G ($J/m^2$) | SD | G ($J/m^2$) | SD |
| 0 | 68 | 21 | 10 | 0 | 101 | 105 |
| 0.5 | 83 | 46 | 27 | 17 | 130 | 80 |
| 1 | 99 | 73 | 35 | 25 | 150 | 83 |
| 2 | 117 | 35 | 46 | 26 | 247 | 95 |
| 3 | 125 | 40 | 81 | 80 | 311 | 29 |
| 5 | 131 | 28 | 150 | 30 | 460 | 91 |
| 10 | 169 | 54 | 145 | 30 | 803 | 181 |
| 15 | 220 | 47 | 175 | 80 | 951 | 168 |
| 20 | 211 | 73 | 284 | 60 | 833 | 65 |
| 25.4 | 223 | 67 | 279 | 50 | 730 | 105 |

#### 6.4.3.2 CSR-modified epoxy

Figure 6.12 and Table 6.6 show the fracture energy values for SENB specimens of CSR modified epoxy tested at different rates. The CSR modified specimens tested at high test rate had very high fracture energy values when compared to the quasi-static ones. The increases in toughness were particularly significant when the wt% of CSR was high, however the standard deviations were higher as well, this was believed to be due to the very unstable fracture causing higher variations in the results. Therefore, the values from 5 wt% onwards at 1 m/s were considered to be unreliable as there were significant increases found, and the increase is likely to be due to the dynamic effects. As large standard deviations (1500 $J/m^2$) in fracture energy were found at 1 m/s, the results were not reliable, therefore low temperature SENB tests were used to provide clarifications to the high test rate results, see Section 6.5.

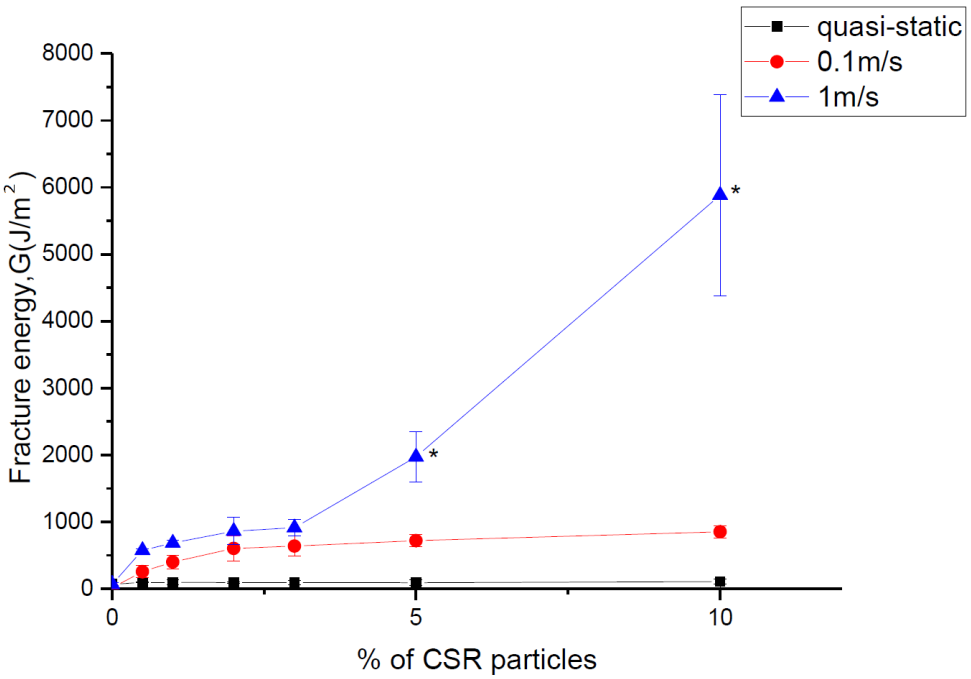


Figure 6.12: Fracture energy of CSR-modified epoxy at different test rates
∗ Dynamic effects are significant and hence the data are unreliable

Table 6.6: Fracture energy of CSR-modified epoxy from SENB tests at different rates

| Rate | quasi-static | | 0.1 m/s | | 1 m/s | |
|---|---|---|---|---|---|---|
| Wt % of CSR particles | G (J/m$^2$) | SD | G (J/m$^2$) | SD | G (J/m$^2$) | SD |
| 0 | 68 | 21 | 13 | 2 | 67 | 21 |
| 0.5 | 96 | 1 | 257 | 94 | 576 | 21 |
| 1 | 96 | 34 | 401 | 100 | 685 | 46 |
| 2 | 93 | 9 | 602 | 188 | 862 | 206 |
| 3 | 92 | 36 | 638 | 150 | 912 | 123 |
| 5 | 91 | 41 | 720 | 90 | 1972 | 380 |
| 10 | 108 | 40 | 852 | 90 | 5883 | 1500 |

#### 6.4.3.3 Hybrid-modified epoxy

Figure 6.13 and Table 6.7 show the fracture energy values for SENB specimens of hybrid-modified epoxy tested at different rates. There was an increase in fracture properties when the wt% of particles increased and when the test rate increased. However, large standard deviations were also found for the hybrid when 10 weight % of each particle type was added. This showed that some uneven distribution of particles (present when weight % of particle CSR added in was high) can produce variations in fracture properties at high rate. There were very large fracture energy values found for the hybrid when the rate was 1 m/s (the highest rate used), the large values with the large standard deviations could be not be considered as reliable. These higher variations were due to the increase in oscillations in the data that affected the accuracy of results as the dynamic effects were significant for all wt%. There were large oscillations before the peak load, see Figure 6.14. The dynamic effects were significant when the rate was at 1 m/s, there were high standard deviations values found (of about 30 %) and hence those data are unreliable.

Hybrid-modified specimens showed higher fracture properties when compared to the CSR and silica specimens. This is due to the different particle sizes which increased the plastic zone size and the amount of plastic deformation. There could be a higher shear when rubber cavitation occurs. The synergy effect was more remarkable when the rate was higher, so this effect is expected to be significant when specimens were tested under low temperature, as low temperature has a similar effect to high test rate. The significance of the synergy effect would be revealed further under low temperature testing. The mechanisms are discussed further with the SEM fractography in Chapter 9.

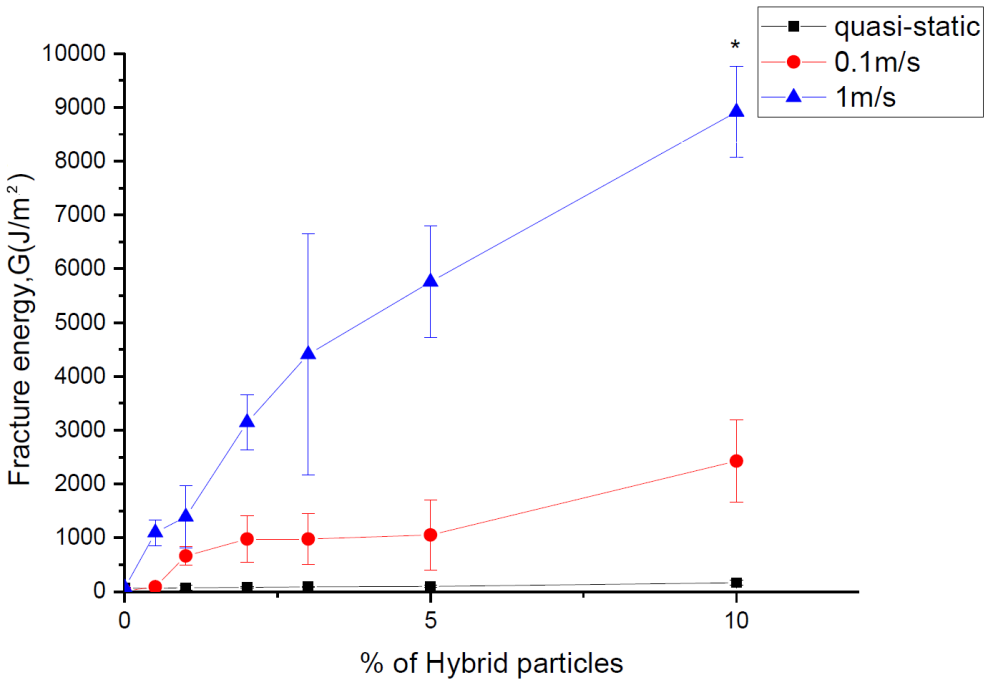


Figure 6.13: Fracture energy of hybrid-modified epoxy from SENB tests at different rates

$*$ Dynamic effects are significant and hence the data are unreliable

Table 6.7: Fracture energy of hybrid-modified epoxy from SENB tests at different rates

| Rate | quasi-static | | 0.1m/s | | 1m/s | |
|---|---|---|---|---|---|---|
| Wt % of hybrid particles | G ($J/m^2$) | SD | G ($J/m^2$) | SD | G ($J/m^2$) | SD |
| 0 | 63 | 11 | 13 | 4 | 67 | 21 |
| 0.5 | 62 | 4 | 91 | 5 | 1096 | 239 |
| 1 | 72 | 44 | 664 | 170 | 1392 | 573 |
| 2 | 80 | 14 | 977 | 436 | 3146 | 515 |
| 3 | 89 | 11 | 977 | 477 | 4409 | 2239 |
| 5 | 97 | 19 | 1054 | 653 | 5757 | 1038 |
| 10 | 166 | 49 | 2428 | 760 | 8918 | 847 |

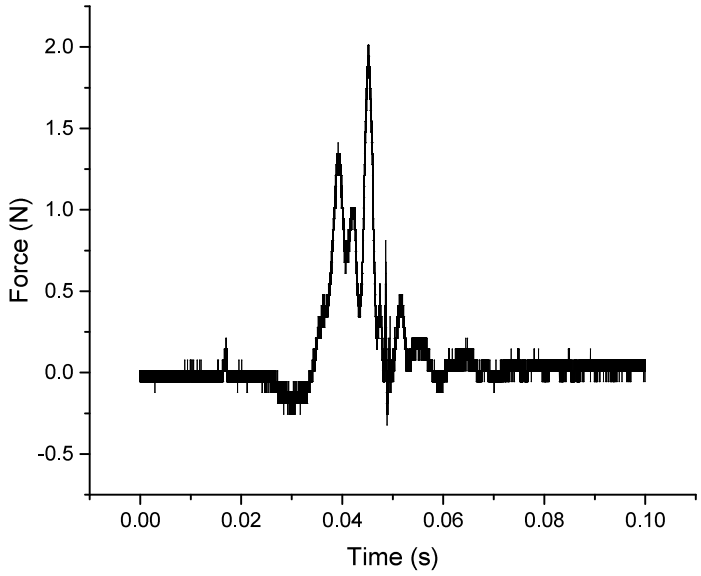


Figure 6.14: Example of force against time graph for SENB test at 1 m/s

## 6.5 Low temperature SENB tests

### 6.5.1 Introduction

SENB testing was performed at -40 and -80$^oC$ to investigate the fracture behaviour under brittle conditions, which was equivalent to testing under high rate. This can provide information about the fracture behaviour under brittle failure from another aspect. More details about the comparison of brittleness of low temperature specimens are included in Chapter 9.

### 6.5.2 Low temperature SENB test procedure

The SENB test setup was placed in a temperature chamber. The chamber was cooled using a supply of liquid nitrogen, by injecting controlled quantities of cold nitrogen gas into the chamber (see Figures 6.15 and 6.16). Specimens were placed inside the chamber for five minutes to reach the same temperature as the environment. Tests were performed at quasi-static rate. After one test had finished, the next test was performed only after the temperature had reached back to the set level, this could ensure all the tests were performed under the same conditions required. However, there were problems with low temperature. The machine could become frozen after a while, this is also related to the amount of liquid nitrogen supply (more at the beginning to reduce the temperature from room temperature). This affected the temperature control, which is maintained by the fan. The large differences in temperature between the inside and outside of the chamber produced large and quick changes in the temperature, the system and the fan may not be able to maintain a constant temperature under these conditions, hence could affect the accuracy of temperature reading. Therefore, small differences in testing temperatures were not suggested, as that would produce a larger variation in the test, so temperatures of -40$^oC$ and -80$^oC$ were used.

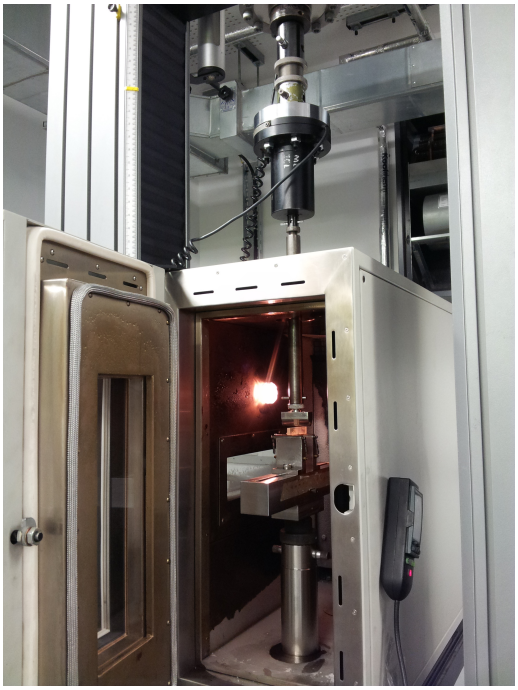

Figure 6.15: Low temperature SENB setup

Figure 6.16: Close-up of low temperature SENB setup

### 6.5.3 Low temperature SENB test results

All of the SENB specimens tested under low temperature had higher fracture toughness and fracture energy values than at quasi-static rate at room temperature, the values were higher when the temperature was lower. The results were more reliable with smaller standard deviations than at room temperature for all formulations. When compared to the quasi-static SENB results, there was a clearer increasing trend in fracture properties when the wt% of particles increased, which showed that the effect of toughening was more significant when the materials were under more brittle failure.

#### 6.5.3.1 Silica modified epoxy

The results from the low temperature tests on the silica specimens are shown in Table 6.8 and Figure 6.17 below. There was a significant increase in fracture energy found in all wt% of silica tested at -80$^oC$ compared to the room temperature tests. The increase was more significant with a high wt% of silica particles, as more than 100 % increase in fracture energy was measured. However, specimens that were tested at -40$^oC$ were found to have lower fracture energy values than those tested at room temperature for 10 wt% or higher of particles. Although it was not significantly lower, as the standard deviations overlap, these results were not expected. This could be due to the variations of readings during the starting of the experiment with the temperature chamber. When the load cell gets moist (due to water condensing when the chamber is cooling down), the reading of load cell can be affected and hence may have affected the results.

Table 6.8: Fracture energy of silica modified epoxy from SENB tests at low temperature

| Temperature | Room temperature (20°C) | | -40°C | | -80 °C | |
|---|---|---|---|---|---|---|
| % of Si particles | G (J/m$^2$) | SD | G (J/m$^2$) | SD | G (J/m$^2$) | SD |
| 0 | 68 | 21 | 93 | 9 | 126 | 15 |
| 0.5 | 83 | 46 | 101 | 30 | 130 | 0 |
| 1 | 99 | 73 | 112 | 0 | 158 | 2 |
| 2 | 117 | 35 | 117 | 14 | 161 | 16 |
| 3 | 125 | 40 | 132 | 0 | 179 | 2 |
| 5 | 131 | 28 | 132 | 15 | 213 | 30 |
| 10 | 169 | 54 | 144 | 6 | 305 | 9 |
| 15 | 220 | 47 | 192 | 18 | 312 | 12 |
| 20 | 211 | 73 | 197 | 27 | 332 | 6 |
| 25.4 | 223 | 67 | 200 | 17 | 349 | 19 |

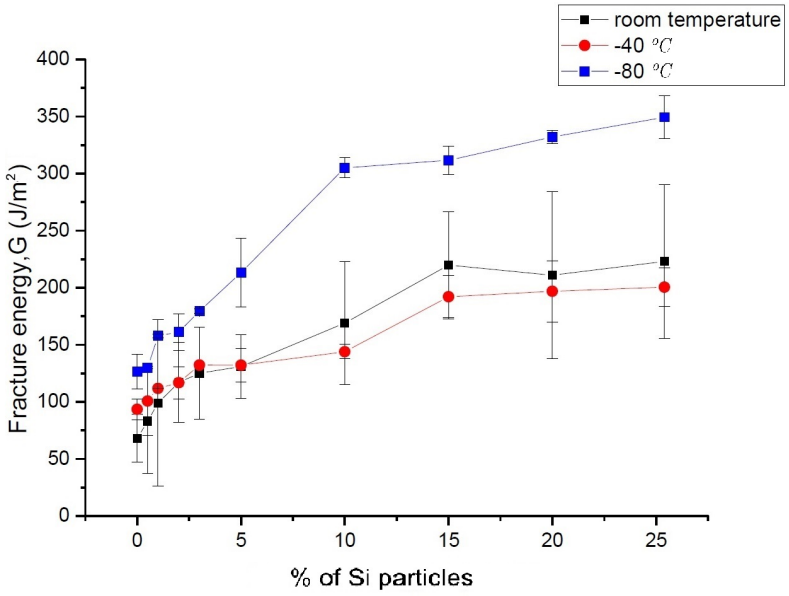


Figure 6.17: Fracture energy of silica modified epoxy from SENB tests at low temperature

#### 6.5.3.2 CSR modified epoxy

The results of the SENB tests at low temperature for CSR modified specimens are shown in Table 6.9 and Figure 6.18 below. There were higher fracture energy values

measured in tests performed at low temperature for all wt% of CSR. The lower the temperature, the more significant is the increase in fracture energy. The fracture energy is approximately doubled for specimens tested at -80$^oC$ when compared to the room temperature tests. There was a trend of an increase in fracture energy when the wt% of particles increased, this trend was also found in tests performed at -40$^oC$, but the fracture energy values were very similar to the room temperature results for all wt%. There was a plateau when the wt% of CSR particles added in was high (10 wt%). This suggested that the high wt% use of CSR is not the optimum % for toughening, medium to toward lower wt% (2 to 5 wt%) would provide a significant toughening effect as increasing the wt% further has no additional toughening effect.

Table 6.9: Fracture energy of CSR modified epoxy from SENB tests at low temperature

| Temperature | Room temperature (20°C) | | -40°C | | -80 °C | |
|---|---|---|---|---|---|---|
| % of CSR particles | G (J/m$^2$) | SD | G (J/m$^2$) | SD | G (J/m$^2$) | SD |
| 0 | 68 | 21 | 93 | 9 | 126 | 15 |
| 0.5 | 96 | 1 | 140 | 37 | 141 | 8 |
| 1 | 96 | 34 | 120 | 24 | 148 | 9 |
| 2 | 93 | 9 | 154 | 15 | 150 | 18 |
| 3 | 92 | 36 | 110 | 15 | 155 | 15 |
| 5 | 91 | 41 | 126 | 7 | 163 | 18 |
| 10 | 108 | 40 | 131 | 12 | 188 | 16 |

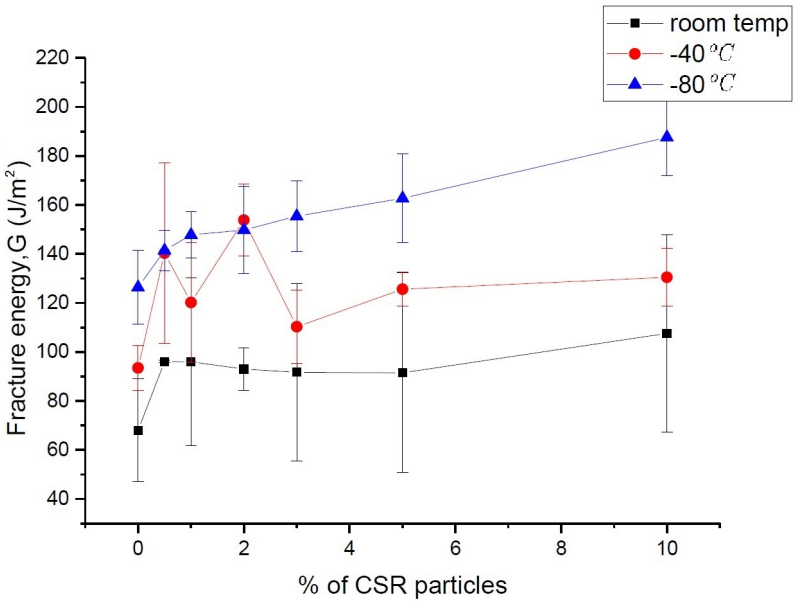


Figure 6.18: Fracture energy of CSR modified epoxy from SENB tests at low temperature

#### 6.5.3.3 CSR / silica hybrid modified epoxy

The results of the SENB tests at low temperature on hybrid modified specimens are shown in Table 6.10 and Figure 6.19 below. The trend for an increase in fracture energy when there is an increase in wt% of particles was even more notable with the use of hybrid CSR / silica particles for all temperature conditions, but the trend is smoother than at quasi-static test rates at room temperature, without any outliers. The lower the temperature, the higher the fracture energy. However, the increase in fracture energy for the low temperature tests was not as significant as with the use of only one type of particle. For the 10 wt% hybrid modified specimens tested at -40$^oC$, the same average fracture energy was found when compared to the tests performed at room temperature. All the fracture energy values at all temperatures were similar to the CSR ones, which were smaller than the silica fracture energies. The hybrid materials were expected to produce a higher toughening effect, but when the particle concentration is too high, the distance between particles is reduced and hence can reduce debonding or pull out of particles. There was some particles pull out but not significant. The values were similar for all temperatures, therefore, this would not be due an error during the test. The optimum amount of hybrid particles used is 10 wt% for all temperatures as this concentration produced the highest fracture energies.

Table 6.10: Fracture energy of CSR / silica hybrid modified epoxy from SENB tests at low temperature

| Temperature | Room temperature (20 °C) | | -40 °C | | -80 °C | |
|---|---|---|---|---|---|---|
| % of Hybrid particles | G (J/m$^2$) | SD | G (J/m$^2$) | SD | G (J/m$^2$) | SD |
| 0 | 63 | 11 | 93 | 9 | 126 | 15 |
| 0.5 | 62 | 4 | 98 | 14 | 130 | 12 |
| 1 | 72 | 44 | 97 | 29 | 134 | 13 |
| 2 | 80 | 14 | 105 | 8 | 134 | 19 |
| 3 | 89 | 11 | 107 | 4 | 136 | 6 |
| 5 | 97 | 19 | 117 | 5 | 138 | 16 |
| 10 | 166 | 50 | 169 | 6 | 192 | 17 |

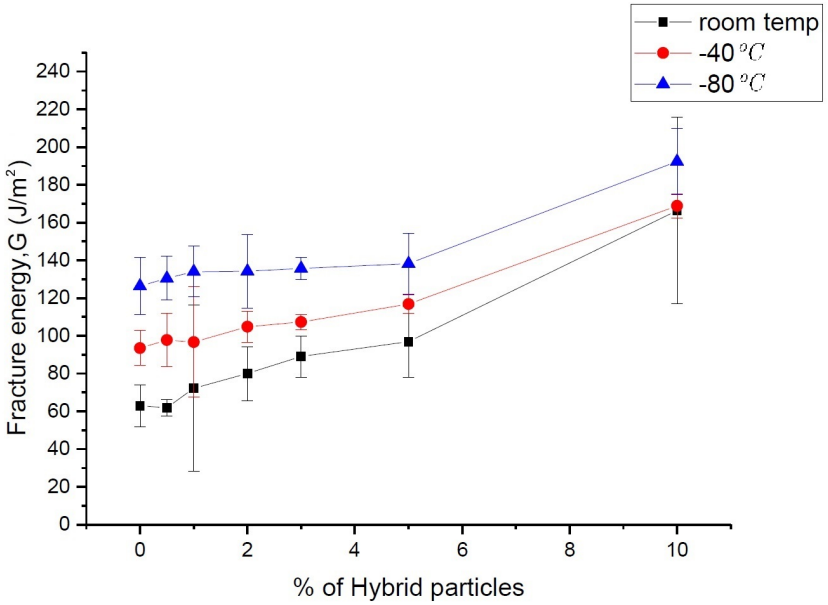


Figure 6.19: Fracture energy of CSR / silica hybrid modified epoxy at low temperature

### 6.5.4 Conclusions

SENB tests of all formulations at quasi-static, high test rates and at low temperature were investigated and compared.

The quasi-static SENB provided fracture energy values without interfacial failure

problem. The values were used as an reference to other brittle testing conditions (high test rates and at low temperature).

The high rate SENB results show more brittle behaviour, higher fracture energy values were found when compare to quasi-static SENB. There is a limitation for the rate that can be used, as the dynamic effect increases when rate increases. The higher the rate generally gives higher fracture energy values for all formulations.

It is shown that there is an increase in fracture energy when the wt% of particles added increases, for all the formulations tested at low temperature. The use of silica / CSR hybrid did not produce higher fracture energy values when compared to silica modified epoxy. The use of silica / CSR hybrid did not improve the fracture properties at low temperature.

Most of the results under brittle failure (high rate and low temperature) had higher standard deviations due to the difficulties in performing tests under the specific conditions required. In order to eliminate the effects caused by variables from the setup, FE modelling predictions were made, more details can be found in Chapter 10. The next Chapter will provide a summary of all the fracture energy values measured experimentally.

# Chapter 7

# Fracture energy comparison

## 7.1 Introduction

In this Chapter, all the fracture energy values measured experimentally for the unmodified, silica, CSR and silica / CSR hybrid formulations are compared. First, the results from two test geometries (TDCB and SENB) at quasi-static rate test will be compared. Then the high rate test results from these geometries will be compared. Finally the high rate SENB results will be compared with the low temperature SENB results. This summary Chapter aims to provide insight about how the fracture energy is affected by the different brittle test conditions, and how this affects the failure mechanisms.

## 7.2 Quasi-static fracture energy (from TDCB and SENB)

The section below compares results from quasi-static tests of TDCB and SENB geometries with silica and CSR formulations. In the TDCB tests, the presence of stick-slips produce initiation and arrest points, which can only be compared separately to propagation values. All three types of fracture results are plotted in the graph with SENB fracture energy.

### 7.2.1 Silica-modified epoxy

Figure 7.1 compares the fracture energies from both quasi-static SENB and TDCB silica-modified specimens. The fracture energy values found from quasi-static SENB from all wt% were higher than all the quasi-static TDCB values, this is due to the interfacial failure in the TDCB tests. There is a similar trend of increase in fracture energy at low wt% of quasi-static SENB when comparing propagation values of quasi-static TDCB.

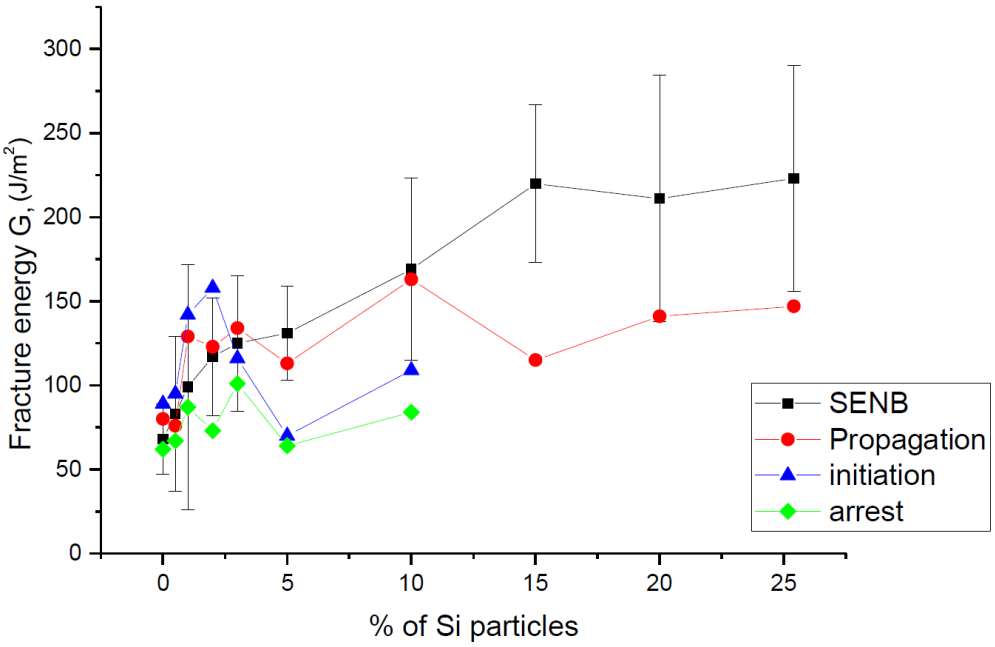


Figure 7.1: Fracture energy of silica-modified epoxy (SENB, TDCB)

### 7.2.2 CSR-modified epoxy

Figure 7.2 compares the fracture energy found from both SENB and TDCB tests on CSR-modified specimens. The fracture energies from TDCB tests were found to be larger than those found from SENB, as the model predictions of the propagation were lower than the TDCB experimental values, it is suggested that the higher $G_c$ values were due to stick-slip and cohesive failure. This concluded that TDCB joints performance can be slightly varied and highly affected by the conditions of testing and joint preparation. The greater mechanical performance when the % of particles increased can also be due to the increase in viscosity of the mixture. When the % of particles added in was low, very low viscosity mixtures were produced and the epoxy ran down from the joint easily. This did not happen when the % of CSR added in were high, therefore the different viscosity in the mixture can alter some of the results.

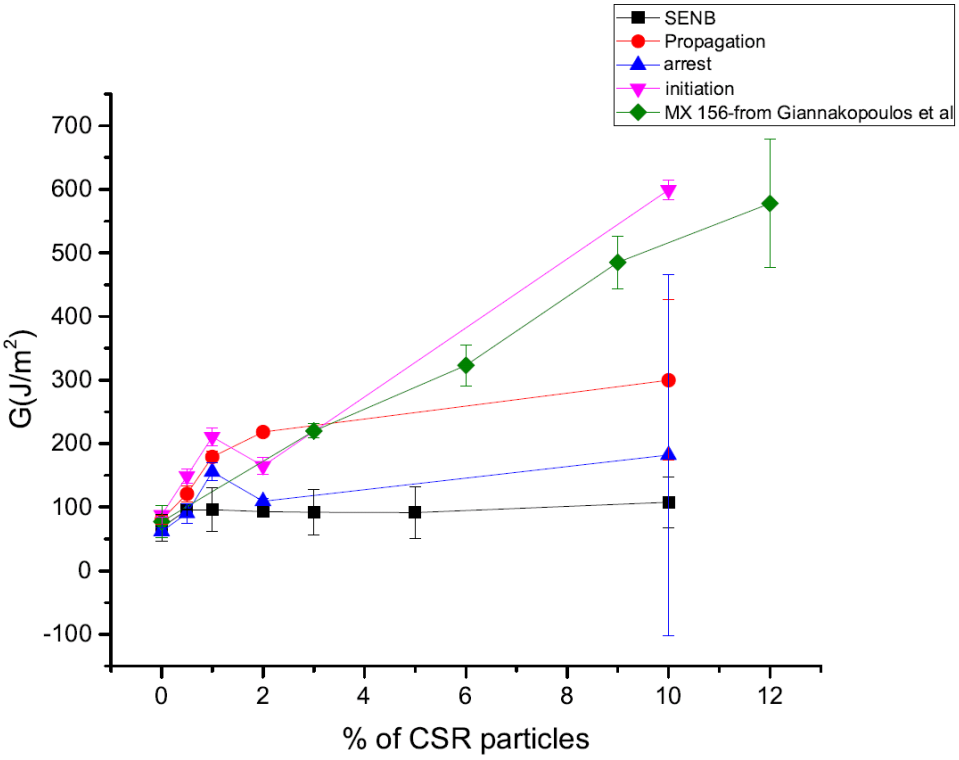


Figure 7.2: Fracture energy of quasi-static CSR (SENB, TDCB) and CSR-MX-156 modified epoxy [11]

Due to the problem with stick-slips, silica / CSR hybrid were compared under different conditions, the high rate SENB and high rate TDCB in the next Section and SENB results from Section 6.3.4 include silica / CSR hybrid results.

### 7.2.3 Summary - Quasi-rate fracture energy

Some degree of interfacial failure is present in all TDCB tests except for standard unmodified epoxy specimens. Therefore, there are very different fracture energy values found in all three graphs. This can be the cause of different fracture energy values found from TDCB and SENB.

## 7.3 High rate fracture energy

### 7.3.1 Introduction

A high rate method was used in both the SENB and TDCB tests. Their fracture energy results are compared below. More information about their fracture surfaces is included in SEM Chapter 9.

Both high rate SENB and high rate TDCB used three specimens for each formulation, performed using the same machine, so their results and standard deviations can be compared and are expected to be similar.

The rates used in SENB are: 0.1 and 1 m/s.

The rates used in TDCB are: 0.1, 1, 2 and 3 m/s.

Specimens of silica, CSR and silica / CSR modified epoxies are used in both high rate tests, but there are only up to 10 wt% of particles used in TDCB, while SENB had the whole range of wt% up to 25.4 wt%. This was due to the limit of memory in the high speed camera used in TDCB. Therefore, only up to 10 wt% results are compared in this Chapter.

### 7.3.2 High rate SENB

In high rate SENB, there was an increase in fracture energy when the wt% of particles increases for all formulations. There was also a higher increase of fracture energy when the rate increases. Same pattern was found for all formulations in high rate SENB at the same rate.

### 7.3.3 High rate TDCB

Figure 7.3 shows the fracture energy for the high rate SENB and high rate TDCB tests at 0.1 m/s. Figure 7.4 shows the fracture energy results for the high rate SENB and high rate TDCB tests at 1 m/s. There was an increase in fracture energy when the rate increases in high rate TDCB, but not as much as in high rate SENB. There are larger fracture energy values found in high rate SENB when compared to high rate TDCB for all formulations. There is a similar trend for both 0.1 m/s and 1 m/s, there is a higher fracture energy when the wt% increases for all particles. But there are very large fracture energies found in high rate SENB when compared to high rate TDCB. The fracture energy values from 1 m/s are larger than those from 0.1 m/s, which indicated that the more brittle test condition results in higher fracture properties of material.

There was a drop in fracture energy at 10 wt% at rates of 1, 2 and 3 m/s in the high rate TDCB tests. All the TDCB fracture energy values were smaller than those in SENB, the presence of stick slips had lower fracture energy values measured.

The standard deviations in TDCB vary, there were some high standard deviations at the high wt%, but other than that, values were similar to the standard deviations in SENB. Therefore, they are similar in reliability.

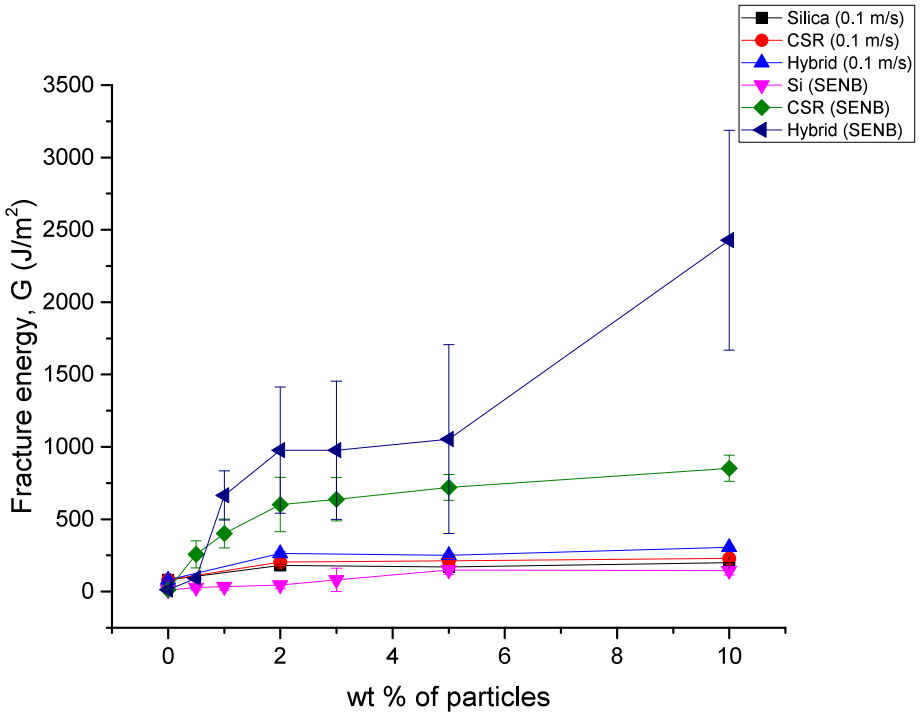


Figure 7.3: Fracture energy at 0.1 m/s for high rate SENB and high rate TDCB for silica, CSR, silica / CSR hybrid modified epoxies

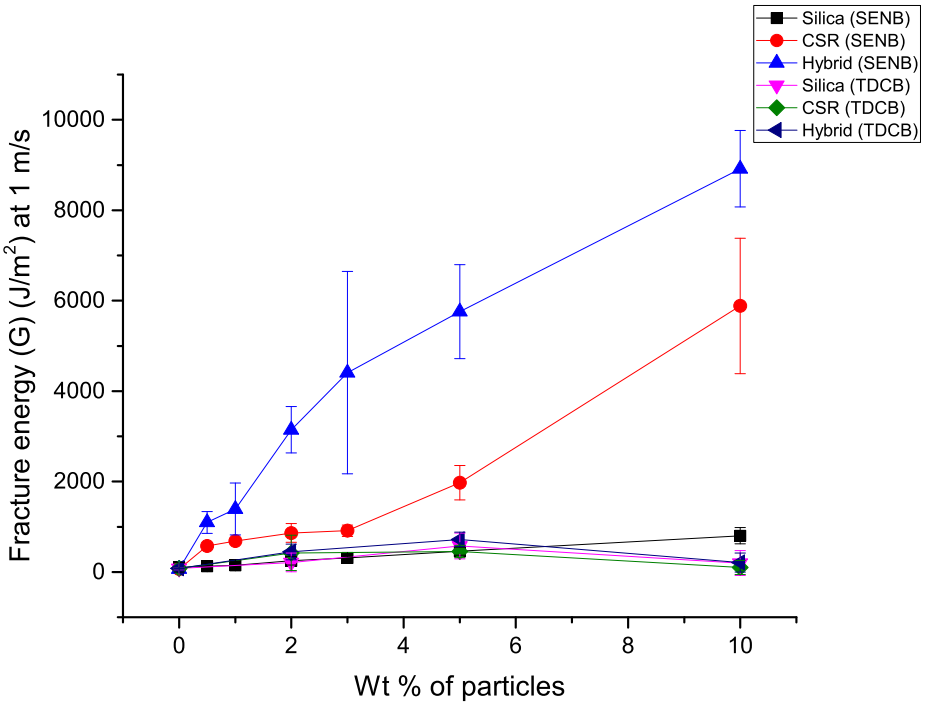


Figure 7.4: Fracture energy at 1 m/s for high rate SENB and high rate TDCB for silica, CSR, silica / CSR hybrid modified epoxies

### 7.3.4 Summary

With the same test rate, high rate TDCB was expected to be similar when compared to high rate SENB. Their results were very different, that could be due to the difficulties in performing high rate tests for both geometries used. There are bigger variations in high rate TDCB results, the pattern of behaviour was not clear there. The differences in the test methods might have some effect on the results. Improvements in both methods are needed, more information regarding further work suggested are included in Chapter 13.

## 7.4 Fracture energy from high rate and low temperature

### 7.4.1 Introduction

As both high rate and low temperature tests means that the specimens are undergoing brittle failure, a comparison between these results would provide some ideas about under what conditions, the fracture behaviour would be highly affected. It may also be possible

to use the low temperature data to predict the fracture energy at higher test rates than can be obtained experimentally if there is agreement between the low temperature and high rate results.

### 7.4.2 High rate and low temperature SENB comparison

The test rate of 1 m/s was chosen to compare to the low temperature of -80$^oC$. As these two are the more brittle conditions in the study, their effect should be more significant for a fair comparison.

Figure 7.5 shows fracture energy at high rate (1 m/s) and low temperature (-80$^oC$) for silica, CSR and hybrid modified epoxies. There were very high fracture energy values found from high rate tests of CSR and hybrid specimens. All other specimens showed similar values, there were only a small increase in fracture energy when the wt% of particles increases. The third highest curve was also found in high rate results, hence all the high rate tests showed a larger increase in fracture properties when compared to the low temperature results. As the fracture energy values were too high in most of the high rate results, low temperature SENB testing was more reliable.

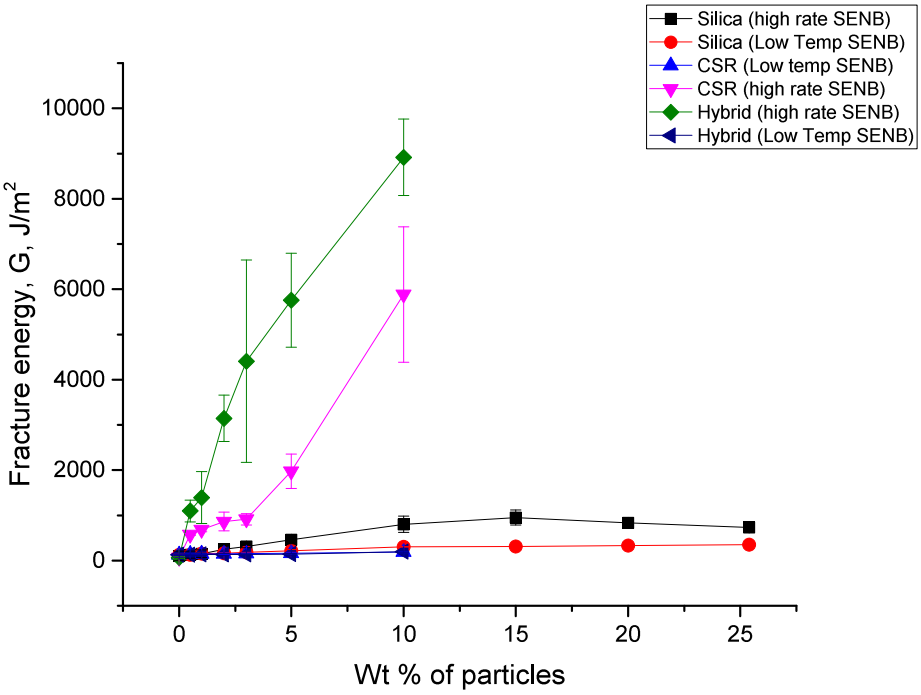


Figure 7.5: Fracture energy at high rate (1 m/s) and low temperature (-80$^oC$) for silica, CSR and hybrid modified epoxies

Figure 7.6 shows fracture energy at high rate (2 m/s) and low temperature (-80$^oC$) for silica, CSR and hybrid modified epoxies. When the results from 2 m/s TDCB are compared with -80$^oC$ SENB, the values are closer but still not similar. Only the 2 m/s TDCB silica results were similar to the low temperature -80$^oC$ SENB results. This is not enough to prove that the TDCB tests at 2 m/s is comparable with the -80$^oC$ SENB.

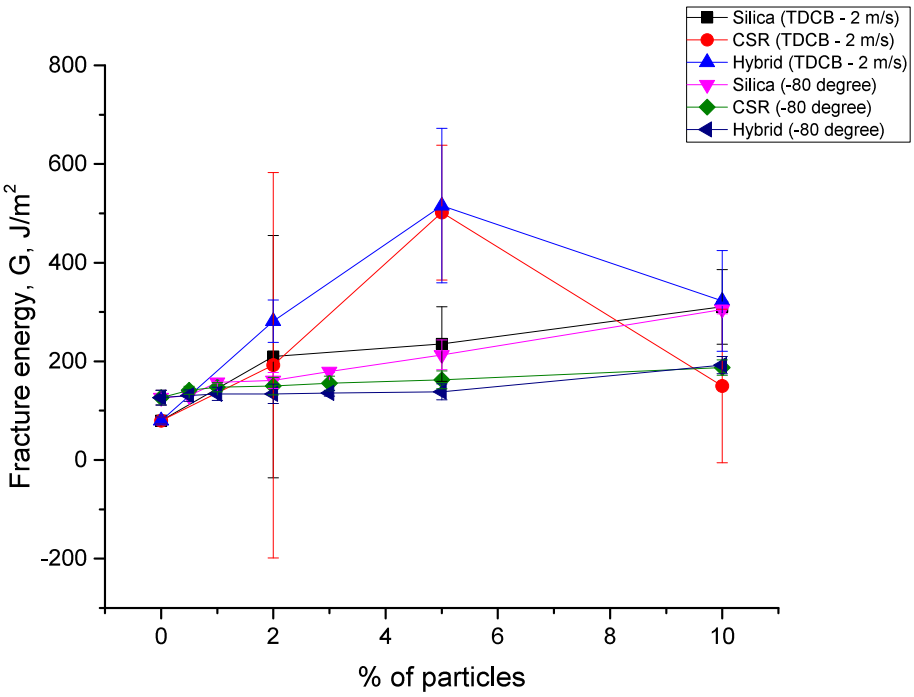


Figure 7.6: Fracture energy at high rate (2 m/s) and low temperature (-80$^oC$) for silica, CSR and hybrid modified epoxies

Other combinations of comparisons were not considered, as they were too different to be compared, the different conditions were not similar in their effects.

### 7.4.3 Summary - fracture energy from high rate and low temperature results

The high rate SENB tests showed a greater effect on the measured fracture energy when compared to low temperature SENB. There is no low temperature TDCB performed previously due to the difficulties in monitoring crack under low temperature conditions and the effect of substrate causing interfacial failure under low temperature. Therefore,

further study on the effect of fracture energy of TDCB under low temperature is needed, in order to confirm the effect of low temperature test conditions on the fracture energy.

## 7.5 Conclusions

Quasi-static rate results gave smaller fracture energy values when compared to low temperature and high rate for both TDCB and SENB tests as expected. Other factors such as the presence of stick-slips had a an influence on the fracture energy measured in the TDCB tests, it is more notable under quasi-static rate as the values were smaller. High rate has a greater effect in fracture energy when compared to low temperature. However, more investigations are needed in order to confirm the relevant levels of effect in both conditions. The dynamic effects and large change of temperature also had a big influence on the results, hence FE models of the low temperature and high rate tests were made to predict the actual fracture properties, see Chapter 10 for more.

# Chapter 8

# Analytical models

## 8.1 Introduction

Analytical models were used to predict the modulus and fracture energy of the modified epoxies. This method identifies the effect of relative contributions of different particles in hybrid systems, as well as the presence of any synergistic effect. The toughening effect for fracture properties is then confirmed by SEM images, in Chapter 9.

Common analytical models for modulus are such as the Nielsen [2] and Halpin-Tsai [2] models. The Halpin-Tsai model is used as it is easy to use and it produced good predictions in the literature [11]. Other modulus models such as the Hirsch model [11] are also often used in predicting modulus of particles reinforced epoxy and composites but mostly for comparison with FE modelling results.

The modulus models predict the modulus of the particle modified epoxy using the modulus values of the individual components (the epoxy and the particles).

## 8.2 Halpin-Tsai model

### 8.2.1 Modulus Predictions from Halpin-Tsai Model

In the Halpin-Tsai model, the particles are assumed to be well-bonded to the matrix and homogenously dispersed in the epoxy [40]. The Halpin-Tsai model predicts the modulus (E) of a material with particles using [2, 3, 11]:

$$E = \frac{(1 + \xi\eta v_f)}{(1 - \eta v_f)} E_u \tag{8.1}$$

where $E_u$ = Young's modulus of the matrix, $v_f$ = volume fraction of particles and $\xi$ = shape or geometry factor, which is equal to 2w/t (where w = particle length and t = particle thickness, so $\xi$= 2) and $\eta$ can be expressed as:

$$\eta = \left(\frac{E_p}{E_u} - 1\right) / \left(\frac{E_p}{E_u} + \xi\right) \tag{8.2}$$

where $E_p$ = modulus of particles and $E_u$ = modulus of unmodified epoxy. The $E_u$ value used for the unmodified epoxy = 3.14 GPa, as measured in the present work.

The hybrid-modified epoxy predictions assume that the modulus for the hybrid-modified epoxy is equal to the sum of the increases due to the addition of each particle.

### 8.2.2 Modulus prediction results

#### 8.2.2.1 Silica-modified epoxy

The predicted modulus values of the silica-modified epoxy are shown in Figure 8.1 and Table 8.1. Most of the predicted modulus values were very close to the measured values. There was a linear increase in modulus in the predictions when the % of silica particles increased, and the gradient of this linear increase was very similar to that measured experimentally. This shows that the Halpin-Tsai model works well for the silica-modified epoxy. It also confirms that the assumption that the modulus of the silica nanoparticles is equal to that of bulk silica (i.e. $E_p$ = 70 GPa).

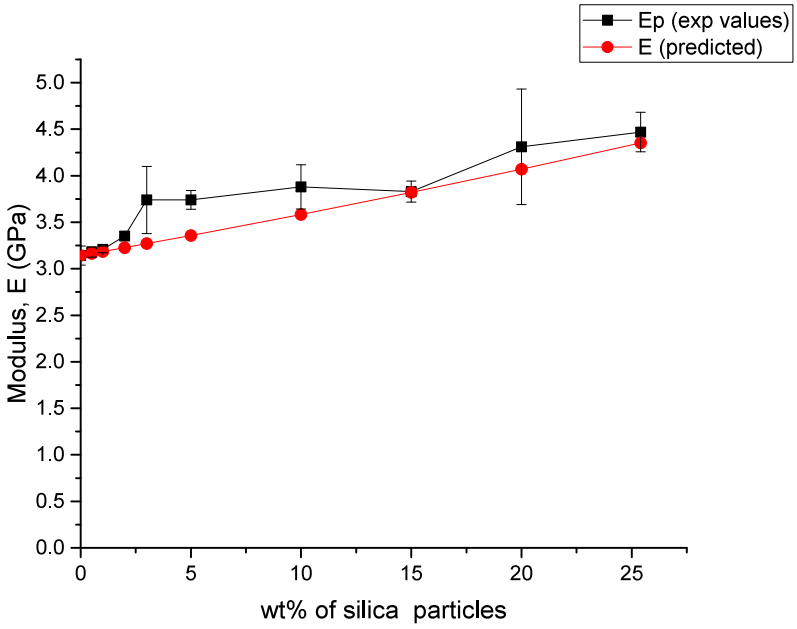


Figure 8.1: Predicted modulus from Halpin-Tsai model of silica-modified epoxy

Table 8.1: Predicted modulus from Halpin-Tsai model of silica-modified epoxy

| Wt% of silica particles | E (GPa) (exp values) | E (GPa) (predicted) |
|---|---|---|
| 0 | 3.14 | 3.14 |
| 0.5 | 3.18 | 3.16 |
| 1 | 3.21 | 3.19 |
| 2 | 3.35 | 3.23 |
| 3 | 3.74 | 3.27 |
| 5 | 3.74 | 3.36 |
| 10 | 3.88 | 3.58 |
| 15 | 3.83 | 3.82 |
| 20 | 4.31 | 4.07 |
| 25.4 | 4.47 | 4.35 |

#### 8.2.2.2 CSR-modified epoxy

The predicted modulus values of the CSR-modified epoxy are shown in Figure 8.2 and Table 8.2 below. There was only a small increase in modulus when the wt% of particles increases in the predicted results, while the increase was more obvious in experimental results. There was an unexpected reduction at CSR 10 wt% in experimental results, which is likely to be due to clustering of particles when the wt% of particles was high (10 wt% was the highest possible wt% of CSR that can be added into the resin). Further discussion of CSR particle clustering is presented in Chapter 9, where the SEM images of the formulations are shown. The predicted value suggested that a higher modulus could be obtained with a better distribution of particles at 10 wt% CSR. Although the rubber core of the CSR particles will have a low modulus when compared to epoxy, the modulus of the CSR-modified epoxy increases with wt%. This indicates that there is the presence of PMMA shell on the CSR particles, and the PMMA shell of the CSR particles has a modulus higher than that of the epoxy. A value of $E_p = 8.0$ GPa was used for the CSR particles.

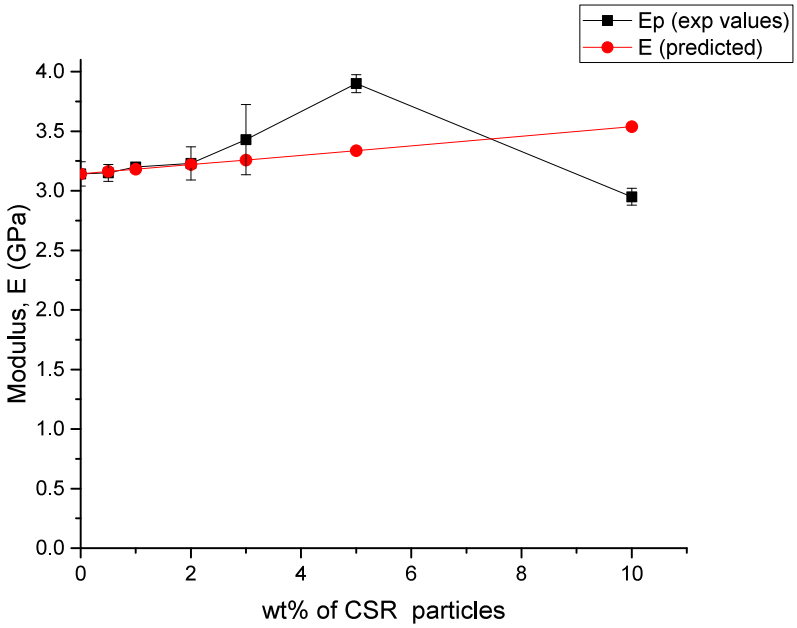


Figure 8.2: Predicted modulus from Halpin-Tsai model of CSR-modified epoxy

Table 8.2: Predicted modulus from Halpin-Tsai model of CSR-modified epoxy

| Wt% of CSR particles | E (GPa) (exp values) | E (GPa) (predicted) |
|---|---|---|
| 0 | 3.14 | 3.14 |
| 0.5 | 3.15 | 3.16 |
| 1 | 3.2 | 3.18 |
| 2 | 3.23 | 3.22 |
| 3 | 3.43 | 3.26 |
| 5 | 3.9 | 3.34 |
| 10 | 2.95 | 3.54 |

#### 8.2.2.3 Silica / CSR hybrid-modified epoxy

The predicted modulus values for the silica / CSR hybrid-modified epoxy are shown in Figure 8.3 and Table 8.3 below. The hybrid predictions were made by adding the modulus increases contributed by each of the two particles predictions. A similar pat-

tern of results was found in the hybrid-modified epoxy predictions when compared to the experimental results, but the experimental values did not show a clear increase in modulus when the wt% of particles is high. There is a drop at 10 wt% silica / CSR hybrid specimens, same as in CSR specimens, as 10 wt% of CSR particles were used. The predicted values suggested that the synergy effect was not found. Investigation of their fracture surfaces revealed more about the mechanisms involved (see Chapter 9).

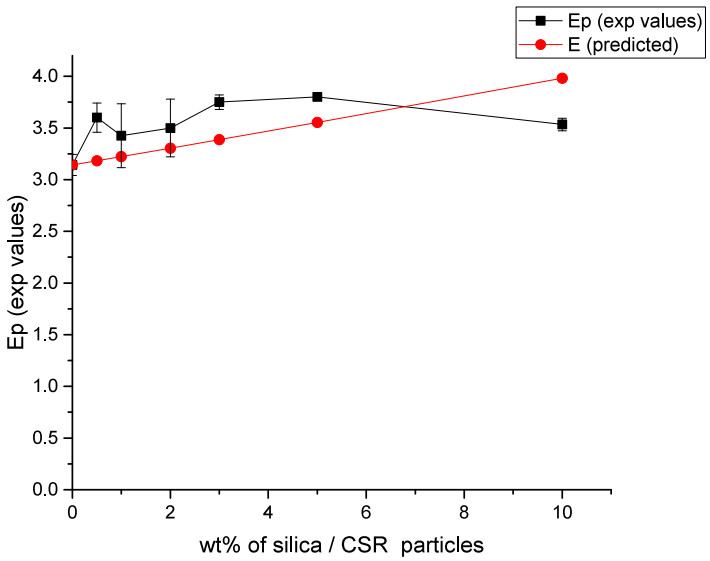


Figure 8.3: Predicted modulus from Halpin-Tsai model of silica / CSR hybrid-modified epoxy

Table 8.3: Predicted modulus from Halpin-Tsai model of silica / CSR hybrid-modified epoxy

| Wt% of silica / CSR particles | E (GPa) (exp values) | E (GPa) (predicted) |
|---|---|---|
| 0 | 3.14 | 3.14 |
| 0.5 | 3.60 | 3.18 |
| 1 | 3.43 | 3.22 |
| 2 | 3.50 | 3.30 |
| 3 | 3.75 | 3.39 |
| 5 | 3.80 | 3.55 |
| 10 | 3.53 | 3.98 |

### 8.2.3 Summary

Most of the predicted modulus values were very similar to the experimental values, and the predictions agreed extremely well with the experimental findings. The silica-modified epoxy predictions agreed best with the experimental results. The modulus of CSR modified epoxy would be expected to be lower than the modulus of the unmodified epoxy, because the modulus of rubber is lower than epoxy, therefore, the addition of CSR particles would reduce the overall modulus of the material. However, the PMMA shell on the CSR particles increases the modulus, hence, higher modulus values were found in the CSR modified epoxy. The drop at CSR 10 wt% was due to clustering of particles. This pattern continues in silica / CSR hybrid-modified epoxy, and caused a drop in the modulus for the 10 wt% hybrid specimens.

Analytical model results can be compared with FE model, but as tensile model is not in the focus of fracture study, FE model of the exact tensile test was not made. However, a one-element tensile model was made to confirm the cohesive values used in other FE models in this study, more about FE tensile model is discussed in Section 10.2.2.

## 8.3 Huang & Kinloch fracture model

### 8.3.1 Introduction

The Huang and Kinloch model [9] has commonly been used to predict the toughening contribution of particles [2, 3, 11]. This is because it takes into account the principal toughening mechanisms of shear banding, and void growth after cavitation or debonding of the particles. Previous work has reported that some epoxy polymers exhibit shear banding, but others do not [2, 3, 11]. For rubber-modified epoxies, the rubber particles may cavitate to create voids which then grow by plastic deformation of the epoxy and hence increase the toughness. It has been reported that 100% of the rubber particles cavitate, but cavitation is easier for soft and large particles, so small particles or those with a stiffer rubber core may not cavitate [11]. For silica-modified epoxies, the main toughening mechanism is debonding and void growth. The % of void growth, i.e. the proportion of the silica particles which debond, has been found to be 14.3%, and this % does not increase when a higher % of particles is used, as debonding is highly affected by the distances between particles [2, 3].

Hence three different cases are modelled, where:

1. Assume 100% of particles show plastic void growth.
2. Assume 14.3% of particles show plastic void growth.
3. Shear bond yielding only.

All three assumptions are considered in this study, results are included in Section 8.3.7.

### 8.3.2 Fracture energy representation

The overall fracture energy is represented by Huang and Kinloch [9] as:

$$G_c = G_u + \psi \tag{8.3}$$

where $G_u$ = fracture energy of unmodified epoxy and $\psi$ = overall toughening contributions of the particle phase. This is generally:

$$\psi = \delta G_s + \delta G_{db} + \delta G_v \tag{8.4}$$

where $\delta G_s$ represents the increase in fracture energy due to shear-banding, $\delta G_{db}$ represents the debonding (or cavitation) of particles and $\delta G_v$ represents plastic void-growth.

Debonding occurs for hard particles while cavitation occurs for soft particles [2, 3, 11],

but both processes create a void which is then able to grow by plastic deformation of the epoxy surrounding the void due to the triaxial stress state within the plastic zone at the crack tip. Debonding or cavitation do not contribute significantly to the energy absorption [2, 3, 11] and hence can be ignored. Therefore:

$$\psi = \delta G_s + \delta G_v \tag{8.5}$$

The contributions of shear band yielding and void growth can be represented in the equations [2, 3, 11] shown below.

### 8.3.3 Contribution of shear band yielding

The energy contribution of shear band yielding ($\delta G_s$) is given by [5]:

$$\delta G_s = 0.5 v_f \sigma_{ycu} \gamma_{fu} F'(r_y) \tag{8.6}$$

where $v_f$ = volume fraction of particles, $\sigma_{ycu}$ = yield stress and $\gamma_{fu}$ = failure strain of unmodified polymer (measured from plane-strain compression tests), and

$$F'(r_y) = r_y \left[ \left( \frac{4\pi}{3v_f} \right)^{1/3} \left( 1 - \frac{r_p}{r_y} \right)^3 - \frac{8}{5} \left( 1 - \frac{r_p}{r_y} \right) \left( \frac{r_p}{r_y} \right)^{5/2} - \left( \frac{16}{35} \frac{r_p}{r_y} \right)^{7/2} - 2 \left( 1 - \frac{r_p}{r_y} \right)^2 + \frac{16}{35} \right] \tag{8.7}$$

where $r_p$ = radius of particles and $r_y$ = radius of the plastic zone of the modified epoxy which is given by:

$$r_y = K_{sp}^2 \left( 1 + \frac{\mu_m}{3^{1/2}} \right)^2 r_{pzu} \tag{8.8}$$

where $K_{sp}$ = maximum stress concentration around a particle, $\mu_m = 0.2$ is a material constant, and $r_{pzu}$= radius of plastic deformation zone of unmodified epoxy, as discussed below. The value of $K_{sp}$ is a function of the volume fraction of particles and can be expressed as [5]:

$$K_{sp} = 0.59 v_f + 1.65 \tag{8.9}$$

### 8.3.4 Contribution of plastic void growth

The energy contribution from plastic void growth ($\delta G_v$) can be expressed as:

$$\delta G_v = \left(\frac{1-\mu_m^2}{3}\right)(v_{fv} - v_f)\sigma_{ycu} r_{pzu} K_v^2 \tag{8.10}$$

where $v_f$ = volume fraction of voids, $v_{pv}$ = volume fraction of particles, they are different things, $\mu_m$ = material constant, $\sigma_{ycu}$ = compressive yield stress of unmodified polymer, $r_{pzu}$ = radius of plastic zone at fracture (more about the plastic zone size is shown in Section 8.3.6 below), $K_v$ = stress concentration factor for voids, which depends on the volume fraction of reinforcement and can be expressed as:

$$K_v = 0.918 v_f + 2.11 \tag{8.11}$$

There are two assumptions in void growth:
1. Assume 100% of particles show debonding /cavitation and void growth
2. Assume 14.3% of particles show debonding /cavitation and void growth

The 14.3% is the amount of debonding and void growth for silica particles found in most studies such as Hsieh et al. [29] and Bray et al. [63], there is a theoretical prediction that there is a 1/7 chance that a randomly dispersed nanoparticle would be debonded, which makes a 14.3% chance that a nanoparticle will be debonded [63]. For silica-modified epoxy in the present work, similar toughening mechanisms, of shear band yielding between particles and plastic void growth are expected to result from interfacial debonding and plastic deformation of the polymer [29].

The 100% is the amount of cavitation and void growth for rubber particles found in studies such as [25]. The volume fraction of voids, $v_{fv}$, can be calculated by assuming that a void will grow until the circumferential strain equals the failure strain measured from plane strain compression tests. The radius of a void is given by:

$$r_v = (1 + \gamma_{fu}) r_p \tag{8.12}$$

where $\gamma_{fu}$ = failure strain in plane strain compression and $r_p$ = radius of particle. Alternatively the volume fraction of voids can be measured from SEM of the the fracture surfaces. In the present work the strain to failure method was used, as this makes the analytical modelling truly predictive. If the volume fraction of voids was measured from the fracture surfaces then the fracture tests need to be performed before the modelling can be done, so the results are not properly predictive.

### 8.3.5 Contribution of cavitation, debonding and bridging

As cavitation, debonding and bridging have almost no contribution to the overall fracture energy, they are not taken into consideration in this model. According to the study by Giannakopoulos et al. [11], debonding was on all of the fracture surface of the CSR particle modified epoxies. There was a small amount of cavitation, but only when small CTBN particles were used. As the CSR particles are small, bridging can be ignored. Bridging will only occur if the particle diameter is larger than the crack opening displacement, which is not the case in the present work [31].

### 8.3.6 Plastic zone size consideration

Plastic deformation is often the main energy dissipation mechanism in brittle materials. With the use of the linear elastic fracture mechanics (LEFM) method, the radius of the plane-strain plastic deformation zone can be found from the equations below [5]:

For the unmodified epoxy:

$$r_{pzu} = \frac{1}{6}\left(\frac{K_c}{\sigma_{yt}}\right)^2 = \frac{1}{6}\left(\frac{E_u G_u}{(1-v^2)\sigma_{yt}^2}\right) \tag{8.13}$$

where $K_c$ = fracture toughness of unmodified epoxy, $\sigma_{yt}$ = tensile yield stress of unmodified epoxy, $E_u$ = modulus of unmodified epoxy, $G_u$ = fracture energy of unmodified epoxy and $v$ = Poisson's ratio.

For the unmodified epoxy polymer a value of $r_{pzu} = 5.2$ $\mu$m is calculated using $E_u = 3.14$ GPa, $G_u = 68$ $J/m^2$ and $\sigma_{yt} = 88$ MPa, see Table 8.4.

For the nanoparticle-modified epoxy:

$$r_y = K_{sp}^2\left(1 + \frac{\mu_m}{3^{1/2}}\right)^2 r_{pzu} \tag{8.14}$$

where $r_{pzu}$= radius of plastic deformation zone of unmodified epoxy, $\mu_m$ = coefficient of increase of shear yield stress with hydrostatic pressure, for epoxy this is between 0.175 to 0.225 [5]. $K_{sp}$ depends on the volume fraction of particles ($v_f$), and can be expressed as [29]:

$$K_{sp} = 0.59v_f + 1.65 \tag{8.15}$$

The parameters used in the equations are listed in Table 8.4 below.

Table 8.4: Values of parameters used for toughening predictions, from present study and from Hsieh et al. [2]

| Name | Symbol | Units | Value | Source |
|---|---|---|---|---|
| Fracture energy of unmodified epoxy | $G_U$ | $J/m^2$ | 68 | Present study |
| Plane-stain compressive yield stress of unmodified epoxy | $\sigma_{ycu}$ | MPa | 123 | Hsieh et al. |
| Young's modulus of unmodified epoxy | $E_u$ | GPa | 3.14 | Present study |
| Plane strain compressive failure strain of unmodified epoxy | $\gamma_{fu}$ | / | 0.62 | Hsieh et al. |
| Maximum stress concentration around a particle | $K_{sp}$ | / | 1.65-1.709 | Present study |
| Maximum stress concentration around a void | $K_v$ | / | 2.12 | Present study |
| Volume fraction of particles | $v_f$ | / | 0-0.22 | Present study |
| Poisson's ratio of unmodified epoxy | $v$ | / | 0.35 | Hsieh et al. |
| Coefficient for pressure dependence of yield stress | $\mu_m$ | / | 0.2 | Hsieh et al. |

### 8.3.7 Fracture energy predictions from Huang & Kinloch model

The predictions using the Huang and Kinloch model were compared to the fracture energy values measured in experiments, using the compression strain to failure to calculate the void size rather than using the measured void diameter in the predictions. The fracture energies predicted for all three cases (100% void growth, 14.3% void growth and shear only) were used. The fracture energy predictions for the silica-modified epoxy are shown in Table 8.6 and Figure 8.4. In addition the fracture energies predicted from the combination of shear and 14.3% of void growth were calculated and are shown in Table 8.6 and Figure 8.4, as $G_u + 0.143dG_v + dG_s$. The results obtained from experiments for the silica-modified epoxy were found to be very similar to the results found from Hsieh et al. [2], see Table 8.6, except for one of the percentages (15 wt% of silica) although the variation is within experimental error as the standard deviations overlap.

In silica modified epoxy results, shear with 14.3% of void growth had similar fracture energy values when compared to the experimental findings. The effect of toughening is significant when a high wt% of silica is used, it then stays on a plateau when the wt% of silica used was highest. This shows the presence of shear where it cannot be viewed in SEM images. Three of the predictions (shear, 14.3% void growth and 14.3% void growth with shear) were within a similar range when compared to the experimental values (except for 100% void growth). When standard deviations are taken into account, the prediction of 14.3% of void growth with shear results agreed well with the experimental findings. The use of fracture energy analytical model prediction provides more reliable results in silica specimens when compared to the use of the FE model.

Table 8.5: Table showing fracture energy predictions of silica-modified epoxy from Hsieh et al. [3]

| wt% in Hsieh et al. study | Hsieh et al. predicted $G_c$ ($J/m^2$) |
|---|---|
| 0 | 77 |
| 4 | 122 |
| 7.8 | 149 |
| 11 | 169 |
| 15 | 190 |
| 20 | 220 |

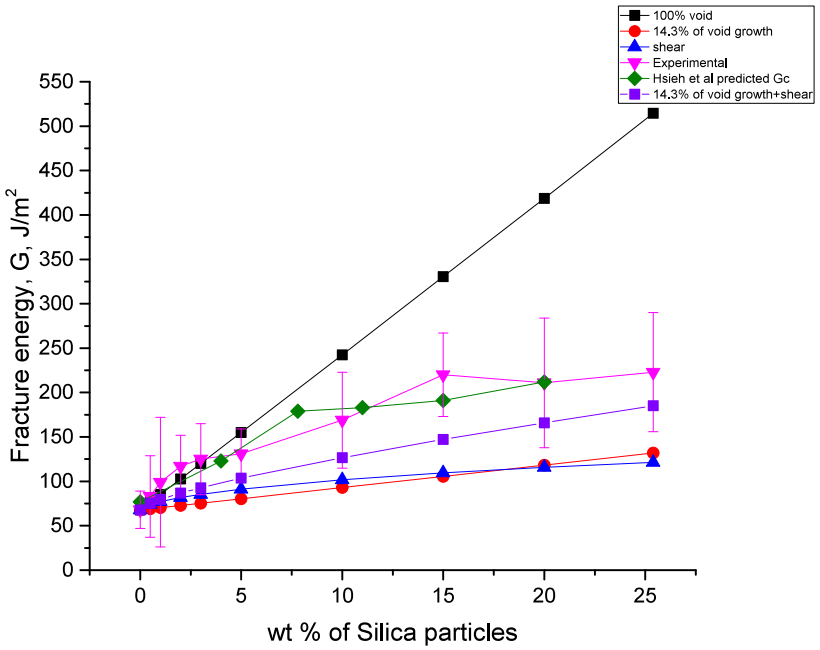


Figure 8.4: Fracture energy prediction of silica-modified epoxy

Table 8.6: Table showing fracture energy predictions of silica-modified epoxy

| Wt% of Silica particles | $dG_v$ ($J/m^2$) | 0.143 $dG_v$ ($J/m^2$) | $dG_s$ ($J/m^2$) | $dG_s$+0.143$dG_v$ ($J/m^2$) | Exp values ($J/m^2$) | SD |
|---|---|---|---|---|---|---|
| 0 | 68 | 68 | 68 | 68 | 68 | 21 |
| 0.5 | 77 | 69 | 74 | 75 | 83 | 46 |
| 1 | 85 | 70 | 77 | 80 | 99 | 73 |
| 2 | 103 | 73 | 82 | 87 | 117 | 35 |
| 3 | 120 | 75 | 85 | 93 | 125 | 40 |
| 5 | 155 | 80 | 91 | 104 | 131 | 28 |
| 10 | 243 | 93 | 102 | 127 | 169 | 54 |
| 15 | 330 | 106 | 110 | 147 | 220 | 47 |
| 20 | 419 | 118 | 116 | 166 | 211 | 73 |
| 25.4 | 514 | 132 | 121 | 185 | 223 | 67 |

The fracture energy values predicted for the CSR-modified epoxy are shown in Table 8.7 and Figure 8.5. The experimental results of the CSR-modified epoxy agreed with shear only and 14.3% void growth predictions (when standard deviations were taken into account), there were debonding found in CSR SEM images, but due to the CSR particles were make up of small CSR particles, this might explain why both shear only and 14.3% void growth predictions fit with experimental results. As the particles were assumed to be of the same size in predictions, an average of the size range was used in the calculations, but it may not represent the average size of all the particles there. There was a large range of particle sizes, hence the average value of the size range provided the best possible estimation to cover most sizes. The prediction model worked successfully in CSR-modified epoxy specimens.

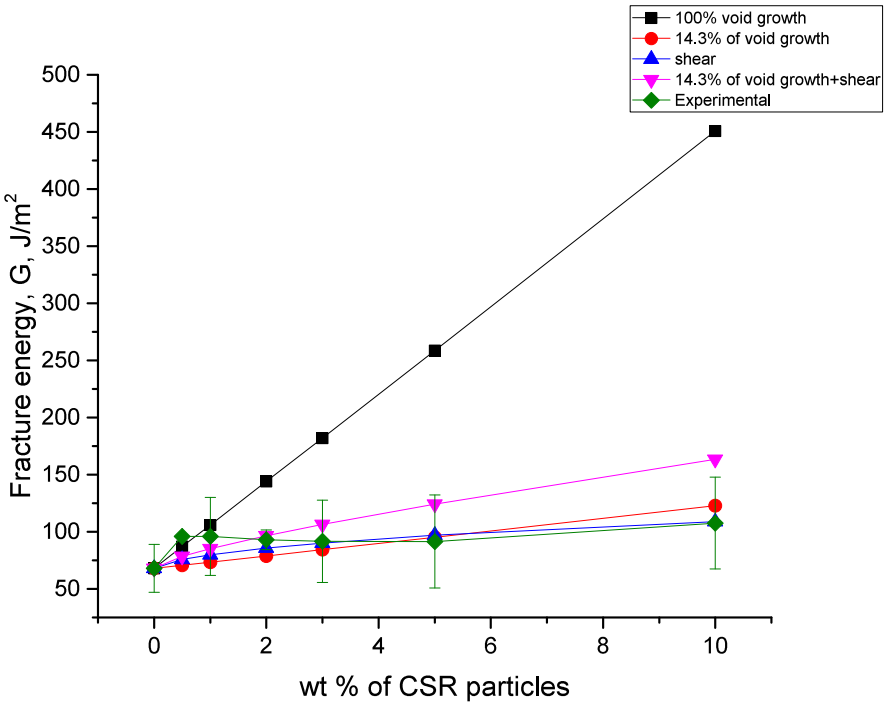


Figure 8.5: Fracture energy prediction of CSR-modified epoxy

Table 8.7: Table showing fracture energy predictions of CSR-modified epoxy

| Wt% of CSR particles | $dG_v$ ($J/m^2$) | 0.143 $dG_v$ ($J/m^2$) | $dG_s$ ($J/m^2$) | $dG_s$+0.143$dG_v$ ($J/m^2$) | Exp values ($J/m^2$) | SD |
|---|---|---|---|---|---|---|
| 0 | 68 | 68 | 68 | 68 | 68 | 21 |
| 0.5 | 87 | 71 | 76 | 79 | 96 | 1 |
| 1 | 106 | 73 | 80 | 85 | 96 | 34 |
| 2 | 144 | 79 | 86 | 97 | 93 | 9 |
| 3 | 182 | 84 | 90 | 106 | 92 | 36 |
| 5 | 259 | 95 | 97 | 124 | 91 | 41 |
| 10 | 451 | 123 | 109 | 164 | 108 | 40 |

The fracture energy values for the hybrids of silica and CSR specimens were calculated using the sum of the increases of the results of the two particles used, as there were equal wt% of each particle in the unmodified epoxy. The fracture energy predictions of the silica / CSR hybrid-modified epoxy are shown in Table 8.8 and Figure 8.6. The 14.3% void growth predictions agreed well with the experimental values, except for the 10 wt% where the standard deviation is much higher than the other experimental results. The prediction with shear only case had very similar results when compared to the assumption of 14.3% of void growth too, these values were also very similar to the experimental results but with slightly higher values at high wt% when compared to the 14.3% predictions. The use of hybrid particles did not show a clear synergy effect in experimental results, this explained the predictions that fitted with shear only predictions.

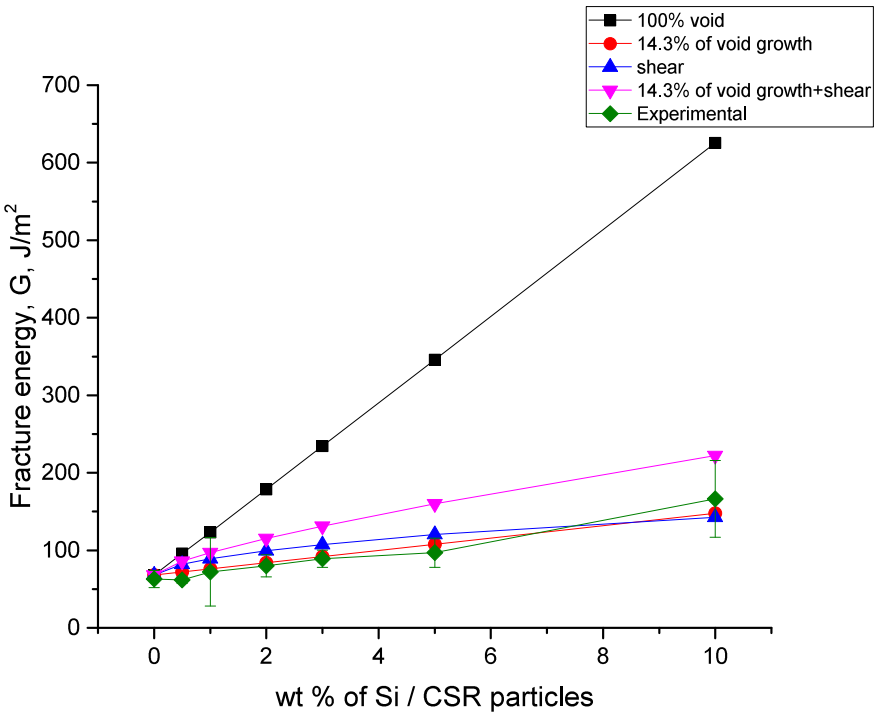


Figure 8.6: Fracture energy prediction of silica / CSR hybrid-modified epoxy

Table 8.8: Fracture energy predictions of hybrid-modified epoxy

| Wt% of silica / CSR particles | $dG_v$ ($J/m^2$) | 0.143 $dG_v$ ($J/m^2$) | $dG_s$ ($J/m^2$) | $dG_s$+0.143$dG_v$ ($J/m^2$) | Exp values ($J/m^2$) | SD |
|---|---|---|---|---|---|---|
| 0 | 68 | 68 | 68 | 68 | 63 | 11 |
| 0.5 | 96 | 72 | 82 | 86 | 62 | 4 |
| 1 | 123 | 76 | 89 | 97 | 72 | 44 |
| 2 | 179 | 84 | 99 | 115 | 80 | 14 |
| 3 | 234 | 92 | 108 | 131 | 89 | 11 |
| 5 | 346 | 108 | 120 | 160 | 97 | 19 |
| 10 | 625 | 148 | 143 | 222 | 166 | 49 |

### 8.3.8 Summary

The fracture energy predictions from the Huang and Kinloch model agree well with the experimental findings. Overall, 100% of void growth would always provide the highest fracture energy, and with shear only, a relatively lower fracture energy would be expected according to predictions. The assumption of 14.3% of void growth agreed with most of the experimental results as well as 14.3% of void growth with shear, the cause of disagreement in some specimens with higher % of particles were justified by their fracture surfaces. Hence, it can be concluded that experimental findings were according to the 14.3% void growth predictions, as some debonding was found on the fracture surfaces. As the model is fully predictive, in future work the fracture energy values can be compared with values found under different test conditions (low temperature, high rate), this would give an estimation in the amount of different failure mechanisms under brittle failure.

## 8.4 Conclusions

The analytical models used (Halpin-Tsai model and Huang and Kinloch model) were found to be useful in predicting the modulus and fracture energy of the modified epoxies. The predicted modulus values agreed extremely well with the experimental findings. Silica increases the modulus of the epoxy. Although CSR would be expected to reduce the modulus, the PMMA shell on the CSR particles increases its modulus, hence, higher modulus values were found in the CSR modified epoxy. Clustering of particles was

found to reduce the experimental modulus compared to the predictions. The fracture energy predictions agree well with the experimental findings. It is estimated that in the silica modified epoxy, 14.3% debonding occurred. The values were not so distinct in the CSR modified epoxy, and the deviation will be considered with SEM of the fracture surfaces. The experimental values lie closest to shear only predictions, but some debonding was found on the fracture surfaces. There were no synergy effect found in the silica / CSR hybrid specimens. The predicted values were found to be more reliable than those from the FE model, as the values were reasonable along all wt% and without the variations from experiments. The predictions also give information of which of the possible toughening mechanisms is occurring in the material. More fracture energy predictions are performed using FE model in Chapter 10.

# Chapter 9

# Scanning electron microscopy

## 9.1 Introduction

Scanning electron microscopy (SEM) was used to investigate the fracture surfaces of the modified epoxy. By viewing the fracture surface under SEM, the microstructure and toughening mechanisms can be identified, as well as the dispersion of particles.

SEM imaging was performed using a Hitachi S-3400N SEM, with an accelerating voltage of 15 kV or 10 kV for low magnification imaging. For small particles, e.g. silica, field emission gun scanning electron microscopy (FEG-SEM) was used. SEM provides a higher resolution of images than optical microscopy, which reveals more information from the fracture surface. Evidence of failure mechanisms such as river lines or particle debonding would provide supporting evidence to explain the experimental results.

The specimens were sputter coated with gold to give electrical conductivity and reducing charging. The amount of coating applied on the specimen needed to be optimum, because a thin coating can allow the specimen to charge up, resulting in difficulties with beam focusing and aperture or stigmation correction. When the coating is too thick, fine details could be masked.

## 9.2 SEM procedure

The fracture surface specimens were cut as thin as possible, the specimens were about 2 mm thick to reduce charging, and the surface of specimen was protected when it was being cut. Computer numerical control (CNC) method was used in cutting the TDCB specimens and an Accutom precision cutter was used in cutting the SENB specimens.

For field emission gun scanning electron microscopy (FEG-SEM):
SEM imaging was performed using a LEO Gemini 1525 field emission gun scanning electron microscope (FEG-SEM), Carl Zeiss, Germany, with an accelerating voltage of

5 kV. Gold coating was applied to increase the conductivity of the specimens and to prevent charging. It was performed using an EMI TECH K575X coater at 120 mA for 1 min. The samples were then attached to a sample holder using conductive tape. Electrical conductivity of the specimens was made certain by applying some silver paint at the side of the specimens, to provide electrical conductivity between the fracture surface and the sample holder.

For scanning electron microscopy (SEM):
An Agar automatic sputter coater was used for gold coating the specimens. Silver paint was also used to ensure conductivity of specimens. The standard sputtering time was 20 seconds, but some of the specimens were coated for slightly longer (30 seconds), to reduce charging problems.

Only a selection of images that are representative of the results have been selected and are shown in the sections below.

## 9.3 Unmodified epoxy

### 9.3.1 Fracture mechanisms

Figures 9.1, 9.2 and 9.3 show SEM images of the fracture surfaces of the unmodified epoxy. The surfaces were smooth and flat with river lines which indicated brittle failure with little energy being absorbed during the fracture process. This agrees with the low fracture energy values ($G_c = 68\ J/m^2$) measured experimentally. The fracture surfaces of unmodified TDCB and SENB specimens were very similar as expected because the fracture energies measured from these tests were very similar. There were more river lines that cover a larger area in TDCB specimens, which indicate the presence of unstable crack growth in some regions of the TDCB specimens.

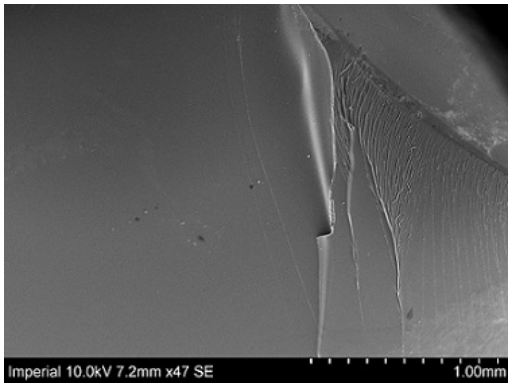


Figure 9.1: SEM image of unmodified epoxy (SENB)

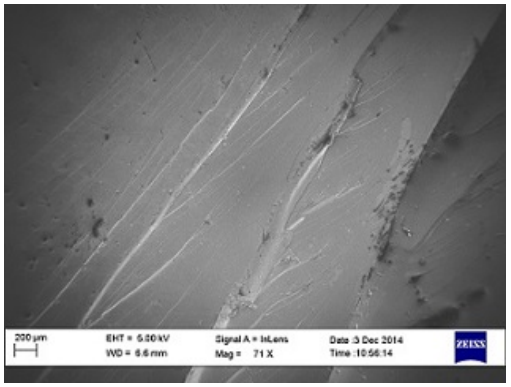

Figure 9.2: SEM image of unmodified epoxy (TDCB)

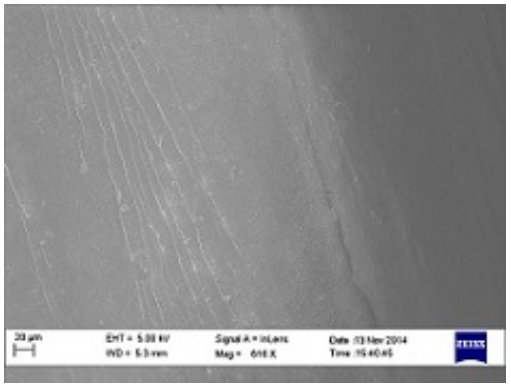

Figure 9.3: SEM image of unmodified epoxy (TDCB)

### 9.3.2 Voids in TDCB and SENB specimens

There were some voids from air bubbles found in both the TDCB and SENB specimens. The voids could be different in size and shape for the different types of particles added in. Figures 9.4 and 9.5 were the only voids found from SEM imaging. There were very few voids present in all specimens and hence they should not affect the fracture properties of the material.

Figure 9.4 shows voids from a CSR-modified epoxy TDCB specimen. As CSR particles were larger, there were bigger voids found, as the air bubbles produced by movement of particles are bigger. Voids were produced during mixing of particles, most of them were removed during the degassing process, but a small amount of air bubbles remain in the mixture. There were also more voids seen for formulations which have a higher viscosity, due to the higher wt% of particles, and hence the greater difficulty of removing all of the air.

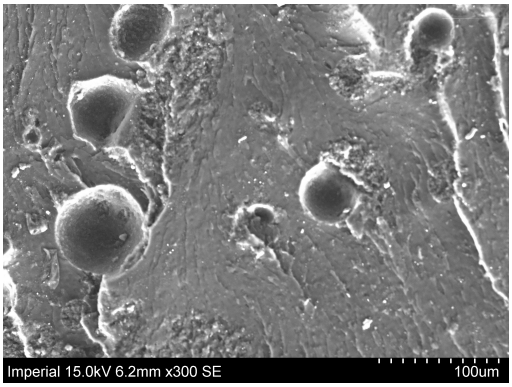


Figure 9.4: SEM image of TDCB voids from CSR modified specimens

The voids found in PES specimens were very small, as the PES particles were dissolved before mixing with epoxy. These voids were only found under high magnifications (50-80k). They were smaller than the PES particles and were found in the epoxy matrix. Therefore, these voids were produced due to air entrapment because of the very high viscosity, and have no significant effect on the measured fracture energy.

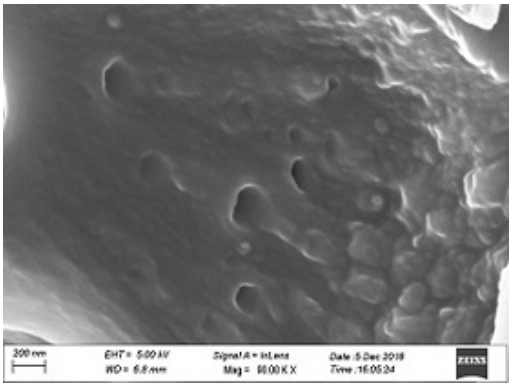

Figure 9.5: SENB voids from PES modified specimens

## 9.4 Silica modified epoxy

### 9.4.1 Fracture and toughening mechanisms

Due to the small particle size (20 nm) of the silica particles according to previous studies, it is very hard to see individual silica particles, which could also be due to the coating used, that covered the details of the particles and voids present. However the pattern found suggested the presence of silica particles, as a similar pattern was found in previous studies [2]. The different conditions (low temperature and high rate) do not show differences in the images. Silica particles cannot be seen easily at low concentrations. It is very hard to find individual silica particles as the particles are very small, but the similarity of the fracture surfaces to those seen in previous studies indicates that similar toughening mechanisms must be present.

### 9.4.2 Effect of concentration of silica particles

Figures 9.6 to 9.10 show SEM images of fracture surfaces for different concentrations of silica particles added into epoxy.

Figure 9.6 below shows a silica 5 wt% SENB specimen tested at quasi-static rate.

Previous authors have seen 10 to 15% of silica particles debonding with voids, others have seen no voids around the silica particles indicating no debonding. This is due to the different formulations used in previous studies, which result in different toughening mechanisms. The void diameter from literature is about 30 nm [4]. Some voids can be seen, the size and the amount of voids are estimated in Figure 9.7.

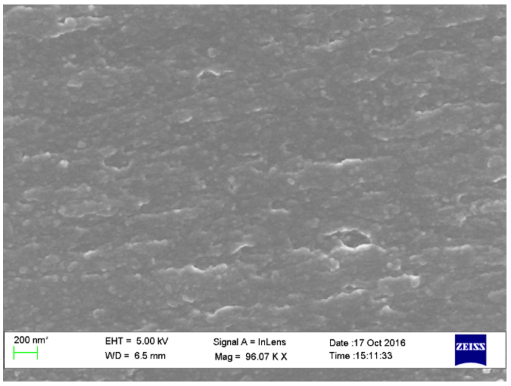


Figure 9.6: SEM image of 5 wt% silica tested under quasi-static rate

With silica particles of 20 nm in diameter, voids were expected to be about 35 nm in diameter. This is because void diameter = particles diameter $x$ (1+ strain to failure). The maximum void growth will be equal to the strain to failure measured from plane strain compression tests, $\gamma_{fu}$. For the unmodified epoxy, $\gamma_{fu} = 0.62$, see Table 8.4. Therefore, when the diameter of the voids were larger than 35 nm, they cannot be from debonding and void growth. In Figure 9.7, the voids were about 100 to 200 nm in diameter. The largest voids in the image were too large to be created by debonding and void growth. No voids of the expected size could be seen, which is due to the voids being hidden by the coating. Debonding and void growth are expected from the measured toughness and analytical modelling of the toughness, hence it was confirmed that debonding and void growth would be present but are obscured by the coating.

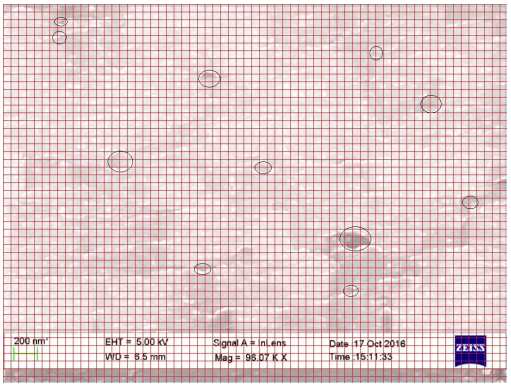


Figure 9.7: Voids in silica modified epoxy

Similar results were found for the samples with 10, 15 and 25.4 wt% of silica. Some particles can be seen, but were not clear. There was a closer arrangement of particles

when wt% used is high. There is a slightly more brittle fracture surface found for the high wt% samples, but not significantly different from other specimens.

The silica 10 wt% image shown in Figure 9.8 had a thicker coating when compared to other images, as the background epoxy cannot be seen easily. Figures 9.8 and 9.9 show silica modified epoxy of 10 wt% and 15 wt%. Both images show a thick coating on the particles.

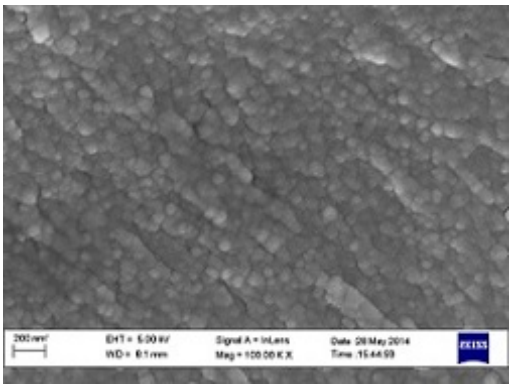

Figure 9.8: SEM image of silica modified epoxy 10 wt%

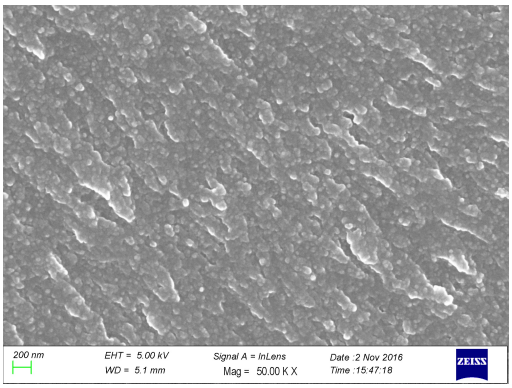


Figure 9.9: SEM image of silica modified epoxy 15 wt%

The higher wt% samples produced the same pattern on the fracture surfaces compared to the fracture surfaces from low wt% silica specimens, indicating that the same mechanisms occur. The proportion of void growth in silica modified epoxy is about 15 wt% according to theory. However, it is impossible to calculate the amount of void growth as the particles are too similar when compared to the background, it is not possible to separate them in the particles count procedure.

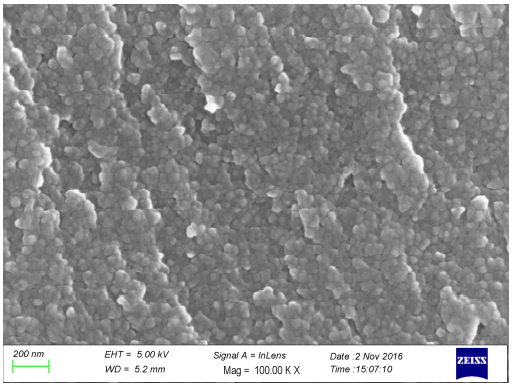


Figure 9.10: SEM image of max wt% (25.4 wt%) silica modified epoxy

### 9.4.3 Effect of high rate

Figures 9.11 to 9.13 below show fracture surfaces of different wt% of silica modified epoxy tested at high rate (0.1 m/s and 1 m/s). The high rate tests produced more brittle failure, this can be found from the SEM images. Imaging was not always possible due to the quality of fracture surfaces. Specimens often fly off from the cutting machine, and it is very hard to protect the fracture surface as they can land anywhere which contaminates the surface.

The fracture surface of silica 15 wt% did not show any differences when compared to the quasi-static specimens.

The particles can be seem more clearly in some of the images, however, it is covered with a layer of coating, hence the particles appear larger than how they should be. Coating use is not easy for silica specimens, as it is not conductive, thinnest layer (5 $\mu m$) would give charging of particles, a thicker layer would cover the small details of the nano-size silica particles. A thickness of 15 $\mu m$ coating was used as it was found as the thinnest coating possible to view the specimens.

Most of the TDCB specimens could not be used for electron microscopy, as they are covered with dust of the material even though the surface was covered with paper for CNC. It is because the surface has to be exposed when the cut is made. Thus it was impossible to use these specimens as particles cannot be identified.

The same coating problem was found in high wt% of silica, but blocks of particles can be found as shown in Figure 9.11. The specimens tested at a rate of 0.1 m/s did not show any difference in the fracture surface compared to the quasi-static specimens.

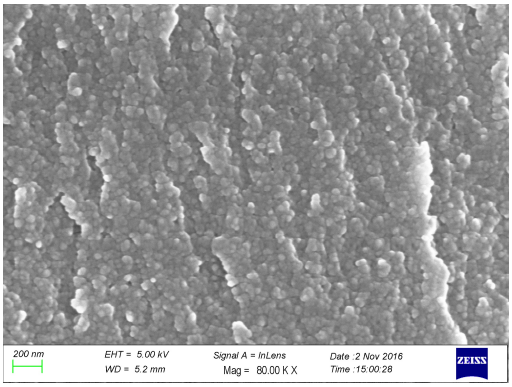


Figure 9.11: SEM image of max wt% (25.4 wt%) silica modified epoxy tested at 0.1 m/s

Similar results were found at a rate of 1 m/s for all wt%, high rate did not produce a significant effect on the fracture surfaces of silica-modified epoxy, see Figures 9.12 and 9.13.

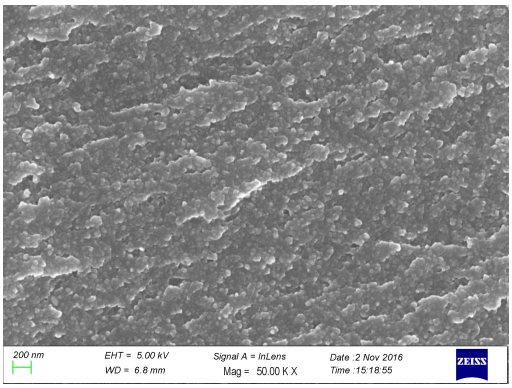


Figure 9.12: SEM image of max wt% (25.4 wt%) silica modified epoxy tested at 1 m/s

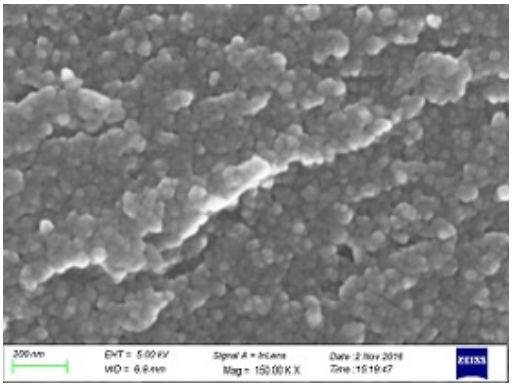

Figure 9.13: SEM image of max wt% (25.4 wt%) silica modified epoxy tested at 1 m/s

### 9.4.4 Effect of low temperature

Figures 9.14 to 9.18 below show SEM images of the fracture surfaces of different wt% of silica modified epoxy tested at low temperature.

There were two temperatures used in low temperature SENB, -40 and -80$^oC$. Images of silica modified epoxy with 5, 15 and 25.4 wt% are shown below. River lines were found but particles could not be found at low wt% of silica specimens. There were similar fracture surfaces found in specimens that were tested at -40$^oC$ and -80$^oC$. There were no particles found in 5 wt% silica specimens tested at -40$^oC$, see Figure 9.14.

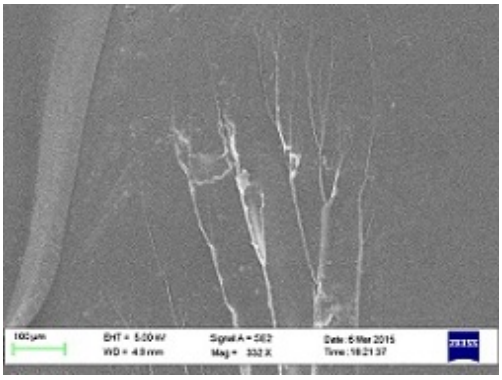

Figure 9.14: SEM image of 5 wt% silica modified epoxy tested at -40$^oC$

Similar results were found for different conditions of 15 wt% silica specimens. There was no significant differences found on the fracture surfaces of low temperature specimens compared to room temperature specimens. The coating was less thick in the silica 15 wt% at -40$^oC$ image, see Figure 9.15, as the features and the epoxy background can be found easier, the image was reliable.

Individual particles can be seen in this image but it is difficult to identify all of the particles due to the coating.

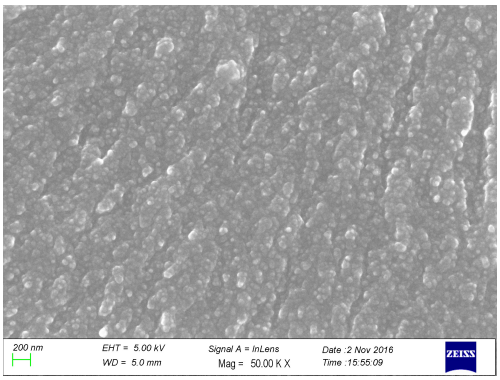


Figure 9.15: SEM image of 15 wt% silica modified epoxy tested at -40$^oC$

Figures 9.16, 9.17 and 9.18 show silica-modified epoxy tested at -80$^oC$. Similar images were found at -80$^oC$ when compared to -40$^oC$ and quasi-static tests, the lower temperature did not show differences in the fracture surfaces.

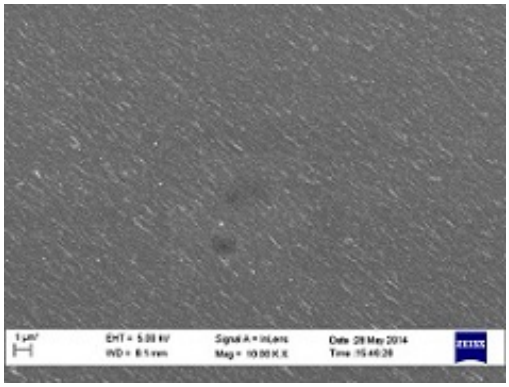

Figure 9.16: SEM image of 5 wt% silica modified epoxy tested at -80$^oC$

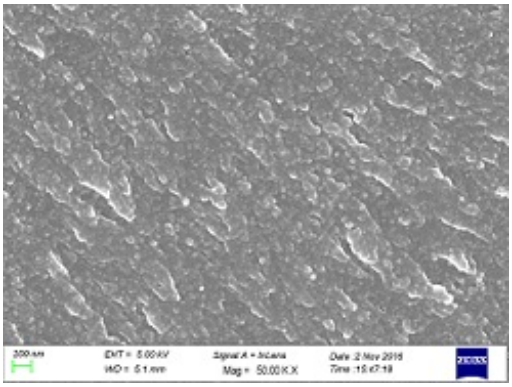

Figure 9.17: SEM image of 15 wt% silica modified epoxy tested at -80$^oC$

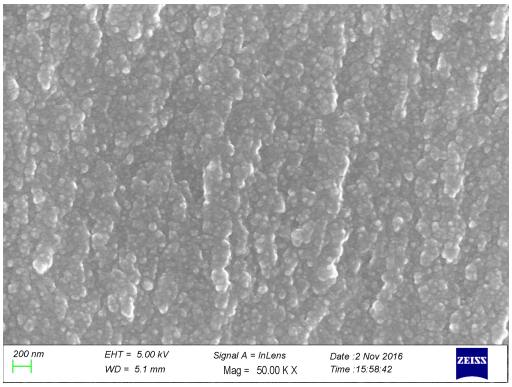


Figure 9.18: SEM image of max% (25.4%) silica modified epoxy tested at -80$^oC$

## 9.5 Core-shell rubber modified epoxy

### 9.5.1 Fracture and toughening mechanisms

### 9.5.2 Deformation of particles

The shape and appearance of the as received CSR particles are shown in Figure 9.19. The sizes of the particles were more varied than the expected range of 38 to 500 $\mu$m in diameter. From the SEM image in Figure 9.19, it is estimated that the CSR particles were about 5 to 20 $\mu$m in diameter. Hence, the Paraloid EXL-2300G contains some small particles. For the experiment, the CSR particles were sieved. The size range is known from sieving and the size of 38 to 106 $\mu$m was used.

The fracture surfaces of the CSR-modified epoxy showed some fractured CSR particles, see Figure 9.21. Figures 9.20 and 9.21 show examples of CSR particles under

a sharp cut and damaged after testing. In order to investigate if the damage in the particles was there before testing or not, particles were viewed under the SEM before and after cutting them with a razor blade. By comparing the shape and structure of the sharply cut particles to the as received particles and the broken particles seen on the fracture surfaces, it is clear that the particles were not damaged before they were mixed with the epoxy resin. The shape of the broken particles also indicates that only some of the deformation occurred during fracture of the specimens. Thus it was concluded that the CSR particles were damaged during mixing of the CSR modified epoxy. There were a large amount of damaged particles found in the epoxy with a high wt% of particles, where the viscosity will be high, confirming the damage occurs during mixing.

It was initially believed that rubber bridging had occurred as no particle cavitation could be found after looking at the individual debonding of the particles under high magnifications. This is because the particles were sieved into a size range of 38 to 106 $\mu$m, the particle size was bigger than the crack opening displacement (see Equation 9.1), therefore, rubber bridging was expected.

The crack opening displacement, $\delta_t$, is given by

$$\delta_t = \frac{K_c^2}{E\sigma_{yt}}(1-\nu^2) \tag{9.1}$$

where $K_c$ = stress intensity factor at the onset of crack growth, $\sigma_{yt}$ = tensile yield stress, E = Young's modulus and $v$ = Poisson's ratio [32].

For example, for the 5 wt% CSR modified epoxy, $G_c = 91\ J/m^2$, so $\delta_t = 1.3\ \mu m$. This is smaller than the total particle size. However, it was found later that the big CSR particles were actually aggregates of small CSR particles, which means the particle size was smaller than crack opening displacement (see Equation 9.1), hence, bridging was not found. As the particles are agglomerates of much smaller particles, it is likely that the damage to the particles seen in Figure 9.21 occurred during manufacture of the CSR modified epoxy.

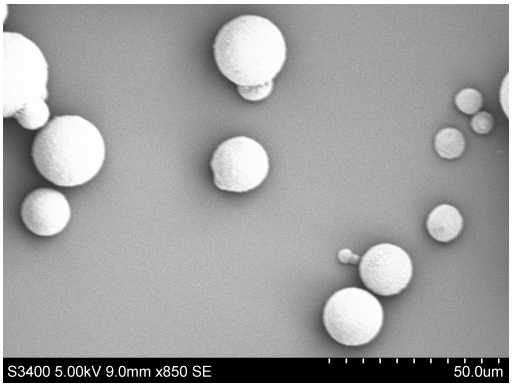


Figure 9.19: As received CSR particles

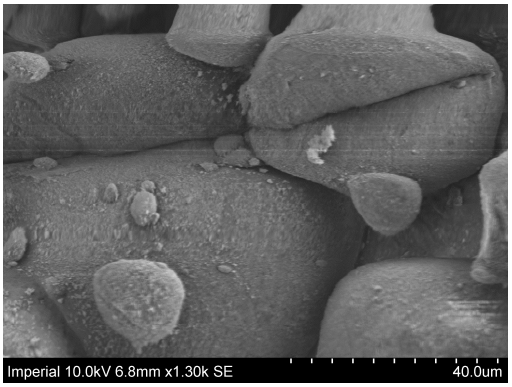


Figure 9.20: Cut CSR particles

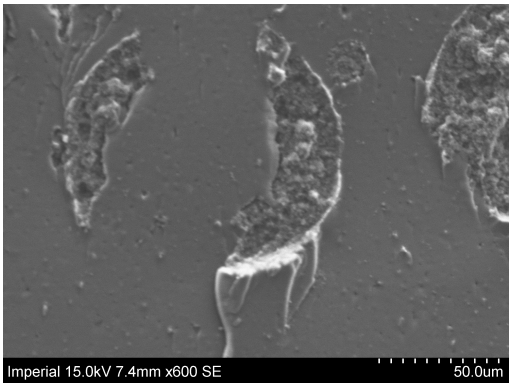


Figure 9.21: Example of damaged CSR particles on fracture surface

### 9.5.3 Effect of concentration of particles

Figures 9.22, 9.23, 9.24 and 9.25 show different wt% of CSR modified epoxy under SEM imaging. There were different fracture surfaces when the % of particles were different. When the % of particles was low, brittle surfaces were found, where particles were very distinct from the bulk epoxy. However, when the % of particles were high, rough surfaces were found, as the particles provided the roughness of the surface, the high amount of them increased the roughness. Due to the high roughness, the particles cannot be recognised as easily, but they are preformed and were not dissolved into the epoxy and therefore no phase inversion occurred. The high fracture energy values found at high wt% of CSR could be explained by their fracture surfaces, as localised deformations were found in more than 90% of the particles, the toughening effect was significant, particles were highly deformed from their original shape, but were not stretched. There were about a quarter of the particle cores completely removed from the particle, leaving an empty space inside (cavitation), see Figures 9.22 to 9.24. The SEM images showed that particles were mixed evenly but most of the particles did not have the same sizes. This is because the large CSR particles were found to be made up of small CSR particles, so tails did not represent crack pinning, more details are included in the particle counts Section 9.12. This could explain why some of the tests showed higher fracture energies than the others, hence the high standard deviations.

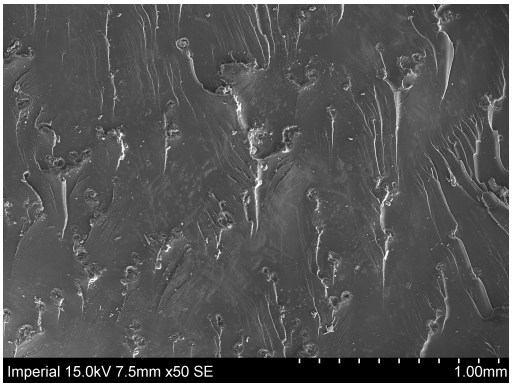


Figure 9.22: SEM image of CSR 0.5 wt% specimen

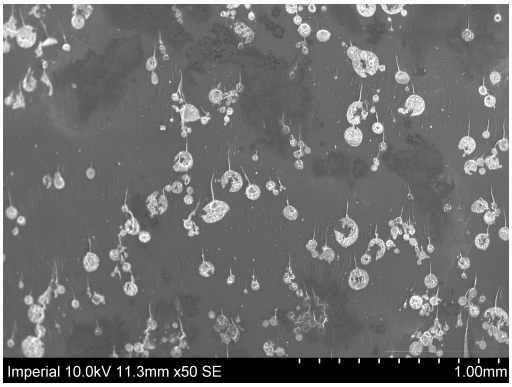


Figure 9.23: SEM image of CSR 3 wt% specimen

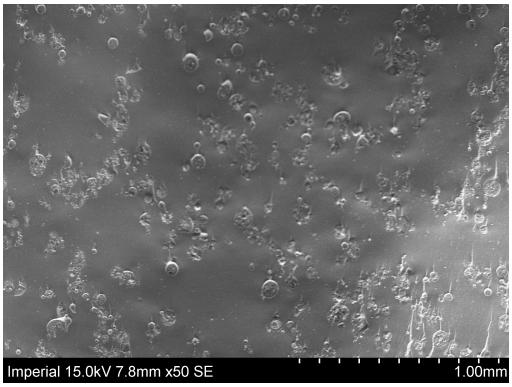


Figure 9.24: SEM image of CSR 5 wt% specimen

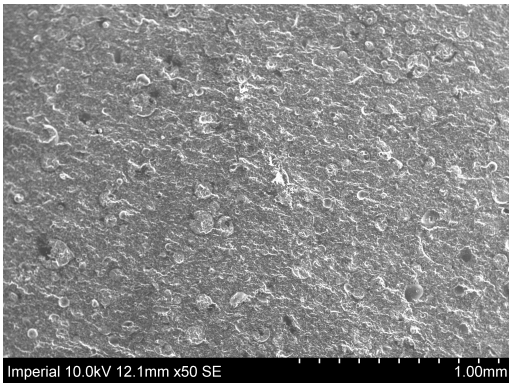


Figure 9.25: SEM image of CSR 10 wt% specimen

Examples of localised deformations in the particles are shown below in Figures 9.26, 9.27, 9.28 and 9.30. The particle size was smaller than the size of void, therefore

there was a large amount of deformation, which allowed the voids to grow. Most of the particles were highly damaged, either by the crack which propagated through the whole particle or by cavitation. All of the damaged particles were highly deformed from their original shape. There were many small voids inside the deformed area of a particle (Figure 9.28), which were formed by cavitation of the individual small rubber particles which are aggregated to make up the large Paraloid EXL-2300G particles. Rough surfaces were observed especially with high wt% of CSR particles (10 wt%), which were produced due to the presence of high amount of deformation when the toughness is high. Localised deformations were also observed when the particles were damaged during manufacturing, leading to epoxy being present inside the large broken CSR particles (Figure 9.29). Further investigations regarding their failure mechanism would be performed by DMA, which would provide more information about the failure properties of CSR modified specimens, more about DMA study is described in Section 11.5.

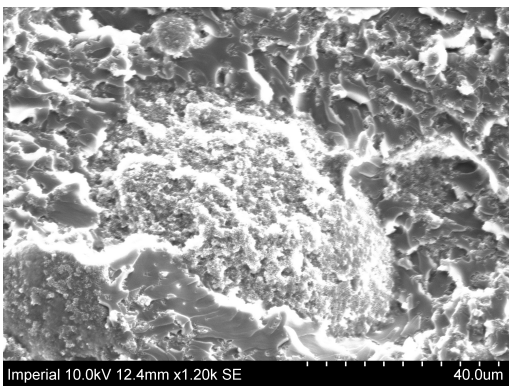


Figure 9.26: SEM image of deformed CSR particles for high wt% of CSR specimen

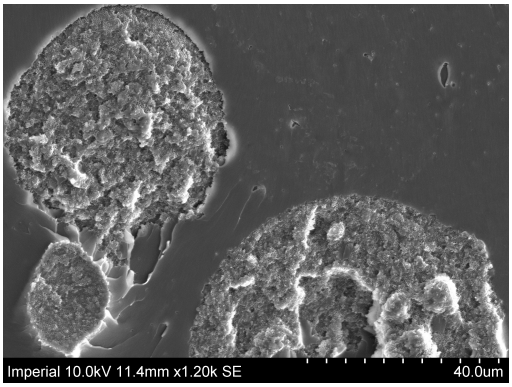


Figure 9.27: SEM image of deformed CSR particles for low wt% of CSR specimen

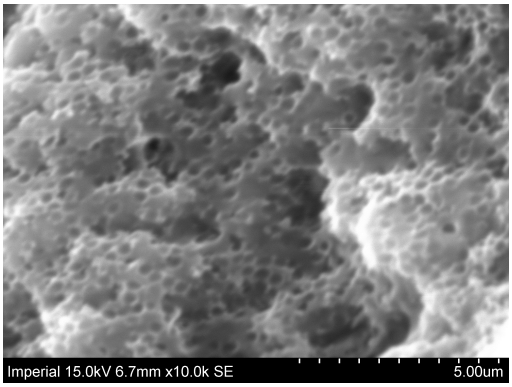


Figure 9.28: SEM image of small voids inside a CSR particle

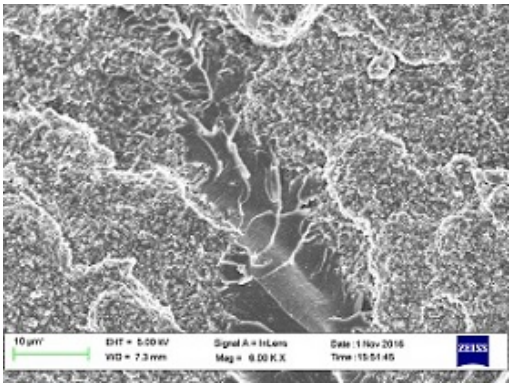

Figure 9.29: SEM image of epoxy inside a large CSR particle

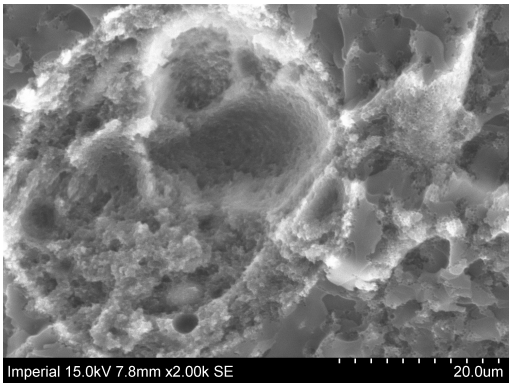


Figure 9.30: Example of CSR particle deformation at high magnification

### 9.5.4 Effect of high rate

Figures 9.31 to 9.33 show SEM images of CSR-modified epoxy at higher test rate. There were some particles fractured but the major toughening mechanism in CSR was local debonding, the river lines on the surface indicated that crack was travelling very quickly, and it then spilt into several paths. The effect of rate did not make any significant changes to the appearance of the fracture surfaces and the toughening effect (cavitation with void growth and possible shear), while there were higher fracture energy values measured. The same conclusion was found in both TDCB and SENB specimens, there were no notable differences between specimens tested at high and low rates.

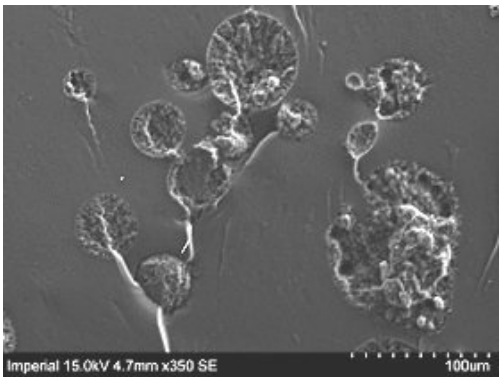


Figure 9.31: SEM image of 0.5 wt% CSR-modified epoxy SENB specimen tested at a rate of 0.1 m/s

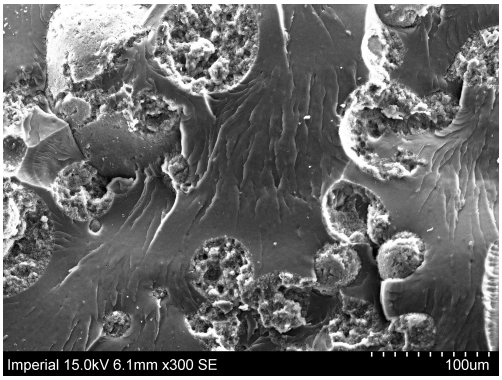


Figure 9.32: SEM image of 5 wt% CSR-modified epoxy specimen tested at a rate of 0.1 m/s

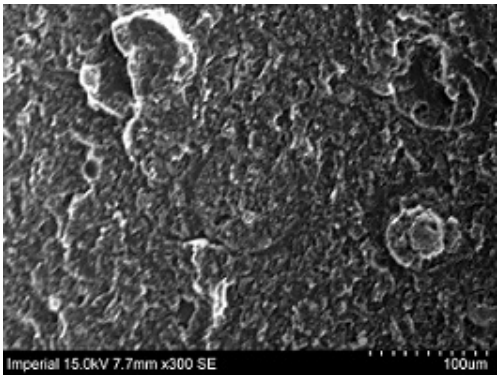


Figure 9.33: SEM image of 10 wt% CSR-modified epoxy specimen tested at a rate of 0.1 m/s

### 9.5.5 Effect of low temperature

Figures 9.34 to 9.39 show SEM images of CSR modified epoxy specimens tested at different temperatures. There were no significant differences between the fracture surfaces of the epoxy tested at low temperature and at room temperature. There were no significant differences between the -40$^oC$ and -80$^oC$ specimens, the lower temperature did not produce much differences in the results. There was a greater toughening effect when comparing the use of high wt% to low wt% of particles at both low temperatures for most of the specimens. There were more river lines in some specimens as the fracture was more brittle, and sharper edges can be observed. There were higher fracture energy values when specimens were tested under low temperature. The low temperature environment produced a more brittle failure, higher fracture toughness and fracture energy values were found.

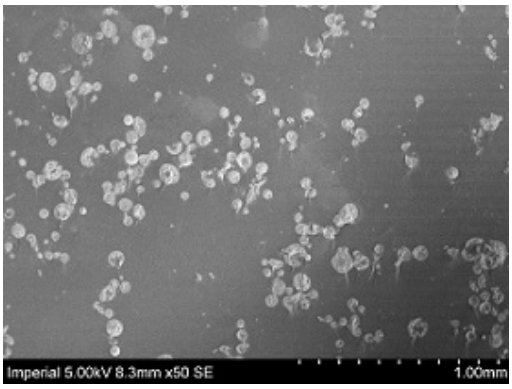


Figure 9.34: SEM image of 0.5 wt% CSR-modified epoxy specimen tested at -40$^oC$

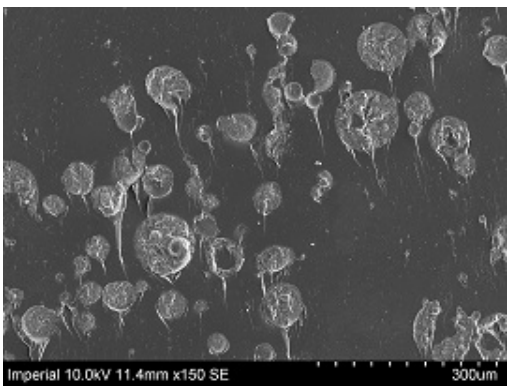


Figure 9.35: SEM image of 5 wt% CSR-modified epoxy specimen tested at -40$^oC$

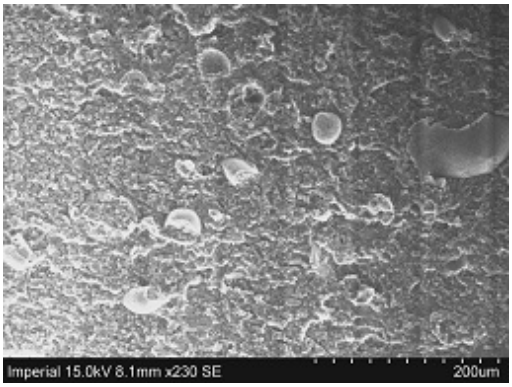


Figure 9.36: SEM image of 10 wt% CSR-modified epoxy specimen tested at -40$^oC$

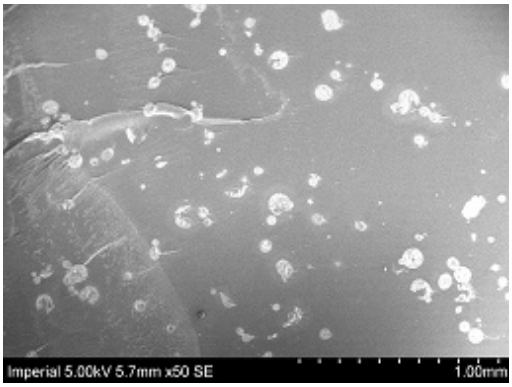


Figure 9.37: SEM image of 1 wt% CSR-modified epoxy specimen tested at -40$^oC$

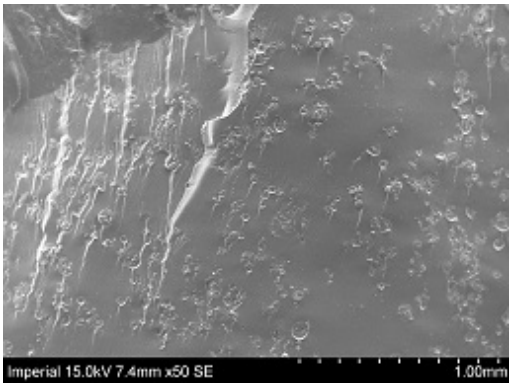


Figure 9.38: SEM image of 5 wt% CSR-modified epoxy specimen tested at -80$^oC$

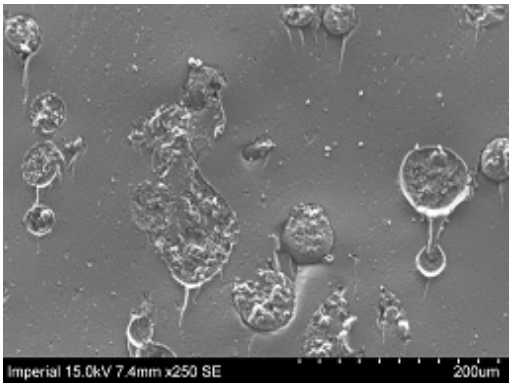


Figure 9.39: SEM image of 10 wt% CSR-modified epoxy specimen tested at -80$^oC$

As there was no bridging in the CSR particles, shear could be a possible toughening mechanism but it cannot be viewed under SEM. Cavitation can be found in some of the images, but the amount of void growth or presence of void growth cannot be confirmed. However, it is expected that void growth is relatively difficult, as the rubber cores of the particles were surrounded by the shell instead of the epoxy matrix, deformation of the shell is not as easy when compared to the epoxy. It is shown from the tensile results, the CSR specimens produced a higher tensile modulus when compared to the unmodified epoxy, this confirmed the presence of the shell and the properties of it.

## 9.6 Silica / CSR hybrid modified epoxy

### 9.6.1 Fracture and toughening mechanisms

The silica / CSR hybrid modified epoxy used the same wt% for silica and CSR particles. In most images, only CSR can be found, as only one pattern can be found in silica particles (not the particles themselves), the additional type of particles made it even harder to find the silica particles, as they increased the roughness of the surface.

### 9.6.2 Effect of concentration of particles

Figures 9.40, 9.41 and 9.42 show different concentrations of silica and CSR particles added into epoxy. An effect of wt% was found in the silica / CSR hybrid modified epoxy, where the fracture energy increased with the wt% of particles added. However, the fracture properties were more similar to the CSR specimens, synergy effect was not found. Big CSR particles were broken and deformed, and that resulted in a lot of river lines in the epoxy. The small CSR particles were then found to be cavitated.

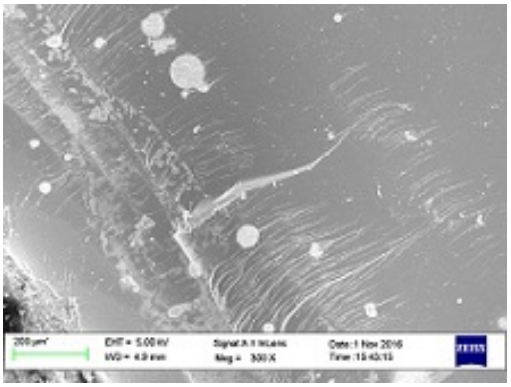

Figure 9.40: SEM image of silica / CSR hybrid-modified epoxy 1 wt% specimen tested at quasi-static rate

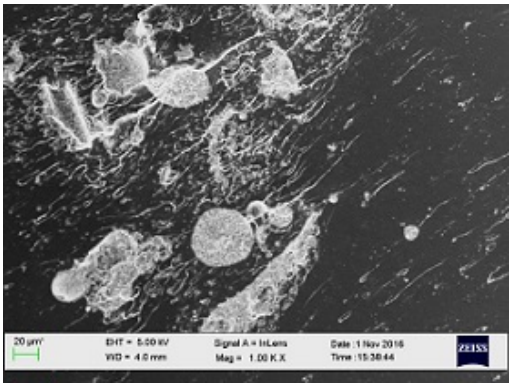

Figure 9.41: SEM image of silica / CSR hybrid-modified epoxy 5 wt% specimen tested at quasi-static rate

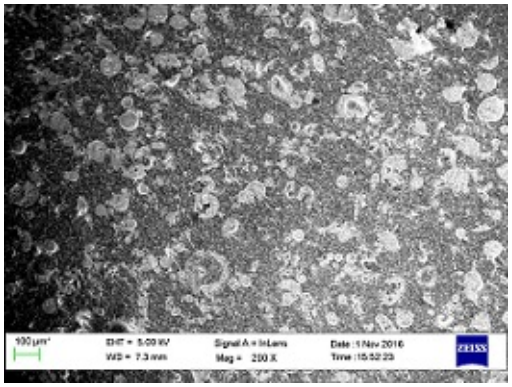

Figure 9.42: SEM image of silica / CSR hybrid-modified epoxy 10 wt% specimen tested at quasi-static rate

Figures 9.43 to 9.49 show silica / CSR hybrid specimens tested at low temperature, at -40$^oC$ and -80$^oC$. There are no significant differences in the SEM images of silica / CSR hybrid modified epoxy tested at low temperature when compared to room temperature. The CSR particles in silica / CSR hybrid modified epoxy had a similar appearance when compared to CSR modified epoxy, not all the particles undergo failure mechanisms and the main mechanism is individual deformations. As the CSR particles were made up from small CSR particles, failure mechanisms were not the same as expected.

Small CSR particles were found at low wt% of silica  CSR hybrid specimens, silica particles were not found. The same cavitation was found in the small CSR particles, large CSR particles were less visible, as the wt% of particles was low, the particles were well mixed, so most of the large CSR particles were broken into small CSR particles.

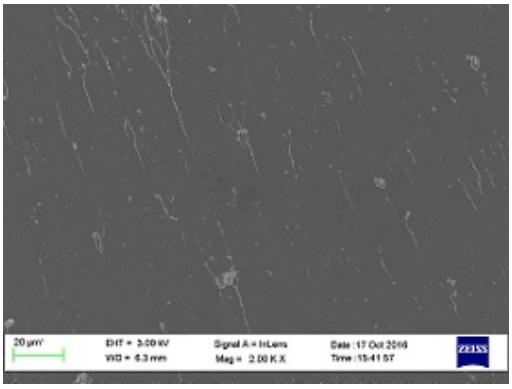

Figure 9.43: SEM image of silica / CSR hybrid-modified epoxy 1 wt% specimen tested at -40$^oC$

Silica / CSR hybrid 5 wt% -40$^oC$

Small regions of silica particles were found for the silica / CSR hybrid 5 wt% -40$^oC$ specimens, see Figure 9.44, but as the particles cannot be viewed clearly their distribution cannot be studied. They had similar level of darkness as the background, there were only some outlines can be found that indicate the presence of CSR particles.

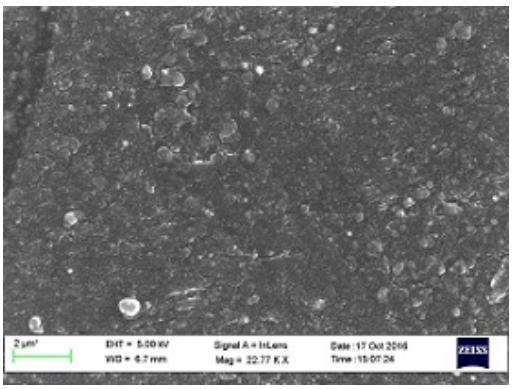

Figure 9.44: SEM image of silica / CSR hybrid-modified epoxy 5 wt% specimen tested at -40$^oC$

The fracture surfaces of the silica / CSR hybrid 10 wt% specimens were evenly covered with small crack propagation lines, see Figure 9.45, due to the higher amount of small CSR particles which de-attached and flowed from the large CSR aggregates in the epoxy when the CSR particles were added. These small river lines were only found in the 10 wt% of CSR SENB specimens due to the large amount of small CSR particles in the epoxy.

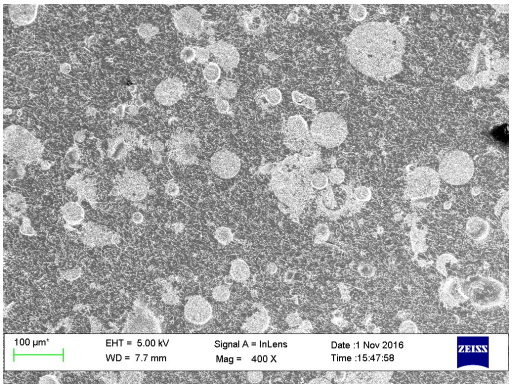


Figure 9.45: SEM image of silica / CSR hybrid-modified epoxy 10 wt% specimen tested at -40$^oC$

The fracture surfaces of the silica / CSR hybrid specimens tested at -80$^oC$ did not

show any significant differences when compared to the -80$^oC$ specimens, see Figures 9.46 to 9.49.

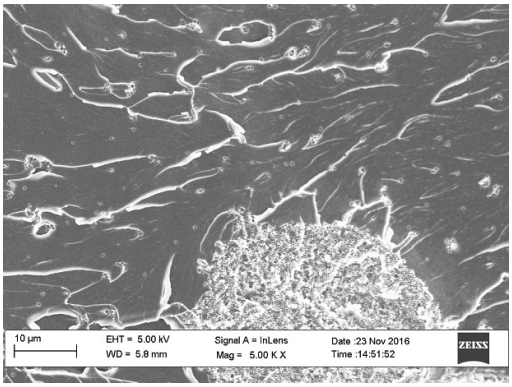


Figure 9.46: SEM zoom in image of silica / CSR hybrid-modified epoxy 1 wt% specimen tested at -80$^oC$

In the silica / CSR hybrid 1 wt% SEM images, large CSR particles can be found and the individual small CSR particles that spread around the epoxy. Silica particles were not found at low wt%, same as in the silica modified specimens. It was not easy to see the small particles especially when mixed with big particles. Failure mechanisms were unclear in this formulation, but are expected to be the same as for higher wt%.

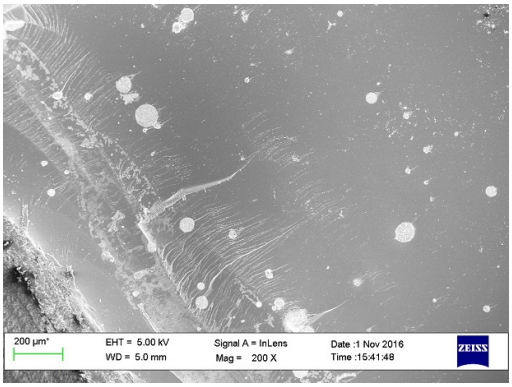


Figure 9.47: SEM image of silica / CSR hybrid-modified epoxy 1 wt% specimen tested at -80$^oC$

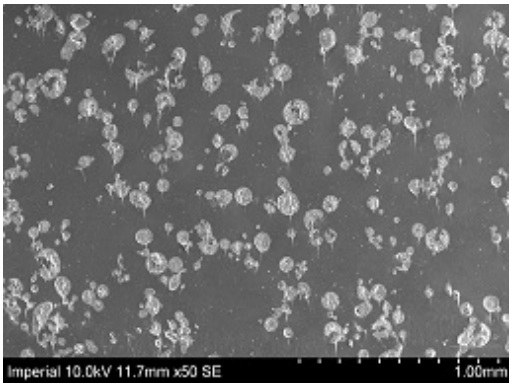


Figure 9.48: SEM image of silica / CSR hybrid-modified epoxy 5 wt% specimen tested at -80$^oC$

A rough surface was found in silica / CSR hybrid 10 wt% specimens tested at$-80^oC$, which was also found in the CSR 10 wt% specimens tested at the quasi-static rate at room temperature. It is due to the high wt% of CSR added which changed the brittleness of the mixture. Some cavitation of CSR particles was found on the fracture surfaces.

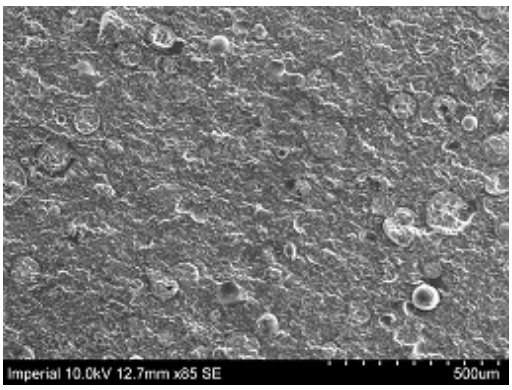


Figure 9.49: SEM image of silica / CSR hybrid-modified epoxy 10 wt% specimen tested at -80$^oC$

### 9.6.3 Effect of high rate

Figures 9.50 and 9.51 below show fracture surfaces for different wt% of silica / CSR hybrid modified epoxy tested at a high rate of 0.1 m/s.

There are no notable differences found for the specimens tested at high rate compared to those tested at quasi-static rate. Silica particles were not found in these hybrid

specimens, only CSR particles can be seen.

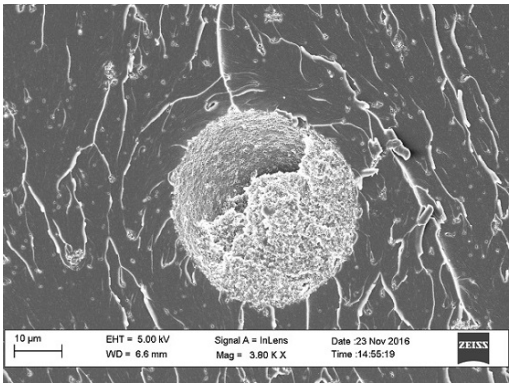


Figure 9.50: SEM image of silica / CSR hybrid-modified epoxy 2 wt% specimen tested at rate of 0.1 m/s

The small CSR particles were distributed in some of the area imaged for the silica / CSR hybrid 5 wt%, see Figure 9.51, and the river lines they produced were a bit different compared to those seen in CSR specimens (curved and overlapped). This could be due to the small size of them and the differences in the distances between particles. This pattern was not found in other CSR studies. Silica particles cannot be found in the images. Particle cavitation was the main failure mechanism for the small CSR particles, amount of void growth is small as the void sizes were small.

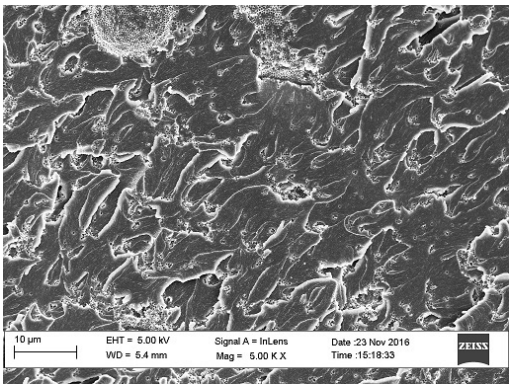


Figure 9.51: SEM image of silica / CSR hybrid-modified epoxy 5 wt% specimen tested at rate of 0.1 m/s

Images of the silica / CSR hybrid modified epoxies tested at 1 m/s are not available due to fracture surfaces having dropped on the floor, whilst being machined, so there was a significant amount of dust on the surfaces that made imaging of particles impossible.

## 9.7 Alumino silicate ceramic microsphere modified epoxy

### 9.7.1 Effect of concentration of particles

Figures 9.52, 9.53 and 9.54 show different concentrations of ceramic microsphere particles added into epoxy.

For the ceramic microsphere 2 wt% specimens, it was very hard to find particles, and the results were not presentable.

There was a relatively even distribution of the ceramic microsphere particles at 5 wt%, see Figure 9.53. The particles were very spherical and relatively small (12 $\mu m$), while crack opening displacement is 208 $\mu m$. The diameter is not large enough to cause crack pinning. The particles were similar to glass particles when viewed under the SEM. The main toughening mechanisms for glass particles are crack pinning, crack deflection and debonding and void growth. There was only debonding and void growth found in the specimens.

Performing particles count for these images was not possible, as the river lines have a very similar colour as the particles, so it is not possible to count the particles without including the lines as well. When compared to glass particles, the ceramic microsphere are similar, and glass has some particle/matrix adhesion problems, so often coupling agent was used to improve adhesion [57]. The dispersion of particles was even in most of the SEM images. Figure 9.52 below shows some void growth, but the amount of void growth is small when compared to the particle size. The sizes of voids were slightly larger when compared to the particle size, so there is some deformation of the epoxy. The use of a coupling agent is typically done with glass particles to improve epoxy to particle adhesion, there was no coupling agent used in making these specimens. There is no adhesion problem in the specimens. However, it could increase the energy needed for debonding and hence increase the fracture energy further. The toughening effect is calculated in analytical modelling in Chapter 8.

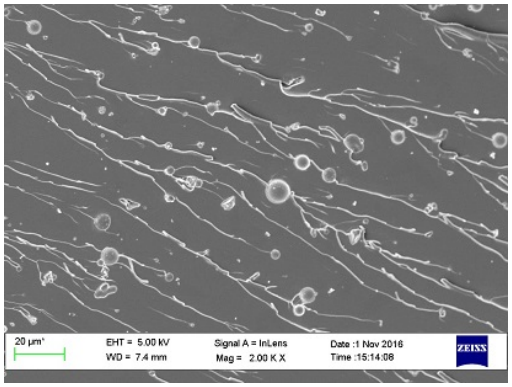


Figure 9.52: Ceramic microsphere 5 wt% SEM image

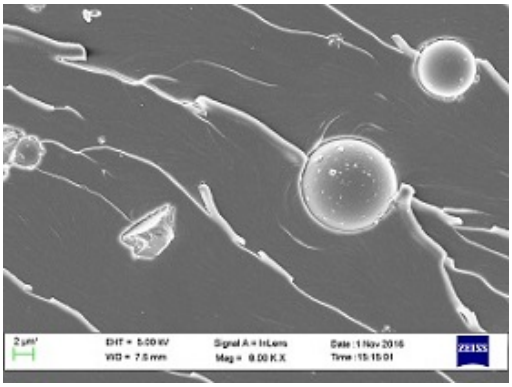


Figure 9.53: Ceramic microsphere 5 wt% SEM image

Some irregular shaped broken particles can be found on the fracture surfaces, so debonding is not the only mechanism occurring. The particles can also be seen during fracture, hence the broken parts were on the fracture surface. Pull out of particles was also shown on this image.

When there is a higher concentration of ceramic microsphere particles, e.g. 10 wt%, see Figure 9.54, debonding and void growth are the only mechanisms that can be found. The river lines that follow were longer and clearer, so more cracks travelled around the particles and continued to propagate in the same direction.

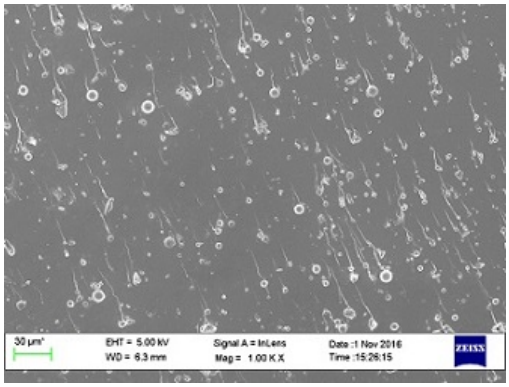

Figure 9.54: Ceramic microsphere 10 wt% SEM image

### 9.7.2 Effect of low temperature

Figures 9.55 to 9.60 below show the fracture surfaces of different wt% of ceramic microsphere modified epoxy tested at low temperature. The fracture surfaces from low temperature specimens were found to be similar (mainly debonding) to quasi-static ceramic microsphere modified epoxy tested specimens. There are no significant differences on the fracture surfaces of the specimens tested at -40$^oC$ and -80$^oC$.

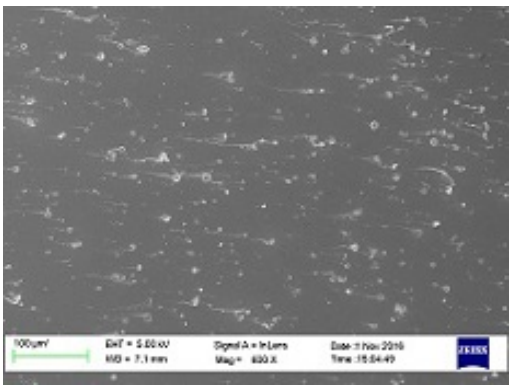

Figure 9.55: Ceramic microsphere 2 wt% SEM image tested at -40$^oC$

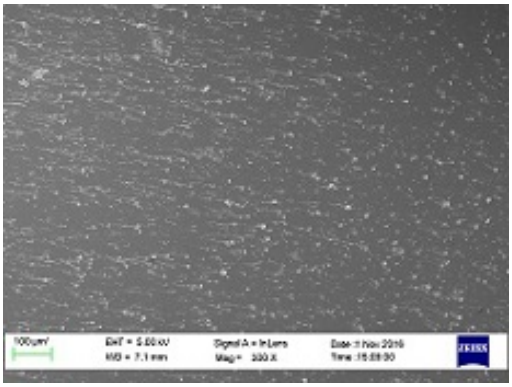

Figure 9.56: Ceramic microsphere 5 wt% SEM image tested at -40$^oC$

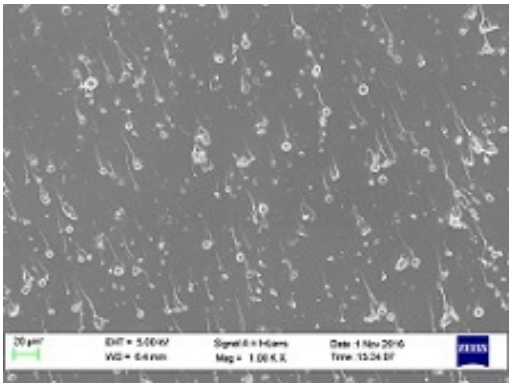

Figure 9.57: Ceramic microsphere 10 wt% SEM image tested at -40$^oC$

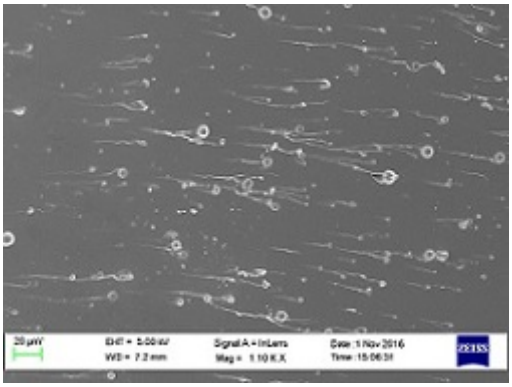

Figure 9.58: Ceramic microsphere 2 wt% SEM image tested at -80$^oC$

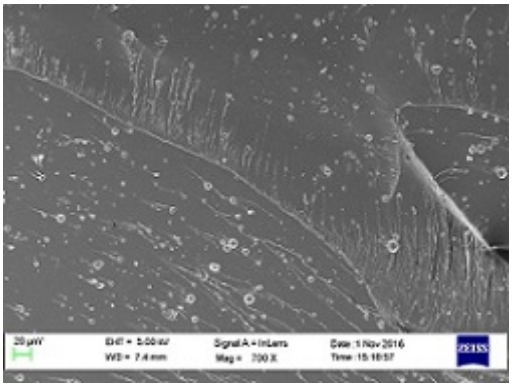

Figure 9.59: Ceramic microsphere 5 wt% SEM image tested at -80$^oC$

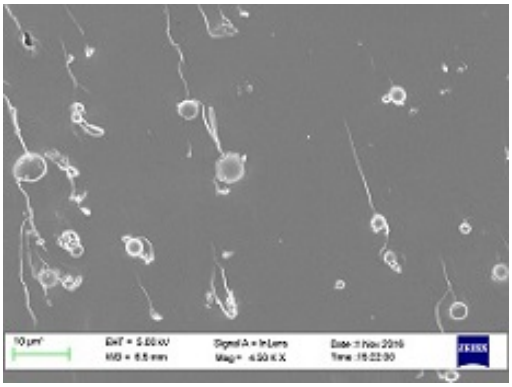

Figure 9.60: Ceramic microsphere 10 wt% SEM image tested at -80$^oC$

## 9.8 Ceramic microsphere / CSR hybrid modified epoxy

### 9.8.1 Effect of concentration of particles

Figures 9.61 to 9.64 below show the fracture surfaces of different wt% of ceramic microphere / CSR hybrid modified epoxy tested at low temperature, the particle size of the CSR particles were 36 to 108 $\mu m$ and the ceramic microspheres were 12 $\mu m$. The wt% ratio of both ceramic microphere and CSR particles were one to one for all wt%. The specimens from quasi-static tests could not be used, due to some plastic film used for protecting the surface stuck on the surface. The dispersions of each particle type were reasonable, as the CSR were large when compared to the ceramic microspheres, more CSR particles can be found easily.

For the hybrid CSR / ceramic microsphere 5 wt% specimens, the two types of particles

are very distinct, as the ceramic particles were smaller and very spherical, and the CSR particles are large and slightly deformed. Figure 9.61 shows the presence of both particles in the specimen, but it is not clear about the % of them. The particles count method cannot be used in this case, as the two types of particles have very similar background, it would be not possible to separate them. Main toughening mechanism for CSR particles were small CSR particles cavitating. Particles were found dispersed on the whole surface, but dispersion was not as good as when only ceramic microspheres were used.

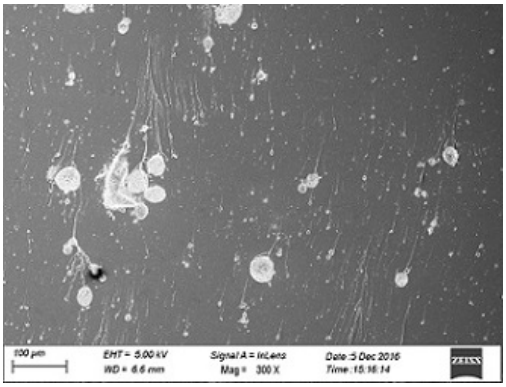


Figure 9.61: Hybrid CSR / ceramic microsphere 5 wt% SEM image

An SEM image of the hybrid CSR / ceramic microsphere 10 wt% fracture surface is shown in Figure 9.62. The deformed large particles of CSR were found as in the CSR specimens, the combination of particles does not affect their failure mechanisms, as the particle sizes were very different. The fracture surface was saturated with particles, as only particles can be seen on the surface. Both types of particles can still be observed, but the large CSR particles had a large % in the area as the particles were bigger, they can be viewed easier. Smaller and more river lines were found in this hybrid specimen, see Figure 9.63.

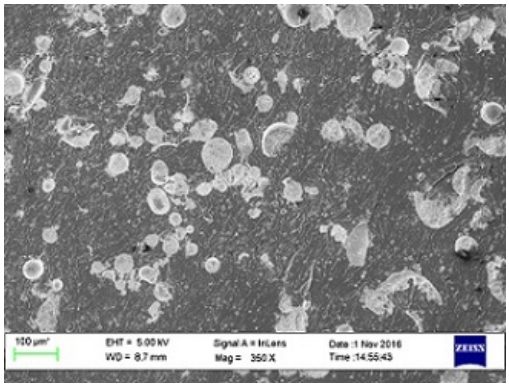


Figure 9.62: Hybrid CSR / ceramic microsphere 10 wt% SEM image

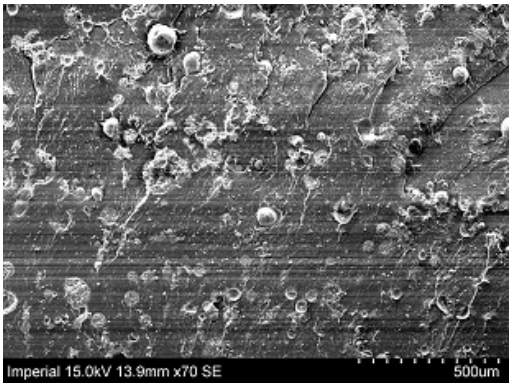


Figure 9.63: Hybrid CSR / ceramic microsphere 10 wt% SEM image

Small ceramic microspheres can be seen (the small particles and voids in Figure 9.64), they were mixed evenly with the CSR particles. Some voids were found, there was more pull out of ceramic microspheres than CSR particles, while in CSR particles, there were more deformations.

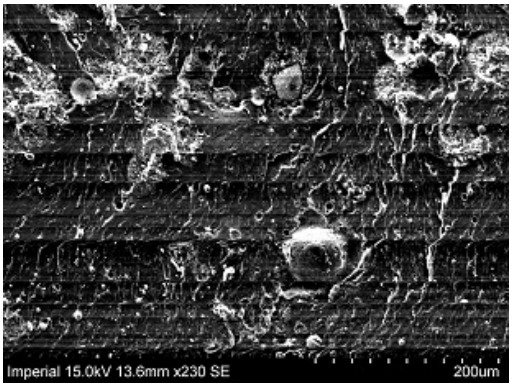


Figure 9.64: Hybrid CSR / ceramic microsphere 10 wt% SEM image

### 9.8.2 Effect of low temperature

Figures 9.65 and 9.66 below show the fracture surfaces of different wt% of CSR / ceramic microsphere hybrids tested at low temperature. There were no special features found in the CSR / ceramic microsphere hybrid specimens that were tested at low temperature, as the fracture surfaces were similar to those of the quasi-static tests at room temperature.

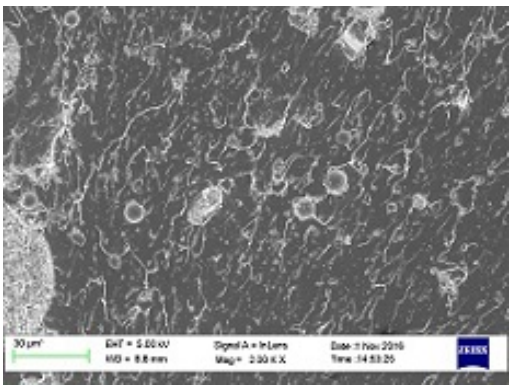

Figure 9.65: SEM image of hybrid CSR / ceramic microsphere 2 wt% specimen tested at -40$^oC$

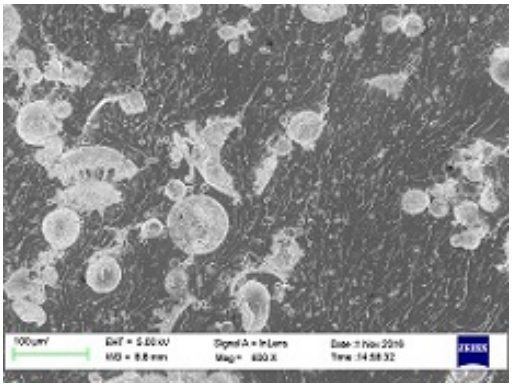

Figure 9.66: SEM image of hybrid CSR / ceramic microsphere 5 wt% specimen tested at -40$^oC$

Other results for high rate tests at 0.1 and 1 m/s were similar to those at -40$^oC$, and hence are not shown here.

## 9.9 Polyethersulfone modified epoxy

### 9.9.1 Effect of concentration of particles

Figures 9.67 to 9.71 show different concentrations of PES particles added into epoxy. The PES particles looked different at different wt% as the particles were dissolved in solvent before mixing into epoxy. It is due to particles formed differently in the epoxy, hence different sizes and shapes of particles can be formed. There were peaks found in the large PES particles, which indicates bridging. It is only found in some images, see Figure 9.67. The large PES particles in this image are estimated to be 186 $\mu$m in diameter, and are larger than the crack opening displacement.

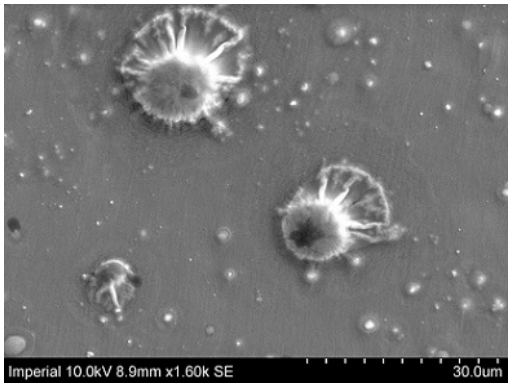


Figure 9.67: SEM image of PES 2 wt% specimen

Some particles were pulled out (the black voids in Figure 9.68) and left voids on the fracture surface, there was about 30% of particles pulled out in the 2 wt% quasi-static tested specimens. There were very different sizes of particles and the particles covered the whole fracture surface. The images show that the particles are well dispersed in the epoxy.

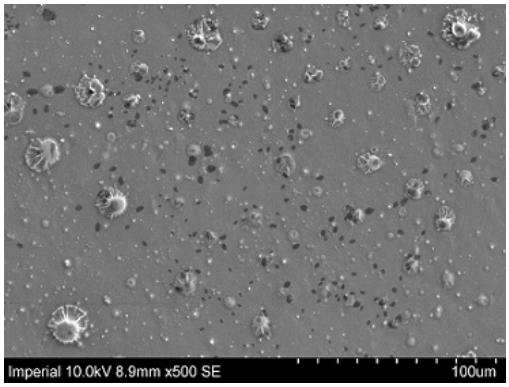


Figure 9.68: SEM image of different sizes of PES particles (PES 2 wt%)

Figure 9.69 shows voids in a low concentration (2 wt%) of PES modified epoxy specimen at a higher magnification.

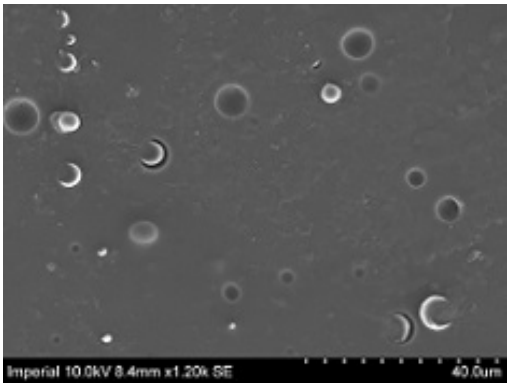


Figure 9.69: SEM image of debonded particles and voids at PES 2 wt%

The fracture surface for PES 5 wt% was similar to PES 2 wt%, but there was more pull out of particles (black circles), leaving slightly enlarged voids on the surfaces, see Figure 9.70. The voids are estimated to be 216 $\mu$m in diameter and the particles were about 150 $\mu$m in diameter.

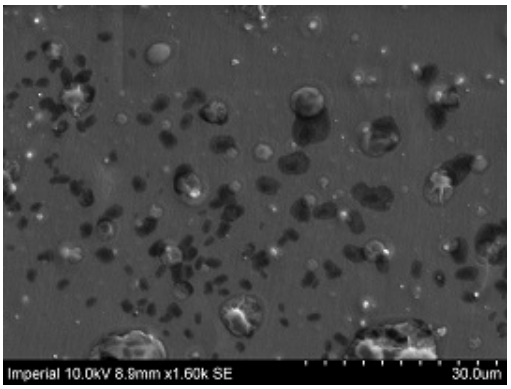


Figure 9.70: SEM image of different sizes of PES particles pull out from surface (PES 5 wt%)

There was more brittle fracture surface found in the PES 10 wt% specimens. There were big blocks of partially dissolved particles, the smaller particles in between the blocks were similar as those found in low wt% of PES. The big blocks were likely to be caused by the high concentration of particles in the mixture. During preparation of the PES specimens, it was found that the PES cannot be mixed completely with the epoxy at high wt%. The dissolved mixture tends to form a sticky ball and sticks onto the stirrer during mixing. Therefore, the PES 10 wt% specimens were not as evenly mixed when compared to the other wt%.

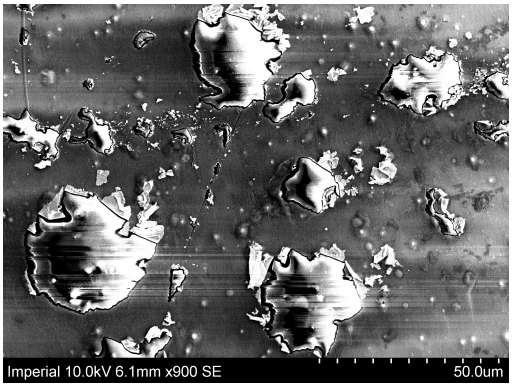


Figure 9.71: SEM image of brittle PES surface (PES 10 wt%)

### 9.9.2 Effect of low temperature

Figures 9.72 to 9.76 below show the fracture surfaces of different wt% of PES modified epoxy tested at low temperature.

For the 2 wt% PES tested at -40°C, the large PES particles were broken and left a rough surface, which is similar to PES 10 wt% quasi-static specimens, but the particles were smaller and more irregular in shape. The average particle size is 364 $\mu$m in diameter. The stretched particles indicated bridging across the crack before fracture, see Figure 9.73. The rest of the fracture surface was smooth, see Figure 9.72. The different microstructure was due to the dissolving of PES.

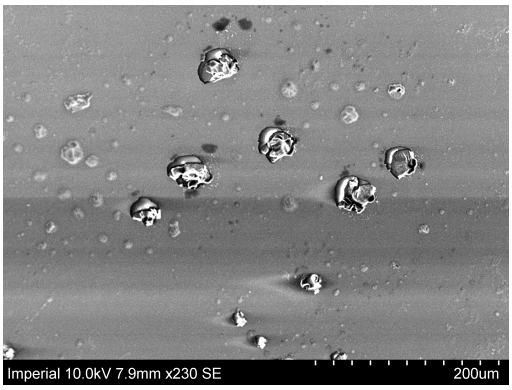


Figure 9.72: SEM image of PES 2 wt% specimen tested at -40$^oC$

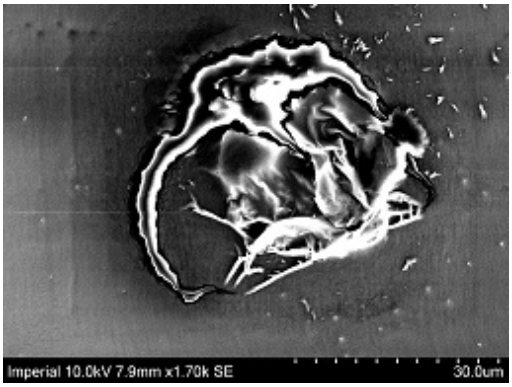


Figure 9.73: SEM image of broken PES (PES 2 wt% tested at -40°C)

With 5 wt% PES, the PES particles were small and spherical, but there were some particles inside a big particles as the particles were dissolved and combined together. The fracture surface of PES 5 wt% at -40$^oC$ was different when compared to the quasi-static PES specimens, but this is due to particles being dissolved and forming different structures, not due to the conditions of the low temperature SENB test.

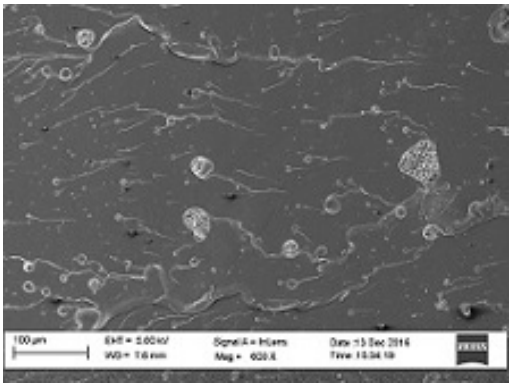

Figure 9.74: SEM images of PES 5 wt% specimen tested at -40$^oC$

Tbe PES 10 wt% fracture surface was fully covered with particles, this indicated saturation of PES particles at 10 wt%. This is found in PES 10 wt% at all testing conditions. The particles were spherical with different sizes. The particles cannot be viewed clearly, but the circular outlines can be found. There are no rough cuts of particles, the fracture surface was smooth. The particles had a very high weight % that it covers the whole area, hence only one structure can be found. The smooth surface was found because the particles were combined with the matrix, there were no bridging of particles. The failure was in the whole material, crack travels directly without going

around the particles. The particle fracture was due to the polymer became brittle at low temperature. The differences in the PES microstructure were due to the sticky lumps formed after dissolving of particles.

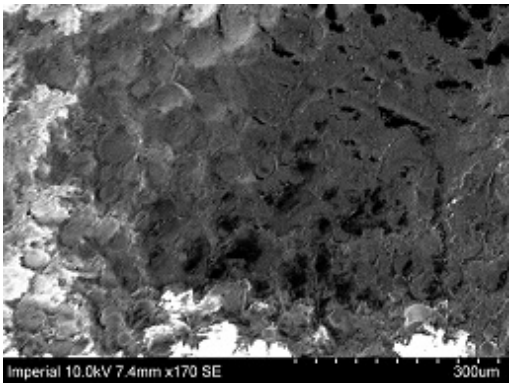


Figure 9.75: SEM image of PES 10 wt% tested at -40$^oC$

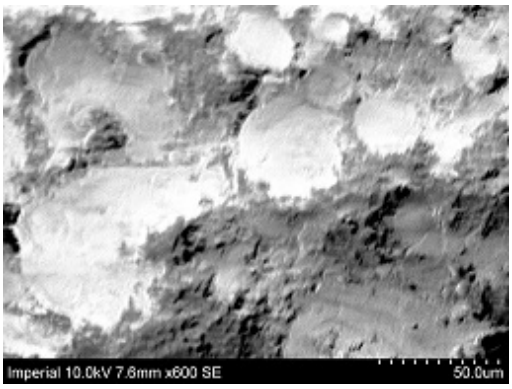


Figure 9.76: SEM image of 10 wt% at -40$^oC$

There were no significant differences on the fracture surface of the PES 5 wt% specimens tested at -80$^oC$ when compared to other PES 5 wt% specimens when tested at room temperature or at -40$^oC$.

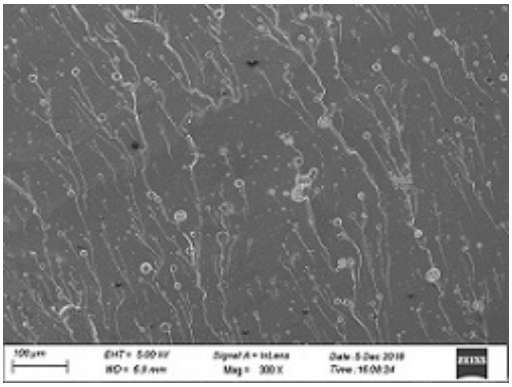

Figure 9.77: SEM image of PES 5 wt% tested at -80$^oC$

For 10 wt% PES, small spherical individual PES particles were found evenly distributed on the fracture surface, see Figure 9.78. Some pull out of particles was found, but there was only a small amount of particle pull out, see Figure 9.79. The particles had similar sizes and a tail was followed with pulled out particles. The failure mechanism was not occurring in all the particles, about 10% of the particles show river lines and about 5% show debonding.

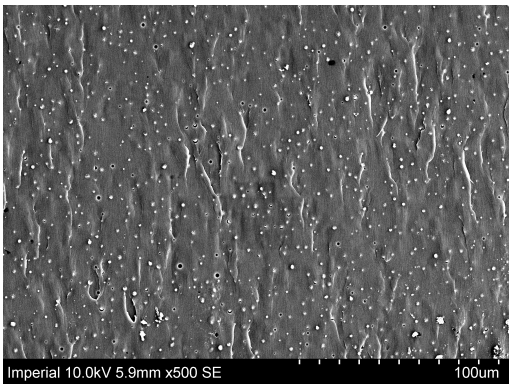


Figure 9.78: SEM image of PES small particles (PES 10 wt%) tested at -80$^oC$

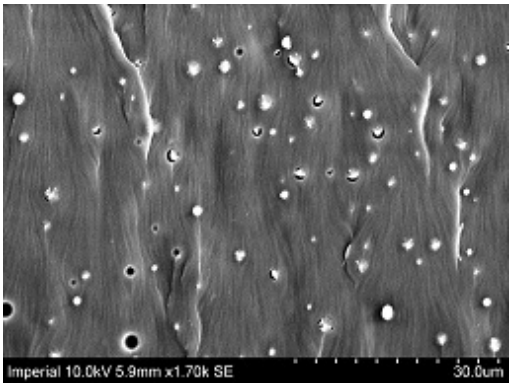


Figure 9.79: Zoom in SEM image of PES small particles (PES 10 wt%) tested at -80$^oC$

## 9.10 Polyethersulfone / Silica hybrid modified epoxy

### 9.10.1 Effect of concentration of particles

Figures 9.80 to 9.83 below show fracture surfaces of different wt% hybrid PES / silica modified epoxy. The PES particles were dissolved in a solvent before adding in with the epoxy and the silica particles, both particles have the same weight%.

For the hybrid PES / silica 2 wt%, some small particles and voids can be found, as there were some bright round edges at the small particles, which indicate the presence of debonding. Figure 9.80 shows some partially dissolved PES particles. The particles were not spherical and therefore can be sure that they are dissolved PES, no debonding can be found in the big particles. Fracture surfaces of hybrid PES / silica 5 wt% were not good, due to the fracture surfaces being contaminated, hence no images could be taken.

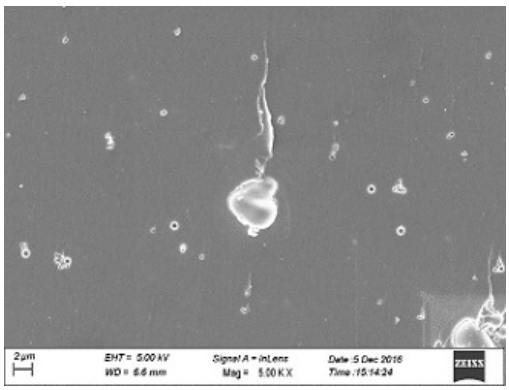


Figure 9.80: Hybrid PES / silica 2 wt% SEM image

Similar behaviour was found in hybrid PES / silica 10 wt% as in PES 10 wt%, but in the hybrid PES / silica specimens, there were some very small particles which can be found in very high magnification images, about 100 nm. The blocks of silica particles were infused in the big dissolved PES particles, as the PES became big sticky chunks after dissolving, hence the pattern was not clear. Void growth from the small dissolved PES particles pull out can be seen, there were some relatively larger deformation of voids shown in this image.

There were blocks of dissolved PES in the epoxy during making of the specimens, it was impossible to mix two types of particles in when the weight% was high. This is because the dissolved particles were very thick and cannot be mixed into the low viscosity epoxy matrix. Therefore, there were some very uneven distributions of particles in PES 10 wt% specimens and hence, it would be hard to estimate their ratio.

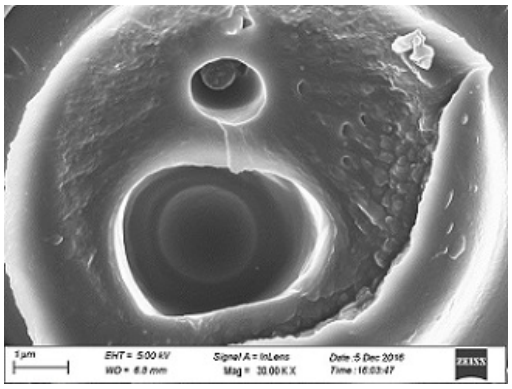


Figure 9.81: Hybrid PES / silica 10 wt% SEM image

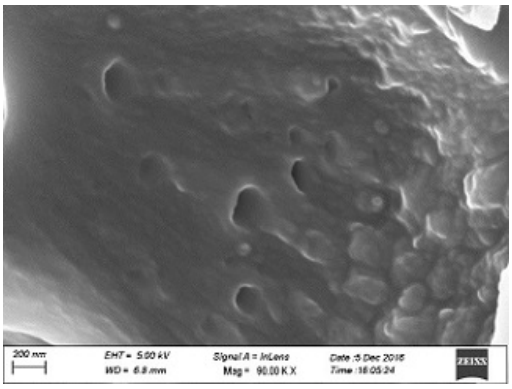


Figure 9.82: Hybrid PES / silica 10 wt% SEM image

Figure 9.83 shows a big dissolved PES particle. Some epoxy was inside this big PES

particle, which indicated local phase inversion. This was the same as in some of the PES 10 wt% specimens. Silica particles were not found due to their very small size.

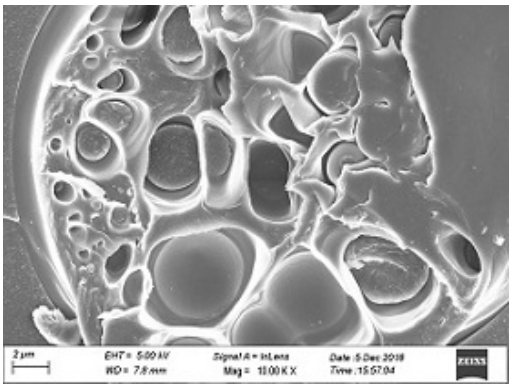

Figure 9.83: Hybrid PES / silica 10 wt% SEM image

### 9.10.2 Effect of low temperature

Figures 9.85 to 9.89 below show fracture surfaces of different wt% of hybrid PES / silica modified epoxy tested at low temperature. Similar fracture surfaces were found for the low temperature tested PES / silica hybrid specimens when compared to PES specimens tested at other conditions. Silica cannot be viewed in the PES / silica hybrid specimens as the particles are too small and are obscured by the conductive coating. Debonding of individual PES particles was the main failure mechanism, the debonding often happened in the clusters of particles.

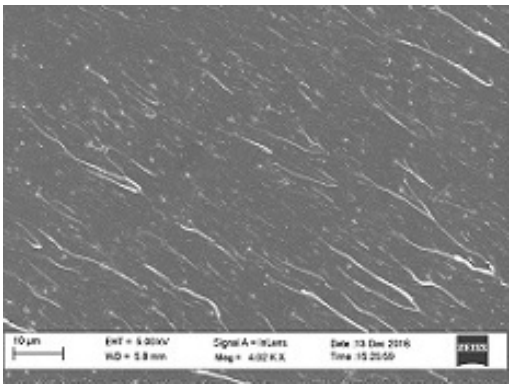

Figure 9.84: SEM image of hybrid PES / silica 2 wt% specimen tested at -40$^oC$

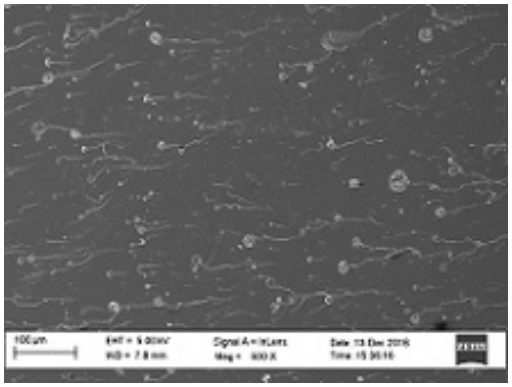

Figure 9.85: SEM image of hybrid PES / silica 5 wt% specimen tested at -40$^oC$

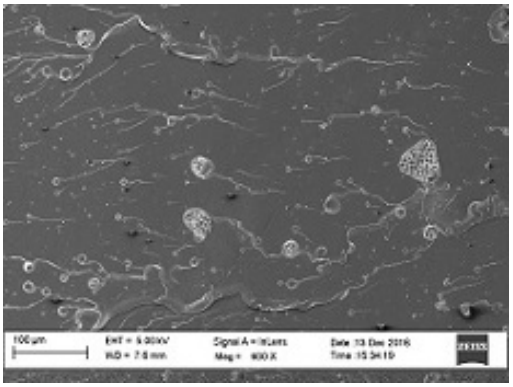

Figure 9.86: SEM image of hybrid PES / silica 5 wt% specimen tested at -40$^oC$

Local phase inversion is shown in Figure 9.87, but there were only about 5% of the areas that were found to have local phase inversion. There were different concentrations of particles throughout the area, this is due to the particles being dissolved before adding in, clusters of dissolved particles were noticed during mixing. As there were phase inversions only at high particles concentrated area, this shows that wt% of higher than 10 wt% would result in local phase inversion.

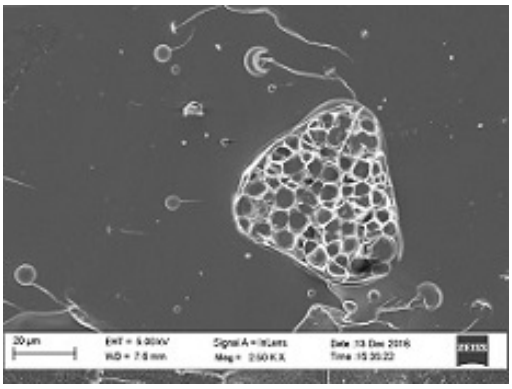

Figure 9.87: Zoom in image of hybrid PES / silica 5 wt% tested at -40$^oC$

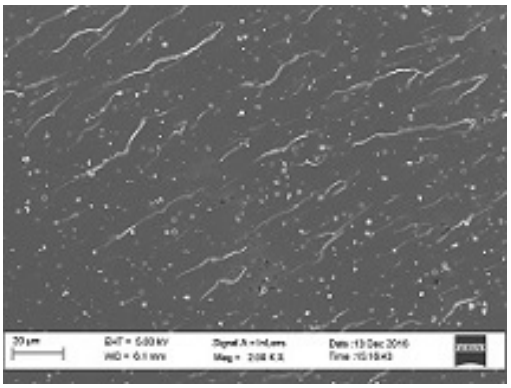

Figure 9.88: SEM image of hybrid PES / silica 10 wt% tested at -40$^oC$

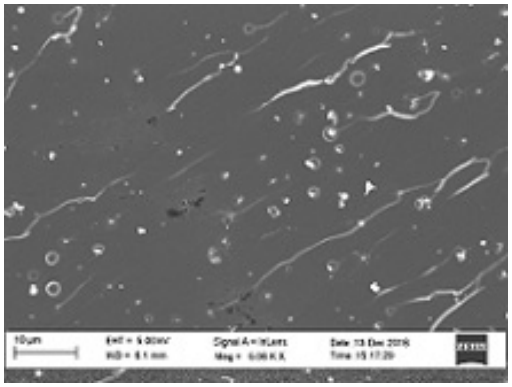

Figure 9.89: SEM image of hybrid PES / silica 10 wt% tested at -40$^oC$

The hybrid PES / silica specimens tested at -80$^oC$ did not show any significant differences when compared to the hybrid PES / silica specimens tested at -40$^oC$.

## 9.11 Summary

Table 9.1 below shows a summary of the toughening mechanisms for each condition, for each individual particle type and hybrid, at room temperature for quasi-static and high rate and at low temperature. Most of the particles showed debonding from the epoxy matrix, and the brittle conditions (high rate and low temperature did not produce significant differences on the fracture surfaces). There was only debonding found in the silica-modified epoxy specimens, as the particles could not be viewed easily using the SEM, even when a thicker coating was applied which masked some features, and hence the amount of void growth cannot be confirmed. For the CSR-modified epoxy, there was first localised deformation in the large CSR particles, then the small CSR particles were debonded. In the silica / CSR hybrid specimens, the silica particles were not clearly viewed as for the silica specimens, debonding of small CSR particles was found. The ceramic microsphere had the most even distributions of particles in the epoxy when compared to other particle types, which was due to the particle size (12 $\mu$m) and relatively even particle size, so that the powder form can be mixed into epoxy easier. There was only debonding found in the ceramic microsphere specimens. A similar debonding mechanism was found in the CSR / ceramic microsphere specimens. There was bridging found for the partially dissolved PES at mostly 5 wt% of PES, some localised phase inversion was found in 10 wt% PES specimens. There was particle debonding and pull out found in the PES-modified epoxy specimens at all conditions. There was debonding and void growth found in the PES / silica hybrid specimens,

where only particles can be found at high wt% (10 wt%), there was no epoxy matrix on the surface, which indicated local saturation of particles.

Table 9.1: Summary of mechanisms of toughening

| Particles type | Conditions | Mechanism of toughening |
|---|---|---|
| Silica | Quasi-static room temperature | Debonding |
| | High rate | Debonding |
| | Low temperature | Debonding |
| CSR | Quasi-static room temperature | Localised deformation, debonding of small particles |
| | High rate | Localised deformation, debonding of small particles |
| | Low temperature | Debonding, cavitation |
| Silica / CSR | Quasi-static room temperature | Debonding |
| | High rate | Debonding |
| | Low temperature | Debonding |
| Ceramic microspheres | Quasi-static room temperature | Debonding, pull out of particles |
| | High rate | Debonding |
| | Low temperature | Debonding |
| CSR / ceramic microspheres | Quasi-static room temperature | Debonding |
| | High rate | Debonding |
| | Low temperature | Debonding |
| PES | Quasi-static room temperature | Pull out, bridging, debonding |
| | High rate | Pull out, bridging, debonding |
| | Low temperature | Pull out, bridging, debonding |
| PES / Silica | Quasi-static room temperature | Debonding, void growth |
| | High rate | Debonding, void growth |
| | Low temperature | Debonding, void growth |

## 9.12 Particles count

### 9.12.1 Introduction

Particles count with the use of imaging software was used in analysing SEM images with only one type of particle. The SEM imaging revealed some information regarding the failure of the materials, but this information is not quantitative. The use of the semi-automatic particles count method can provide better estimates of the amount and concentration of particles present in a specific area, as well as of the particle sizes and even the amount of voids and their sizes. Previous studies did not use this kind of particles estimation method, hence this would provide additional information in investigations of the fracture properties in particle modified epoxy.

Not all of the images could be used for particles count, as the background of the image needs to be distinct from the particles, so that thresholding can be used, to make the image binary for processing. Due to this reason, particles count only provides an estimation of the number of particles in the area, as thresholding can include some of the features which are not particles and may exclude some of the particles. The count gives the area % of particles, which is identical to the volume %. The weight% of particles added can be converted to the volume % using the densities of the particles and the epoxy, and this volume % can then be compared with measured volume %. This method cannot identify two different types of particles accurately, although this could be done by setting two counts with different particle size ranges and then narrowing down the count, however, there are insufficient differences between the two types of particles. There can easily be overlaps and miscounts, which makes the results not accurate enough for this purpose.

### 9.12.2 Particles count example

An example of particles count is described below, using a 2 wt% ceramic microsphere SEM image. Other binary images are included in Appendix A.

Figure 9.90 shows a 2 wt% ceramic microsphere image where the particles are light and the epoxy background is dark, which would be used in particles count. Before conversion to binary, the image was cropped to remove the footer bar combining the micron bar and image information.

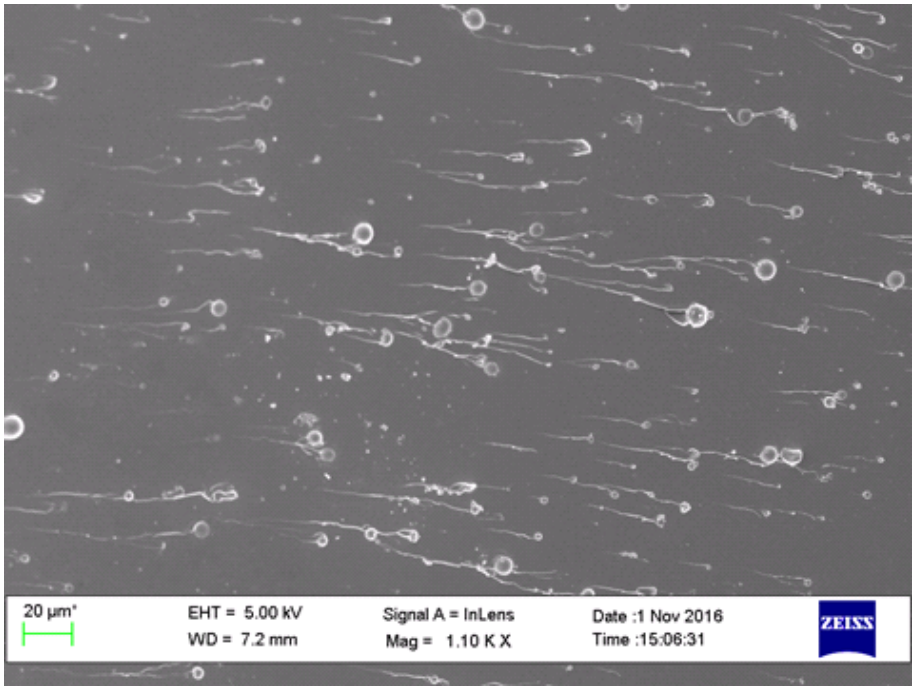


Figure 9.90: SEM image of ceramic microsphere 2 wt% used for particles count

Figure 9.91 shows the binary image after conversion. The image was made binary in the same ImageJ software in order to produce consistent information of the image for the whole process. The background and particle colours were reversed, as the program used identified dark regions as objects.

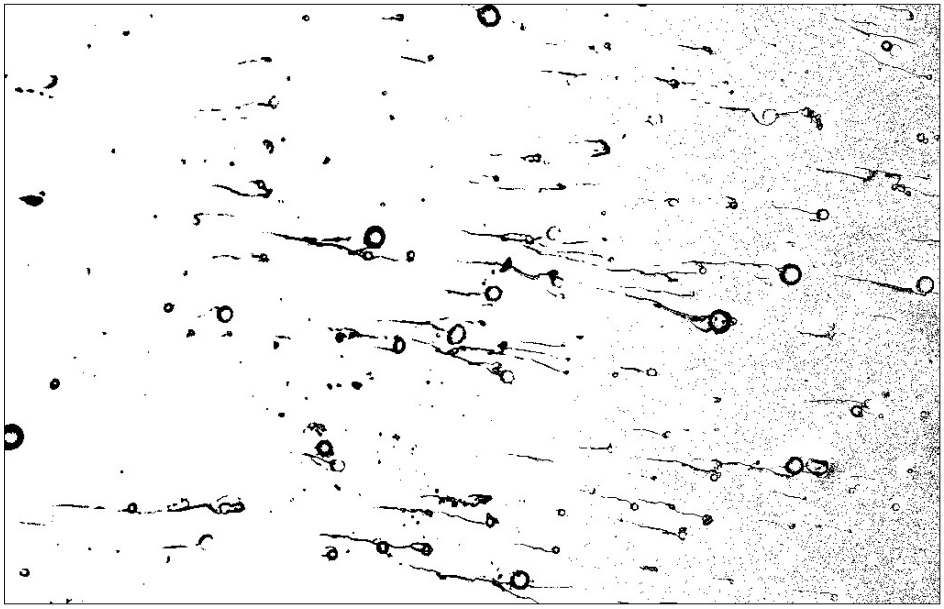

Figure 9.91: Binary image of ceramic microsphere 2 wt% used for particles count

Figure 9.92 shows the particles count of the binary ceramic microsphere 2 wt% SEM image. All of the particles identified were numbered with their size information. A second count with a narrowed size range (according to the size information from the first count) was then performed, until all of the particles and only the particles are covered.

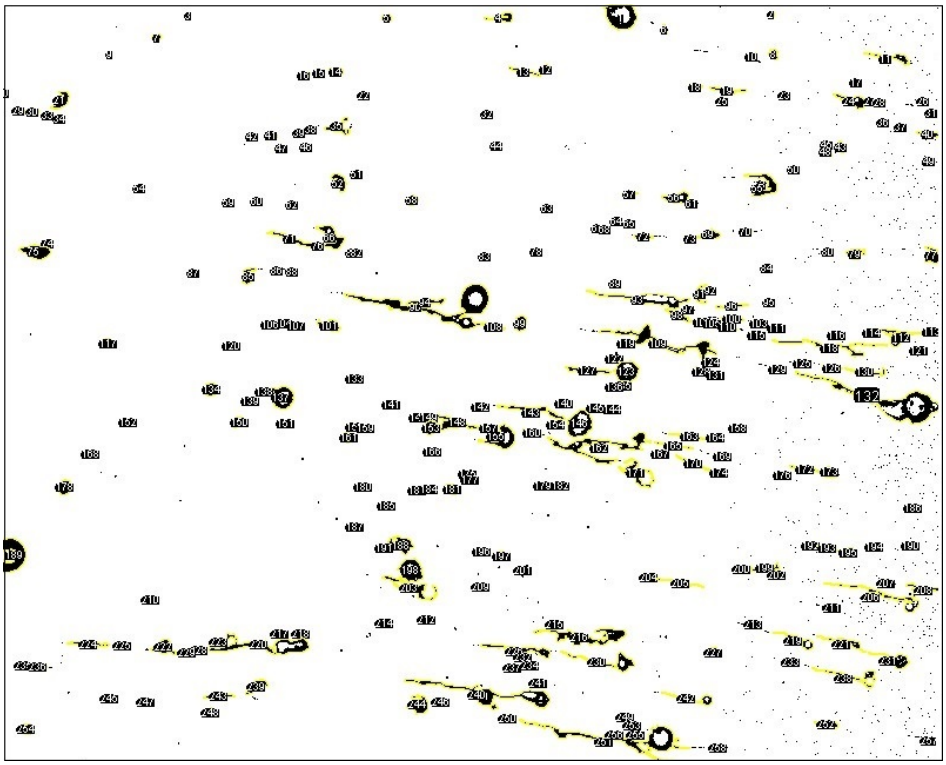

Figure 9.92: Particles count of 2 wt% ceramic microsphere SEM image

The void diameters were estimated with the use of software ImageJ.

### 9.12.3 Particles count results

The Table 9.2 below shows the densities of the particles used in finding the expected volume % from the weight% which was added to the epoxy.

Table 9.2: Densities of particles and epoxy used for particles count [62][64][65]

| Particles | Density ($g/cm^3$) |
|---|---|
| CSR | 1.1 |
| Silica | 2.65 |
| Ceramic microspheres | 2.4 |
| PES | 1.4 |
| Epoxy | 1.2 |

The expected particles volume % values were found by the ratio of density and wt%. Tables 9.3 to 9.6 below show the expected volume % calculated from the wt% and the counted area % of the silica, CSR, ceramic microsphere and PES particles.

It was not possible to perform particles count in 2 wt% and 10 wt% silica specimens as the background cannot be separated from the particles in the image, because there is insufficient contrast so it is too similar to the particles. The silica particles had a size of 20 nm. The same issue was found in CSR 10 wt%, when the fracture surface became very rough at this high wt%, so the particles could not be readily identified.

Table 9.3 shows the counted area % and the expected vol% of silica modified epoxy. Most of the counted area % were very different from expected vol%. All the results show a larger counted area % than the expected vol%. This is due to the aggregation of particles when the weight% used is low, it is found from SEM imaging that particles were not spread evenly on the surface, hence the images with particles had a higher concentration than the original, this would affect the counting result. As the particles and background had similar colour which is hard to separate, some images cannot even be used, with this difficulty in counting silica particles, over-counting is possible. Therefore, the actual vol% is expected to be lower than the counted result.

Table 9.3: Particles count results of silica modified epoxy

| Wt% of silica | Counted area % | Expected vol% |
|---|---|---|
| 2 | not possible | 0.9 |
| 5 | 22.5 | 2.3 |
| 10 | not possible | 4.8 |
| 15 | 38.6 | 7.4 |
| 25.4 | 15.2 | 11.7 |

Table 9.4 shows the counted area % and the expected vol% of CSR modified epoxy. The CSR particles had a size range of 38 to 106 $\mu$m diameter. As the 10 wt% was saturated with particles, which cannot be made binary with the image, so the particles count was not possible. In the CSR specimens, expected vol% values were a lot lower than the counted area%. This could be due to the big CSR being broken into small CSR particles and flow into the epoxy matrix. The count considers the big CSR particles as they were more visible for the process. These counts do not count the leaked small particles, hence this reduced the amount of particles counted. As the CSR particles were a lot larger than silica, there are more particles that are touching. This caused more problems in the count, as the particles that are in contact would be counted as one big particle, sometimes even if there is epoxy inside the big CSR particle (the big CSR particles are made up of small CSR particles).

Table 9.4: Particles count results of CSR modified epoxy

| Wt% of CSR | Counted area % | Expected vol% |
|---|---|---|
| 2 | 10.6 | 2.2 |
| 5 | 13.5 | 5.4 |
| 10 | not possible | 11 |

Table 9.5 shows the counted area% and the expected vol% of the alumino silicate ceramic microsphere modified epoxy. It is found from the tensile data in Chapter 6.3 that there were agglomeration of ceramic microsphere at 10 wt%. The ceramic microsphere particles had a diameter of 12 $\mu$m. All of the counted results were not according to the expected vol%, but as all the values are so small, due to the high density of the

ceramic, the counts were not that different when compare to expected vol%. They were not too far off when compared to the results from other specimens. It was found from SEM images that the ceramic microsphere were the most evenly spread when compared to other particles used, this could explain the count results. closer examination of the particles count showed that some of the river lines were counted, as their colour was significantly different from the background. The large diameters from river lines were then taken away, but this also means some of the particles with the river lines were taken away which improved the accuracy of the counted area%. Particles count was not possible when the image cannot be made completely binary as the colour of river lines confused the system.

Table 9.5: Particles count results of ceramic microsphere modified epoxy

| Wt% of Ceramic microspheres | Counted area % | Expected vol% |
|---|---|---|
| 2 | 2 | 1.0 |
| 5 | 3.1 | 2.6 |
| 10 | 2.6 | 5.3 |

Table 9.6 shows the counted area % and the expected vol% of the polyethersulfone modified epoxy. The counted area% values were different from the expected vol%, and all the count area% were larger than the expected vol%. It is due to the partially dissolved PES particles which stick together and cannot be separated. As the images were taken where there were particles, there were more particles in those areas and this resulted in an increase in the counted area%. This is more significant when wt% of PES was high. The particles count for the PES modified epoxy was the most accurate among all of the modified epoxy. According to the count images (see Appendix A.2 for more), there were fewer river lines being selected, and all the particles were covered which should give more accurate count results. When the PES particles are not broken and spherical, a more accurate count can be performed, as the particle properties are closer to what the counting software expects.

Table 9.6: Particles count results of PES modified epoxy

| Wt% of PES | Counted area % | Expected vol% |
|---|---|---|
| 2 | 6 | 1.7 |
| 5 | 9.7 | 4.3 |
| 10 | 11.7 | 8.6 |

### 9.12.4 Summary

The use of imageJ for particles count provided results of the area % of particles for images where there was a high contrast in between the background (epoxy) and the objects (particles). The calculated area% values were different from the expected volume % for some of the results, but this could be due to variables in the image processing, such as the counting of river lines as particles. Another factor that can give large variations could be the poor mixing of particles.

## 9.13 Conclusions

The main toughening mechanisms in the epoxy modified using silica particles were debonding and void growth, while particle cavitation debonding was the main mechanism in CSR particles (as the CSR particles were made up of small CSR particles). Ceramic microspheres were expected to behave like glass particles, but there was only debonding and void growth found for the ceramic microspheres. There were also some particles pulled out found in the PES-modified epoxy, and some local phase inversion at high wt% of PES. Specimens tested at high rate and low temperature did not produce any significant differences in their toughening mechanisms for all formulations.

Particles counts were not possible for some SEM images, due to the problem with making the images binary which required sufficient contrast between the particles and epoxy background. Most of the area% count results were not the same as the expected vol%. This could be due to the difficulty in producing accurate counts, as well as uneven mixing of particles. However, particles count can be used for comparison of particles distribution in different wt% of specimens, even the results might not be exactly accurate, they can provide some ideas of the particles distribution.

The next chapter will include the use of FEA models for predicting the fracture properties of TDCB and SENB models for all the conditions tested.

# Chapter 10

# Finite element analysis

## 10.1 Introduction

The tapered double cantilever beam (TDCB) experimental results found will be compared with the results of a TDCB modelling study using Abaqus. Finite element analysis (FEA) with the use of cohesive elements can provide predictions of the fracture properties of adhesives without the effects from experimental variables. TDCB models with the use of different adhesives and cohesive zone properties have been studied in a few previous studies [34][73][74] with the same cohesive element method. Their resultant force values were compared with the force measured from the experiments. There were no stick-slips present in the predictions in the literature, hence the results could be compared directly with the propagation values measured from the experiments. TDCB tests at different brittle conditions (low temperature, high rate) have never been modelled. Instead the authors typically studied the three differeent modes of testing (fracture in mode I, mode II and mode III).

Therefore, the modelling of TDCB tests in this study would provide more information regarding the ideal fracture properties of TDCB tests at brittle conditions. The force results from the FE model cannot be compared with experimental force values, as there were stick-slips in experiments, while only stable crack propagation can be assumed in Abaqus. Therefore, only propagation values of the fracture energy were used in the model. The overall trend and the relationship between the fracture energy and resultant force required for completing the fracture will be compared.

Although FEA of TDCB joints has been made in previous studies, but rarely has FEA been performed for single edge notch bend (SENB) specimens. The SENB model of different conditions (low temperature and high rate) has not been performed before, and this would provide more information regarding the ideal fracture properties that particle modified epoxies can reach. SENB models of all the conditions tested experimentally

were performed in FEA predictions. This has provided a lot of information regarding the predicted load and fracture energy of the materials used.

The method used in making of the SENB model was the same as used for the TDCB model, in order to produce the same effect for similar results. A zero thickness cohesive zone was made at the middle of the specimen, the whole model was drawn in one piece to ensure the same number and position of nodes for the tie to the cohesive zone.

This Chapter is divided into two main sections discussing the TDCB model and SENB model, with details of the models and their results within the same section. The TDCB model and the resulting predictions are discussed first.

## 10.2 Finite element analysis of TDCB

### 10.2.1 TDCB model

The TDCB model for mode I fracture was made with the same conditions used in experiments. The boundary conditions would be at the loading pin, where the force was applied in the experiments, and Figure 10.1 shows the movements in the beams. For the lower beam, as there would be a small rotation in the beam during the mode I test, so rotation would be allowed. No movement in any direction other than y would be allowed. For the front of the upper beam, only the mode I opening (y-direction) would be allowed to move.

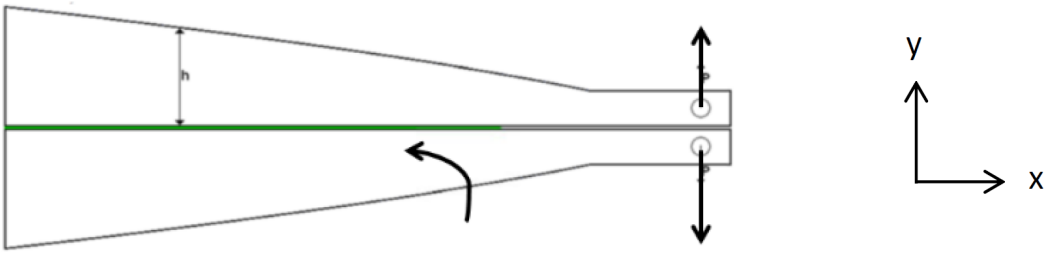


Figure 10.1: Forces in TDCB (modified from [34])

Table 10.1 below shows the material properties information for this study. The properties of the epoxy which were not measured in the present work were obtained from calibration of the stress-strain data from other studies in the group. The properties of the aluminium alloy beams were obtained from the literature [34].

Table 10.1: Properties of aluminium alloy (EN AW 2014-A) [34] and epoxy [39] for the TDCB FE model

| Property | Al alloy | Epoxy (Standard) |
|---|---|---|
| E (GPa) | 72.4 | 3.14 |
| $\sigma_y$ (MPa) | 430 | - |
| UTS (MPa) | 485 | - |
| $\rho_s$ (kg/m$^3$) | 2700 | 1200 |
| $v_s$ | 0.33 | 0.35 |

The cohesive law traction-separation parameters used in the simulation are shown in Figure 10.2. When only mode I fracture is under consideration, the parameters for describing cohesive law are the stiffness, $K_I$, the separation at damage initiation, $\delta_{n0}$, and the critical energy release rate (fracture energy), $G_c$ [34]. The cohesive zone parameters were found by calculating initial values as shown in the equations below, then trying different combinations of values to find values which allowed the model to solve, and those that produced the correct breaking of the TDCB joint were used.

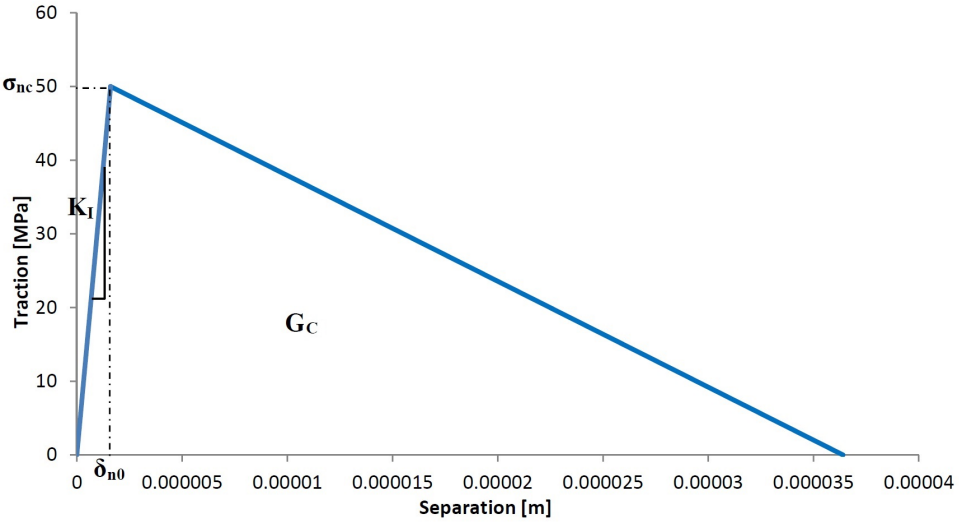


Figure 10.2: Traction-separation curve [34]

The initial values for the traction-separation curve are calculated as follows [34]. The initial stiffness is given by:

$$K_I = \frac{E}{t_a} \tag{10.1}$$

where $t_a$ is the thickness of the adhesive layer (0.4 mm) and E is the modulus of the epoxy. The separation at damage initiation is given by:

$$\delta_{n0} = \frac{\sigma_y}{E t_a} \tag{10.2}$$

where $\sigma_y$ is the yield stress of the cohesive zone. The $\sigma_{n0}$ (stress at damage initiation) is given by

$$\sigma_{nc} = \delta_{n0} K_I \tag{10.3}$$

where $\sigma_{nc}$ is the separation at damage initiation.

The force during crack propagation was found from the force and the status information. From the status data: 0 represents no load, which means that the element is broken, and the element is present when the value is 1 and hence the crack length against force information was found.

### 10.2.2 One element tensile model

One element tensile model was performed for finding out the cohesive properties values (see Figure 10.3). Only one element was used because it simplifies the conditions and reduces computation time. The model was built using tensile data from the experiments and the cohesive properties were found by adjusting the initial values to produce an exact fit to the expected failure properties.

The tensile properties of the unmodified epoxy were input:
Young's modulus (E): 3.14 GPa
Poisson's ratio ($v$): 0.35

The cohesive properties were first guessed until the tensile response of the model matched the tensile response found from the experiment. Below shows the final cohesive values used.
The cohesive properties found were:
Quads Damage ($\sigma_{n0}$): 60
Damage Evolution (fracture energy) ($G_C$): 50
Elastic ($\delta_{nc}$): 1000

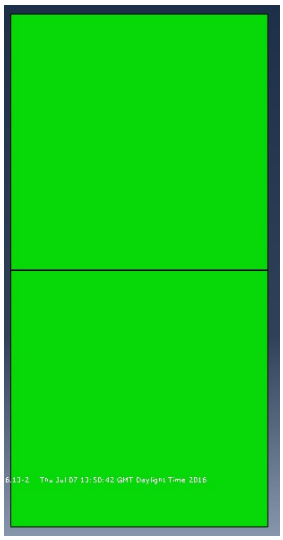

Figure 10.3: One element tensile model

The triangle produced is shown in Figure 10.4, which is the traction-separation curve for the epoxy. The stress and displacement graph was generated by the stress and displacement obtained separately from time against displacement results and time against stress results in Abaqus. The cohesive elements were selected and the data from one of the elements was chosen for the final graph. Measured fracture energy was used as an input. Only fracture energy is changed for each specimen, as changing the two other values (quads damage and elastic) could results in different shape of the graph or even errors.

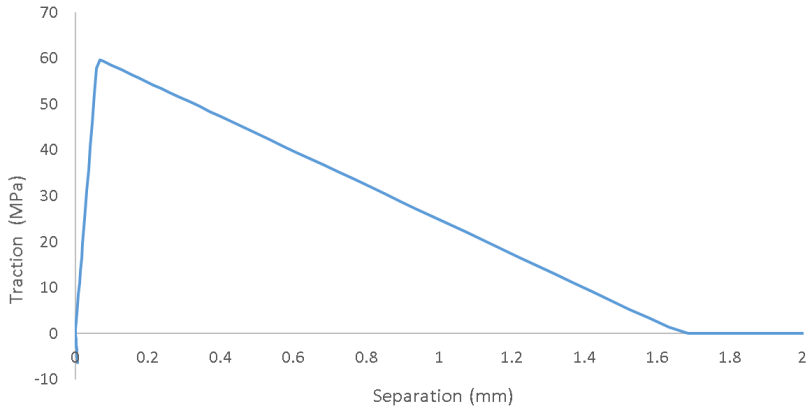


Figure 10.4: Traction-separation curve deduced from tensile model

The values of the cohesive zone:

$$G_C = \frac{1}{2} K_I \delta_{n0} \delta_{nc} \tag{10.4}$$

$$K_I = 595 \times 10^6 \text{ MPa/m}$$
$$\sigma_{n0} = 60 \text{ MPa}$$
$$\delta_{nc} = 1.68 \times 10^{-3} \text{m}$$

### 10.2.3 TDCB model results

As it is not possible to find the fracture energy from FE results, so the force results were used. The results show the highest load for breaking the joint completely. Due to the presence of stick-slips in experiments, the force results cannot be compared directly with experimental force, as there were initiation and arrest points seen. There were only stable crack propagations assumption in the model, hence only propagation values of $G_c$ were used in the model. The overall trend of the resultant force, such as the toughening effect from particles, brittleness of the joint and the relationship with the fracture energy were considered instead.

The measured mean propagation load values were larger than the predicted load values, this means that the stick-slips contribute more to the failure, as there were more stick-slips with higher load that affects results of predictions.

#### 10.2.3.1 Silica-modified epoxy

Figure 10.5 and Table 10.2 show predictions of the quasi-static TDCB specimens using the silica modified epoxy. Most of the predicted load values were proportional to fracture energy values, the predictions were within the range of experimental load found. The results show reasonable agreement.

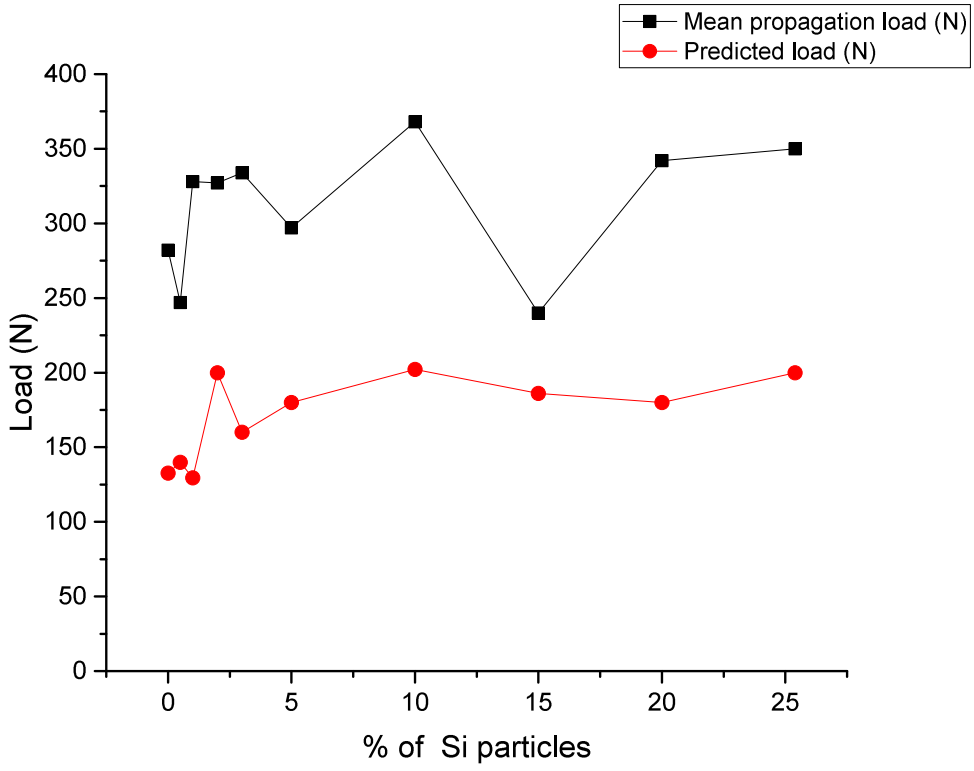


Figure 10.5: TDCB model - silica results predictions graph

Table 10.2: TDCB model - silica results predictions table

| % of Si particles | Exp ($J/m^2$) | Mean propagation load (N) | Standard Deviation | Predicted load (N) |
|---|---|---|---|---|
| 0 | 80 | 282 | 18 | 133 |
| 0.5 | 76 | 247 | 33 | 140 |
| 1 | 129 | 328 | 30 | 129 |
| 2 | 123 | 327 | 32 | 200 |
| 3 | 56 | 334 | 13 | 160 |
| 5 | 113 | 297 | 13 | 180 |
| 10 | 163 | 368 | 14 | 202 |
| 15 | 115 | 240 | 30 | 186 |
| 20 | 141 | 342 | 18 | 180 |
| 25.4 | 147 | 350 | 33 | 200 |

#### 10.2.3.2 CSR-modified epoxy

A similar correlation was found for the CSR-modified epoxy, the results were according to expectation. with a very good agreement between the measured mean propagation load and the predicted load from the model, see Figure 10.6 and Table 10.3. Only the fracture energy was changed in the cohesive model, other parameters were the same for the different materials. There was an increase of predicted load when the wt% of particles increases and most mean propagation load values were only slightly larger than the prediction values, this same trend was found in the fracture energy from the experimental results.

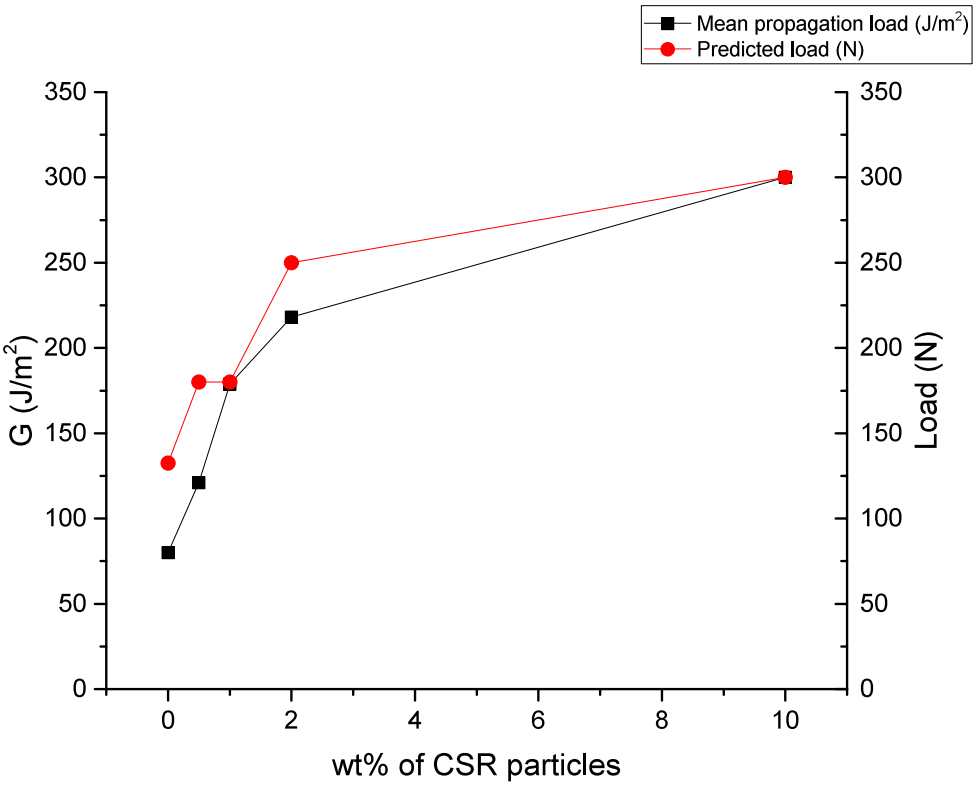


Figure 10.6: TDCB model - CSR results predictions graph

Table 10.3: TDCB model - CSR results predictions table

| % of CSR particles | Exp ($J/m^2$) | Mean propagation load (N) | Standard Deviations | Predicted load (N) |
|---|---|---|---|---|
| 0 | 80 | 282 | 18 | 133 |
| 0.5 | 121 | 293 | 30 | 180 |
| 1 | 179 | 387 | 40 | 180 |
| 2 | 218 | 428 | 20 | 250 |
| 10 | 300 | 372 | 30 | 300 |

Quasi-static TDCB summary

Quasi-static tests were not performed on silica / CSR hybrid TDCB specimens, hence FE predictions cannot be made. The predictions of quasi-static TDCB for the silica and the CSR modified epoxies were found to be according to expectation, as the predicted loads agreed well with the experimental values, although they tended to be lower, so the FE model was reliable. The high rate TDCB predictions are included in the next Section.

### 10.2.4 High rate TDCB

In the high rate TDCB tests which were conducted at 1 m/s, the measured force was not used to calculate the fracture energy. This was because the force was affected by dynamic effects, and the fracture was by stick-slips. As only a few data are available, these results cannot be put into graphs for comparison, as they would not be presentable for the results. Average values of each set were used for input. Because the predictions only showed the highest force, while in the high rate method used. The force was not used in obtaining fracture energy, it is not possible to compare the load results. However, the predictions provided an estimation of the load values of high rate TDCB, which allows some comparisons to be made.

Si 2 wt%

The predicted load values from the model for the epoxy with 2 wt% of silica were all reasonable, see Table 10.4. However, there was a very low fracture energy (33 $J/m^2$) from the experimental data. This value did not result in unreasonably low load prediction, but there were some difficulties in running the model. This also showed that

this fracture energy value was not sensible for this model, therefore more investigations into the very low fracture energies from the high rate results are needed.

Table 10.4: High rate TDCB model - Si 2 wt% results predictions table

| Exp $G_c$ ($J/m^2$) | Predicted load (N) |
|---|---|
| 499 | 347 |
| 102 | 160 |
| 33 | 90 |

Si 5 wt%

The predicted load were all higher than 2 wt% in the 5 wt% wt silica modified epoxy model, but they were still reasonable, see Table 10.5. The increase in the wt% of silica particles showed a more notable improvement in fracture properties under brittle failure (at high rate). The largest load was found at the end point where the joint finally fractured and was opened completely. This was similar to other joint models built using Abaqus; often the further the crack travels, the larger the force and displacement which is needed for breaking the joint.

Table 10.5: High rate TDCB model - Si 5 wt% results predictions table

| Exp $G_c$ ($J/m^2$) | Predicted load (N) |
|---|---|
| 173 | 250 |
| 822 | 451 |
| 730 | 490 |

Si 10 wt%

Similar fracture energy values were found for the 10 wt% silica modified epoxy specimens when compared to the 5 wt% silica, except for one low fracture energy point, see Table 10.6, which could be an outlier. The predictions showed similar load values, the highest load for the 10 wt% of silica was slightly higher than for the 5 wt% silica. The 10 wt% silica specimens were found to have similar toughening effect as the 5 wt% silica modified epoxy under high rate brittle failure.

Table 10.6: High rate TDCB model - Si 10 wt% results predictions table

| Exp $G_c$ ($J/m^2$) | Predicted load (N) |
|---|---|
| 29 | 71 |
| 110 | 176 |
| 452 | 499 |
| 786 | 499 |

CSR 2 wt%

There was a very large fracture energy value (973 $J/m^2$) measured for the epoxy with CSR 2 wt% at the end of the crack. This resulted in errors in the modelling run, hence this value was out of the range of the cohesive zone properties set. This model showed that this experimental result might have been affected by the dynamic effects from high rate testing and hence was not accurate.

Table 10.7: High rate TDCB model - CSR 2 wt% results predictions table

| Exp $G_c$ ($J/m^2$) | Predicted load (N) |
|---|---|
| 112 | 177 |
| 182 | 280 |
| 973 | Did not work |

CSR 5 wt%

A relatively large fracture energy (644 $J/m^2$) was found in CSR 5 wt% experimental results, but this did not caused any problems in the predicted load, it was therefore still in the range of values possible for this cohesive zone properties. A higher load prediction was found (440N) from this point of crack, this load value was high but was reasonable for high rate fracture even it is a lot lower than experimental load, this result suggested the reasonable load without dynamic effect.

Table 10.8: High rate TDCB model - CSR 5 wt% results predictions table

| G ($J/m^2$) | predictions |
|---|---|
| 328 | 310 |
| 644 | 440 |
| 391 | 340 |

CSR 10 wt%

Two smaller fracture energy values were also found in CSR 10 wt% specimen, predictions did not show very small values, but the highest load value was lower than results found in silica, see Table 10.9. A large improvement in the fracture energy from the use of high wt% of CSR under high test rate test was not found.

Table 10.9: High rate TDCB model - CSR 10 wt% results predictions table

| Exp $G_c$ ($J/m^2$) | Predicted load (N) |
|---|---|
| 22 | 77 |
| 56 | 160 |
| 228 | 260 |
| 413 | 353 |

#### 10.2.4.1 High rate TDCB conclusion

Due to the limitations of high rate testing, very few data points were recorded. Therefore, predictions that can be made were very limited. In the future, these load predictions can be used for finding out the fracture energy in high rate without variations from experiments, such as dynamic effects. There were no stick-slips in the model, therefore only propagation values were used for the input values. This can causes differences in predicted values, as the epoxy used was brittle. The stick-slips from experimental values also make fracture energies not comparable. Hence, the predicted load results can only provide an expected range of load values and indicate whether dynamic effect is significant.

### 10.2.5 The relationship between fracture energy and displacement

The different displacements from the model (displacements measured from y direction) found in all the results were included and compared in this section, see Figure 10.7 and Table 10.10. There was a larger displacement when the fracture energy increased, most of the increase was steady and stable, but there is no relationship can be found.

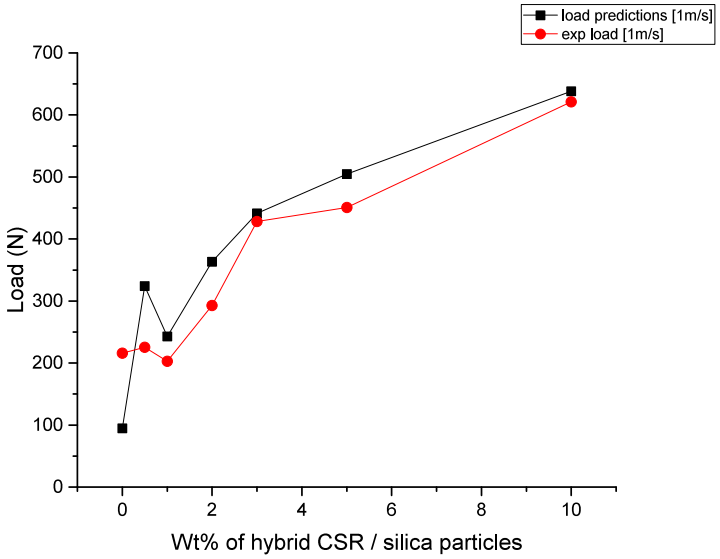


Figure 10.7: High rate (1 m/s) hybrid silica / CSR modified epoxy load predictions graph

Table 10.10: Table showing the corresponding displacement of the fracture energies used

| Fracture energy,G, ($J/m^2$) | Displacement (mm) |
|---|---|
| 33 | 4 |
| 56 | 8.7 |
| 76 | 6.4 |
| 102 | 7.7 |
| 113 | 9 |
| 121 | 9.8 |
| 123 | 9 |
| 129 | 8.7 |
| 130 | 9.6 |
| 141 | 8.8 |
| 179 | 9.8 |
| 218 | 12.6 |
| 500 | 24.7 |

## 10.3 Finite element analysis of SENB

### 10.3.1 SENB model

An FE study of the single edge notch bend model (SENB) was performed to compare the predicted fracture load with the experimental results. The same geometry of SENB specimen as used in the experiments was modelled, with a notch and three steel rollers: two rollers as supports and the centre roller moving towards the specimen (see Figure 10.8). The three steel rollers were in contact with the specimen with hard contact, so there would not be an impact and the centre roller would move down with the specimen. The material properties of the epoxy used were the same as in the TDCB model (see Section 10.2.2). Standard steel properties (modulus of 200GPa and Poisson's ratio of 0.3) were used from the literature [34]. A zero thickness cohesive layer was used in the centre of specimen to demonstrate the cohesive behaviour. Due to the properties of this cohesive layer, no initial crack is needed to be inserted. A cohesive zone of 6 mm in length (with zero thickness) was used. A tie was put in between the cohesive layer and the rest of the specimen to ensure a good level of contact. The centre part of the specimen is partitioned into 3 regular shapes for better mesh properties (see

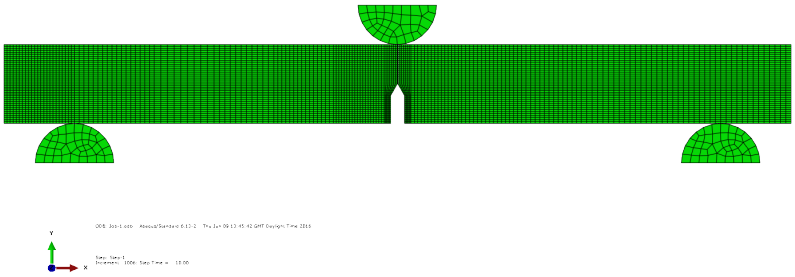

Figure 10.8: SENB finite element mesh

Figure 10.9), and this partition extended to the rest of the specimen to provide the same pattern of mesh throughout the model. A very fine structural mesh was used in the centre region of the specimen and the mesh number gradually reduced along the sides of the specimen. A free mesh was used in the steel rollers as they were circular and their properties were not of interest in this study.

The force was applied as a rate of 10 mm/min, which is the same as in experiments. A small amount of friction was added between the rollers and the specimen, as the specimen was sliding and flying off from the setup when no friction was used.
The boundary conditions were (see Figure 10.9 below):

1. Centre roller: no movement in x and z directions. Displacement is set as a rate in the y direction.

2. Left and right rollers: no movement for all directions.

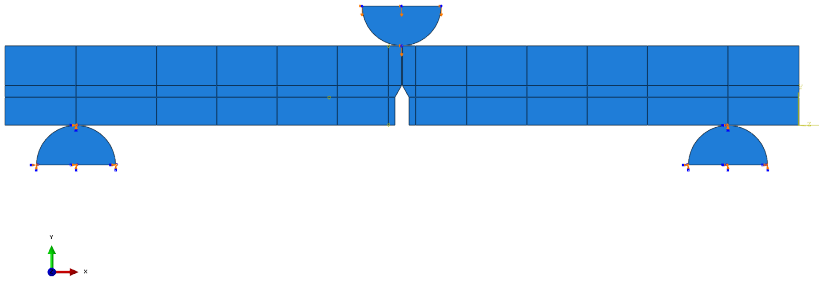

Figure 10.9: SENB mesh partitions and boundary conditions for finite element analysis

The amount of friction used was changed slightly according to the different conditions (from 0.3 to 0.7), in order to prevent excess bending of the specimen, as too much friction gave excessive bending.

Figure 10.10 below shows fracture of SENB specimen, the stress was not high overall but was highly concentrated at the crack tip as expected because the energy dissipation during fracture is confined to the plastic zone. (Rigid body conditions were used in the rollers.)

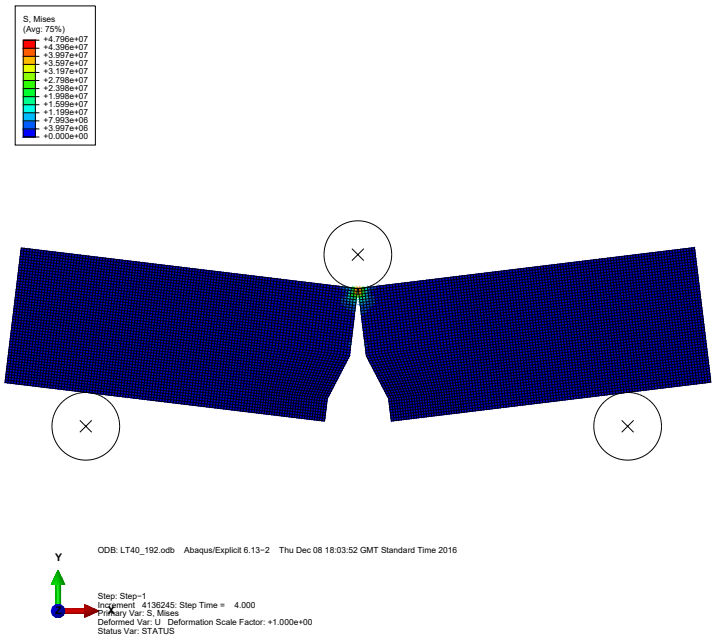


Figure 10.10: Fracture of SENB specimen

The fracture energy values input into the cohesive zone model were taken from the SENB experimental results. Tables 10.11 to 10.17 show the fracture energy values used for the modelling work.

Table 10.11: Fracture energy of modified epoxy from SENB tests at quasi-static test rate (Unmodified epoxy has been done every time when particles used were different)

| particles | Silica | | CSR | | Hybrid | |
|---|---|---|---|---|---|---|
| Wt % of particles | G ($J/m^2$) | SD | G ($J/m^2$) | SD | G ($J/m^2$) | SD |
| 0 | 68 | 21 | 68 | 21 | 63 | 11 |
| 0.5 | 83 | 46 | 96 | 1 | 62 | 4 |
| 1 | 99 | 73 | 96 | 34 | 72 | 44 |
| 2 | 117 | 35 | 93 | 9 | 80 | 14 |
| 3 | 125 | 40 | 92 | 36 | 89 | 11 |
| 5 | 131 | 28 | 91 | 41 | 97 | 19 |
| 10 | 169 | 54 | 108 | 40 | 166 | 49 |
| 15 | 220 | 47 | | | | |
| 20 | 211 | 73 | | | | |
| 25.4 | 223 | 67 | | | | |

Table 10.12: Fracture energy of silica-modified epoxy at different test rates

| Rate | quasi-static | | 0.1 m/s | | 1 m/s | |
|---|---|---|---|---|---|---|
| Wt% of Silica particles | G ($J/m^2$) | SD | G ($J/m^2$) | SD | G ($J/m^2$) | SD |
| 0 | 68 | 21 | 10 | 0 | 101 | 105 |
| 0.5 | 83 | 46 | 27 | 17 | 130 | 80 |
| 1 | 99 | 73 | 35 | 25 | 150 | 83 |
| 2 | 117 | 35 | 46 | 26 | 247 | 95 |
| 3 | 125 | 40 | 81 | 80 | 311 | 29 |
| 5 | 131 | 28 | 150 | 30 | 460 | 91 |
| 10 | 169 | 54 | 145 | 30 | 803 | 181 |
| 15 | 220 | 47 | 175 | 80 | 951 | 168 |
| 20 | 211 | 73 | 284 | 60 | 833 | 65 |
| 25.4 | 223 | 67 | 279 | 50 | 730 | 105 |

Table 10.13: Fracture energy of CSR-modified epoxy from SENB tests at different test rates

| Rate | quasi-static | | 0.1 m/s | | 1 m/s | |
|---|---|---|---|---|---|---|
| Wt % of CSR particles | G (J/m$^2$) | SD | G (J/m$^2$) | SD | G (J/m$^2$) | SD |
| 0 | 68 | 21 | 13 | 2 | 67 | 21 |
| 0.5 | 96 | 1 | 257 | 94 | 576 | 21 |
| 1 | 96 | 34 | 401 | 100 | 685 | 46 |
| 2 | 93 | 9 | 602 | 188 | 862 | 206 |
| 3 | 92 | 36 | 638 | 150 | 912 | 123 |
| 5 | 91 | 41 | 720 | 90 | 1972 | 380 |
| 10 | 108 | 40 | 852 | 90 | 5883 | 1500 |

Table 10.14: Fracture energy of hybrid-modified epoxy from SENB tests at different test rates

| Rate | quasi-static | | 0.1m/s | | 1m/s | |
|---|---|---|---|---|---|---|
| Wt % of hybrid particles | G (J/m$^2$) | SD | G (J/m$^2$) | SD | G (J/m$^2$) | SD |
| 0 | 63 | 11 | 13 | 4 | 67 | 21 |
| 0.5 | 62 | 4 | 91 | 5 | 1096 | 239 |
| 1 | 72 | 44 | 664 | 170 | 1392 | 573 |
| 2 | 80 | 14 | 977 | 436 | 3146 | 515 |
| 3 | 89 | 11 | 977 | 477 | 4409 | 2239 |
| 5 | 97 | 19 | 1054 | 653 | 5757 | 1038 |
| 10 | 166 | 49 | 2428 | 760 | 8918 | 847 |

Table 10.15: Fracture energy of silica modified epoxy from SENB tests at low temperature

| Temperature | Room temperature (20°C) | | -40°C | | -80 °C | |
|---|---|---|---|---|---|---|
| % of Si particles | G (J/m$^2$) | SD | G (J/m$^2$) | SD | G (J/m$^2$) | SD |
| 0 | 68 | 21 | 93 | 9 | 126 | 15 |
| 0.5 | 83 | 46 | 101 | 30 | 130 | 0 |
| 1 | 99 | 73 | 112 | 0 | 158 | 2 |
| 2 | 117 | 35 | 117 | 14 | 161 | 16 |
| 3 | 125 | 40 | 132 | 0 | 179 | 2 |
| 5 | 131 | 28 | 132 | 15 | 213 | 30 |
| 10 | 169 | 54 | 144 | 6 | 305 | 9 |
| 15 | 220 | 47 | 192 | 18 | 312 | 12 |
| 20 | 211 | 73 | 197 | 27 | 332 | 6 |
| 25.4 | 223 | 67 | 200 | 17 | 349 | 19 |

Table 10.16: Fracture energy of CSR modified epoxy from SENB tests at low temperature

| Temperature | Room temperature (20°C) | | -40°C | | -80 °C | |
|---|---|---|---|---|---|---|
| % of CSR particles | G (J/m$^2$) | SD | G (J/m$^2$) | SD | G (J/m$^2$) | SD |
| 0 | 68 | 21 | 93 | 9 | 126 | 15 |
| 0.5 | 96 | 1 | 140 | 37 | 141 | 8 |
| 1 | 96 | 34 | 120 | 24 | 148 | 9 |
| 2 | 93 | 9 | 154 | 15 | 150 | 18 |
| 3 | 92 | 36 | 110 | 15 | 155 | 15 |
| 5 | 91 | 41 | 126 | 7 | 163 | 18 |
| 10 | 108 | 40 | 131 | 12 | 188 | 16 |

Table 10.17: Fracture energy of CSR / silica hybrid modified epoxy from SENB tests at low temperature

| Temperature | Room temperature (20 °C) | | -40 °C | | -80 °C | |
|---|---|---|---|---|---|---|
| % of Hybrid particles | G ($J/m^2$) | SD | G ($J/m^2$) | SD | G ($J/m^2$) | SD |
| 0 | 63 | 11 | 93 | 9 | 126 | 15 |
| 0.5 | 62 | 4 | 98 | 14 | 130 | 12 |
| 1 | 72 | 44 | 97 | 29 | 134 | 13 |
| 2 | 80 | 14 | 105 | 8 | 134 | 19 |
| 3 | 89 | 11 | 107 | 4 | 136 | 6 |
| 5 | 97 | 19 | 117 | 5 | 138 | 16 |
| 10 | 166 | 50 | 169 | 6 | 192 | 17 |

### 10.3.2 SENB model results

In the FE model of the SENB tests, the load against displacement results were obtained from the contact load as the central roller, as this would provide more accurate results than the reaction force. The highest loads from experiment were used as the experimental load in the tables. The failure behaviour was similar when compared to the experiments, as unstable crack growth was found. The crack growth rate was similar when compared to the TDCB model, as the same materials were used. The crack rate was constant but there was a hinge at the end of the test where the specimen does not break fully but a small ligament of epoxy remains, which can also occur in experiments. The predicted failures were as expected, and the highest load values were within the normal range. The low temperature and high rate SENB predictions are included in the following Section but the quasi-static results are discussed first.

#### 10.3.2.1 Silica-modified epoxy

The highest load (109N) in silica predictions lied in 15 wt% of silica, but it was only 1 N different from the load of the highest wt%. The load value (107 N) of the highest wt% of silica (25.4 wt%) was almost the same as the highest load value in the experiment (110 N), see Figure 10.11. There was only a very small increase with wt% of a silica in the load in the model prediction, the unmodified epoxy gave a load of 92 N, and the load values were between 94 to 103 N, from silica 0.5 wt% to silica 20 wt%. While in the experiments, there was a noticeable increase of the highest load when the wt% of

particles increased. The higher the wt% of silica used, the higher the load value that was measured in the SENB experiments, see Table 10.18.
However, the SENB highest load value can be very different for each specimen as it is highly affected by the crack length at the notch. The crack length at the notch is not used in the model, as with the use of cohesive zone, a pre-defined crack is not required. This could cause some differences in the experimental values and the prediction values. This could be due to the fracture energy values input into Abaqus, as the fracture energy values were not increasing for all increases in wt%, see Table 10.18.

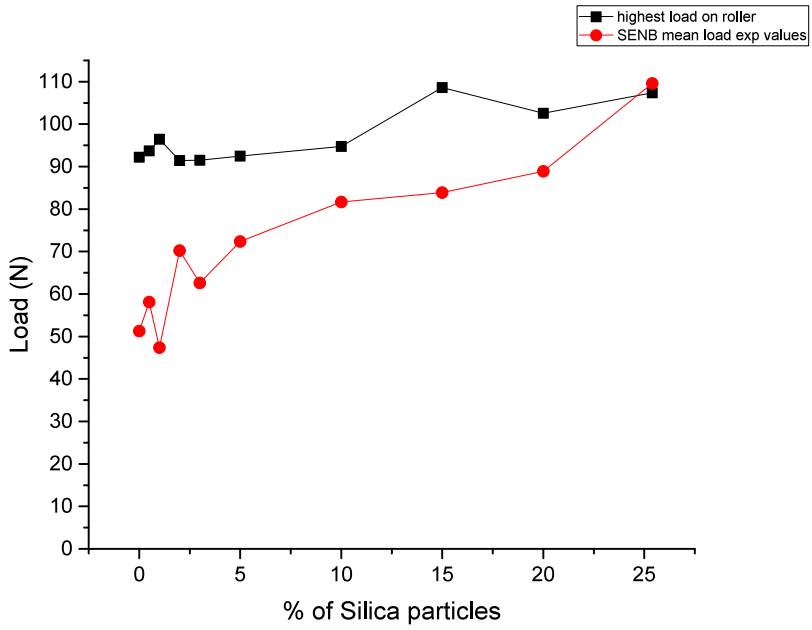


Figure 10.11: SENB silica load predictions graph

Table 10.18: SENB silica load predictions table

| particles | Silica | Silica |
|---|---|---|
| Wt% of particles | Predicted Load (N) | Experimental Load (N) |
| 0 | 92 | 51.3 |
| 0.5 | 94 | 58.1 |
| 1 | 96 | 47.4 |
| 2 | 91 | 70.2 |
| 3 | 91 | 62.6 |
| 5 | 93 | 72.4 |
| 10 | 95 | 81.7 |
| 15 | 109 | 83.9 |
| 20 | 103 | 88.9 |
| 25.4 | 107 | 109.6 |

#### 10.3.2.2 CSR-modified epoxy

A similar situation when compared to the silica modified specimens was found for the CSR-modifed epoxy SENB results, see Figure 10.12. All the prediction values were found to be higher than the experimental values, most of the predicted values being around 90 N, see Table 10.19. The predicted values fluctuated less than in the experiments, results were stable along all wt% of CSR. Most of the experimental load values were around 50 N, which were lower than expected, therefore the prediction provided the highest load that the CSR-modified specimens can actually achieve. All the predicted values were between 89 to 93 N. The highest wt% possible was 10wt% but the highest load prediction was at CSR 3 wt% and CSR 5 wt%. The differences with the different wt% were very small with a slight increase at the high wt% of CSR used. The optimal wt% was in the medium wt% used, which agreed well with the experimental findings. However, it was not reasonable for CSR 2 wt% to have a slightly lower load value when compared to the unmodified epoxy specimens, but the difference was too small (3 N) to be significant. This could be due to the differences in crack length that affects the highest load values in the experiments.

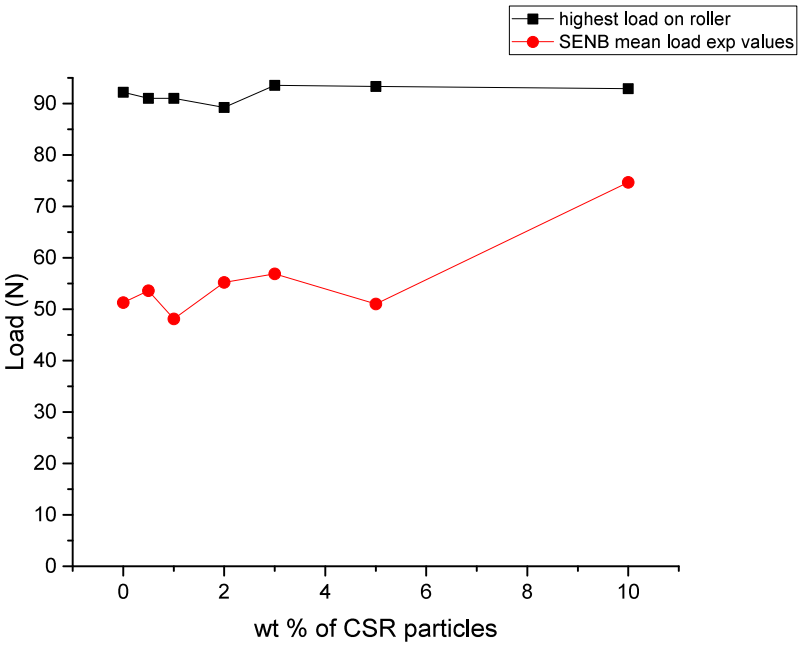


Figure 10.12: SENB CSR load predictions graph

Table 10.19: SENB CSR load predictions table

| particles | CSR | CSR |
|---|---|---|
| Wt% of particles | Predicted Load (N) | Experimental Load (N) |
| 0 | 92 | 51 |
| 0.5 | 91 | 52 |
| 1 | 91 | 48 |
| 2 | 89 | 55 |
| 3 | 94 | 57 |
| 5 | 93 | 51 |
| 10 | 93 | 75 |

#### 10.3.2.3 Hybrid (silica / CSR) modified epoxy

The hybrid of CSR and silica produced slightly higher overall predictions than the CSR modified epoxy. The model showed that the increases in the hybrid wt% do not produce an improvement in the fracture properties, see Figure 10.13. The highest load values of the 1 to 5 wt% hybrid modified epoxies were all 93 N, see Table 10.20. The highest load (101 N) was with the highest wt% of hybrid particles of 10 wt%, but the increase of load was not large. The results of using the different wt% were very stable. The fracture properties were also overestimated when compared to the experimental results. It was observed from SEM imaging that there was presence of uneven mixed area, especially when a high wt% of particles were used, as there were both type of particles present at a relatively high wt%, some degree of uneven mixture was not avoidable. However, a significantly higher fracture energy (166 $J/m^2$) was found in the 10 wt% hybrid from experimental results. It was 70 $J/m^2$ higher than the hybrid 5 wt%. With this much higher fracture energy input, the resultant load was only 7 N higher. This showed that the effect of fracture energy in the model was not very significant, and that the prediction results could be more affected the other inputs.

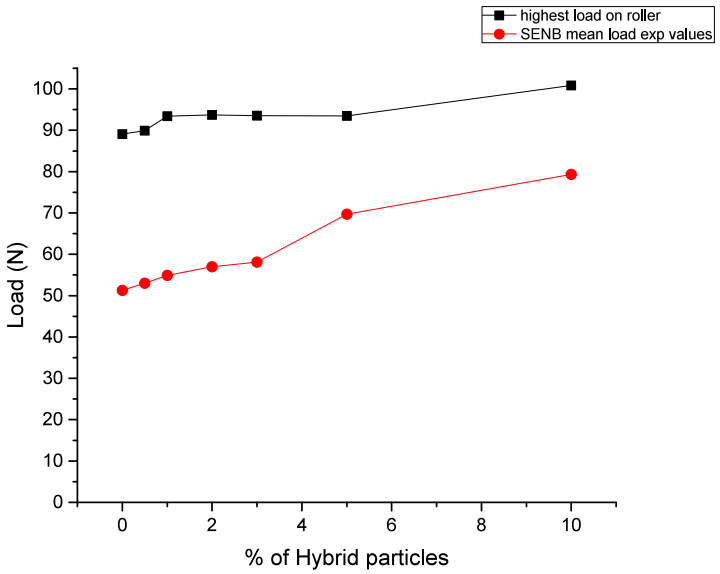


Figure 10.13: SENB (silica / CSR) hybrid-modified epoxy load predictions graph

Table 10.20: SENB silica / CSR hybrid load predictions table

| particles | Hybrid silica / CSR | Hybrid silica / CSR |
|---|---|---|
| Wt% of particles | Predicted Load (N) | Experimental Load (N) |
| 0 | 89 | 51 |
| 0.5 | 90 | 53 |
| 1 | 93 | 55 |
| 2 | 94 | 57 |
| 3 | 94 | 58 |
| 5 | 93 | 70 |
| 10 | 101 | 79 |

#### 10.3.2.4 Ceramic microsphere-modified epoxy

For the SENB model of the ceramic microsphere-modified epoxy, the highest load was with the use of 5 wt% of ceramic microsphere, which had a prediction of a 100% higher load than measured in experiments, see Figure 10.14. All the results had similar values, see Table 10.21. The highest fracture energy was found in ceramic microsphere 10 wt%, as well as the highest load. This finding was the same as in the CSR-modified epoxy, as the medium amount of particles used produced the optimal predicted load.

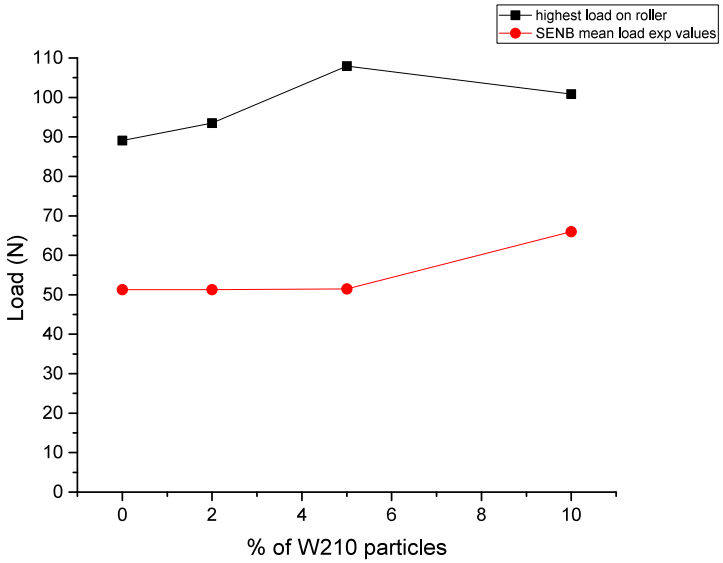


Figure 10.14: SENB ceramic microsphere load predictions graph

Table 10.21: SENB ceramic microsphere load predictions table

| particles | Ceramic microspheres | Ceramic microspheres |
|---|---|---|
| Wt% of particles | Predicted Load (N) | Experimental Load (N) |
| 0 | 89 | 51 |
| 2 | 94 | 51 |
| 5 | 108 | 52 |
| 10 | 101 | 66 |

#### 10.3.2.5 Hybrid CSR / ceramic microsphere-modified epoxy

The use of the hybrid CSR / ceramic microsphere modified epoxy did not produce an increase in results compared to the CSR or ceramic microsphere modified epoxy, see Figure 10.15. The predicted results were almost the same among the different wt%, they were in between 91 to 94 N, see Table 10.22. This was not expected, as the fracture energies inputs were very different for 5 wt% and 10 wt%, the results were not sensible as there were a larger differences in experimental load and this does not deflect in the predicted load. This could be due to the insensitivity in load measurements in the model. This shows that the model responses more to the change in quads damage,

damage evolution (fracture energy) and elastic.

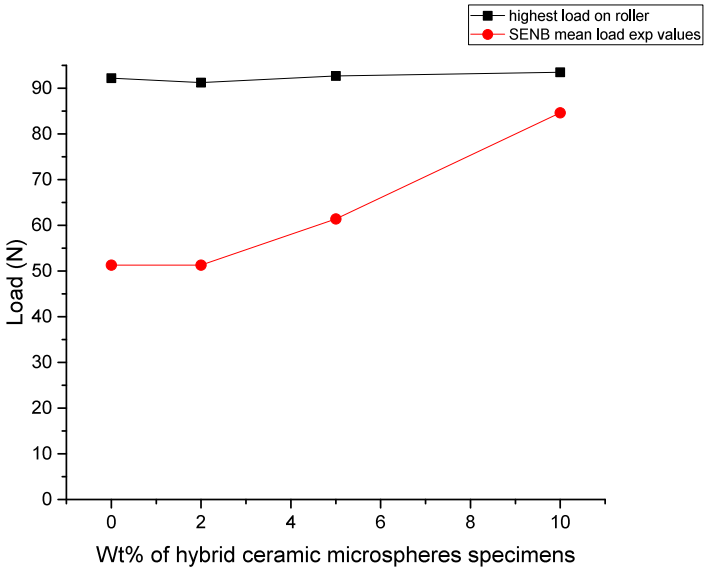


Figure 10.15: SENB CSR / ceramic microsphere hybrid specimens load predictions graph

Table 10.22: SENB ceramic microsphere specimens load predictions table

| particles | Hybrid CSR / ceramic microspheres | Hybrid CSR / ceramic microspheres |
|---|---|---|
| Wt% of particles | Predicted Load (N) | Experimental Load (N) |
| 0 | 92 | 51 |
| 2 | 91 | 51 |
| 5 | 93 | 61 |
| 10 | 94 | 85 |

#### 10.3.2.6 PES-modified epoxy

Very similar range of result values were found in PES predictions when compare to ceramic microsphere specimens, in between 89 to 94 N, see Figure 10.16 and Table 10.23. The values were too similar, so toughening effect was not found.

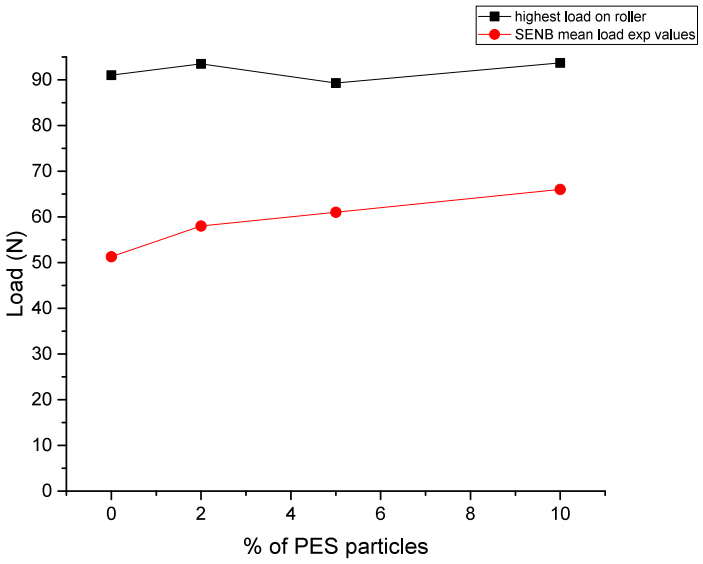


Figure 10.16: SENB PES specimens load predictions graph

Table 10.23: SENB PES specimens load predictions table

| particles | PES | PES |
|---|---|---|
| Wt% of particles | Predicted Load (N) | Experimental Load (N) |
| 0 | 91 | 51 |
| 2 | 94 | 58 |
| 5 | 89 | 61 |
| 10 | 94 | 66 |

#### 10.3.2.7 Hybrid PES / silica modified epoxy

Hybrid PES / silica specimens had similar result values as in PES, see Figure 10.17, this could be due to the similar fracture energies input from experimental results, see Table 10.24. This showed that the use of silica and PES particles did not produce an improvement in fracture energy. All the predicted loads were higher than experimental load, it shows the same pattern as found in ceramic microsphere specimens. The experimental loads were similar for all wt%, hence the predicted loads were similar.

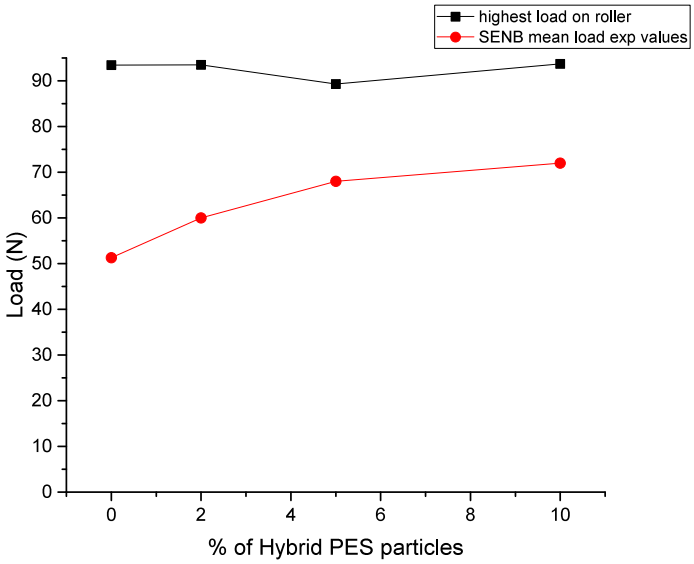


Figure 10.17: SENB PES / silica hybrid specimens load predictions graph

Table 10.24: SENB PES / silica hybrid specimens load predictions table

| particles | Hybrid PES | Hybrid PES |
|---|---|---|
| % of particles | Predicted Load (N) | Experimental Load (N) |
| 0 | 91 | 51 |
| 2 | 94 | 58 |
| 5 | 89 | 61 |
| 10 | 94 | 66 |

#### 10.3.2.8 SENB model results conclusion

The use of SENB model provided some predictions of SENB tested under different conditions, this is more useful in brittle testing conditions, such as low temperature and high rate, as the results predicted were not affected by dynamic factors or unstable temperature. However, by comparing predicted load with experimental load, predicted loads were systemic with very small changes when experimental load is different. It shows that using load as an comparison is not representative in SENB model. This shows that the model responses more to the change in quads damage, damage evolution (fracture energy) and elastic.

### 10.3.3 Low temperature SENB

#### 10.3.3.1 Silica-modified epoxy at $-40^oC$

Figure 10.18 shows the low temperature ($-40^oC$) silica modified epoxy load predictions and Table 10.25 shows their predicted values. There was a stable increase in the highest load when the wt% of silica particles increased except for 0.5 wt% silica. This seems to be an outlier, which was not be representative. The changes in load values were significantly smaller than in the experiments. The highest load was at 25.4 wt% silica, the highest point was with the same wt% and of the same value as in experiment. The range of predicted load values was between 91 to 108 N. The load values were very similar when the silica wt% was low, a larger fracture improvement was seen from 15 wt%. This agreed with previous findings from the group, that around 15 wt% of silica produced the maximum amount of debonding and hence the greatest failure load and fracture energy.

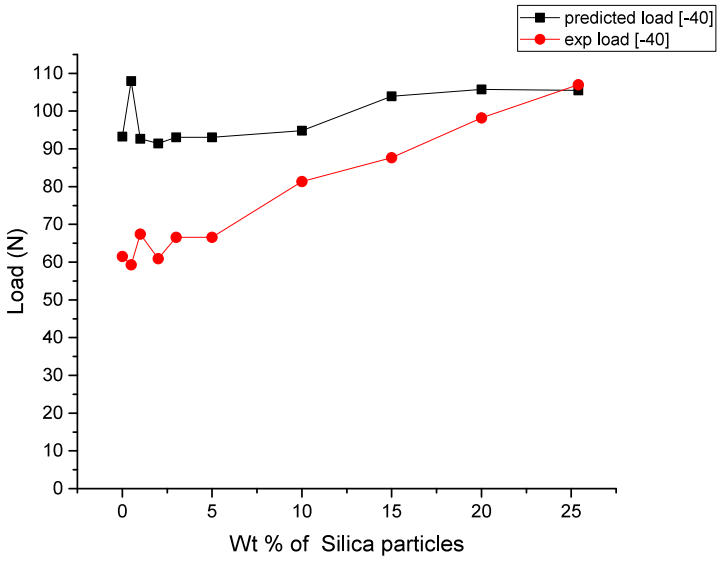


Figure 10.18: Low temperature ($-40^oC$) silica modified epoxy load predictions graph

Table 10.25: Low temperature ($-40^oC$) silica modified epoxy load predictions table

| % of silica | Predicted load (-40°C) (N) | exp load (-40°C) (N) |
|---|---|---|
| 0 | 93 | 62 |
| 0.5 | 108 | 59 |
| 1 | 93 | 67 |
| 2 | 91 | 61 |
| 3 | 93 | 67 |
| 5 | 93 | 67 |
| 10 | 95 | 81 |
| 15 | 104 | 88 |
| 20 | 106 | 98 |
| 25.4 | 105 | 107 |

#### 10.3.3.2 Silica-modified epoxy at $-80^oC$

Figure 10.19 shows the low temperature ($-80^oC$) silica modified epoxy load predictions from the SENB model, and Table 10.26 shows their predicted values. There was a significantly higher highest load in -$80^oC$ prediction results. The highest point was also at max wt%, while there was a notable drop in experimental result. This could be due to the uneven mixing with highest possible % of silica, as the SENB specimens are very small, the three specimens used here could be at the very imbalanced agglomerated region (as particles were found only in some regions in SEM images). There was a steady increase the in predicted load when the wt% of silica increased. The load results from 2 wt% to 5 wt% silica were almost the same, while there was a 20 N increase for 10 wt% silica, the increase remained comparatively small after this. All the predicted values were higher than the experimental values, but the difference was smaller than in room temperature SENB. There was about a 20 N difference for all wt% of silica, this difference was similar for all wt%. The small rise and drop points along the wt% of predictions had the same pattern as the experimental load graph. The pattern of prediction results agreed well with the experimental results.

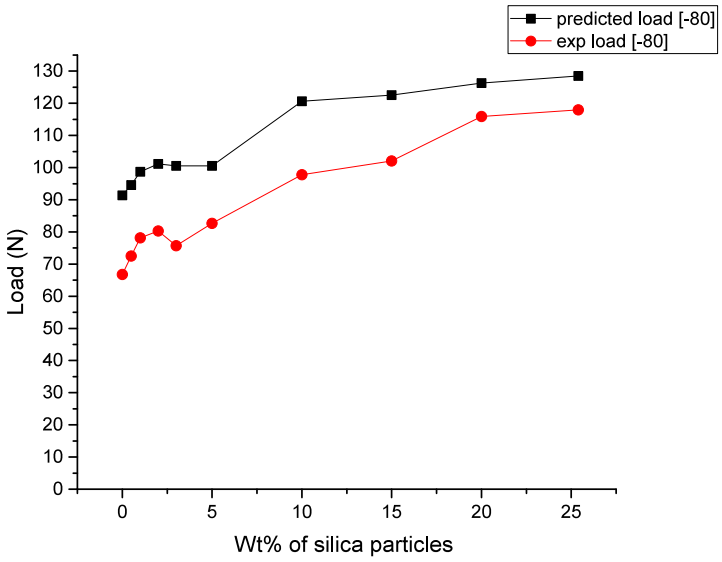


Figure 10.19: Low temperature ($-80^oC$) SENB silica-modified epoxy load predictions graph

Table 10.26: Low temperature ($-80^oC$) silica modified epoxy load predictions table

| % of silica | predicted load [-80°C] (N) | exp load [-80°C] (N) |
|---|---|---|
| 0 | 91 | 67 |
| 0.5 | 95 | 73 |
| 1 | 99 | 78 |
| 2 | 101 | 80 |
| 3 | 101 | 76 |
| 5 | 101 | 83 |
| 10 | 121 | 98 |
| 15 | 123 | 102 |
| 20 | 126 | 116 |
| 25.4 | 129 | 118 |

#### 10.3.3.3 CSR-modified epoxy at $-40^oC$

For the SENB model, figure 10.20 shows the low temperature ($-40^oC$) CSR-modified epoxy load predictions, and Table 10.27 shows the predicted values. There was no very clear pattern in the trend of the results. The predicted values were similar (all around 90 N), the values increased slightly with increasing wt% and then followed by slightly reduced values throughout the whole graph. The highest point was at 2 wt% CSR and the lowest force was at 5 wt% CSR. It was also noted that the higher load from experiments resulted in more accurate predictions (so the predictions were closer to the experimental values). The ratio of difference between the predicted and the experimental results were not the same among all wt%, however, it was the fracture energy that was the input, where only the load was compared. The fracture energies input were up and down across the wt%, hence resulting in ups and downs in the predicted and experimental load values. Other than that, no very clear pattern can be found within the relationship of fracture energy to predicted load. The range of predicted load was within 91 to 100 N.

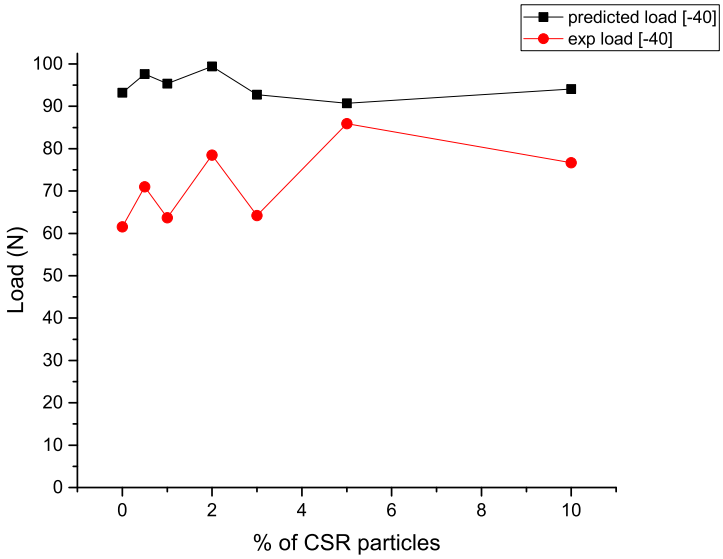


Figure 10.20: Low temperature ($-40^oC$) SENB CSR modified epoxy load predictions graph

Table 10.27: Low temperature ($-40^oC$) SENB CSR modified epoxy load predictions table

| % of CSR | predicted load [-40°C] (N) | exp load [-40°C] (N) |
|---|---|---|
| 0 | 93 | 62 |
| 0.5 | 98 | 71 |
| 1 | 95 | 64 |
| 2 | 100 | 79 |
| 3 | 93 | 64 |
| 5 | 91 | 86 |
| 10 | 94 | 77 |

#### 10.3.3.4 CSR-modified epoxy at $-80^oC$

Figure 10.21 shows the load predictions for the low temperature ($-80^oC$) CSR-modified epoxy from the SENB model, and Table 10.28 shows their predicted values. There is a general increase in the load when wt% of CSR particles increases, but the differences were small in both the experimental results and the predictions. The predictions were according to experimental results.

The predicted load values range from 96 to 102 N, which was a very small increase among the -80$^oC$ SENB specimens. The highest load was found at 10 wt% CSR, see Table 10.28. There was the same graph pattern in between the two results, but the predicted load had a very stable graph when compare. The overall -80$^oC$ results were higher than at -40$^oC$ for CSR, but the change was not as significant as in the other results.

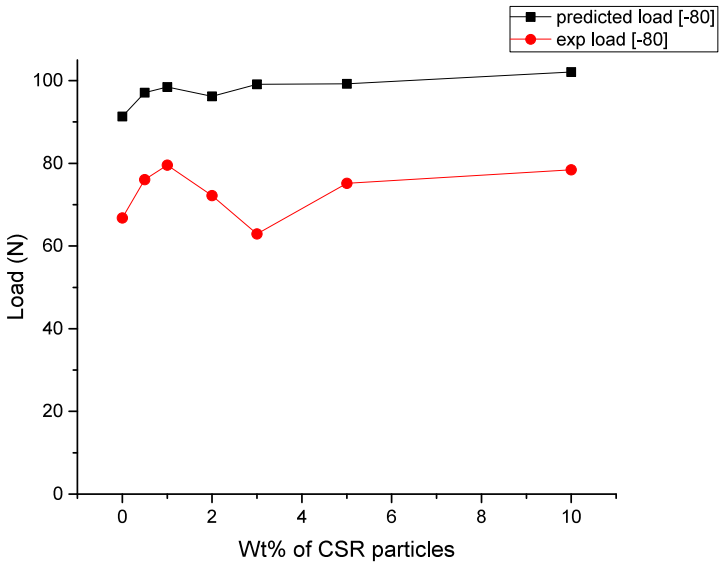


Figure 10.21: Low temperature ($-80^oC$) SENB CSR modified epoxy load predictions graph

Table 10.28: Low temperature ($-80^oC$) SENB CSR modified epoxy load predictions table

| % of CSR | predicted load [-80] | exp load [-80] |
|---|---|---|
| 0 | 91 | 67 |
| 0.5 | 97 | 76 |
| 1 | 99 | 80 |
| 2 | 96 | 72 |
| 3 | 99 | 63 |
| 5 | 99 | 75 |
| 10 | 102 | 78 |

#### 10.3.3.5 Hybrid (silica / CSR) modified epoxy at $-40^oC$

Figure 10.22 shows the low temperature ($-40^oC$) silica / CSR-hybrid modified epoxy load predictions from the SENB model and Table 10.29 shows the prediction values. The same pattern of graphs was found here as well, compared to the room temperature data. The range of the predicted load was from 91.6 to 99.9 N, all within 90 to 100N. This was the same as in most of the results. The highest load was for the 10 wt% hybrid,

which was the highest wt% used, which was the same as in experimental results. There was a sudden increase of the predicted load for the 2 wt% hybrid but not as great as at the maximum %. It seems that when the materials were under brittle failure, such as at low temperature, the high wt% specimens often resulted in a higher failure load.

The increased in fracture energy produced a very small increase in the predicted load. When there was an about 50 $J/m^2$ increase in the fracture energy, the predicted load was only increased by less than 10 N. Therefore, even small changes were produced in the predicted load results, there were more differences in between the experimental load results when compare to expected predicted load. The increase in experimental input values does not always results in a significant increase in predicted values, but this relationship agreed with the set of values found to use in this study. Only this set of cohesive zone input values work for this case, any larger changes in the input values would cause unreasonable results or problems in the model, eg. when the model cannot finish running, the joint does not breaking or large deformation of cohesive zone occurs without the joint breaking. This emphasises the importance of more understanding of the cohesive zone. In this set of results, the slightly lower wt% of hybrid particles had a slightly higher load than medium wt%, but the differences were too small to be significant.

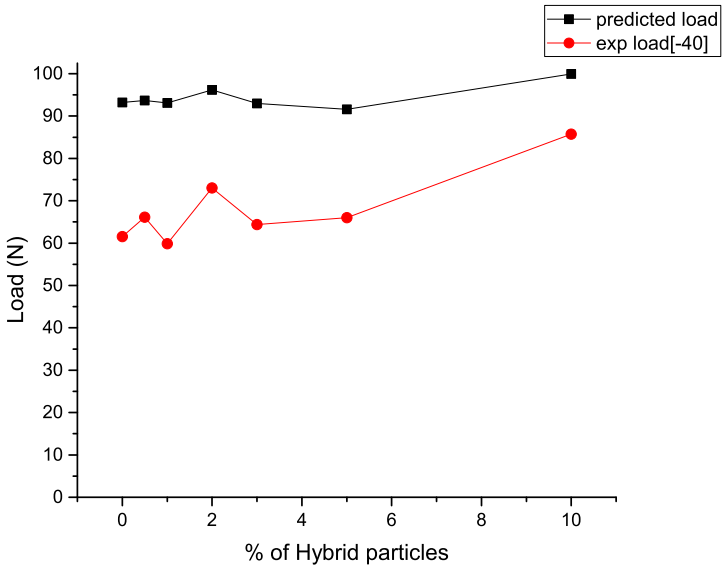


Figure 10.22: SENB low temperature ($-40^oC$) hybrid (silica / CSR) modified epoxy load predictions graph

Table 10.29: SENB low temperature ($-40^oC$) hybrid (Silica / CSR) load predictions table

| Wt% of Si / CSR hybrid | predicted load [-40°C] (N) | exp load [-40°C] (N) |
|---|---|---|
| 0 | 93 | 62 |
| 0.5 | 94 | 66 |
| 1 | 93 | 60 |
| 2 | 96 | 73 |
| 3 | 93 | 64 |
| 5 | 92 | 66 |
| 10 | 100 | 86 |

#### 10.3.3.6 Hybrid (silica / CSR) modified epoxy at $-80^oC$

Figure 10.23 shows the low temperature ($-80^oC$) silica / CSR hybrid modified epoxy load predictions, and Table 10.30 shows the predicted values. The ratio of the experimental load to the predicted load was similar here as in other cases. The load range from 91 to 104 N, which was similar to the predictions to the predictions at -40$^oC$. The highest load at the highest wt% was 104 N, a bit higher than the predicted load at -40$^oC$, but the input fracture energy was 192 $J/m^2$. The pattern of the load graphs was not the same, there was no drops in the predicted graph at -80$^oC$, while there was a sudden jump for the experimental data for the 1 wt% hybrid, but it was not reflected in the predictions. This showed the predicted load was not as accurate as fracture energies in the comparison. The fracture energies input was increasing along increase of the wt%, therefore this also explains the increasing trend of the result graphs.

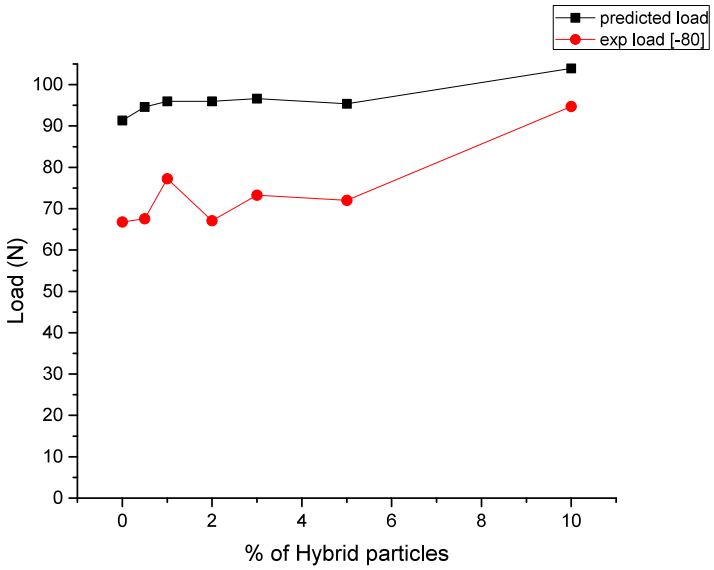


Figure 10.23: SENB low temperature ($-80^oC$) silica / CSR hybrid modified epoxy load predictions graph

Table 10.30: SENB low temperature ($-80^oC$) silica / CSR hybrid modified epoxy load predictions table

| Wt% of Si / CSR hybrid | predicted load [-80°C] (N) | exp load [-80°C] (N) |
|---|---|---|
| 0 | 91 | 67 |
| 0.5 | 95 | 68 |
| 1 | 96 | 77 |
| 2 | 96 | 67 |
| 3 | 97 | 73 |
| 5 | 95 | 72 |
| 10 | 104 | 95 |

#### 10.3.3.7 Ceramic microsphere modified epoxy at $-40^oC$

Figure 10.24 shows the low temperature ($-40^oC$) ceramic microsphere modified epoxy load predictions, and Table 10.31 shows the predicted values. The predictions showed that an increase in the wt% of ceramic microsphere particles did not provide an improvement in their fracture properties. There were similar results found in the experimental loads, see Figure 10.24, although overall fracture energies increased slightly.

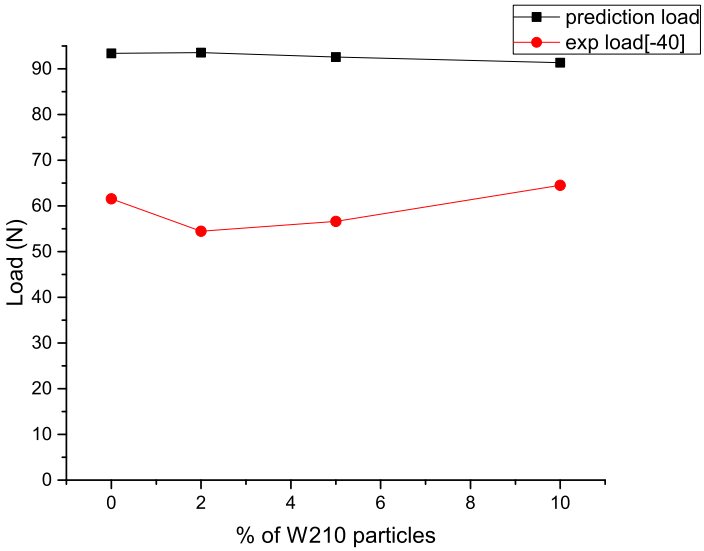


Figure 10.24: SENB low temperature ($-40^oC$) ceramic microsphere modified epoxy load predictions graph

Table 10.31: SENB low temperature ($-40^oC$) ceramic microsphere modified epoxy load predictions table

| Wt% of W210 particles | prediction load [-80°C] (N) | exp load [-80°C] (N) |
|---|---|---|
| 0 | 93 | 67 |
| 2 | 91 | 57 |
| 5 | 92 | 65 |
| 10 | 91 | 77 |

#### 10.3.3.8 Ceramic microsphere modified epoxy at $-80^oC$

Figure 10.25 shows the low temperature ($-80^oC$) ceramic microsphere modified epoxy load predictions and Table 10.32 shows the predicted values. Similar results were found for the -80$^oC$ results compared to the room temperature predictions, low temperature did not have an effect to the results.

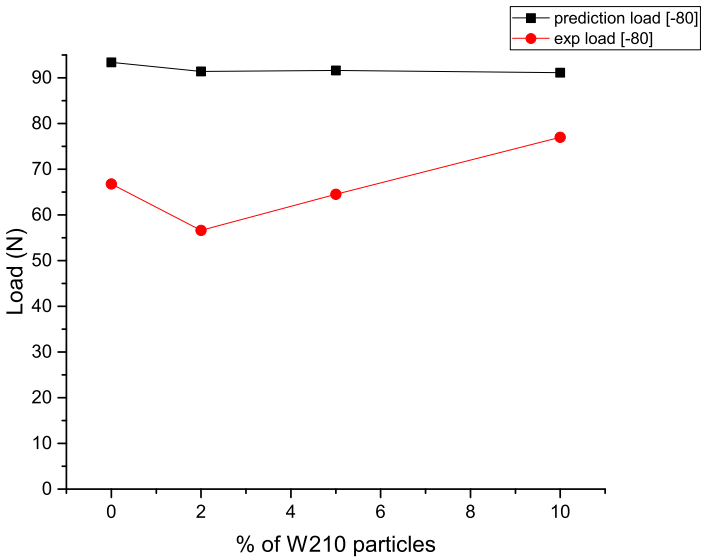


Figure 10.25: SENB low temperature ($-80^oC$) ceramic microsphere modified epoxy load predictions graph

Table 10.32: SENB low temperature ($-80^oC$) ceramic microsphere modified epoxy load predictions table

| Wt% of W210 particles | prediction load [-80°C] (N) | exp load [-80°C] (N) |
|---|---|---|
| 0 | 93 | 67 |
| 2 | 91 | 57 |
| 5 | 92 | 65 |
| 10 | 91 | 77 |

#### 10.3.3.9 Hybrid ceramic microsphere / CSR modified epoxy at $-40^oC$

The shows low temperature ($-40^oC$) hybrid ceramic microsphere / CSR modified epoxy load predictions are shown in Figure 10.26, and Table 10.33 shows the predicted values. The results were very similar to the ceramic microsphere modified epoxy predictions. It seems that the small changes in input values cannot produce big differences in the prediction results. However, the predicted load was very stable when compare to the experimental data.

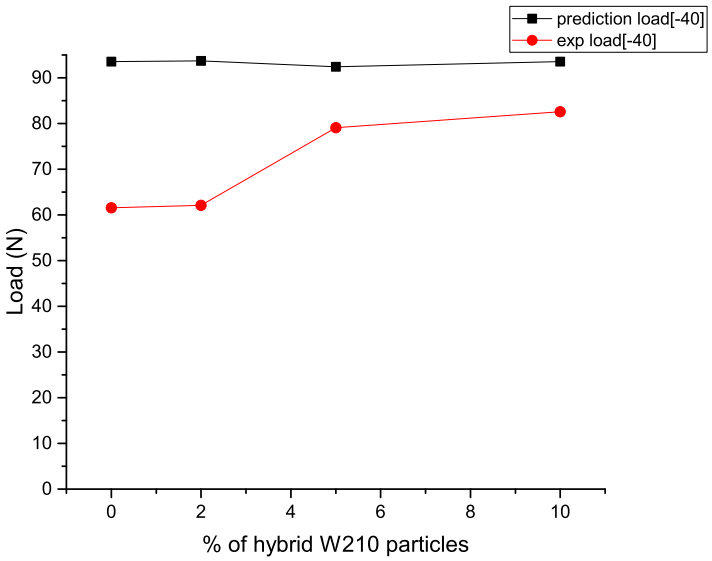


Figure 10.26: SENB low temperature ($-40^oC$) hybrid ceramic microsphere modified epoxy load predictions graph

Table 10.33: SENB low temperature ($-40^oC$) hybrid ceramic microsphere / CSR modified epoxy load predictions table

| Wt% of hybrid W210 particles | prediction load [-40°C] (N) | exp load [-40°C] (N) |
|---|---|---|
| 0 | 94 | 62 |
| 2 | 94 | 62 |
| 5 | 93 | 79 |
| 10 | 94 | 83 |

#### 10.3.3.10 Hybrid ceramic microsphere / CSR modified epoxy at $-80^oC$

Figure 10.27 shows the low temperature ($-80^oC$) ceramic microsphere / CSR hybrid modified epoxy load predictions, and Table 10.34 shows the predicted values. There were only very slight increases in the values at -80$^oC$ compared to the values at room temperature, low temperature had no effect on the predicted properties. This could be due to the similar input data from the experimental results. In the future, more low temperature tests should be performed to ensure this accurate low temperature results.

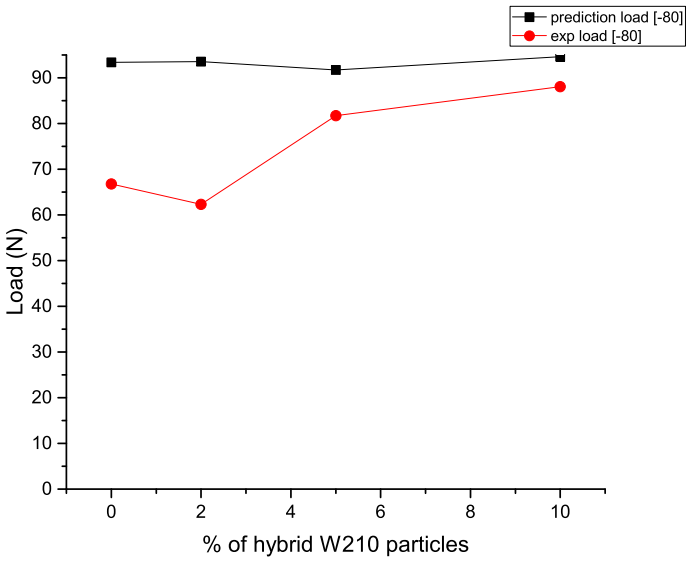


Figure 10.27: SENB low temperature ($-80^oC$) hybrid ceramic microsphere / CSR modified epoxy load predictions graph

Table 10.34: SENB low temperature ($-80^oC$) hybrid ceramic microsphere / CSR modified epoxy load predictions table

| Wt% of hybrid W210 particles | prediction load [-80°C] (N) | exp load [-80°C] (N) |
|---|---|---|
| 0 | 93 | 67 |
| 2 | 94 | 62 |
| 5 | 92 | 82 |
| 10 | 95 | 88 |

#### 10.3.3.11 PES modified epoxy at $-40^oC$

Figure 10.28 shows the low temperature ($-40^oC$) PES modified epoxy load predictions and Table 10.35 shows the predicted values. Similar results were found in PES modified epoxy when compare to ceramic microsphere modified epoxy.

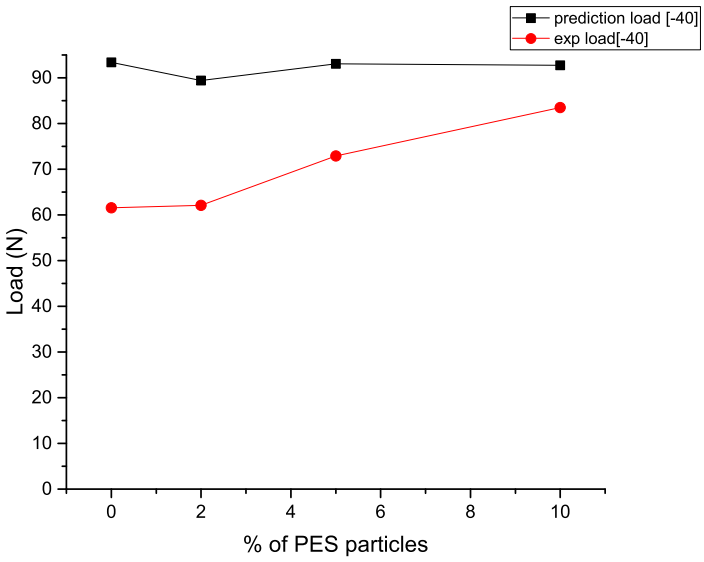


Figure 10.28: SENB low temperature ($-40^oC$) PES modified epoxy load predictions graph

Table 10.35: SENB low temperature ($-40^oC$) PES modified epoxy load predictions table

| Wt% of PES particles | prediction load [-40°C] (N) | exp load [-40°C] (N) |
|---|---|---|
| 0 | 93 | 62 |
| 2 | 89 | 62 |
| 5 | 93 | 73 |
| 10 | 93 | 84 |

#### 10.3.3.12 PES modified epoxy at $-80^oC$

Figure 10.29 shows the low temperature ($-80^oC$) PES modified epoxy load predictions and Table 10.36 shows the predicted values. There was a larger increase at 5 wt% PES than other %, and it was the highest load among the low temperature results of ceramic microsphere, PES and their hybrid modified specimens. As the experimental load at 5 wt% was not higher, the difference in predicted load was properly due to the different in crack length in different specimens.

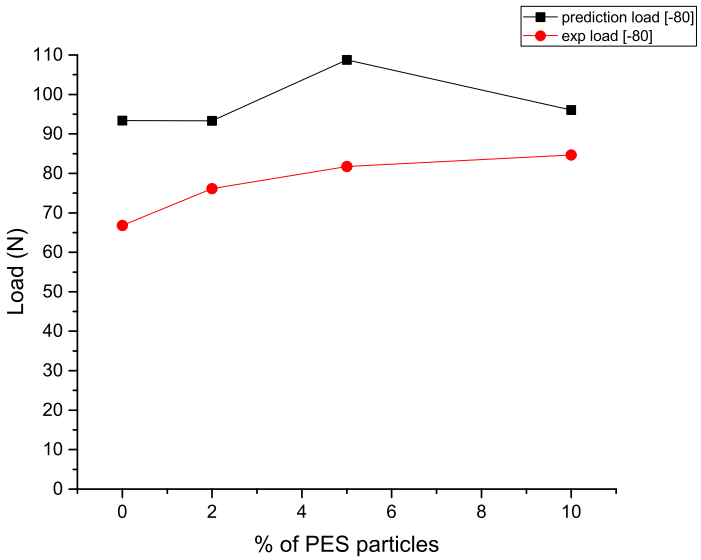


Figure 10.29: SENB low temperature ($-80^oC$) PES modified epoxy load predictions graph

Table 10.36: SENB low temperature ($-80^oC$) PES modified epoxy load predictions table

| Wt% of PES particles | prediction load [-80°C] (N) | exp load [-80°C] (N) |
|---|---|---|
| 0 | 93 | 67 |
| 2 | 93 | 76 |
| 5 | 109 | 82 |
| 10 | 96 | 85 |

#### 10.3.3.13 Hybrid PES / silica modified epoxy at $-40^oC$

Figure 10.30 shows the low temperature ($-40^oC$) hybrid PES / silica modified epoxy load predictions and Table 10.37 shows the predicted values. The predicted values were only a few Newtons different from each other for all the wt% used, so the hybrid PES / silica modified epoxy, did not show a significant toughening effect when the wt% of PES and silica particles increases.

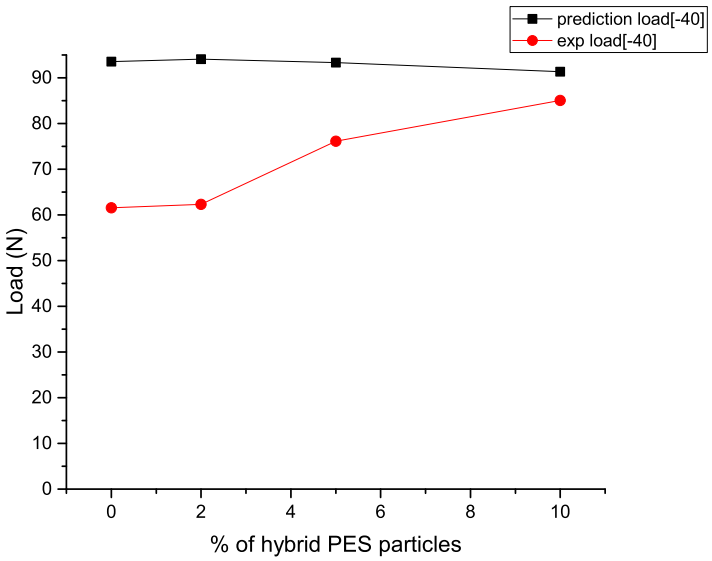


Figure 10.30: SENB low temperature ($-40^oC$) hybrid PES / silica modified epoxy load predictions graph

Table 10.37: SENB low temperature ($-40^oC$) hybrid PES / silica modified epoxy load predictions table

| Wt% of hybrid PES particles | prediction load [-40°C] (N) | exp load [-40°C] (N) |
|---|---|---|
| 0 | 94 | 62 |
| 2 | 94 | 62 |
| 5 | 93 | 76 |
| 10 | 91 | 85 |

#### 10.3.3.14 Hybrid PES / silica $-80^oC$

Figure 10.31 shows the low temperature ($-80^oC$) hybrid PES / silica load predictions and Table 10.38 shows the predicted values. There was a drop in the hybrid PES / silica 2 wt% predictions, which was the lowest load among all (68 N). All other values remained similar. This could be due the fracture energy changed in the input was not in the range of the workable combinations for the cohesive zone, therefore results can be slightly unexpected.

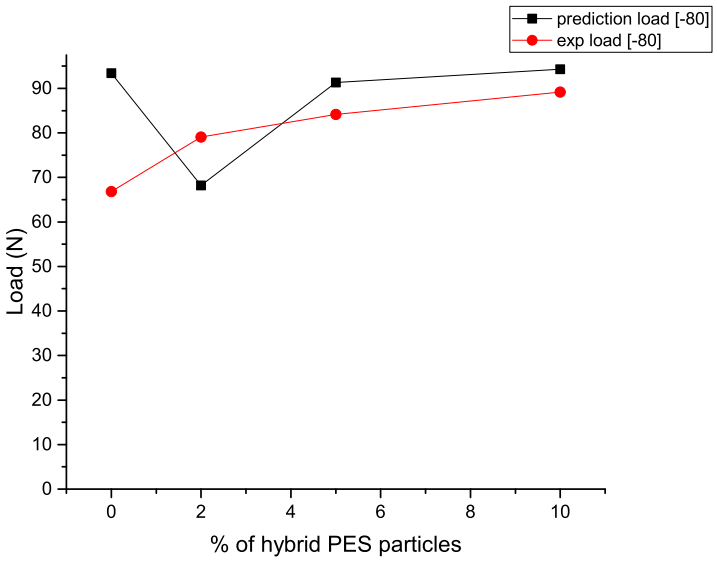


Figure 10.31: SENB low temperature ($-80^oC$) hybrid PES / silica load predictions graph

Table 10.38: SENB low temperature ($-80^oC$) hybrid PES / silica modified epoxy load predictions table

| Wt% of hybrid PES particles | prediction load [-80°C] (N) | exp load [-80°C] (N) |
|---|---|---|
| 0 | 93 | 67 |
| 2 | 68 | 79 |
| 5 | 91 | 84 |
| 10 | 94 | 89 |

#### 10.3.3.15 Summary - Low temperature SENB predictions

There were no significant differences in the predictions of the -40$^oC$ SENB model compared to room temperature while the -80$^oC$ predictions were closer to the expected values as there were smaller differences between the predictions and experimental values, and the pattern of the graph was the same. There seems to be less of a mismatch between the results when the values load were higher.

### 10.3.4 High rate SENB

High rate SENB tests and FE model simulations were performed with silica, CSR and hybrid (CSR+silica) specimens. The same method of finding the predictions of the maximum load was used as has been described previously in Section 10.3.3.

#### 10.3.4.1 Silica modified epoxy - 0.1 m/s

Figure 10.32 shows the high rate (0.1 m/s) silica SENB specimens load predictions and Table 10.39 shows the predicted values. Unlike in the quasi-static SENB tests described previously, most of the load predictions were lower than the experimental values. There was a steady increase in the predicted load with wt% and the highest load was predicted to occur at the highest wt% of silica. The highest load from experiment was from 20 wt% of silica, where there was a big difference between the predictions and the experimental results (77 N), see Table 10.39. But the highest three wt% had similar high load too, so results were the same as in predictions.

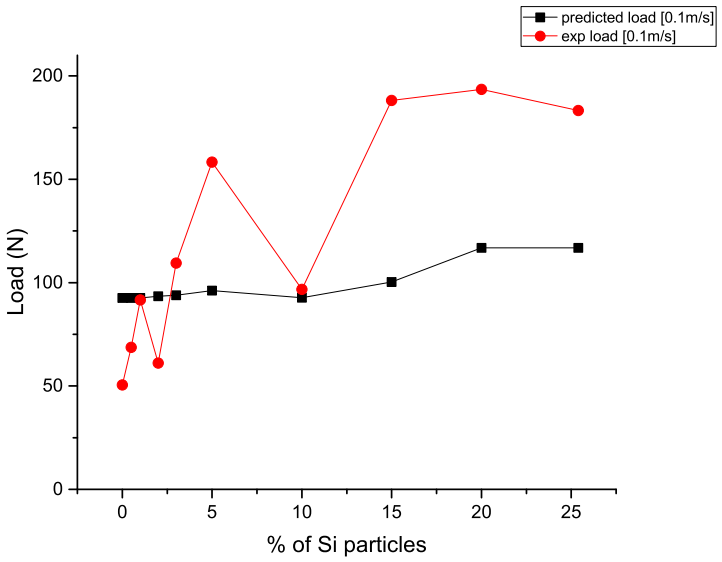


Figure 10.32: High rate (0.1 m/s) silica SENB specimens load predictions graph

Table 10.39: High rate (0.1 m/s) SENB silica specimens load predictions table

| Wt% of silica | predicted load [0.1m/s] | exp load [0.1m/s] |
|---|---|---|
| 0 | 93 | 51 |
| 0.5 | 93 | 69 |
| 1 | 93 | 92 |
| 2 | 93 | 61 |
| 3 | 94 | 109 |
| 5 | 96 | 158 |
| 10 | 93 | 97 |
| 15 | 100 | 188 |
| 20 | 117 | 193 |
| 25.4 | 117 | 183 |

#### 10.3.4.2 Silica modified epoxy - 1 m/s

Figure 10.33 shows the high rate (1 m/s) silica SENB load predictions and Table 10.40 shows the predicted values. There were very high fracture energies found in the experimental results. These large fracture energies should significantly increase the predicted load values, however, the increase was not as great as in the fracture energies. The load predictions remain in a reasonable range of values. The graphs showed different patterns of maximum loads between the experimental and the predicted results. There were a lot of ups and downs in the experimental results and this was not observed in the prediction graphs. Due to the big differences in between the graphs, predictions were found to not agree well with the experimental results. This can also caused by the dynamic effect from high rate experimental test.

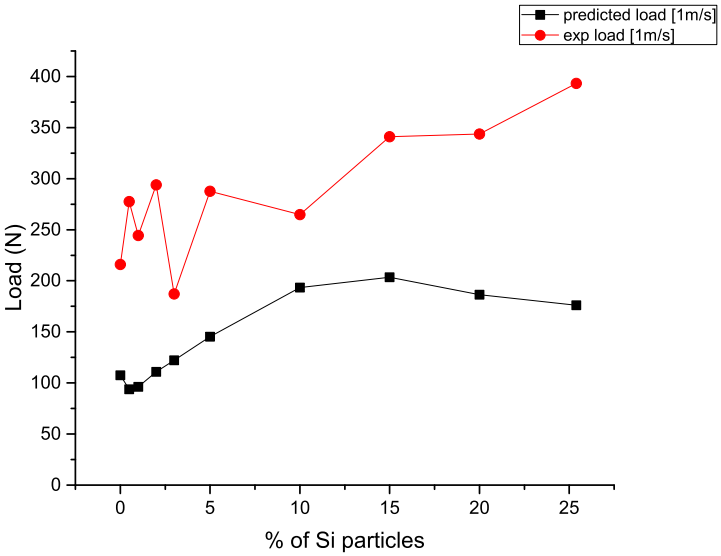


Figure 10.33: High rate (1 m/s) silica SENB load predictions graph

Table 10.40: High rate (1 m/s) silica SENB load predictions table

| Wt% of silica | predicted load [N] | exp load [N] |
|---|---|---|
| 0 | 108 | 216 |
| 0.5 | 94 | 277 |
| 1 | 96 | 244 |
| 2 | 111 | 294 |
| 3 | 122 | 187 |
| 5 | 145 | 288 |
| 10 | 193 | 265 |
| 15 | 203 | 341 |
| 20 | 186 | 344 |
| 25.4 | 176 | 393 |

#### 10.3.4.3 CSR modified epoxy - 0.1 m/s

Figure 10.34 shows the high rate (0.1 m/s) CSR SENB load predictions and Table 10.40 shows the predicted values. There was an even higher difference between the model predictions of CSR and the experimental load when compare to quasi-static rate results. There was a 2 to 3 times overall differences, which didn't make sense. However, the experimental load values were too high when compare to expectations. From the prediction results, it was the predicted values often were not highly affected by the fracture energies input, there were often very stable smaller amount of increase of values.

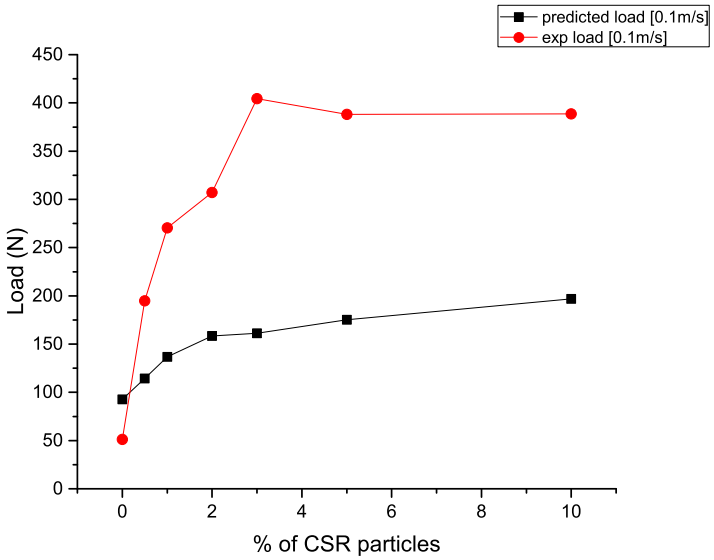


Figure 10.34: High rate (0.1 m/s) CSR SENB load predictions graph

Table 10.41: High rate (0.1 m/s) CSR SENB load predictions table

| Wt% of CSR | predicted load [N] | exp load [N] |
|---|---|---|
| 0 | 93 | 51 |
| 0.5 | 114 | 195 |
| 1 | 137 | 270 |
| 2 | 159 | 307 |
| 3 | 161 | 405 |
| 5 | 175 | 388 |
| 10 | 197 | 389 |

#### 10.3.4.4 CSR modified epoxy - 1 m/s

Figure 10.35 shows the high rate (1 m/s) CSR SENB load predictions and Table 10.42 shows the predicted values. There was a very high fracture energy (5883 $J/m^2$) found measured for 10 wt% CSR at 1 m/s, however, this had produced a drop in the maximum load prediction, the prediction was similar to a CSR low wt% specimen. This could be due to the unreasonably high fracture energy was not a correct input for the relationship that was used, only within the range of the combination of the values could maintain the same relationship and expected results. The highest load was predicted at 5 wt% CSR, the prediction was very similar to experimental load value, but still most of the experimental values were higher than the predictions. Most of the fracture energy values were very large in the high rate results, while the experimental load were not as big when compare, this could be due to the slight different of high rate method in SENB and TDCB, as well as the increased in the presence of stick-slip in TDCB. The two graphs were very different in trends and values, so predictions did not agree well with the experiments.

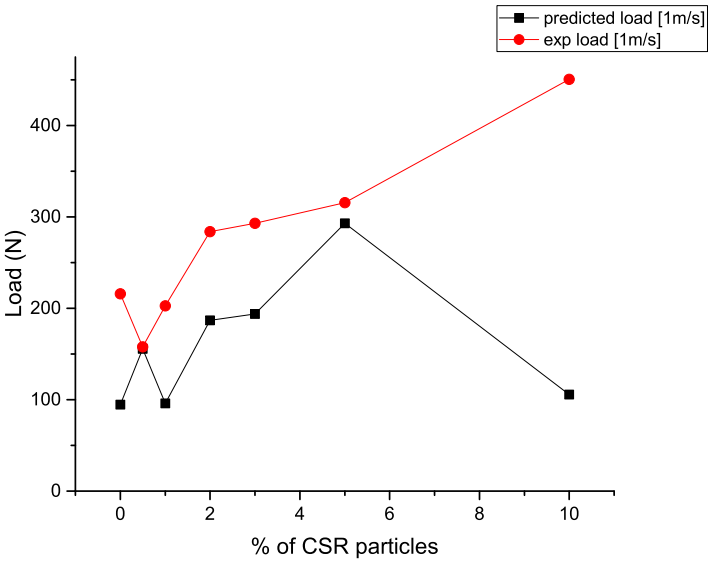


Figure 10.35: High rate (1 m/s) CSR SENB load predictions graph

Table 10.42: High rate (1 m/s) CSR SENB load predictions table

| Wt% of CSR | predicted load [N] | exp load [N] |
|---|---|---|
| 0 | 95 | 216 |
| 0.5 | 156 | 158 |
| 1 | 96 | 203 |
| 2 | 187 | 284 |
| 3 | 194 | 293 |
| 5 | 293 | 316 |
| 10 | 106 | 451 |

#### 10.3.4.5 Hybrid silica / CSR modified epoxy - 0.1 m/s

Figure 10.35 shows the high rate (0.1 m/s) CSR SENB load predictions and Table 10.42 shows the predicted values. The high rate (0.1 m/s) CSR SENB load predictions show an increasing trend of load when wt% of particles increases. The load predictions agreed with experimental results. This could be due to dynamic effect is not significant at the

rate of 0.1 m/s and hence results were more reliable for comparison.

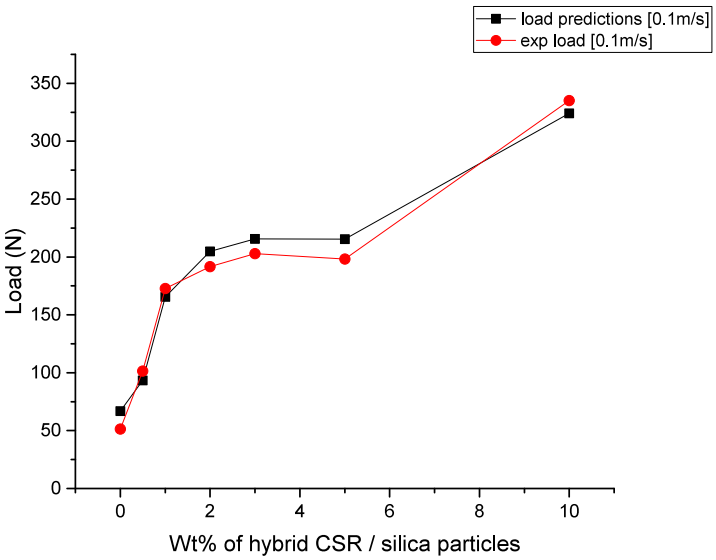


Figure 10.36: High rate (0.1 m/s) hybrid silica / CSR modified epoxy load predictions graph

Table 10.43: High rate (0.1 m/s) SENB hybrid silica / CSR modified epoxy load predictions table

| Wt% of Si/CSR | predicted load [N] | exp load [N] |
|---|---|---|
| 0 | 67 | 51 |
| 0.5 | 93 | 101 |
| 1 | 166 | 173 |
| 2 | 205 | 192 |
| 3 | 216 | 203 |
| 5 | 216 | 198 |
| 10 | 324 | 335 |

#### 10.3.4.6 Hybrid silica / CSR modified epoxy - 1 m/s

Figure 10.37 shows the high rate (1 m/s) hybrid silica / CSR modified epoxy load predictions and Table 10.44 shows the predicted values. For the 1 m/s silica / CSR

hybrid, there was a very similar trend and values found in predictions and experimental load values when compared to the quasi-static rate results, where the highest point and lowest point were the same. The predictions agree with experimental results in hybrid silica / CSR modified epoxy 1 m/s tests.

Most of the predicted and experimental values were similar and lead to a similar pattern, see Figure 10.37. Differences were only at the hybrid 5 wt%. Very large fracture energies were recorded at high wt% of hybrid modified specimens, these were the highest among the silica, CSR and hybrid of both SENB tests. The values were too large for this material, and hence should be treated as an outlier. This was due to the dynamic effects of the high rate test.

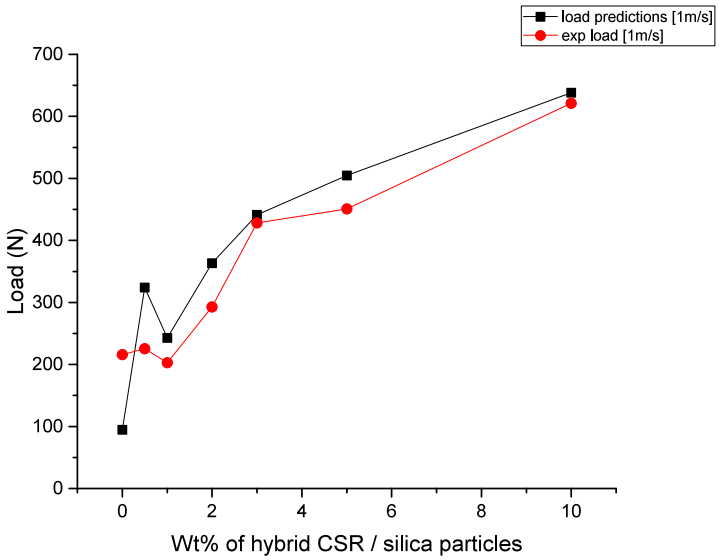


Figure 10.37: High rate (1 m/s) hybrid silica / CSR modified epoxy load predictions graph

Table 10.44: High rate (1 m/s) SENB hybrid silica / CSR modified epoxy load predictions table

| Wt% of Si/CSR | predicted load [N] | exp load [N] |
|---|---|---|
| 0 | 95 | 216 |
| 0.5 | 324 | 225 |
| 1 | 243 | 203 |
| 2 | 363 | 293 |
| 3 | 441 | 428 |
| 5 | 505 | 451 |
| 10 | 638 | 621 |

## 10.4 Summary - High rate SENB

Similar patterns of results were found in high rate SENB predictions, only small differences were recorded in the different formulations. Due to the dynamic effect from high rate experiments, the predicted results were more affected when compare to other FE model results. Most of the predicted loads were different when compare to experimental loads. However, all the combinations of results ran completely in the model, and the SENBs were broken completely. Hence, the high rate SENB predictions were successfully performed.

## 10.5 Load predictions range

The Figures 10.45 to 10.52 below shown the range of the load values predicted in all the FE model predictions.

### 10.5.1 SENB FE prediction load ranges

For SENB model: The minimum load were mostly about 90 N, while maximum load were different in different quasi-static rate, high rate tests and low temperature. At quasi-static rate, maximum load were at 90 - 100 N. At low temperature tests (for both -80°C and -40°C), most of the values were around 90 N, the difference between minimum and maximum load was not a lot. At high rate, both rates (0.1 and 1 m/s) had almost all of the minimum load at 90 N. While there were higher maximum load found in 1 m/s (200 - 600 N) when compare to 0.1 m/s (100 - 300 N).

Table 10.45: Load range of quasi-static SENB predictions

| **SENB** | min load (N) | max load (N) |
|---|---|---|
| Silica | 94 | 103 |
| CSR | 89 | 93 |
| Hybrid (CSR+Silica) | 89 | 101 |
| W210 | 89 | 108 |
| W210 hybrid | 91 | 94 |
| PES | 89 | 94 |
| Hybrid PES | 89 | 94 |

Table 10.46: Load range of low temperature SENB at -40$^oC$ predictions

| **minus 40 Low temperature SENB** | min load (N) | max load (N) |
|---|---|---|
| Silica | 91 | 108 |
| CSR | 91 | 99 |
| Hybrid | 92 | 100 |
| W210 | 91 | 94 |
| Hybrid W210 | 92 | 94 |
| PES | 89 | 93 |
| Hybrid PES | 91 | 94 |

Table 10.47: Load range of low temperature SENB at -80$^oC$ predictions

| **minus 80 Low temperature SENB** | min load (N) | max load (N) |
|---|---|---|
| Silica | 91 | 129 |
| CSR | 91 | 102 |
| Hybrid | 91 | 104 |
| W210 | 91 | 93 |
| Hybrid W210 | 92 | 95 |
| PES | 93 | 109 |
| Hybrid PES | 91 | 94 |

Table 10.48: Load range of SENB tested at 0.1 m/s predictions

| **0.1m/s High rate SENB** | min load (N) | max load (N) |
|---|---|---|
| Silica | 93 | 117 |
| CSR | 93 | 197 |
| Hybrid | 67 | 324 |

Table 10.49: Load range of SENB tested at 1 m/s predictions

| **1m/s High rate SENB** | min load (N) | max load (N) |
|---|---|---|
| Silica | 94 | 203 |
| CSR | 95 | 293 |
| Hybrid | 95 | 638 |

### 10.5.2 TDCB FE prediction load ranges

The load range of quasi-static TDCB predictions were from about 100 - 300 N for both silica and CSR specimens. There were different load ranges in TDCB high rate predictions. There were higher maximum load at 1 m/s for both silica and CSR specimens, while minimum loads were different for different formulations.

Table 10.50: Load range of quasi-static TDCB predictions

| Normal TDCB | min load (N) | max load (N) |
|---|---|---|
| Silica | 129 | 202 |
| CSR | 133 | 300 |

Table 10.51: Load range of predictions of silica-modified TDCB specimens tested at 1 m/s

| Silica % | min load (N) | max load (N) |
|---|---|---|
| 2 | 90 | 347 |
| 5 | 250 | 490 |
| 10 | 71 | 499 |

Table 10.52: Load range of predictions of CSR-modified TDCB specimens tested at 1 m/s

| CSR % | min load (N) | max load (N) |
|---|---|---|
| 2 | 177 | 280 |
| 5 | 310 | 440 |
| 10 | 77 | 353 |

## 10.6 Conclusions

The FE modelling of fracture of particle-modified epoxy of the two models (TDCB, SENB) of all the conditions (quasi-static, low temperature, high rate) tested were performed. Cohesive zone model with zero thickness of cohesive layer was made in mode I direction. The cohesive properties of the the cohesive layer used was found from an one element tensile model. The tensile response of the model was found based on experimental tensile results.

The fracture energy values cannot be compared directly for TDCB model, as there were stick-slips in experimental results but only propagations were assumed in the FE

model. For the force values, only propagation values from experimental results can be compared, as there are only propagations assumed in the FE model. For high rate TDCB, because of the dynamic effect from high rate experimental tests, there were not a lot of data points can be used for the FE model. There were more differences in the predicted results when compare to experimental results, but it is believed to be due to significant dynamic effect at high rate. It is also found that the larger the predicted fracture energy, the larger the resultant displacement. The displacement values were larger than values from experimental results, but within reasonable range and trend.

The same geometry of SENB model was also made with a zero thickness cohesive zone at the middle (where the crack is), no initial crack was needed for cohesive element model. A small amount of friction was added to prevent specimen from flying off, and a quasi-static rate was applied. While the highest force predictions of SENB is comparable to the experimental results, but not always reliable, as the crack length has an effect on the SENB fracture. Most of the highest load from predictions were not the same as experimental load, but the predicted load values were closer to expected values. Often there is a higher difference in between experimental load and predicted load at low wt%, but values were similar at high wt%. The load range of SENB predictions were compared, there seem to be a base level of load for this model setup, this could be due to the use of the same cohesive properties.

The use of FE model of cohesive zone in adhesive material has provided more information regarding the fracture properties of particle-modified epoxy. However, there are limitations in modelling studies, as there are other variables in experiments that can affect the behaviour of material and hence the failure mechanisms. Therefore, the results from FE model can be different when compared to the experimental results.

# Chapter 11

# Ceramic microsphere and PES modified epoxy results comparisons

## 11.1 Introduction

The use of ceramic microsphere and PES modified epoxy was introduced to compare fracture properties with the other particles used in this study (silica, CSR and hybrid of them). Tensile and SENB tests at quasi-static rate at room temperature and low temperature were performed, and the experimental results were used in analytical modelling and FE modelling predictions. SEM images of the epoxies modified with the two particles were included in SEM Chapter 9.

## 11.2 Tensile tests

Tensile tests at the same standard conditions were performed to measure the modulus for calculating the fracture energy in the LEFM method. The tensile tests were performed at a rate of 1 mm/min with six replicate specimens. The young's modulus was calculated by curve fitting of the slope of the stress versus strain curve in the linear region.

### 11.2.1 Tensile results of PES and hybrid PES / silica modified epoxy

Tensile results of PES and hybrid PES / silica specimens are showed below (Table 11.1 and Figure 11.1). There were similar modulus values measured as those found in CSR and hybrid (silica / CSR) specimens. However, the curve was more stable with small standard deviations, hence, the trends observed were more reliable. There was a gradual increase in modulus when the wt% of particles increased, but the amount of improvement was small, there was only a 17% of increase in modulus when the maximum amount of particles were added. The trends for PES and hybrid PES / silica

were found to be very similar. Hybrid PES / silica showed a higher modulus when the wt% of particles added in was moderate, but similar values were found with the maximum wt%, see Table 11.1.

Table 11.1: Tensile modulus results of PES modified epoxy

| particles | PES | | Hybrid PES | |
|---|---|---|---|---|
| % of particles | Young's Modulus (GPa) | SD | Young's Modulus (GPa) | SD |
| 0 | 3.14 | 0.83 | 3.14 | 0.63 |
| 2 | 3.28 | 0.074 | 3.46 | 0.89 |
| 5 | 3.33 | 0.092 | 3.52 | 0.28 |
| 10 | 3.62 | 0.089 | 3.66 | 0.46 |

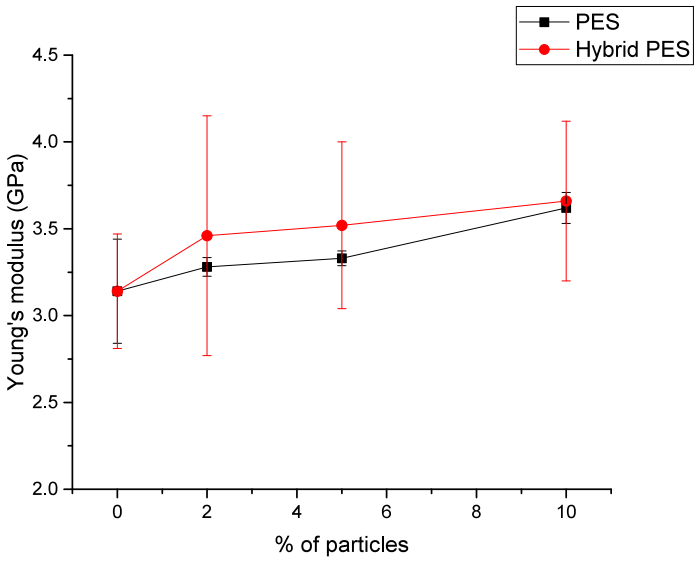


Figure 11.1: Tensile modulus results of PES modified epoxy

### 11.2.2 Tensile results of ceramic microsphere and hybrid ceramic / CSR modified epoxy

Tensile results of ceramic microsphere and hybrid ceramic microsphere (ceramic microsphere/CSR) specimens are showed below (Table 11.2 and Figure 11.2). There are steady increase in the Young's modulus of both ceramic microsphere and hybrid ceramic

microsphere modified epoxy specimens when the wt% of particles increases. The use of higher wt% of ceramic microsphere provided an increase in tensile properties, the rate of increase was reduced when 10 wt% (the highest wt% used) of ceramic microspheres and hybrid ceramic microspheres were used, but it still had the highest Young's modulus.

Table 11.2: Tensile modulus results of ceramic microsphere modified epoxy

| particles | W210 | | Hybrid W210 | |
|---|---|---|---|---|
| % of particles | Young's Modulus (GPa) | SD | Young's Modulus (GPa) | SD |
| 0 | 3.14 | 0.10 | 3.14 | 0.10 |
| 2 | 3.37 | 0.05 | 3.46 | 0.15 |
| 5 | 3.46 | 0.01 | 3.66 | 0.12 |
| 10 | 3.5 | 0.03 | 3.76 | 0.17 |

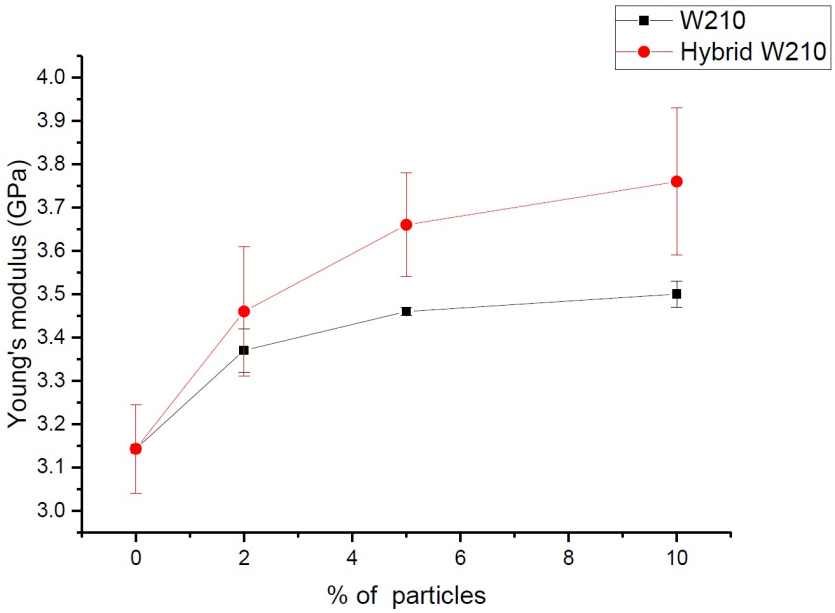


Figure 11.2: Tensile modulus results of ceramic microsphere modified epoxy

## 11.3 Single edge notch bending tests

### 11.3.1 Introduction

Single edge notch bending (SENB) tests were performed according to ISO 13586 standard [30], at the same conditions as tests performed using the CSR and silica modified epoxy, including low temperature SENB tests.

### 11.3.2 PES modified epoxy

The PES modified specimens are expected to show a different fracture behaviour than the other particles compared here, due to the nature of the PES particles.

The results from the room and low temperature PES modified epoxy specimens are showed in Table 11.3 and Figure 11.3 below. The differences in fracture energy of unmodified epoxy was due to the differences in temperature in the cooling chamber, as the temperature of the chamber was maintained using only liquid nitrogen. This is showed that there were similar trends in the PES and ceramic microsphere modified specimens when compared to silica and CSR modified specimens, fracture energy was higher when tests were performed at a lower temperature as well as when wt% of particles increased. All of these had lower fracture energy values when compared to silica and CSR. However, these results have smaller standard deviations and smoother graphs when compared to results with silica and CSR. There is a higher reliability in these results, as they are more consistent. SEM imaging revealed more information regarding their fracture behaviour. The SEM images of the fracture surfaces in Chapter 9 showed that there were some debonding, pull out of particles and local phrase inversion in PES modified epoxy specimens. Overall, the silica modified specimens showed to have the greatest toughening effect when compared to all these different types of particles.

Specimens tested at -40$^oC$ had the same trend of fracture energy values when compared to room temperature specimens, while a significant increase is shown from specimens tested at -80$^oC$. The toughening effect was small when the PES modified specimens were tested at room temperature and -40$^oC$. A large increase (100% increase when compared to unmodified specimens) was shown in the 10wt% PES modified specimens tested at -80$^oC$.

Table 11.3: Fracture energy of PES modified epoxy at room and low temperature

| Temperature | Room temperature | | -40 °C | | -80°C | |
|---|---|---|---|---|---|---|
| % of PES particles | G ($J/m^2$) | SD | G ($J/m^2$) | SD | G ($J/m^2$) | SD |
| 0 | 65 | 21 | 63 | 9 | 73 | 15 |
| 2 | 70 | 1 | 75 | 12 | 94 | 2 |
| 5 | 77 | 4 | 83 | 6 | 106 | 5 |
| 10 | 80 | 5 | 109 | 8 | 149 | 6 |

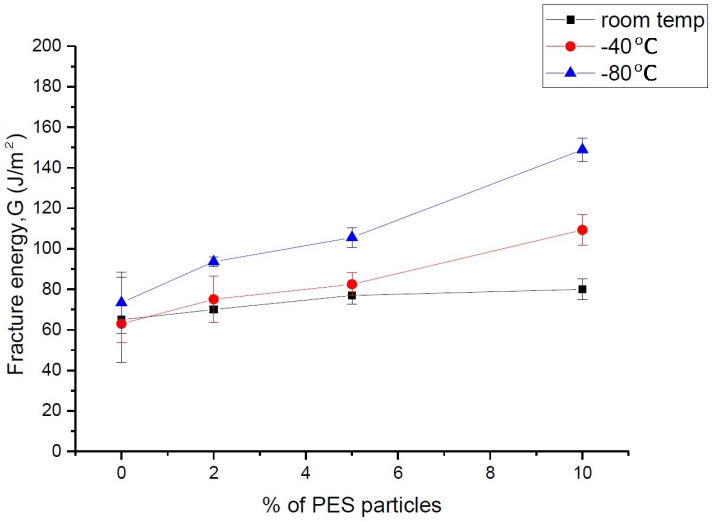


Figure 11.3: Fracture energy of PES modified epoxy at room and low temperature

### 11.3.3 Hybrid PES / silica modified epoxy

The values measured using the hybrid PES / silica modified specimens are shown in Table 11.5 and Figure 11.4 below. The same trend an increase in the fracture energy when the temperature reduced and especially when the wt% used was high was found in hybrid PES / silica modified specimens. The fracture energy values were also found to be similar to the PES modified specimens, with small standard deviations (10% or less). Therefore, results were reliable but the toughening effect of hybrid PES / silica is not clear. It is assumed that significantly higher fracture properties would be produced when hybrid particles were used. It could be due to the % of the particles that could undergo toughening mechanisms (debonding, void growth) is limited. With the high concentration of particles added in, a small amount of clusters were found. Dissolving the PES particles increased the viscosity of the mixture, hence, hybrid particles was not well mixed when the wt% used was high. This also explains why the hybrid modified specimens had slightly lower fracture energy values when compared to the silica modified specimens.

Table 11.4: Fracture energy of hybrid PES / silica modified epoxy at room and low temperature

| Temperature | Room temperature | | -40°C | | -80 °C | |
|---|---|---|---|---|---|---|
| % of Hybrid PES particles | G ($J/m^2$) | SD | G ($J/m^2$) | SD | G ($J/m^2$) | SD |
| 0 | 63 | 11 | 93 | 9 | 126 | 15 |
| 2 | 70 | 1 | 77 | 4 | 90 | 10 |
| 5 | 77 | 4 | 94 | 6 | 110 | 6 |
| 10 | 80 | 5 | 109 | 4 | 143 | 10 |

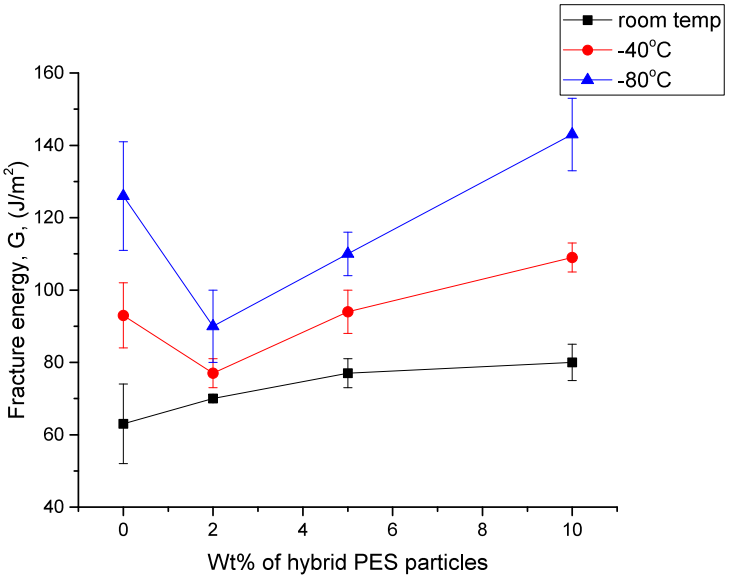


Figure 11.4: Fracture energy of hybrid PES / silica modified epoxy at room and low temperature

### 11.3.4 Ceramic microsphere modified epoxy

Fracture energy results of low temperature ceramic microsphere modified epoxy specimens were shown in Table 11.5 and Figure 11.5 below. There was a steady increase in fracture energy in the room temperature results, the toughening effect was significant at high wt%. The low temperature results show similar fracture energy values when the -40°C data are compared to those at -80°C. Low temperature testing did not show a large increase in fracture properties. There were small standard deviations found in low temperature results when compared to the room temperature results, low temperature results were reliable. This shows that ceramic microsphere modified epoxy is not sensitive to brittle testing conditions.

Table 11.5: Fracture energy of ceramic microsphere modified epoxy at room and low temperature

| Temperature | Room temperature | | -40 °C | | -80 °C | |
|---|---|---|---|---|---|---|
| % of W210 particles | G ($J/m^2$) | SD | G ($J/m^2$) | SD | G ($J/m^2$) | SD |
| 0 | 68 | 21 | 63 | 9 | 73 | 15 |
| 2 | 82 | 6 | 72 | 6 | 112 | 17 |
| 5 | 101 | 23 | 112 | 5 | 117 | 2 |
| 10 | 147 | 25 | 127 | 5 | 127 | 5 |

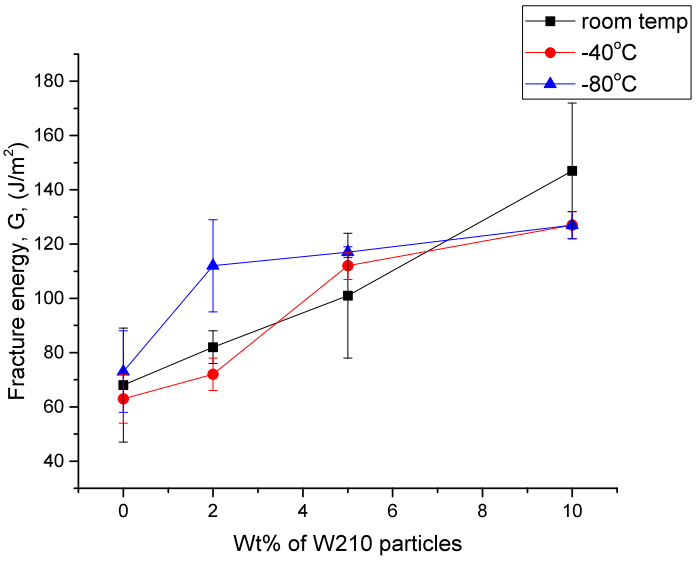


Figure 11.5: Fracture energy of ceramic microsphere modified epoxy at room and low temperature

### 11.3.5 Hybrid ceramic microsphere / CSR modified epoxy

The fracture energy results of the ceramic microsphere / CSR modified epoxy specimens are showed in Table 11.6 and Figure 11.6 below. There were higher fracture energy values for the hybrid ceramic microsphere / CSR modified epoxy when compared to the ceramic microsphere modified epoxy. There were slightly higher standard deviations, but the results were still reliable. The room temperature results had similar fracture energy values when compared to the low temperature results, the ceramic microsphere

particles produced the same effect in the hybrid ceramic microsphere / CSR modified epoxy.

Table 11.6: Fracture energy of hybrid ceramic microsphere / CSR modified epoxy at room and low temperature

| Temperature | Room temperature | | -40 °C | | -80 °C | |
|---|---|---|---|---|---|---|
| % of Hybrid W210 particles | G (J/m$^2$) | SD | G (J/m$^2$) | SD | G (J/m$^2$) | SD |
| 0 | 68 | 21 | 65 | 9 | 86 | 15 |
| 2 | 95 | 9 | 83 | 10 | 92 | 10 |
| 5 | 112 | 1 | 113 | 0 | 118 | 15 |
| 10 | 155 | 15 | 127 | 10 | 130 | 13 |

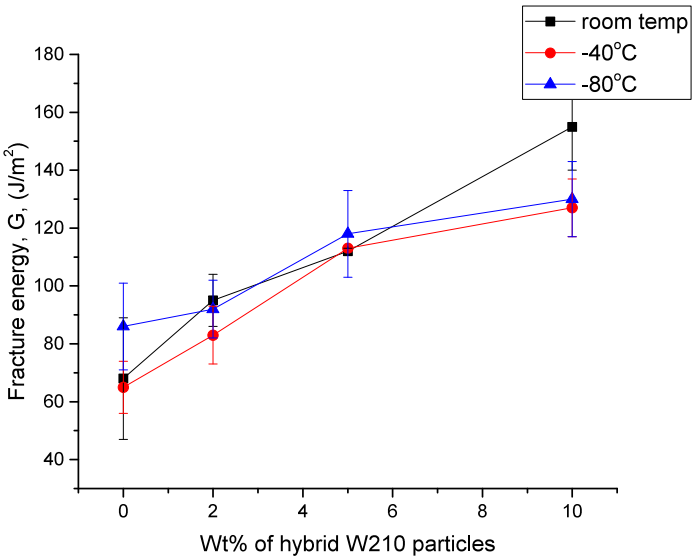


Figure 11.6: Fracture energy of ceramic microsphere modified epoxy at room and low temperature

The increasing trend of the fracture energy in ceramic microsphere was not as clear as PES, curves were not as stable. Specimens tested at room and low temperature generally produced an increased in fracture energy, but this was not clear in ceramic microsphere modified specimens. Highest fracture energy was found at 10 wt% tested at room temperature. There were also slightly bigger standard deviations found in these results when compared, but still within an acceptable range.

## 11.4 Analytical modelling

### 11.4.1 Introduction

The analytical models of Halpin-Tsai and Huang and Kinloch were used to predict the modulus and fracture energy of the ceramic microsphere and PES modified epoxy and, same assumptions are made as in Chapter 8.

### 11.4.2 Halpin-Tsai model modulus predictions

The predicted modulus of the ceramic microsphere, ceramic microsphere / CSR hybrid, PES and PES / silica hybrid modified epoxy are shown in Figures 11.7 to 11.10 and Tables 11.7 to 11.10. The particle modulus used for PES was 8.14 GPa [64] and 53 GPa for ceramic microspheres [65].

The predicted modulus of the ceramic microsphere modified epoxy is shown in Figure 11.7 and Table 11.7. In the ceramic microsphere-modified epoxy, overall results were similar for all particles, higher wt% of particles used showed a higher improvement as expected and most of the predictions were similar to experimental results. Predicted modulus agreed with experimental results. The saturation of particles were not found in ceramic microsphere SEM images, distributions of particles was rather even. This suggested that the accuracy of this predictions is affected by the distribution of particles. The use of ceramic microsphere modified epoxy for this study model has not been performed before, this study proved that this prediction model works very well with ceramic microspheres.

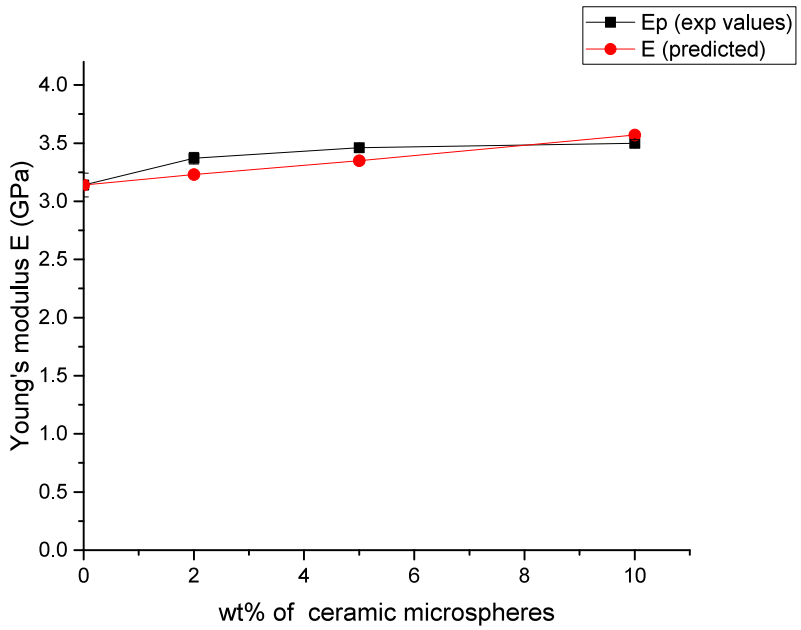


Figure 11.7: Predicted modulus of ceramic microsphere-modified epoxy

Table 11.7: Predicted modulus of ceramic microsphere-modified epoxy

| Wt% of ceramic microspheres | E (GPa) (exp values) | E (GPa) (predicted) |
|---|---|---|
| 0 | 3.14 | 3.14 |
| 2 | 3.37 | 3.23 |
| 5 | 3.46 | 3.35 |
| 10 | 3.5 | 3.57 |

The predicted modulus of the ceramic microsphere / CSR modified epoxy is shown in Figure 11.8 and Table 11.8. The predicted modulus values for the hybrids of ceramic microsphere and CSR specimens were calculated using the sum of the increases of the results of the two particles used, as there were equal wt% of each particle in the un-modified epoxy. It is shown that the experimental results from the ceramic microsphere / CSR hybrid modified epoxy were close to predictions except for 10 wt%. There were higher prediction values for the ceramic microsphere / CSR hybrid modified specimens, but overall, they were predicted to have similar behaviour when compare to ceramic

microsphere modified epoxy.

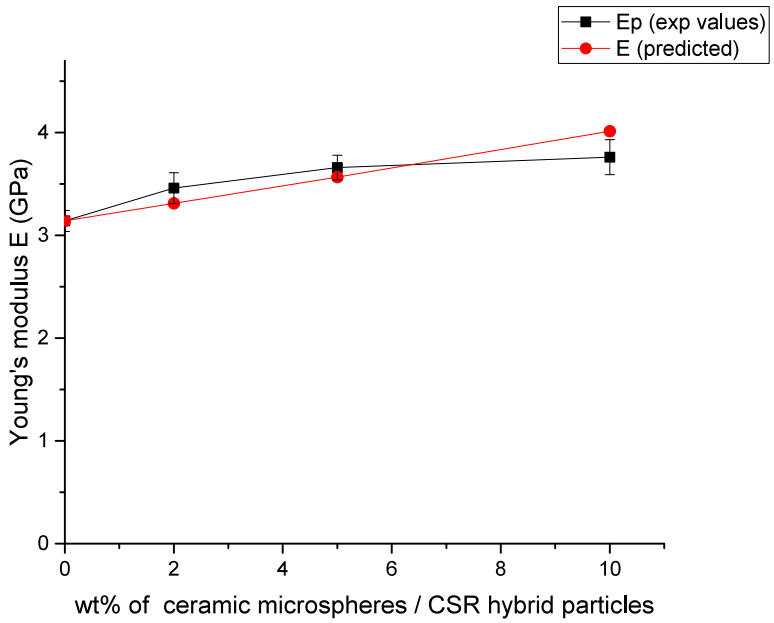


Figure 11.8: Predicted modulus of ceramic microsphere / CSR hybrid modified epoxy

Table 11.8: Predicted modulus of ceramic microsphere hybrid / CSR-modified epoxy

| Wt% of ceramic microspheres / CSR hybrid particles | E (GPa) (exp values) | E (GPa) (predicted) |
|---|---|---|
| 0 | 3.14 | 3.14 |
| 2 | 3.46 | 3.31 |
| 5 | 3.66 | 3.57 |
| 10 | 3.76 | 4.01 |

The predicted modulus values for the PES modified epoxy are shown in Figure 11.9 and Table 11.9. The predictions were similar to the experimental results. However, there was a smaller increase in fracture energy when wt% of PES particles increases in predicted values when compare to experimental results. However, the use of PES did not produce a significant increase in modulus in both experimental and predicted

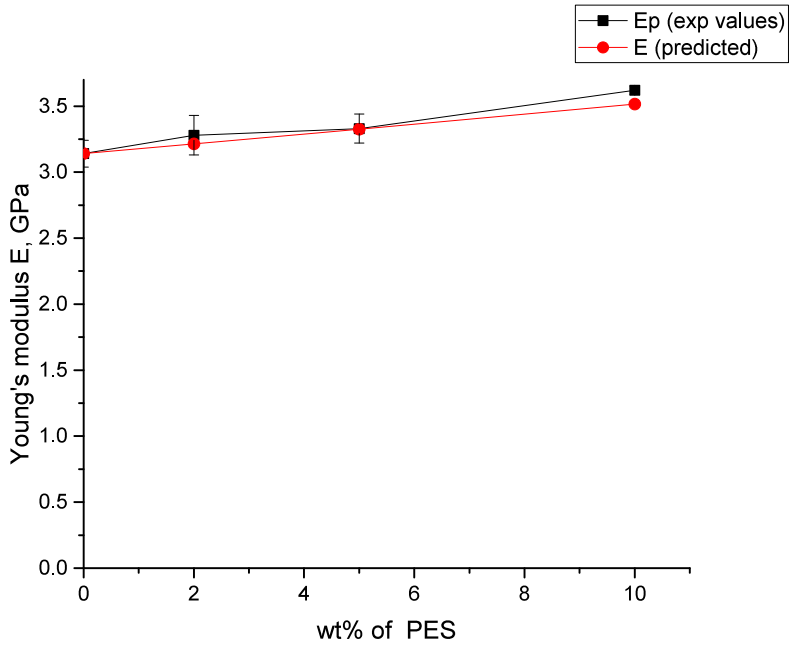


Figure 11.9: Predicted modulus of PES-modified epoxy

results, this could be due to difficulty in dissolving PES particles into epoxy. Clusters of particles were found in the PES SEM images.

Table 11.9: Predicted modulus of PES-modified epoxy

| Wt% of PES particles | E (GPa) (exp values) | E (GPa) (predicted) |
|---|---|---|
| 0 | 3.14 | 3.14 |
| 2 | 3.28 | 3.21 |
| 5 | 3.33 | 3.33 |
| 10 | 3.62 | 3.52 |

The predicted modulus values for the hybrid PES / silica modified epoxy are shown in (Figure 11.10 and Table 11.10). There were slightly higher modulus values found in hybrid PES / silica modified epoxy for both predicted and experimental results, but there were all very similar. The use of PES / silica hybrid did not show improvement in modulus of the epoxy. There was some local phase inversion at 10 wt% PES / silica hybrid specimens and uneven distributions of particles in some other wt% specimens.

This might have reduced the toughening effect of the particles used.

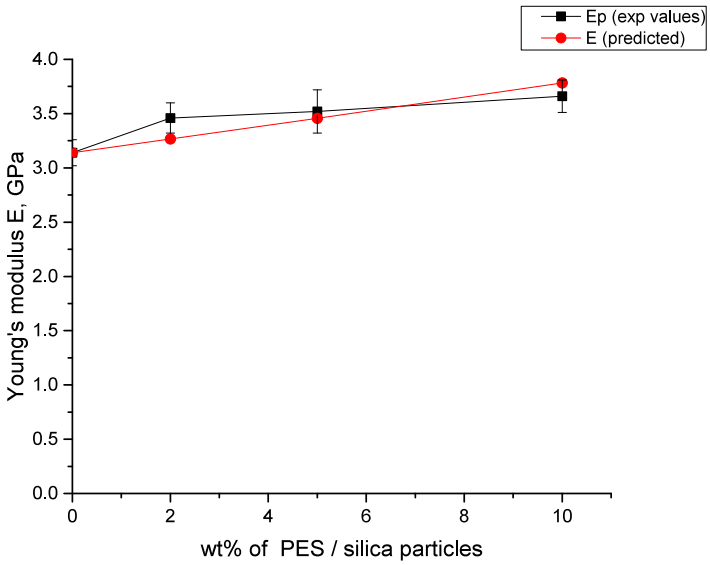


Figure 11.10: Predicted modulus of PES / silica hybrid-modified epoxy

Table 11.10: Predicted modulus of PES / silica hybrid-modified epoxy

| Wt% of PES / silica hybrid particles | E (GPa) (exp values) | E (GPa) (predicted) |
|---|---|---|
| 0 | 3.14 | 3.14 |
| 2 | 3.46 | 3.28 |
| 5 | 3.52 | 3.48 |
| 10 | 3.66 | 3.83 |

### 11.4.3 Huang and Kinloch fracture energy predictions

There was a range of sizes found in PES particles (350-500 micrometres according to the manufacturer's information, while some small particles were seen, e.g. Figure 9.67 (186 micron) and Figure 9.70 (150 micron)), therefore, an average size was used in the predictions. Average size was also used in hybrid materials, and predictions were reasonable. The hybrid materials were found to have higher fracture energy predictions

similar to the modulus predictions, but there were significantly higher values for the hybrid ceramic microspheres than silica, and hybrid PES / silica showed higher predictions than CSR. Synergy effect was found. Experimental results were found to be smaller than 14.3% void growth prediction, this suggested that specimens could perform better with improvement in preparation method, but experimental values were reasonable, so it could be a normal variation in results, and that was not at the highest performance range. Shear was found to have the lowest values, as it was assuming shear only, same case was found here for all wt% in all particles except for high wt% of hybrid CSR / ceramic microsphere and hybrid PES / silica specimens.

The parameters used in the equations are listed in Table 11.11 below.

Table 11.11: Values of parameters used for toughening predictions, measured in the present work or from Hsieh et al. [2].

| Name | Symbol | Units | Value | Source |
|---|---|---|---|---|
| Fracture energy of unmodified epoxy | $G_U$ | $J/m^2$ | 68 | Present study |
| Plane-stain compressive yield stress of unmodified epoxy | $\sigma_{ycu}$ | MPa | 123 | Hsieh et al. |
| Young's modulus of unmodified epoxy | $E_u$ | GPa | 3.14 | Present study |
| Plane strain compressive failure strain of unmodified epoxy | $\gamma_{fu}$ | / | 0.62 | Hsieh et al. |
| Maximum stress concentration around a particle | $K_{sp}$ | / | 1.65-1.709 | Present study |
| Maximum stress concentration around a void | $K_v$ | / | 2.12( case 1) | Present study |
| Volume fraction of particles | $v_f$ | / | 0-0.22 | Present study |
| Poisson's ratio of unmodified epoxy | $v$ | / | 0.35 | Hsieh et al. |

Table 11.12 and Figure 11.11 show the fracture energy predictions and experimental fracture energy values of ceramic microsphere modified epoxy. In ceramic microsphere modified specimens, the predictions were as expected, 100% void growth had the highest fracture energy, followed by 14.3% of void with shear, 14.3% of void growth and lastly shear only. The experimental results were similar to 14.3% void growth with shear

except for 10 wt%, but if standard deviations were considered (as there were higher standard deviations when weight % of particles added is high), the experimental values are similar to predictions. When comparing the different assumptions with experimental results, 14.3% of void with shear is the only assumption that agreed well with the experimental results. Debonding was found in the ceramic microsphere SEM images, and the fracture energy prediction model suggested the presence of shear yielding.

Table 11.12: Table showing fracture energy predictions of ceramic microsphere-modified epoxy

| wt% of ceramic microspheres particles | $G_v$ (J/m$^2$) | 0.143 $\Delta G_v$ (J/m$^2$) | $G_s$ (J/m$^2$) | $dG_s$+0.143$dG_v$ (J/m$^2$) | Exp (J/m$^2$) | SD |
|---|---|---|---|---|---|---|
| 0 | 68 | 68 | 68 | 68 | 68 | 21 |
| 2 | 103 | 73 | 82 | 87 | 82 | 6 |
| 5 | 155 | 80 | 91 | 104 | 101 | 23 |
| 10 | 243 | 93 | 102 | 127 | 147 | 25 |

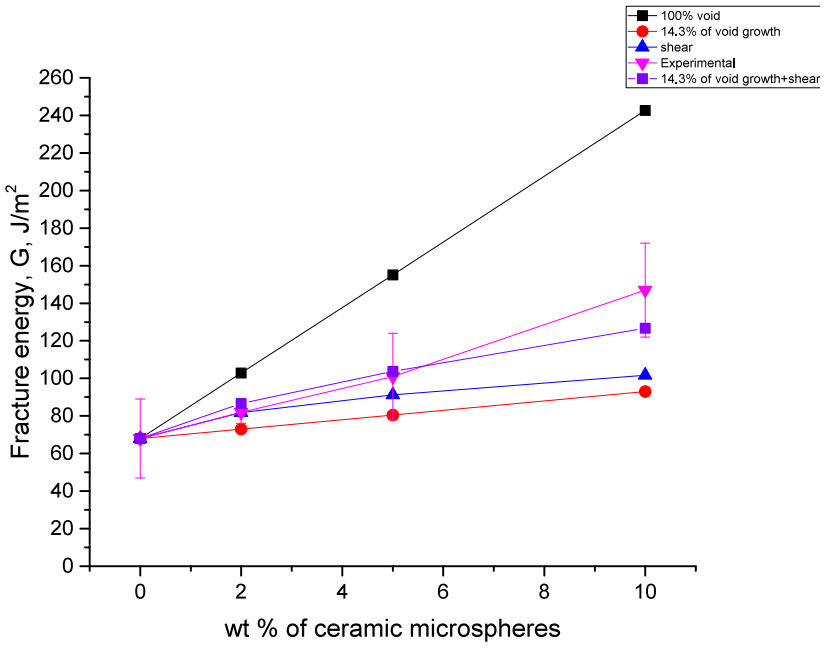


Figure 11.11: Figure showing fracture energy predictions of ceramic microsphere-modified epoxy

Table 11.13 and Figure 11.12 show the fracture energy predictions of hybrid ceramic microsphere modified specimens when compared to the experimental results. For most of the wt%, this shows that the shear values were higher than 14.3% of void growth. Experimental values were very similar to shear only assumption, it is not the same as results found in ceramic microsphere specimens. 14.3% of void with shear is the only assumption that agreed with experimental results of ceramic microsphere modified epoxy. However, shear only was not suggested in SEM images, but as the CSR particles were made up of small CSR particles, most of the debonding found could be from deformed big CSR particles. The ceramic microspheres were surrounded by small CSR particles that flow into epoxy matrix, hence it was not possible to confirm the amount of debonding from ceramic microspheres only. The big CSR particles have affected prediction values, same as results found in CSR modified epoxy.

Table 11.13: Table showing fracture energy predictions of hybrid ceramic microsphere / CSR-modified epoxy

| wt% of ceramic microspheres / CSR particles | $G_v$ ($J/m^2$) | 0.143 $\Delta G_v$ ($J/m^2$) | $G_s$ ($J/m^2$) | $dG_s$+0.143$dG_v$ ($J/m^2$) | Exp ($J/m^2$) | SD |
|---|---|---|---|---|---|---|
| 0 | 68 | 68 | 68 | 68 | 68 | 21 |
| 2 | 179 | 84 | 99 | 115 | 95 | 10 |
| 5 | 346 | 108 | 120 | 160 | 112 | 1 |
| 10 | 625 | 148 | 143 | 222 | 155 | 15 |

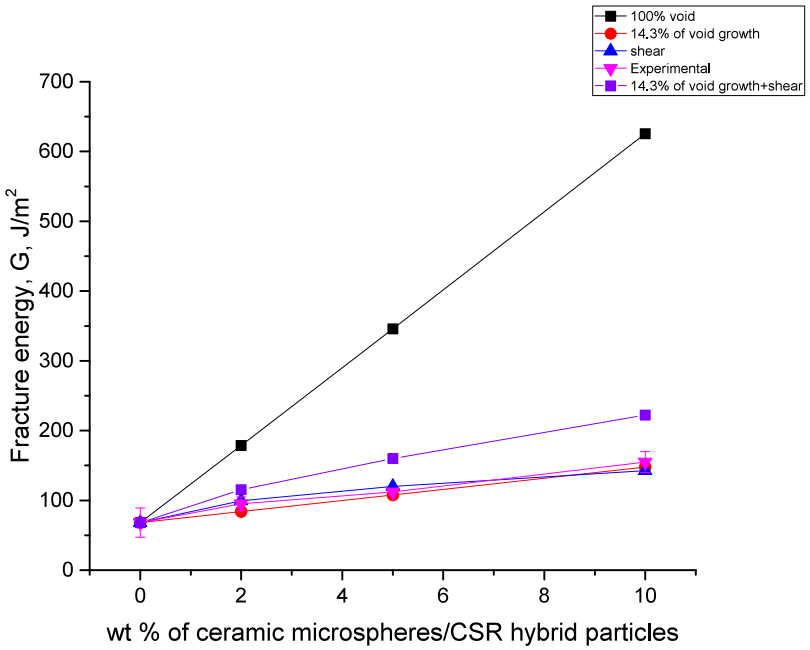


Figure 11.12: Figure showing fracture energy predictions of hybrid ceramic microsphere / CSR-modified epoxy

Table 11.14 and Figure 11.13 show the fracture energy predictions of PES modified specimens when compared to the experimental results. The experimental results were found to be slightly smaller than most of the assumptions. 100% void growth showed the highest fracture energy values as expected. The shear only and 14.3% void growth predictions fit the experimental results.

There were different appearances in the fracture surfaces of PES specimens, because the PES particles were dissolved before mixing with epoxy. Therefore, it is hard to estimate the amount of debonding. It was found there was some bridging in low wt% of PES, hence this prediction was reasonable.

Table 11.14: Table showing fracture energy predictions of PES-modified epoxy

| wt% of PES particles | $G_v$ ($J/m^2$) | 0.143 $\Delta G_v$ ($J/m^2$) | $G_s$ ($J/m^2$) | $dG_s+0.143dG_v$ ($J/m^2$) | Exp ($J/m^2$) | SD |
|---|---|---|---|---|---|---|
| 0 | 68 | 68 | 68 | 68 | 65 | 21 |
| 2 | 129 | 77 | 83 | 92 | 70 | 1 |
| 5 | 221 | 90 | 93 | 115 | 77 | 4 |
| 10 | 375 | 112 | 103 | 147 | 80 | 5 |

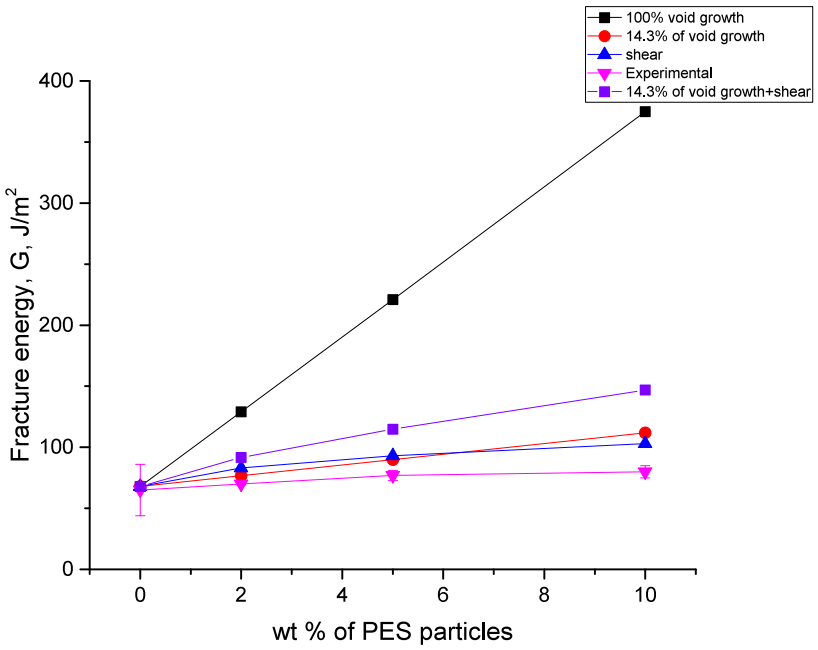


Figure 11.13: Figure showing fracture energy predictions of PES-modified epoxy

Table 11.15 and Figure 11.14 show the fracture energy predictions of hybrid PES / silica modified specimens when compared to experimental results. Experimental data were found to be smaller than most of the assumptions, same as in PES modified epoxy results. All the assumptions do not fit with experimental results. As a different appearance of dissolved PES was found in both PES and PES / silica hybrid specimens, there could be uneven distributions of particles, and the measured experimental results could be coming from regions of the specimens with fewer particles.

Table 11.15: Table showing fracture energy predictions of hybrid PES / silica-modified epoxy

| wt% of PES / silica particles | $G_v$ (J/m$^2$) | 0.143 $\Delta G_v$ (J/m$^2$) | $G_s$ (J/m$^2$) | $dG_s$+0.143$dG_v$ (J/m$^2$) | Exp (J/m$^2$) | SD |
|---|---|---|---|---|---|---|
| 0 | 68 | 68 | 68 | 68 | 63 | 9 |
| 2 | 61 | 82 | 97 | 110 | 70 | 12 |
| 5 | 153 | 102 | 116 | 151 | 77 | 6 |
| 10 | 307 | 137 | 137 | 206 | 80 | 8 |

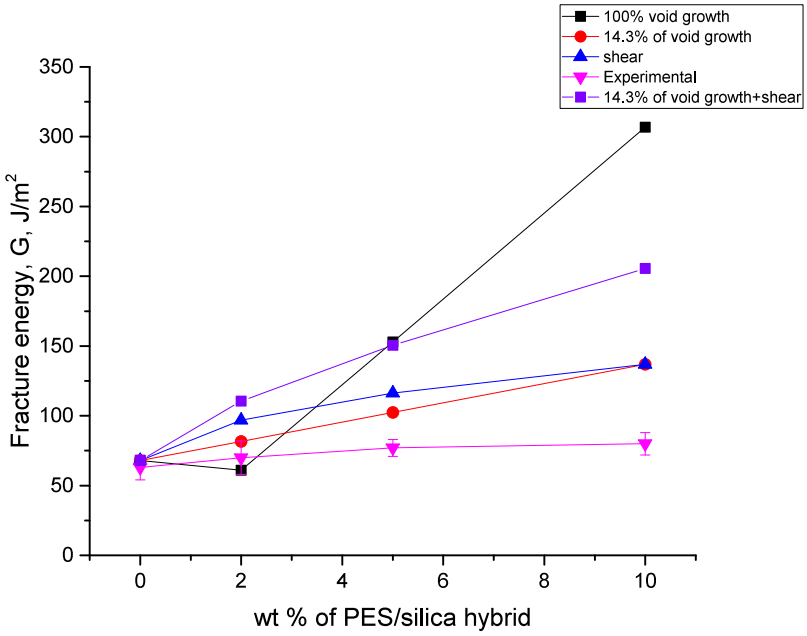


Figure 11.14: Figure showing fracture energy predictions of hybrid PES / silica-modified epoxy

### 11.4.4 Conclusions

The results showed similar behaviour for both ceramic microsphere and PES materials. The effect of saturation in the mixture was large, this was the reason why the experimental results were significantly lower than the predictions, therefore, the optimum toughening effect lies in the medium range of particles used.

## 11.5 Dynamic Mechanical Analysis

### 11.5.1 Introduction

Dynamic mechanical analysis (DMA) was used in determining the rate effect with the use of the time-temperature superpositioning technique [75]. This method is based on the time-temperature equivalence of the viscoelastic properties of polymers. A shifting factor can be found with the use of a master curve, which is the curve at a frequency of 1 Hz.

All the combinations of particles used in this study were tested at low wt% (2 wt%) and high wt% (10 wt%). The glass transition temperature, $T_g$, was found using by curve fitting of the $tan\delta$.

### 11.5.2 DMA tests

Dynamic mechanical analysis was performed using a Q800 dynamic mechanical thermal analyser (DMTA) from TA Instruments, UK. Rectangular specimens of 17.5 mm x 12 mm x 2.9 mm were tested in single cantilever bending of a single frequency using an applied cyclic strain of 0.5 %, in a temperature range from -100 to 200°C, and a temperature ramp of $2^oC$/min. The specimen was clamped in between the movable and stationary grips, while temperature was controlled with five minutes of thermal-soak time to ensure uniform heating in the specimen [30]. In order to prevent problems with missing data, a frequency sweep test is used, which is time-consuming, so there is only 1 test for each sample. The frequency cycle used was:

-Equlibrate at -100$^o$C

-Start measurement loop

  -Isothermal for 5 minutes

  -Frequency Sweep

  -Increment by 10$^o$C

  -Isothermal for 5 minutes

  -Frequency sweep

-Repeat measurement loop until 200$^o$C

When multiple frequencies were used, missing data occurs when the machine switches frequency used. The system would try to stabilise each frequency when switching, but it may not be able to do so sometimes and this causes missing data as it would not be able to oscillate at the same rate as the change in temperature. Ideally tests at individual frequencies would be performed, but because the time of each test is not identical,

hence the results would not overlap properly. There were four logarithmically spaced frequencies (0.1, 1, 10 and 100) tested for each formulation. The increase in frequency had the same effect as increases in test rate, so the 4 frequencies used represent 4 different rates of testing and the effect of rate would be determined. These results would be compared with the low-temperature SENB test results and the overall trend could be obtained without variations from dynamic effects. The rate of each test was found from the displacement against time graph. Storage modulus values were used in determining DMA results. This method measured the elastic and loss moduli of each material at different frequencies, time or temperature, hence characterising the thermomechanical behaviour of the material. The functional properties such as damping behaviour and effectiveness of cure can be represented by plotting moduli and tan delta graphs. The peak in the Tan$\delta$ curve represents the glass transition temperature [30]. Therefore, DMA is often used in determining effects of treatments and additives [30]. DMA measures the complex modulus and the phase difference between the oscillatory loading of the sample and its response, and these are used to calculate the storage modulus and the loss modulus. The relationship between the Tan$\delta$ and the moduli is given by:

$$Tan\delta = \frac{E''}{E'} \tag{11.1}$$

where $E'$ = storage (elastic) modulus in bending, $E''$ = loss (viscous) modulus in bending, and Tan $\delta$ = tan delta.

The time-temperature superpositioning study from Huang et al. [75] used similar testing conditions and found that a shift factor can be applied to shift the data along the frequency axis to forms a master curve. Different sets of shifting factors can be obtained from the different master curves of each material, this shift factor indicates the similarity in their behaviour at high rate. The standard frequency used was 1 Hz, the shift factor is the difference between the standard frequency and the frequency used. However, in this case, results would be forced to be in factor of 10, so the use of curve fitting for the shift factor was more reliable.

### 11.5.3 DMA results

The DMA results are presented using a log scale to show a better comparison. The curve at a frequency of 1 Hz acts as a master curve for the shift. Some of the results showed that no shift is required, and the other shifted data were all in factors of 10, except for CSR 10 wt% and hybrid ceramic microsphere 10 wt%, they had 20$^o$C shift. The shift pattern was very similar for the low wt% materials, most of them had the

same shift curve. Most of the results did not show a very clear relationship, but silica modified specimens showed the same curve for both low and high wt% used. There was a higher shift factor in the higher wt% specimens for all of the formulations. When the frequency used was increased, a higher $T_g$ was found and hence produced a higher shift factor.

The results were similar to previous studies [11], but with different formulations used, the results cannot be compared directly. There were only unmodified epoxy DSC results, hence they cannot be compared with the results here. High and low wt% comparison was considered. Figures 11.18 to 11.20 show the $T_g$ of low and high wt% of particles and the curve fit gradient of them.

The $T_g$ obtained from storage modulus is used instead of tan delta, as it can provide more precise results. This is because the results were in a factor of 10 measurements (as the temperature measurements were at 10 °C intervals), the resulting temperature from these data could only be in the factor of 10 in the results table. As factor of 10 results would put results not in a factor of 10 into the same value, the differences in $T_g$ cannot be found. However, with the tangent fitting method, the results region is not affected with the factor of 10 temperature scale. $T_g$ is found by the intercept of tangents to the plot of storage modulus, see Figure 11.15. A curve fit gradient graph was produced by comparing the difference of gradient between the standard and the wt% tested, see Figure 11.20. An example of storage modulus and tan delta graphs of unmodified epoxy are included in Figures 11.16 and 11.17, and show the effect of test frequency.

$T_g$ increases as frequency increases, as expected, and the $T_g$ gradient against frequency is constant for all materials. As the epoxy matrix was the same in all cases, it is expected that $T_g$ does not change for all the formulations for a single frequency [63], and the materials would have a higher $T_g$ when the test rate increases. Some of the $T_g$ is reduced, particles appear to be reducing the crosslink density - interfering with the formation of polymer network. There was an about 40°C difference in $T_g$ for all frequencies tested for all formulations in 2 wt% specimens, and about 45°C difference in 10 wt% specimens. The drop of $T_g$ was different for the different wt%. $T_g$ for 2 wt% CSR modified epoxy was lower than $T_g$ of unmodified epoxy, this could be due to the modulus effect with CSR particles. Frequency sweep was not used in other studies, the difference in setting can affect the results produced, and hence caused some variations in $T_g$.

There is no trend that can be found and the shift factors were different for the different particles. It is generally assumed that the different types of particles will behave in a

similar manner and have a similar effect but this is not indicated in these results. The different, unpredictable effect of each formulation shows that the method used might not be appropriate for finding the changes in behaviour, for example taking the gradient may not be the best approach for this. This method may be useful only for some materials.

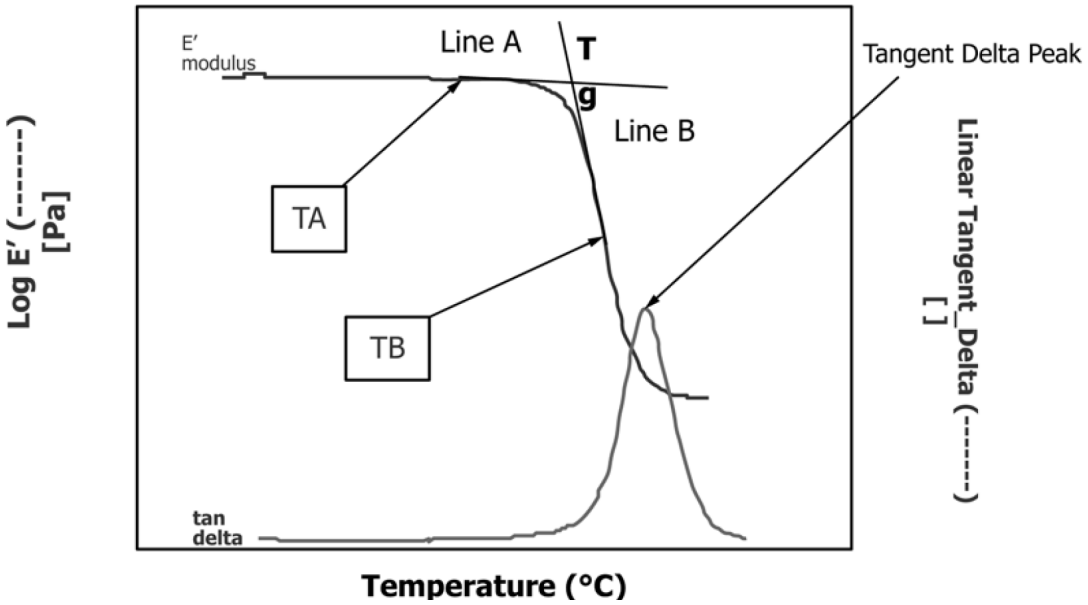


Figure 11.15: DMA tangents for calculation of $T_g$ [76]

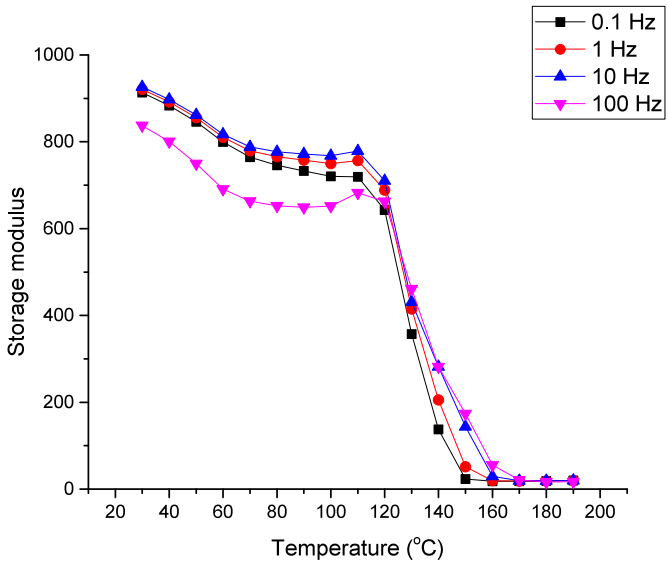


Figure 11.16: Storage modulus of unmodified epoxy DMA specimen

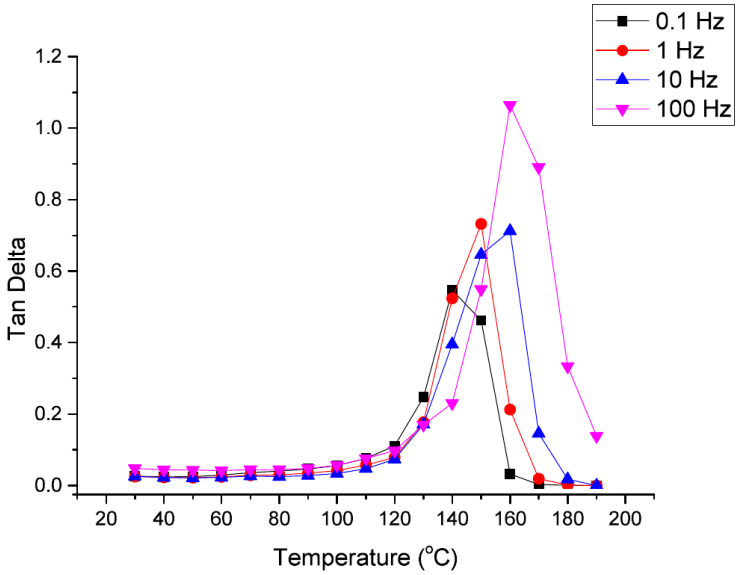


Figure 11.17: Tan delta graph of unmodified epoxy DMA specimen

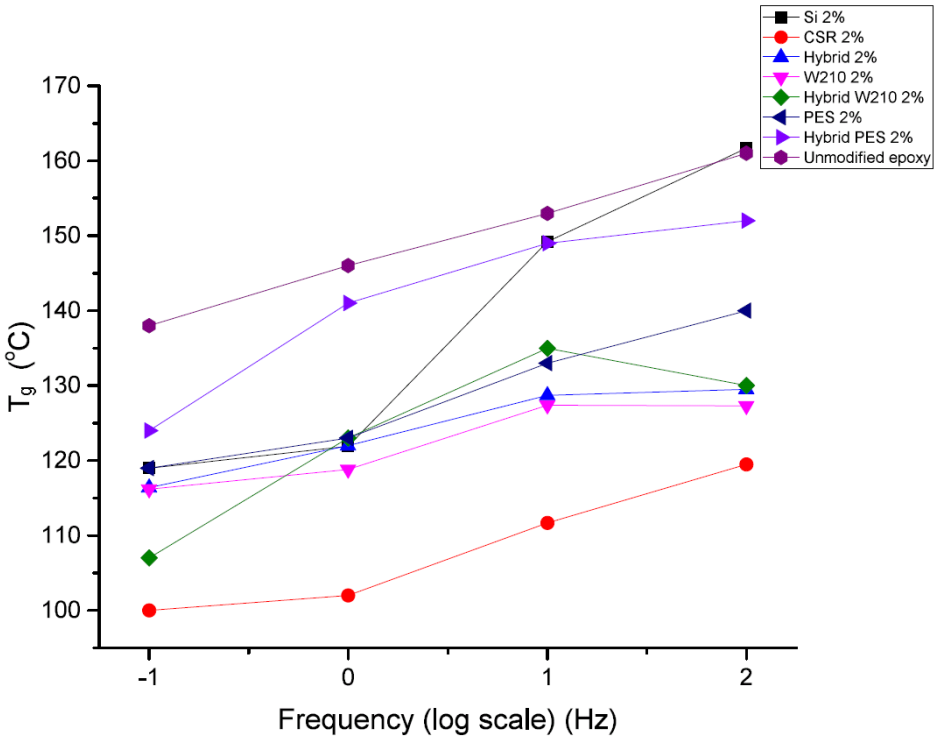


Figure 11.18: $T_g$ versus frequency for epoxy modified with 2 wt% of particles

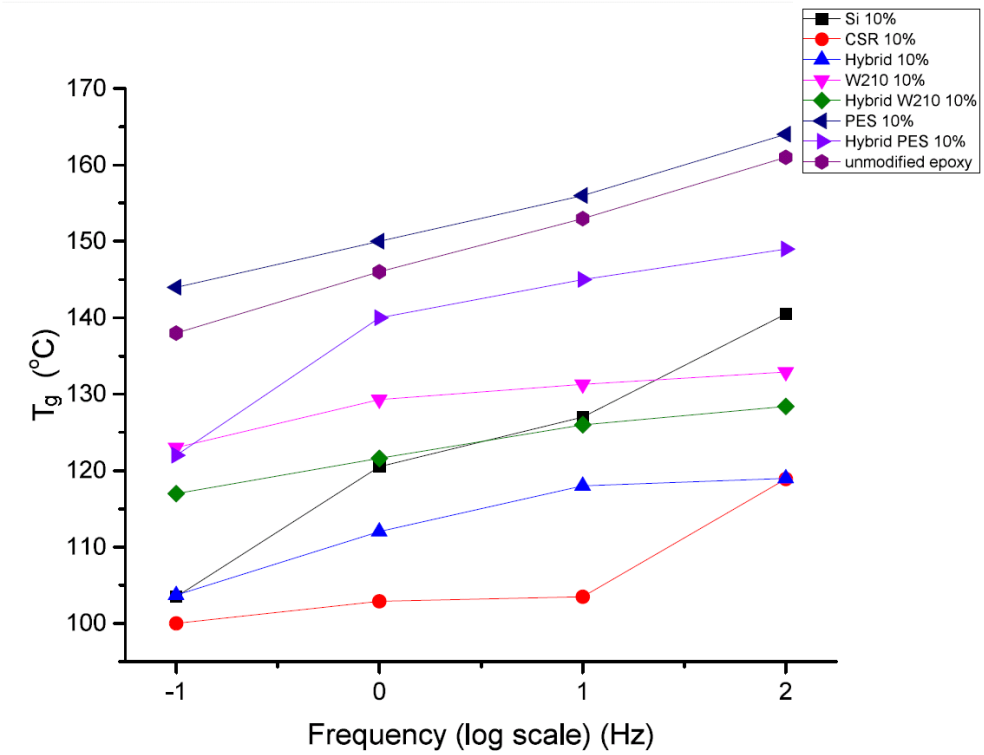


Figure 11.19: $T_g$ versus frequency for epoxy modified with 10 wt% of particles

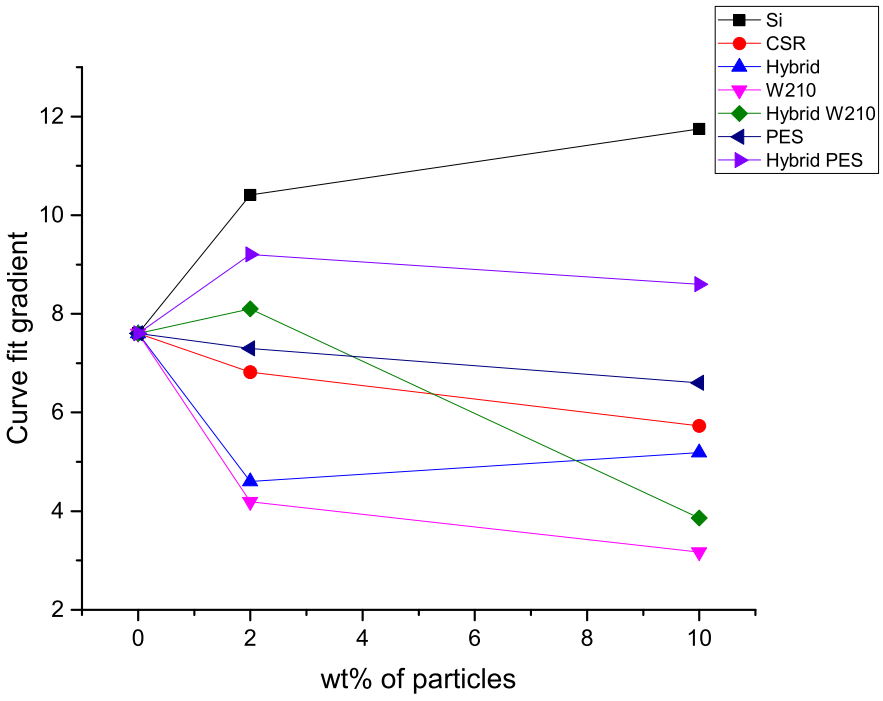


Figure 11.20: $T_g$ curve fit gradient

### 11.5.4 DMA conclusions

The use of DMA study has provided some insight of rate-controlled mechanical testing without dynamic effects. Rate effect was investigated with the use of time-temperature superpositioning technique. It is expected that the DMA results would explain more regarding the rate effects seen in the tests and in SEM images. A shifting factor was found by comparing the storage modulus curves different frequencies with the master curve (1 Hz). High and low wt% comparison was considered. A curve fit gradient graph was produced by comparing the difference of gradient between the standard and the wt% tested, see Figure 11.20.

There is no trend that can be found and the shift factors were different for different particles. It is suggested that different approach (for example, different from taking the gradient for $T_g$) in finding the changes in behaviour should be performed, as the differences in response to the method can be due to the different materials used.

# Chapter 12

# Conclusions

This project studied the properties of epoxy modified using hard or soft particles and hybrids which combined both types. Both nanoparticles and microparticles were used. The hard particles were silica nanoparticles (20 nm in diameter) and ceramic microspheres (13 $\mu$m in diameter). The soft particles were core-shell rubber (CSR) particles (nominally 360 $\mu$m in diameter) and polyethersulfone (PES) which phase separates into particles during curing of the epoxy. The hybrids used silica / CSR, ceramic microspheres / CSR and PES / silica nano-particles.

This work aimed to provide insight to the fracture of modified epoxies using the established fracture mechanics approach. The first stage of the work was to compare the different weight % of silica, CSR and hybrid particles added into epoxy, studying their fracture surfaces by imaging using field emission gun scanning electron microscopy, and comparing their mechanical properties with finite element modelling predictions using Abaqus software. An anhydride-cured epoxy was used, which was cured at 165°C and has a glass transition temperature, $T_g$, of about 140°C. A fracture energy of 68 $J/m^2$ was measured for the unmodified epoxy. The next step of the project was to investigate the effect of test rate on the fracture behaviour. It was expected that high rate would enhance brittle failure, and toughening mechanisms would be reduced, due to the lower energy dissipation at the crack tip. There were higher fracture energy values found at high rate tests but SEM images did not reveal significant changes on the fracture surfaces.

Tensile tests were performed to allow the fracture energy to be calculated from the SENB results. The Young's modulus increased when the wt% of particles was increased for all formulations, but the increase was small, there were similar Young's modulus values among all specimens. The fracture energy values from the SENB tests generally showed a more stable increase among all wt% of particles. Due to the presence of stick-slips in the TDCB tests, it is not possible to compare these fracture energy values with

non-stick-slip situations. However, these data were also compared with the model predictions, and hence, correct estimations of fracture energy values were possible. There were difficulties in analysing the data due to the dynamic effects at high rate, and large standard deviations were found. There was no clear trend of increase in fracture energy found in all 3 formulations (silica, CSR and hybrid), although some results from higher rate show higher fracture energy.

To account for the dynamic effects seen in high rate SENB, low temperature SENB tests were performed. It was found that fracture of the rubber-modified-epoxy was highly affected by temperature and test rate, fracture energy increased when specimens were tested at low temperature, and this effect was more significant at -80°C.

SEM imaging was performed for investigating the failure mechanisms of the particle modified epoxies. The toughening mechanisms of the silica particles were not clear, as the particles cannot be revealed very well in the images. Particle debonding and void growth were expected for the silica particles, and from the fracture results, similar behaviour was observed when compared to previous studies. A higher % of debonding and void growth expected when a small wt% of silica nanoparticles is added, and this is supported by the relatively high fracture energies measured at low wt% of silica. The nominally 360 $\mu$m diameter CSR particles used were made up of small CSR particles approximately less than 1 $\mu$m in diameter, hence the mechanisms were not expected. There were a lot of small particles broken and flow in the epoxy during mixing, a lot of river lines and debonding was found on the fracture surfaces. In the large CSR particles, particles deformation was found. There was no synergy found in silica / CSR modified epoxy.

For ceramic microsphere modified specimens, the particles diameter was relatively small (13 $\mu m$) compared to the crack opening displacement, so crack pinning cannot occur, only debonding and void growth can be found. The particles were found to be very evenly spread in the images. As the PES particles were dissolved in a solvent before mixing in with the epoxy, particles formed different shapes and sizes at different concentrations or even at different regions. There was some local phase inversion found in the high wt% specimens, and failure looked different for different wt% specimens. There was pull out of the particles in most images and some brittle particles pull off was found in the 5 wt% specimens.

All the results produced were then used in finite element modelling of TDCB and SENB specimens the models predicted the force at fracture, but due to the presence of stick-slips in TDCB, force to force comparison cannot be made. There were some good agreements for the TDCB quasi-static model, but due to the difficulty in analysing

high rate TDCB results, there were only three crack lengths that can be found in each specimen, and with stick-slips and dynamic effects, experimental values were very different in each set and hence affected the prediction values when these input values were used. There was an increase in displacement when fracture energy increases for all TDCB specimens, the displacements were larger than experimental displacements, but within a reasonable range.

FEA models of all the SENB tested conditions were produced, the predictions were not similar to experimental results but were within a reasonable range. This could be due to the variation produced during experiments. The highest forces in SENB were affected by the crack length, which can produce variations in the comparisons. The range of predictions were similar, this can be because the properties of cohesive zone were the same. Therefore, more investigations in FE model predictions of adhesive models are needed, especially for understanding cohesive properties.

However, the analytical modelling shows rather successful results in predicting the modulus and fracture energy. This is due to the specific understanding of the polymer behaviour in the models, so it is more reliable in this application when compared to other modelling methods.

Summary of key findings:

An increase in fracture energy when wt% of particles increases is found for most specimens for both TDCBs and SENBs. Higher fracture energy values were found in both high rate and low temperature tests for all formulations when compared to quasi-static and room temperature tests.

SEM imaging did not reveal all the mechanisms, but the relatively high fracture energy at low wt% of silica confirms the hypothesis that at low wt%, more than 14.3% of the silica particles undergo debonding and void growth. For ceramic microsphere modified epoxy, as the particles were relatively small (13 $\mu$m), main toughening mechanisms were debonding and void growth. PES modified epoxy shows different structures at different wt% as they were dissolved before mixing with the epoxy. Some brittle particles tear off were found at low wt%, while some local phase inversion was found at high wt%. Debonding and cavitation were found as the main toughening mechanisms for the other particles used. The different testing conditions did not produce different fracture surfaces.

FEA models and analytical models were produced for all combinations of formulations, predictions were not similar to experimental results in FEA model but predictions agreed very well with experimental results in analytical models.

# Chapter 13

# Further work

There are three aspects of further work suggested from this study: the experimental processes, the materials (particles) with different geometries used and the FE modelling approach.

1.Experimental Processes

In this study, single edge notch bend (SENB) and tapered double cantilever beam (TDCB) geometries were used to measure the fracture energies of the particle modified epoxies. With the use of SENB, cohesive failure was unstable; while TDCB had interfacial failure or a mixture of stick / slips and stable crack growth. It has been found that tough materials often give cohesive, stable failure for TDCB, therefore brittle materials, such as the formulations in this study, do not give stable crack growth and failure can be interfacial. With the use of different geometries, such as compact tension (CT), stable and cohesive cracks can be measured. This can produce more data per sample when compared to SENB tests, although the samples are much larger and so require more material and more machining to produce the specimens. The CT geometry also has an advantage in high rate testing when compared to TDCB, because CT has larger displacement as the samples are less stiff, which makes displacement recording more accurate using the high speed camera. The reduced stiffness may also reduce the dynamic effects seen in the high rate tests.

It may also be useful to study the formulations with the use of other geometries: e.g. double lap joint (DLJ), peel test, four point bending, and to then compare their fracture energies under different conditions (under low temperature, high rate). The different geometries used can produce different effects at different conditions, as only DCB and TDCB had been used in high rate study. By using different geometries, the variables regarding geometries used can be compared, especially for the stick-slips which occur in the TDCB tests, and therefore the SENB geometry used provided unstable and cohesive cracks.

It is difficult to increase the intervals of low temperature measurements, but more low temperature testing can be performed to reduce variations of results due to rapid temperature changes. With the use of low temperature TDCB geometry, the measured fracture energy can be compared with the low temperature results from the SENB tests performed. Low temperature TDCB tests can be performed using the same temperature chamber used for the SENB tests. The high speed camera can be set up at the window of the chamber and the crack growth would be monitored, with the crack times recorded, hence all the crack information can be found. The use of TDCB may allow more data to be collected, as only one $G_c$ value can be calculated from an SENB specimen even if failure is stick/slip. However, interfacial failure can occur with the TDCB, as explained above.

The load predictions from the high rate FE model can be used in finding the predicted fracture energies, as there is no accurate measurement of load can be done under high rate test.

The duration of breaking of a high rate TDCB joint at 1 m/s had an average of 32.82 $\mu$s, with 145 frames. As the speed increases, the number of frames was not enough for finding the crack length. The whole ruler is needed for all of the frames, with this specimen length (240 mm), the number of frames available for analysis was limited. The use of a higher resolution high speed camera would allow more data to be acquired. Reduction of dynamic effects would allow data to be used at higher test rates. This could be done by using a locking lost motion device for the TDCB tests, preventing bouncing between the contact points.

2. Materials

It would be useful to test the formulations with a target specific application (e.g. in automotive, aerospace or denture use), by producing relevant composite, film or coating specimens for fracture and hardness testing. With the use of fibre composite specimens, fracture testing in other modes (mode II and mixed mode I/II) is possible. Other properties tests such as fatigue and durability tests would be useful to fully characterise the performance of the materials.

An investigation into the effect of adding a bonding agent can also be performed, as a use of a bonding agent such as a silane in particle-modified epoxy is not commonly used. However, the used of bonding agent was found very useful in improving bonding strength in dental adhesive applications. Bonding produces a linkage between the particles and the matrix, increasing the adhesion and potentially increasing the fracture energy due to higher deformation before the particles debond from the epoxy. The use of bonding agent in the particles use in this study (silica, CSR, ceramic microsphere and PES) had

never been performed.

There were different geometries found with the PES particles, most of the particles used in epoxy are spherical, hence the effect of particles with different geometries is not clearly known. More study into the effect of the geometries of particles can be performed initially in FE modelling for predicting the fracture properties of particle modified epoxies. Different geometries of the same size particles could be used for comparison. FE models of different geometry particles using experimental tensile and fracture values can show some different behaviour, when different geometries with different sizes of particles were used, e.g. large and small particles and hard and soft particles. Also analytical modelling can be performed for predictions of the modulus and fracture properties.

There is a more significant effect in the use of different volume fractions than in the use of different particle sizes, therefore more investigation into the volume fraction effect should be performed, for example with analytical modelling, for calculating the predicted fracture energy. It is also useful to model the effect of volume fraction, as there is a limit to the amount of volume fraction can be done in experiments (due to the increase in viscosity of the particle modified epoxy resin), the use of FE models can predict the effect of volume fraction. This would provide an indication of whether there is a need for the use of high volume fractions with a different processing method.

For the particles count, the use of images with the same brightness, contrast, resolution and image size would improve the consistency of the count results. By inputting more selection specifications of different particles, and customising the conditions with the materials used (which means write it all out in matlab, not using packages available, as they are designed for cells counting), would provide more accurate counts of the particles present. This would allow features such as river lines to be automatically excluded from the calculated area%. Automation of the analysis would also allow more SEM images to be analysed, giving more information about the distribution of the particles.

3. Finite Element Modelling

Ways to improve the FE modelling predictions include to write scripts to make a more automatic testing system, input more information of the material and the properties expected in the input file.

There needs to be a better understanding of the parameters that affect the cohesive element and cohesive zone behaviour in the FE modelling, and the relationship of the material properties to their failure mechanisms. The cohesive zone properties are uncertain even in tough materials, hence there is even less understanding in brittle materials. There were different cohesive properties values found in different studies, sometimes only one set of values can be fitted, which is not repeatable, so the suitability of cohesive

zone model approach is questionable. There are other studies that use the other factors there (such as damage initiation, stress at damage initiation and initiation stiffness), but the results were similar. This means that a systematic variation of the cohesive zone parameters cannot be undertaken at present, which would help to understand the behaviour of the cohesive zone. The use of different FE modelling software (such as MSC. Marc, OOfem and ANSYS) to compare the results found with Abaqus may be beneficial. As different software solves problems slightly differently, more information about the cohesive element behaviour can be found.

Measurement of the cohesive properties directly from experiments e.g. using circumferentially notched tensile specimens has been attempted in the literature, but the predicted values of $G_c$ produced have not given good agreement with experimental fracture energies. However, this method has the potential to enable greater understanding of the cohesive zone properties.

# References


[1] B. B. Johnsen, A. J. Kinloch, R. D. Mohammed, A. C. Taylor, and S. Sprenger, "Toughening mechanisms of nanoparticle-modified epoxy polymers," *Polymer*, vol. 48, no. 2, pp. 530–541, 2007.

[2] T. H. Hsieh, A. J. Kinloch, K. Masania, A. C. Taylor, and S. Sprenger, "The mechanisms and mechanics of the toughening of epoxy polymers modified with silica nanoparticles," *Polymer*, vol. 51, no. 26, pp. 6284–6294, 2010.

[3] T. H. Hsieh, A. J. Kinloch, K. Masania, J. Sohn Lee, A. C. Taylor, and S. Sprenger, "The toughness of epoxy polymers and fibre composites modified with rubber microparticles and silica nanoparticles," *Journal of Materials Science*, vol. 45, no. 5, pp. 1193–1210, 2010.

[4] R. D. Mohammed, B. B. Johnsen, A. J. Kinloch, A. C. Taylor, and S. Sprenger, *Toughening mechanisms of nanoparticle-modified epoxy polymers*. Boca Raton: Crc Press-Taylor & Francis Group, 2008.

[5] J. Chen, "Toughening Epoxy Polymers and Carbon Fibre Composites with Core-Shell Particles, Block Copolymers and Silica Nanoparticles," *Mechanical Engineering Department, Imperial College London, PhD*, 2013.

[6] A. J. Kinloch, "Adhesives in engineering," *Proceedings of the Institution of Mechanical Engineers Part G-Journal of Aerospace Engineering*, vol. 211, no. G5, pp. 307–335, 1997.

[7] P. Dittanet and R. A. Pearson, "Effect of silica nanoparticle size on toughening mechanisms of filled epoxy," *Polymer*, vol. 53, no. 9, pp. 1890–1905, 2012.

[8] M. Imanaka, Y. Takeuchi, Y. Nakamura, A. Nishimura, and T. Iida, "Fracture toughness of spherical silica-filled epoxy adhesives," *International Journal of Adhesion and Adhesives*, vol. 21, no. 5, pp. 389–396, 2001.

[9] Y. Huang and A. J. Kinloch, "Modelling of the toughening mechanisms in rubber-modified epoxy polymers - Part I Finite element analysis studies," *Journal of Materials Science*, vol. 27, no. 10, pp. 2753–2762, 1992.

[10] A. J. Kinloch, S. J. Shaw, D. A. Tod, and D. L. Hunston, "Deformation and fracture behaviour of a rubber-toughened epoxy: 1. Microstructure and fracture studies," *Polymer*, vol. 24, no. 10, pp. 1341–1354, 1983.

[11] G. Giannakopoulos, K. Masania, and A. C. Taylor, "Toughening of epoxy using coreshell particles," *Journal of Materials Science*, vol. 46, no. 2, pp. 327–338, 2011.

[12] A. C. Garg and Y.-W. Mai, "Failure mechanisms in toughened epoxy resins A review," *Composites Science and Technology*, vol. 31, no. 3, pp. 179–223, 1988.

[13] A. C. Garg, "Failure Prediction in Toughened Epoxy Resins," *Composites Science and Technology (1988) 225-242*, vol. 31.

[14] J. Pan and S.-H. Lin, "6 - Fracture Mechanics and Fatigue Crack Propagation," in *Fatigue Testing and Analysis* (Y.-L. Lee, J. Pan, R. B. Hathaway, and M. E. Barkey, eds.), pp. 237–284, Burlington: Butterworth-Heinemann, 2005.

[15] J. H. Lee, "The fracture behaviour of nano-particle toughened epoxy adhesives," *Mechanical Engineering Department, Imperial College London, PhD*, 2006.

[16] S. Bandyopadhyay, "Review of the microscopic and macroscopic aspects of fracture of unmodified and modified epoxy-resins," *Materials Science and Engineering A-Structural Materials Properties Microstructure and Processing*, vol. 125, no. 2, pp. 157–184, 1990.

[17] R. Bagheri, B. T. Marouf, and R. A. Pearson, "Rubber-Toughened Epoxies: A Critical Review," *Polymer Reviews*, vol. 49, no. 3, pp. 201–225, 2009.

[18] C. W. Wise, W. D. Cook, and A. A. Goodwin, "CTBN rubber phase precipitation in model epoxy resins," *Polymer*, vol. 41, no. 12, pp. 4625–4633, 2000.

[19] T. Adachi, M. Osaki, W. Araki, and S.-C. Kwon, "Fracture toughness of nano- and micro-spherical silica-particle-filled epoxy composites," *Acta Materialia*, vol. 56, no. 9, pp. 2101–2109, 2008.

[20] P. Dittanet and R. A. Pearson, "Effect of bimodal particle size distributions on the toughening mechanisms in silica nanoparticle filled epoxy resin," *Polymer*, vol. 54, no. 7, pp. 1832–1845, 2013.

[21] P. Dittanet and R. A. Pearson, "Effect of silica nanoparticle size on toughening mechanisms of filled epoxy," *Polymer*, vol. 53, no. 9, pp. 1890–1905, 2012.

[22] B. B. Johnsen, A. J. Kinloch, and A. C. Taylor, "Toughness of syndiotactic polystyrene/epoxy polymer blends: microstructure and toughening mechanisms," *Polymer*, vol. 46, no. 18, pp. 7352–7369, 2005.

[23] C. M. Manjunatha, N. Jagannathan, K. Padmalatha, A. C. Taylor, and A. J. Kinloch, "The fatigue and fracture behavior of micron-rubber and nano-silica particles modified epoxy polymer," *International Journal of Nanoscience*, vol. 11, no. 03, p. 1240002, 2012.

[24] H.-Y. Liu, G.-T. Wang, Y.-W. Mai, and Y. Zeng, "On fracture toughness of nanoparticle modified epoxy," *Composites Part B: Engineering*, vol. 42, no. 8, pp. 2170–2175, 2011.

[25] J. Chen, A. J. Kinloch, S. Sprenger, and A. C. Taylor, "The mechanical properties and toughening mechanisms of an epoxy polymer modified with polysiloxane-based core-shell particles," *Polymer*, vol. 54, no. 16, pp. 4276–4289, 2013.

[26] J. H. Hodgkin, G. P. Simon, and R. J. Varley, "Thermoplastic toughening of epoxy resins: a critical review," *Polymers for Advanced Technologies*, vol. 9, no. 1, pp. 3–10, 1998.

[27] J. Chen and A. C. Taylor, "Epoxy modified with triblock copolymers: morphology, mechanical properties and fracture mechanisms," *Journal of Materials Science*, vol. 47, no. 11, pp. 4546–4560, 2012.

[28] H. M. Chong, "Toughening mechanisms of block copolymer and graphene nanoplatelet modified epoxy polymers," *Mechanical Engineering Department, Imperial College London, PhD*, 2015.

[29] R. D. Mohammed, "Material properties and fracture mechanisms of epoxy nanocomposites," *Mechanical Engineering Department, Imperial College London, PhD*, 2007.

[30] ASTM D5023, "Standard Test Method for Plastics: Dynamic Mechanical Properties: In Flexure (Three-Point Bending)," *ASTM West Conshohocken*, 2007.

[31] A. J. Kinloch, *Adhesion and Adhesives Science and Technology*. London: Chapman and Hall, 1990.

[32] T.-H. Hsieh, "Properties and toughening of silica nanoparticle-and carbon nanotube-modified epoxy polymers," *Mechanical Engineering Department, Imperial College London, PhD*, 2011.

[33] A. J. Kinloch, M. L. Yuen, and S. D. Jenkins, "Thermoplastic-toughened epoxy polymers," *Journal of Materials Science*, vol. 29, no. 14, pp. 3781–3790, 1994.

[34] M. Brett, "Prediction of the preformance of adhesively-bonded composite joints," *Mechanical Engineering Department,Imperial College London, PhD*, 2011.

[35] A. J. Kinloch, S. J. Shaw, and D. L. Hunston, "Deformation and fracture behaviour of a rubber-toughened epoxy: 2. Failure criteria," *Polymer*, vol. 24, no. 10, pp. 1355–1363, 1983.

[36] A. J. Kinloch, "Protocol for the determination of the mode I adhesive fracture energy, $G_{IC}$, of structural adhesives using the double cantilever beam (DCB) and tapered double cantilever beam," *ESIS*, 2008.

[37] BS7991, "Determination of the mode I adhesive fracture energy, $G_{IC}$, of structural adhesives using the double cantilever beam (DCB) and tapered double cantilever beam (TDCB) specimens," *BSI London*, 2009.

[38] B. R. K. Blackman, A. J. Kinloch, M. Paraschi, and W. S. Teo, "Measuring the mode I adhesive fracture energy, $G_{IC}$, of structural adhesive joints: the results of an international round-robin," *International Journal of Adhesion and Adhesives*, vol. 23, no. 4, pp. 293–305, 2003.

[39] A. Adnan and C. T. Sun, "Effect of adhesive thickness on joint strength: A molecular dynamics perspective," *Journal of Adhesion*, vol. 84, no. 5, pp. 401–420, 2008.

[40] ISO13586, "Plastics. Determination of fracture toughness ($G_{IC}$ and $K_{IC}$). Linear elastic fracture mechanics (LEFM) approach," *BSI London*, 2000.

[41] A. Karac, B. R. K. Blackman, V. Cooper, A. J. Kinloch, S. R. Sanchez, W. S. Teo, and A. Ivankovic, "Modelling the fracture behaviour of adhesively-bonded joints as a function of test rate," *Engineering Fracture Mechanics*, vol. 78, no. 6, pp. 973–989, 2011.

[42] R. Bagheri and R. A. Pearson, "Role of particle cavitation in rubber-toughened epoxies: II. Inter-particle distance," *Polymer*, vol. 41, no. 1, pp. 269–276, 2000.

[43] Y. Huang and A. J. Kinloch, "Modelling of the toughening mechanisms in rubber-modified epoxy polymers - Part II A quantitative description of the microstructure-fracture property relationships," *Journal of Materials Science*, vol. 27, no. 10, pp. 2763–2769, 1992.

[44] Blackman B. R. K., A. J. Kinloch, Rodriguez Sanchez, F. Teo, and W. Williams, "The fracture behaviour of structural adhesives under high rates of testing," *Engineering Fracture Mechanics*, vol. 76, no. 18, pp. 2868–2889, 2009.

[45] B. R. K. Blackman, A. J. Kinloch, F. S. Rodriguez-Sanchez, and W. S. Teo, "The fracture behaviour of adhesively-bonded composite joints: Effects of rate of test and mode of loading," *International Journal of Solids and Structures*, vol. 49, no. 13, pp. 1434–1452, 2012.

[46] F. S. Rodriguez Sanchez, "Fracture Behaviour of Automotive Adhesive Joints," *Mechanical Engineering Department, Imperial College London, PhD*, 2008.

[47] B. R. K. Blackman, A. J. Kinloch, Y. Wang, and J. G. Williams, "The failure of fibre composites and adhesively bonded fibre composites under high rates of test. 2. Mode I loading - Dynamic effects," *Journal of Materials Science*, vol. 31, no. 17, pp. 4451–4466, 1996.

[48] B. R. K. Blackman, J. P. Dear, A. J. Kinloch, H. Macgillivray, Y. Wang, J. G. Williams, and P. Yayla, "The failure of fibre composites and adhesively bonded fibre composites under high rates of test. 1. Mode I loading - Experimental studies," *Journal of Materials Science*, vol. 30, no. 23, pp. 5885–5900, 1995.

[49] J. B. Babu, "Predicting the fatigue behaviour of matrices and fibre-composites based upon modified epoxy polymers," *Mechanical Engineering Department, Imperial College London, PhD.*

[50] A. J. Kinloch, D. Maxwell, and R. J. Young, "Micromechanisms of crack-propagation in hybrid-particulate composites," *Journal of Materials Science Letters*, vol. 4, no. 10, pp. 1276–1279, 1985.

[51] A. C. Moloney, H. H. Kausch, T. Kaiser, and H. R. Beer, "Parameters determining the strength and toughness of particulate filled epoxide resins," *Journal of Materials Science*, vol. 22, no. 2, pp. 381–393, 1987.

[52] C. B. Bucknall, "Quantitative approaches to particle cavitation, shear yielding, and crazing in rubber-toughened polymers," *Journal of Polymer Science Part B-Polymer Physics*, vol. 45, no. 12, pp. 1399–1409, 2007.

[53] Y. Huang and A. J. Kinloch, "The sequence of initiation of the toughening micromechanisms in rubber-modified epoxy polymers," *Polymer*, vol. 33, no. 24, pp. 5338–5340, 1992.

[54] F. J. Guild, A. J. Kinloch, and A. C. Taylor, "Particle cavitation in rubber toughened epoxies: the role of particle size," *Journal of Materials Science*, vol. 45, no. 14, pp. 3882–3894, 2010.

[55] T. Kawaguchi and R. A. Pearson, "The effect of particle-matrix adhesion on the mechanical behavior of glass filled epoxies. Part 2. A study on fracture toughness," *Polymer*, vol. 44, no. 15, pp. 4239–4247, 2003.

[56] S. Kunz-Douglass, P. W. R. Beaumont, and M. F. Ashby, "A model for the toughness of epoxy-rubber particulate composites," *Journal of Materials Science*, vol. 15, no. 5, pp. 1109–1123, 1980.

[57] J. Spanoudakis and R. J. Young, "Crack propagation in a glass particle-filled epoxy resin," *Journal of Materials Science*, vol. 19, no. 2, pp. 473–486, 1984.

[58] L. J. Broutman and S. Sahu, "The effect of interfacial bonding on the toughness of glass filled polymers," *Materials Science and Engineering*, vol. 8, no. 2, pp. 98–107, 1971.

[59] Y. Huang and A. J. Kinloch, "The role of plastic void growth in the fracture of rubber-toughened epoxy polymers," *Journal of Materials Science Letters*, vol. 11, no. 8, pp. 484–487, 1992.

[60] Huntsman, "Araldite LY556 Safety data sheet," *Huntsman Advanced Materials, Belgium*, 2004.

[61] Nano-resins, "Albidur HE600 Safety Data Sheet," *Nano resins, Germany*, 2006.

[62] Evonik-Industries, "Nanopox F Products Technical Bulletin," *Evonik Industries, Germany*, 2008.

[63] K. Masania, "Toughening mechanisms of silica nanoparticle-modified epoxy polymers," *Mechanical Engineering Department, Imperial College London, PhD*, 2010.

[64] Sumitomo Chemical, "Technical note: High heat Resistance Amorphous Polymer," *Sumitomo Chemical Company, Tokyo*, 2010.

[65] 3M, "3M Ceramic Microspheres Product information," *3M Center, USA*, 2010.

[66] 3M, "3M Glass Bubbles for resin systems," *3M Center, USA*, 2015.

[67] B. R. K. Blackman, J. P. Dear, A. J. Kinloch, H. MacGillivray, Y. Wang, J. G. Williams, and P. Yayla, "The failure of fibre composites and adhesively bonded fibre composites under high rates of test. 3. Mixed-mode I/II and mode II loadings," *Journal of Materials Science*, vol. 31, no. 17, pp. 4467–4477, 1996.

[68] D. Alvarez Feito, "Fracture mechanics of carbon fibre reinforced plastic to Ti-alloy adhesive joints," *Mechanical Engineering Department, Imperial College London, PhD*, 2012.

[69] K. Masania, A. C. Taylor, A. J. Kinloch, and S. Sprenger, "The fracture of nanosilica and rubber toughened epoxy fibre composites," *Proceedings of American Composites Manufacturing Association (ACMA) Composites and POLYCON '09. Tampa, USA. 2009, ACMA, Arlington, USA.*

[70] F.J. Guild A.J. Kinloch, and A.C. Taylor, "The Debonding of Nanoparticles in Toughened Adhesives, Annual Meeting of the Adhesion Society, 2014, The Adhesion Society: San Diego"

[71] Y. Huang and A. J. Kinloch, "The sequence of initiation of the toughening micromechanisms in rubber-modified epoxy polymers," *Polymer*, vol. 33, no. 24, pp. 5338–5340, 1992.

[72] B. R. K. Blackman, H. Hadavinia, A. J. Kinloch, M. Paraschi, and J. G. Williams, "The calculation of adhesive fracture energies in mode I: revisiting the tapered double cantilever beam (TDCB) test," *Engineering Fracture Mechanics*, vol. 70, no. 2, pp. 233–248, 2003.

[73] P. Martiny, F. Lani, A. J. Kinloch, and T. Pardoen, "A maximum stress at a distance criterion for the prediction of crack propagation in adhesively-bonded joints," *Engineering Fracture Mechanics*, vol. 97, no. 0, pp. 105–135, 2013.

[74] D. Álvarez, B. R. K. Blackman, F. J. Guild, and A. J. Kinloch, "Mode I fracture in adhesively-bonded joints: A mesh-size independent modelling approach using cohesive elements," *Engineering Fracture Mechanics*, vol. 115, pp. 73–95, 2014.

[75] D. Teutenberg, G. Meschut, and O. Hahn, "Estimation of the temperature influence on adhesively bonded joints with time-temperature-superposition," *Proceedings of Annual Meeting of the Adhesion Society 2013, Daytona Beach, USA,2013, The Adhesion Society, Blacksburg.*

[76] ASTM D7028-07 , "Standard Test Method for Glass Transition Temperature (DMA Tg) of Polymer Matrix Composites by Dynamic Mechanical Analysis (DMA)," ASTM West Conshohocken, 2015.

# Appendix A

# Appendix

## A.1 Finite element analysis input files

### A.1.1 Input file-TDCB model

```
*Heading
** Job name: BC=30 Model name: CopyOfload=600X
** Generated by: Abaqus/CAE 6.13-2
*Preprint, echo=NO, model=NO, history=NO, contact=NO
**
** PARTS
**
*Part, name=BOTTOMPART
*Node
      1,    10.019454,          0.
      2,          10., -0.400000006
…
4274, 4275, 4276, 4277, 4278, 4279, 4280, 4281, 4282, 4283
*Nset, nset=BOTTOMLOAD
 23,
** Section: Section-2-ADHESIVE1
*Solid Section, elset=ADHESIVE1, material=ADHESIVE(STANDARD)
,
** Section: Section-3-ADHESIVE3
*Solid Section, elset=ADHESIVE3, material=ADHESIVE(STANDARD)
,
** Section: Section-4-BOTTOMBEAM
*Solid Section, elset=BOTTOMBEAM, material=ALUMINIUM
,
** Section: Section-5-ADHESIVE2
*Solid Section, elset=ADHESIVE2, material=ADHESIVE(STANDARD)
,
*End Part
**
*Part, name=COHESIVE-MESH-1
*Node
```

```
     1,       -310.,          0.


*Nset, nset=ADHESIVE1
   1,   2,   3,   4,  33,  34,  35,  36,  37,  38,  39,  40,  41,  42,  43,  44
  45,  46, 1017, 1018, 1019, 1020, 1021, 1022, 1023, 1024, 1025, 1026, 1027, 1028
*Elset, elset=ADHESIVE1
   1,   2,   3,   4,   5,   6,   7, 4324, 4325, 4326, 4327, 4328, 4329, 4330
*Elset, elset=ADHESIVE2, generate
 4284,  4323,     1
*Nset, nset=ADHESIVE3
...
*Nset, nset=TOPPARTTIE
  5,  8,  10,  11,  13, 117, 118, 119, 120, 121, 122, 123, 124, 125, 126, 127
 …
6449, 6450, 6451, 6452
*Nset, nset=TOPLOAD
 22,
** Section: Section-6-ADHESIVE1
*Solid Section, elset=ADHESIVE1, material=ADHESIVE(STANDARD)
,
** Section: Section-7-ADHESIVE3
*Solid Section, elset=ADHESIVE3, material=ADHESIVE(STANDARD)
,
** Section: Section-8-TOPBEAM
*Solid Section, elset=TOPBEAM, material=ALUMINIUM
,
** Section: Section-9-ADHESIVE2
*Solid Section, elset=ADHESIVE2, material=ADHESIVE(STANDARD)
,
*End Part
**
```

```
**
** ASSEMBLY
**
*Assembly, name=Assembly
**
*Instance, name=COHESIVE-MESH-1-1, part=COHESIVE-MESH-1
      370.,          0.,          0.
*End Instance
**
*Instance, name=BOTTOMPART-1, part=BOTTOMPART
*End Instance
**
*Instance, name=TOPPART-1, part=TOPPART
*End Instance
**
*Nset, nset=Set-3, instance=TOPPART-1
  21,   22,   25,   26,   28,   29,   31,   32,  696,  697,  698,  699,  700,  701,  722,  723
 724,  725,  737,  738,  739,  740,  741,  742,  752,  753,  754,  755,  770,  771,  772,  773
 774,  775,  776,  777,  778,  784,  785,  786,  787,  788,  789,  804,  805,  806,  807,  808
 809,  810,  811,  812, 1029, 1030, 1031, 1032, 1033, 1034
*Nset, nset=Set-4, instance=BOTTOMPART-1
  20,   23,   24,   27,   28,   31,   32,   33,  770,  771,  772,  773,  774,  775,  776,  777
 778,  779,  794,  795,  796,  797,  798,  799,  806,  807,  808,  809,  824,  825,  826,  827
 828,  829,  830,  831,  832,  842,  843,  844,  845,  846,  847,  864,  865,  866,  867,  868
 869,  870,  871,  872, 1029, 1030, 1031, 1032, 1033, 1034
*Nset, nset=BOTTOMPART-1_BOTTOMPARTTIE_CNS_, internal, instance=BOTTOMPART-1
  5,   8,  10,  11,  13,  97,  98,  99, 100, 101, 102, 103, 104, 105, 106, 107
 …
934, 935, 936, 937, 938, 939, 940, 941, 942, 943, 944
*Nset, nset=TOPPART-1_TOPPARTTIE_CNS_, internal, instance=TOPPART-1
  5,   8,  10,  11,  13, 117, 118, 119, 120, 121, 122, 123, 124, 125, 126, 127
```

…

849, 850, 851, 852, 853, 854, 855, 856, 857, 858, 859, 860, 861, 862, 863, 864

865, 866, 867, 868, 869, 870, 871, 872, 873, 874, 875

*Surface, type=NODE, name=BOTTOMPART-1_BOTTOMPARTTIE_CNS__CNS_, internal

BOTTOMPART-1_BOTTOMPARTTIE_CNS_, 1.

*Surface, type=NODE, name=TOPPART-1_TOPPARTTIE_CNS__CNS_, internal

TOPPART-1_TOPPARTTIE_CNS_, 1.

** Constraint: BOTTOMCOHESIVE-1

*Tie, name=BOTTOMCOHESIVE-1, adjust=yes

COHESIVE-MESH-1-1.Surf-2, BOTTOMPART-1_BOTTOMPARTTIE_CNS__CNS_

** Constraint: TOPCOHESIVE-1

*Tie, name=TOPCOHESIVE-1, adjust=yes

COHESIVE-MESH-1-1.Surf-1, TOPPART-1_TOPPARTTIE_CNS__CNS_

*End Assembly

**

** ELEMENT CONTROLS

**

*Section Controls, name=EC-1, ELEMENT DELETION=YES

1., 1., 1.

*Amplitude, name=Amp-1

0., 0., 1., 1.

**

** MATERIALS

**

*Material, name=ADHESIVE(STANDARD)

*Elastic

2900., 0.35

*Material, name=ALUMINIUM

*Elastic

70000., 0.3

```
*Material, name=COHESIVE
*Damage Initiation, criterion=QUADS
60.,60.,60.
*Damage Evolution, type=ENERGY
20.,
*Elastic, type=TRACTION
 1e+06, 1e+06, 1e+06
** ----------------------------------------------------------------
**
** STEP: Step-1
**
*Step, name=Step-1, nlgeom=YES, inc=1000000
*Static, stabilize=0.0002, allsdtol=0.05, continue=NO
0.0001, 1., 1e-08, 0.01
**
** BOUNDARY CONDITIONS
**
** Name: BC-1 Type: Displacement/Rotation
*Boundary, amplitude=Amp-1
Set-3, 1, 1
Set-3, 2, 2, 25.
Set-3, 6, 6
** Name: BC-2 Type: Displacement/Rotation
*Boundary, amplitude=Amp-1
Set-4, 1, 1
Set-4, 2, 2, -25.
Set-4, 6, 6
**
** OUTPUT REQUESTS
**
*Restart, write, frequency=0
```

```
**
** FIELD OUTPUT: F-Output-1
**
*Output, field
*Node Output
CF, RF, U
*Element Output, directions=YES
LE, PE, PEEQ, PEMAG, S, STATUS
*Contact Output
CDISP, CSTRESS
**
** HISTORY OUTPUT: H-Output-3
**
*Output, history
*Node Output, nset=Set-4
RF1, RF2, RF3, RM1, RM2, RM3
**
** HISTORY OUTPUT: H-Output-1
**
*Output, history, frequency=1000
*Node Output, nset=BOTTOMPART-1.BOTTOMLOAD
RF1, RF2, RF3, RM1, RM2, RM3, U1, U2
U3, UR1, UR2, UR3
**
** HISTORY OUTPUT: H-Output-2
**
*Node Output, nset=TOPPART-1.TOPLOAD
RF1, RF2, RF3, RM1, RM2, RM3, U1, U2
U3, UR1, UR2, UR3
*End Step
```

### A.1.2 Input file-SENB model

```
*Heading
** Job name: TDCB_391 Model name: CopyOfload=600X
** Generated by: Abaqus/CAE 6.13-2
*Preprint, echo=NO, model=NO, history=NO, contact=NO
**
** PARTS
**
*Part, name=BOTTOMPART
*Node
      1,    10.019454,          0.
      2,          10., -0.400000006
      3,    20.038908, -0.400000006
      4,    20.038908,          0.
      5,   259.699158,          0.
      6,   259.699158, -0.400000006
      7,         310., -0.400000006
      8,         310.,          0.
      9,   131.189209, -0.400000006
…
6433, 6434, 6435, 6436, 6437, 6438, 6439, 6440, 6441, 6442, 6443, 6444, 6445, 6446, 6447, 6448
 6449, 6450, 6451, 6452
*Elset, elset=Top_load
 3919, 3925, 3931, 3937, 3943, 3949, 3955, 3956, 3962, 3968, 3974, 3980, 3986, 3992, 3998, 4004
 4010, 4016, 4022, 4028, 4034, 4040, 4046, 4052, 4058, 4064, 4070, 4076, 4082, 4088, 4094, 4100
 4106, 4112, 4118, 4124, 4130, 4136, 4142, 4148, 4154, 4160, 4166, 4172, 4178, 4184, 4190, 4196
 4202, 4208, 4214, 4336, 4342, 4348, 4354, 4360, 4366, 4372
** Section: Section-6-ADHESIVE1
*Solid Section, elset=ADHESIVE1, material=ADHESIVE(STANDARD)
,
** Section: Section-7-ADHESIVE3
*Solid Section, elset=ADHESIVE3, material=ADHESIVE(STANDARD)
```

,

** Section: Section-8-TOPBEAM

*Solid Section, elset=TOPBEAM, material=ALUMINIUM

,

** Section: Section-9-ADHESIVE2

*Solid Section, elset=ADHESIVE2, material=ADHESIVE(STANDARD)

,

*End Part

**

**

** ASSEMBLY

**

*Assembly, name=Assembly

**

*Instance, name=COHESIVE-MESH-1-1, part=COHESIVE-MESH-1

      370.,          0.,          0.

*End Instance

**

*Instance, name=BOTTOMPART-1, part=BOTTOMPART

*End Instance

**

*Instance, name=TOPPART-1, part=TOPPART

*End Instance

**

*Nset, nset=Set-3, instance=TOPPART-1

  21,  22,  25,  26,  28,  29,  31,  32, 696, 697, 698, 699, 700, 701, 722, 723

 724, 725, 737, 738, 739, 740, 741, 742, 752, 753, 754, 755, 770, 771, 772, 773

 774, 775, 776, 777, 778, 784, 785, 786, 787, 788, 789, 804, 805, 806, 807, 808

 809, 810, 811, 812, 1029, 1030, 1031, 1032, 1033, 1034

*Nset, nset=Set-4, instance=BOTTOMPART-1

  20,  23,  24,  27,  28,  31,  32,  33, 770, 771, 772, 773, 774, 775, 776, 777

778, 779, 794, 795, 796, 797, 798, 799, 806, 807, 808, 809, 824, 825, 826, 827

828, 829, 830, 831, 832, 842, 843, 844, 845, 846, 847, 864, 865, 866, 867, 868

869, 870, 871, 872, 1029, 1030, 1031, 1032, 1033, 1034

*Nset, nset=top_load, instance=TOPPART-1

21, 22, 25, 26, 28, 29, 31, 32, 696, 697, 698, 699, 700, 701, 722, 723

724, 725, 737, 738, 739, 740, 741, 742, 752, 753, 754, 755, 770, 771, 772, 774

775, 776, 777, 778, 784, 785, 786, 787, 788, 789, 804, 805, 806, 807, 808, 809

810, 812, 1029, 1030, 1031, 1032, 1033, 1034

*Nset, nset=BOTTOMPART-1_BOTTOMPARTTIE_CNS_, internal, instance=BOTTOMPART-1

5, 8, 10, 11, 13, 97, 98, 99, 100, 101, 102, 103, 104, 105, 106, 107

108, 109, 110, 111, 112, 113, 114, 115, 116, 117, 118, 119, 120, 121, 122, 123

…

918, 919, 920, 921, 922, 923, 924, 925, 926, 927, 928, 929, 930, 931, 932, 933

934, 935, 936, 937, 938, 939, 940, 941, 942, 943, 944

*Nset, nset=TOPPART-1_TOPPARTTIE_CNS_, internal, instance=TOPPART-1

5, 8, 10, 11, 13, 117, 118, 119, 120, 121, 122, 123, 124, 125, 126, 127

…

849, 850, 851, 852, 853, 854, 855, 856, 857, 858, 859, 860, 861, 862, 863, 864

865, 866, 867, 868, 869, 870, 871, 872, 873, 874, 875

*Surface, type=NODE, name=BOTTOMPART-1_BOTTOMPARTTIE_CNS__CNS_, internal

BOTTOMPART-1_BOTTOMPARTTIE_CNS_, 1.

*Surface, type=NODE, name=TOPPART-1_TOPPARTTIE_CNS__CNS_, internal

TOPPART-1_TOPPARTTIE_CNS_, 1.

** Constraint: BOTTOMCOHESIVE-1

*Tie, name=BOTTOMCOHESIVE-1, adjust=yes

COHESIVE-MESH-1-1.Surf-2, BOTTOMPART-1_BOTTOMPARTTIE_CNS__CNS_

** Constraint: TOPCOHESIVE-1

*Tie, name=TOPCOHESIVE-1, adjust=yes

COHESIVE-MESH-1-1.Surf-1, TOPPART-1_TOPPARTTIE_CNS__CNS_

*End Assembly

**

```
** ELEMENT CONTROLS
**
*Section Controls, name=EC-1, ELEMENT DELETION=YES
1., 1., 1.
*Amplitude, name=Amp-1
        0.,          0.,          1.,          1.
**
** MATERIALS
**
*Material, name=ADHESIVE(STANDARD)
*Elastic
2900., 0.35
*Plastic
80.,  0.
81., 0.1
82.,  1.
*Material, name=ALUMINIUM
*Elastic
70000., 0.3
*Material, name=COHESIVE
*Damage Initiation, criterion=QUADS
60.,60.,60.
*Damage Evolution, type=ENERGY
391.,
*Elastic, type=TRACTION
1000.,1000.,1000.
** ----------------------------------------------------------------
**
** STEP: Step-1
**
*Step, name=Step-1, nlgeom=YES, inc=1000000
```

```
*Static, stabilize=0.0002, allsdtol=0.05, continue=NO
0.0001, 1., 1e-12, 0.001
**
** BOUNDARY CONDITIONS
**
** Name: BC-1 Type: Displacement/Rotation
*Boundary, amplitude=Amp-1
Set-3, 1, 1
Set-3, 2, 2, 40.
Set-3, 6, 6
** Name: BC-2 Type: Displacement/Rotation
*Boundary, amplitude=Amp-1
Set-4, 1, 1
Set-4, 2, 2, -40.
Set-4, 6, 6
**
** OUTPUT REQUESTS
**
*Restart, write, frequency=0
**
** FIELD OUTPUT: F-Output-1
**
*Output, field
*Node Output
CF, RF, U
*Element Output, directions=YES
LE, PE, PEEQ, PEMAG, S, STATUS
*Contact Output
CDISP, CSTRESS
**
** HISTORY OUTPUT: H-Output-2
```

**

*Output, history, frequency=1000

*Node Output, nset=Set-3

RF1, RF2, RF3, RM1, RM2, RM3, U1, U2

U3, UR1, UR2, UR3

**

** HISTORY OUTPUT: H-Output-1

**

*Node Output, nset=Set-4

RF1, RF2, RF3, RM1, RM2, RM3, U1, U2

U3, UR1, UR2, UR3

*End Step

## A.2 Particles count images

### A.2.1 Silica modified epoxy

Silica 5 wt%

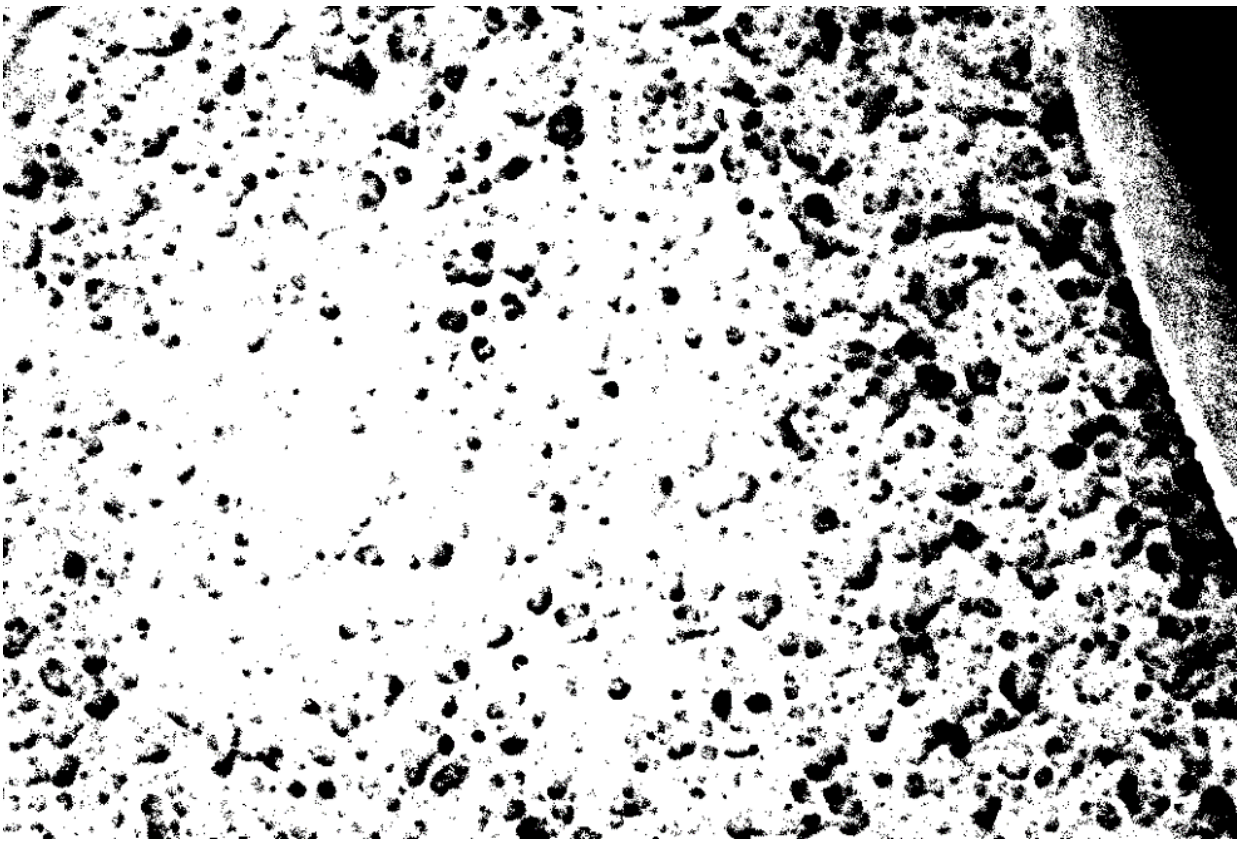

Figure A.1: Binary image of silica 5 wt%

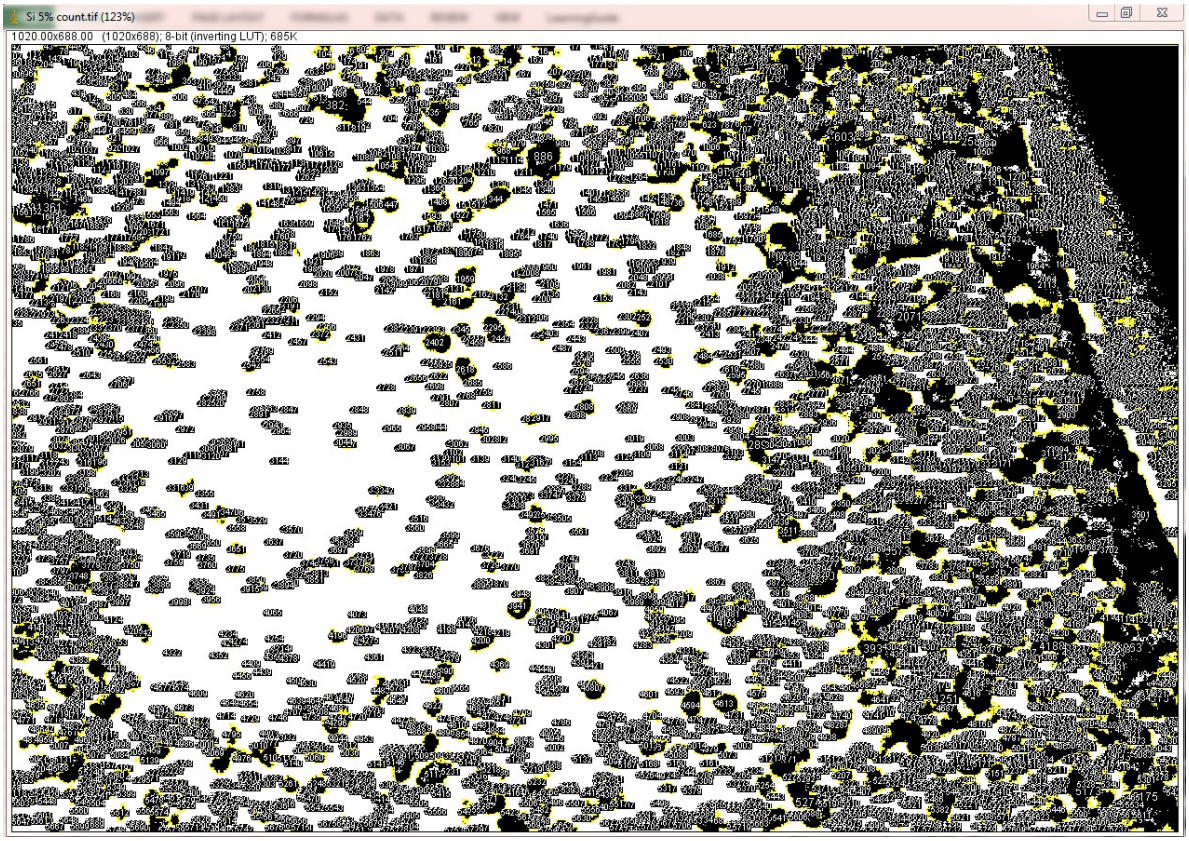


Figure A.2: Particles count images of silica 5 wt%

Silica 15 wt%

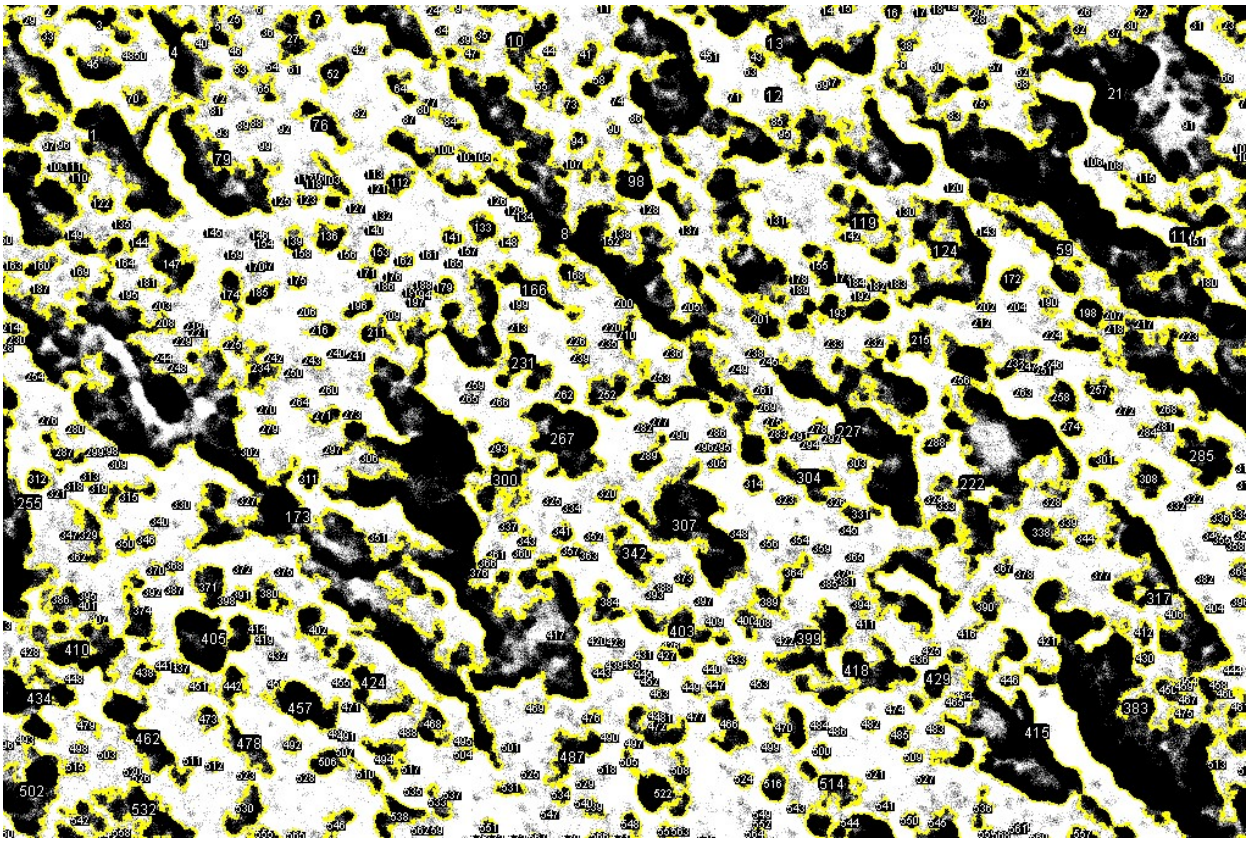

Figure A.3: Particles count images of silica 15 wt%

### A.2.2 Core-shell rubber modified epoxy

CSR 2 wt%

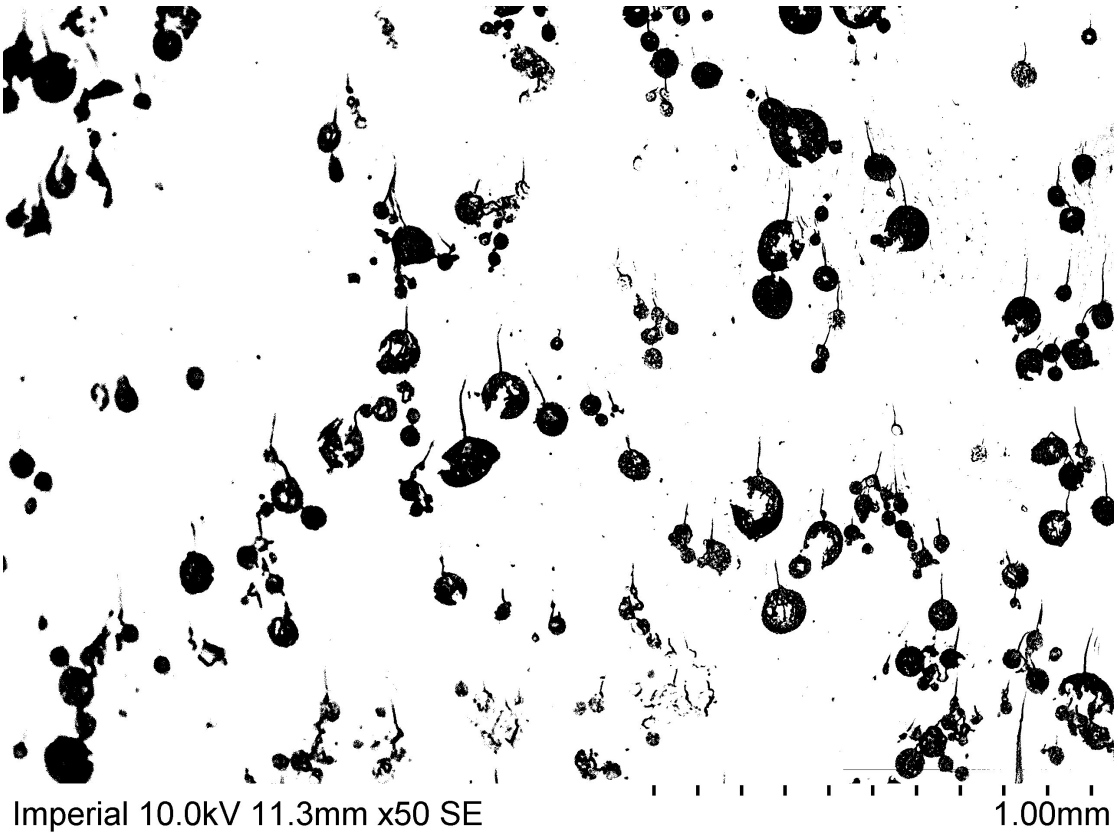


Figure A.4: Binary image of CSR 2 wt%

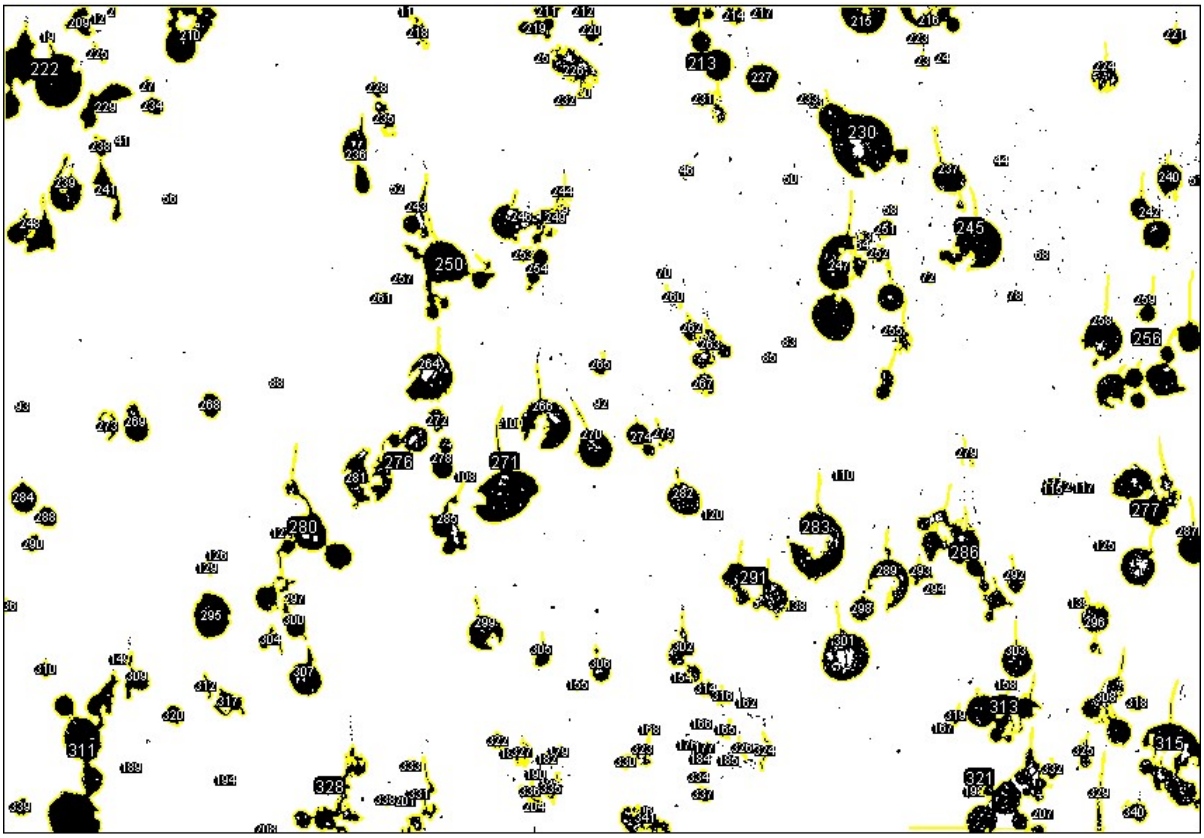

Figure A.5: Particles count images of CSR 2 wt%

CSR 5 wt%

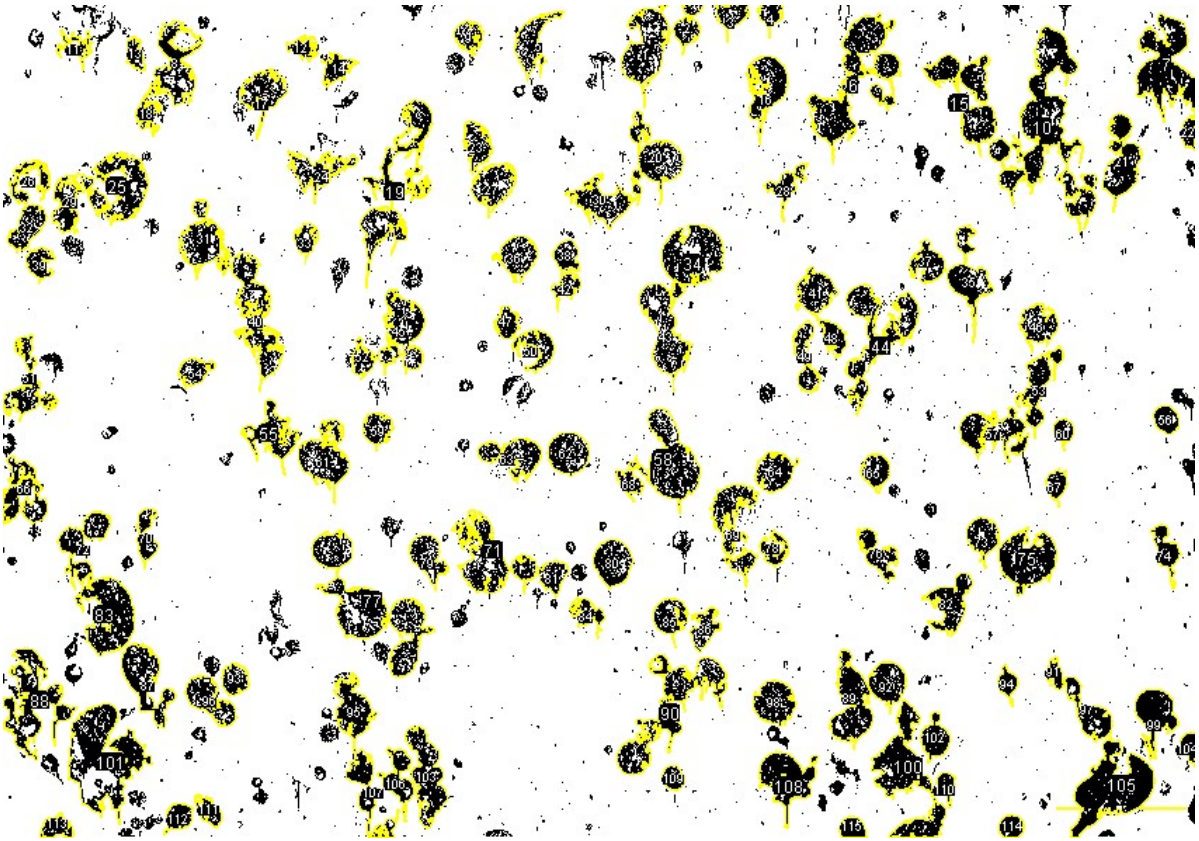

Figure A.6: Particles count images of CSR 5 wt%

Small CSR particles in a big CSR particle

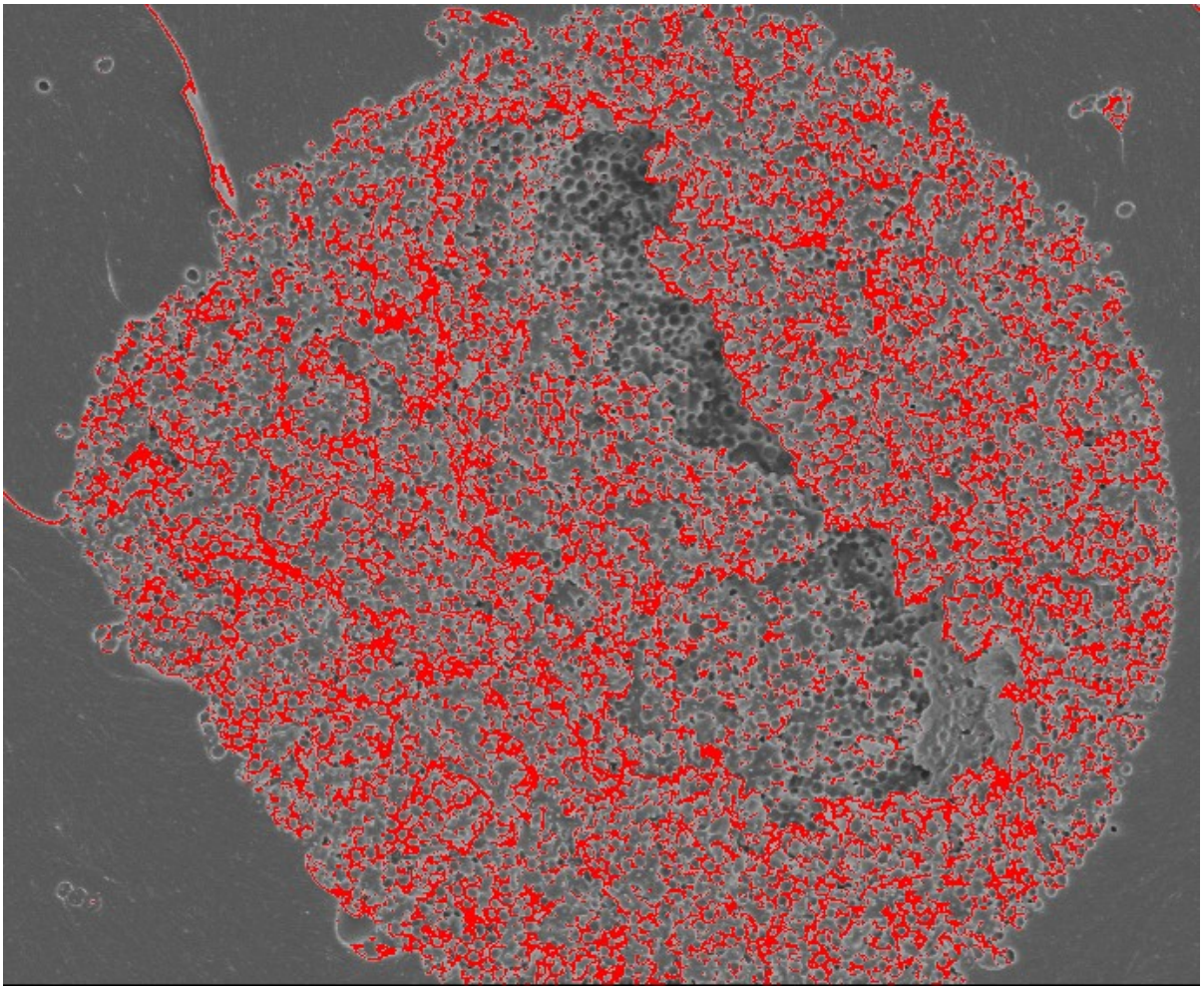

Figure A.7: Binary image of a big CSR particle

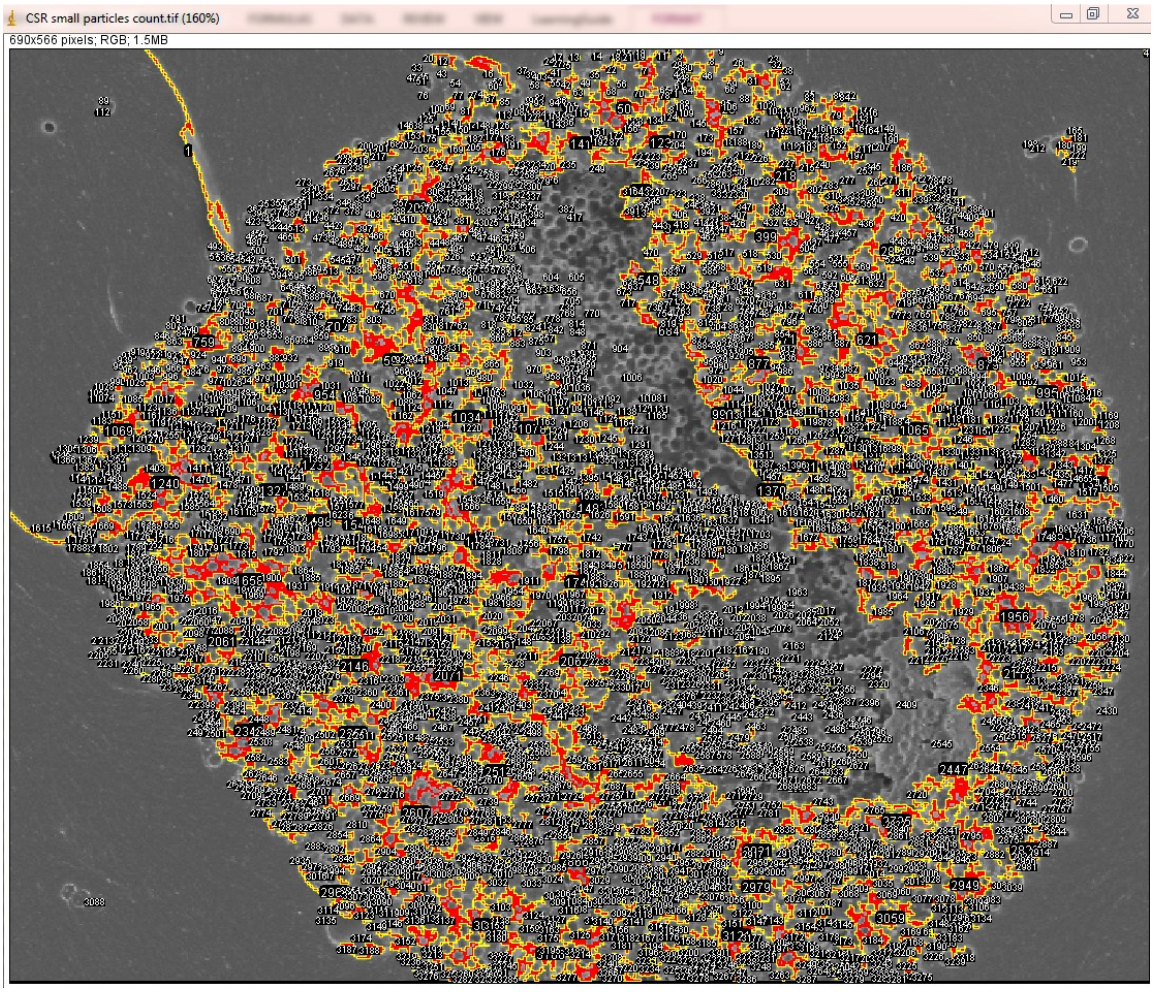


Figure A.8: Particles count images of a big CSR particle

### A.2.3 Alumino silicate ceramic microsphere modified epoxy (W210)

ceramic microsphere 2 wt%

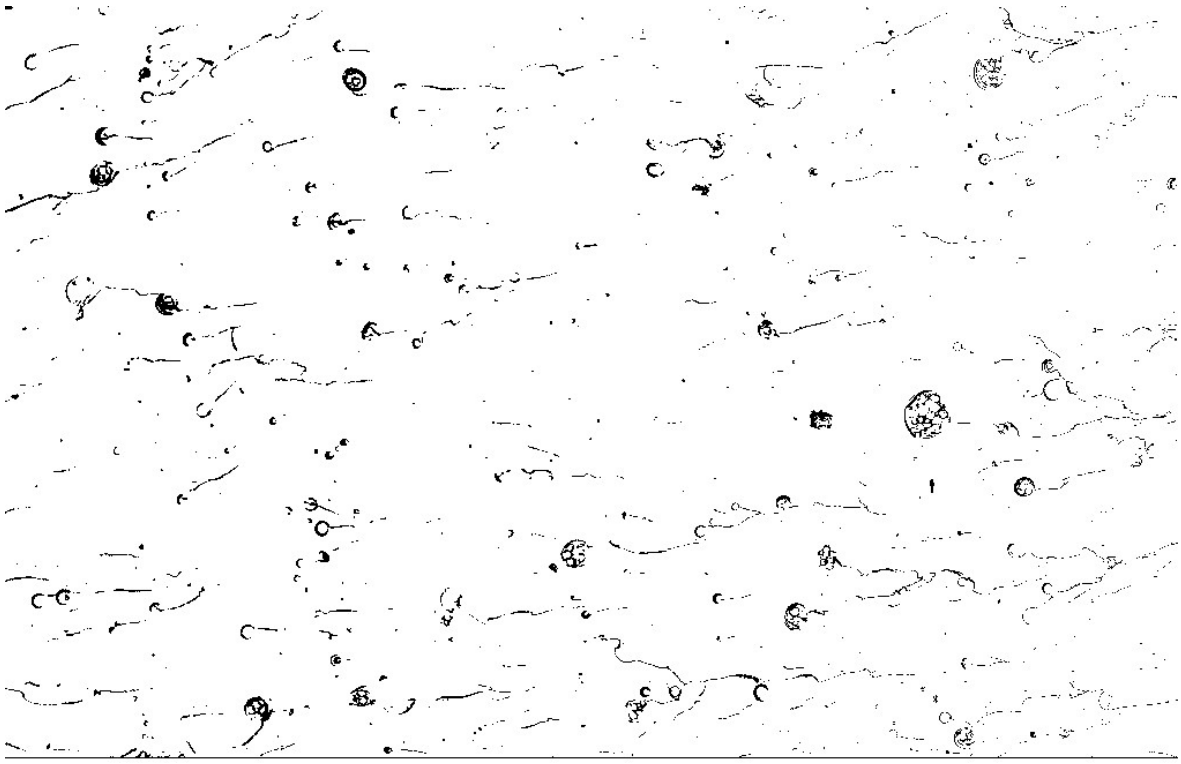

Figure A.9: Binary image of ceramic microsphere 2 wt%

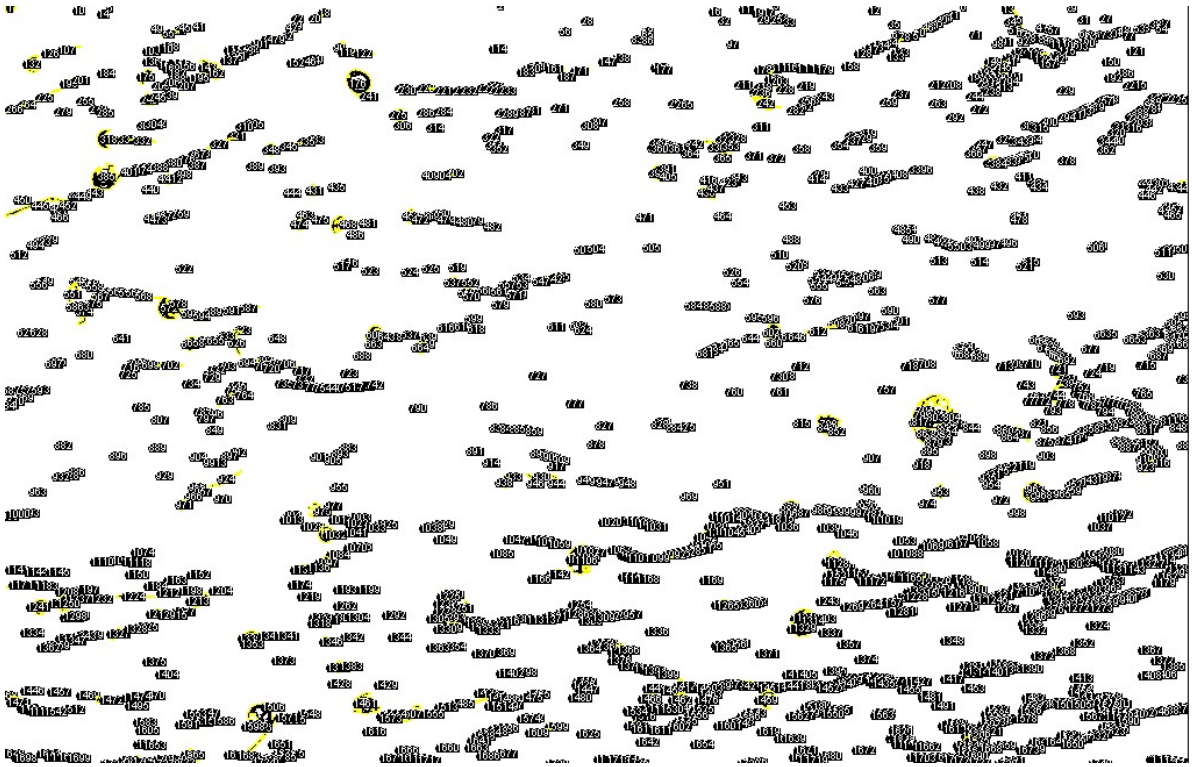

Figure A.10: Particles count images of ceramic microsphere 2 wt%

ceramic microsphere 5 wt%

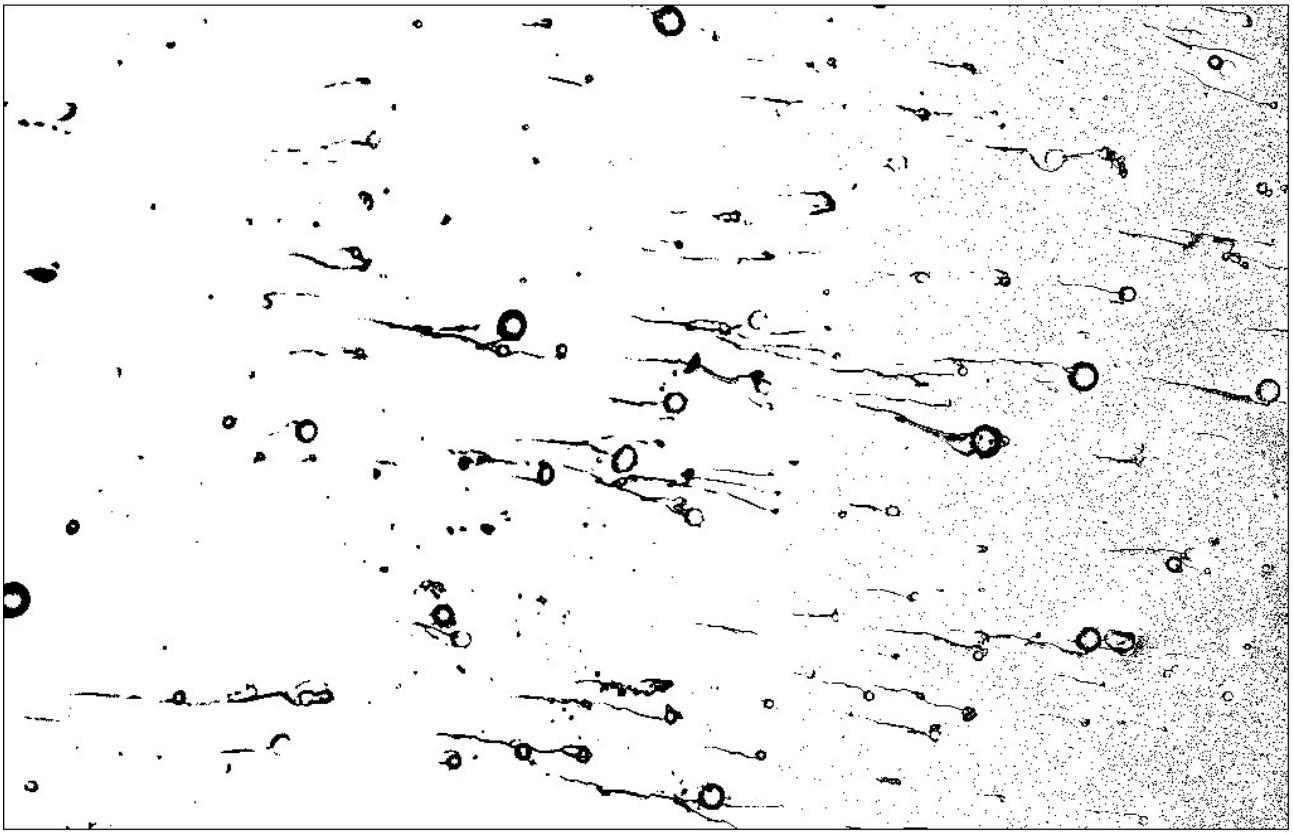

Figure A.11: Binary image of W210 5 wt%

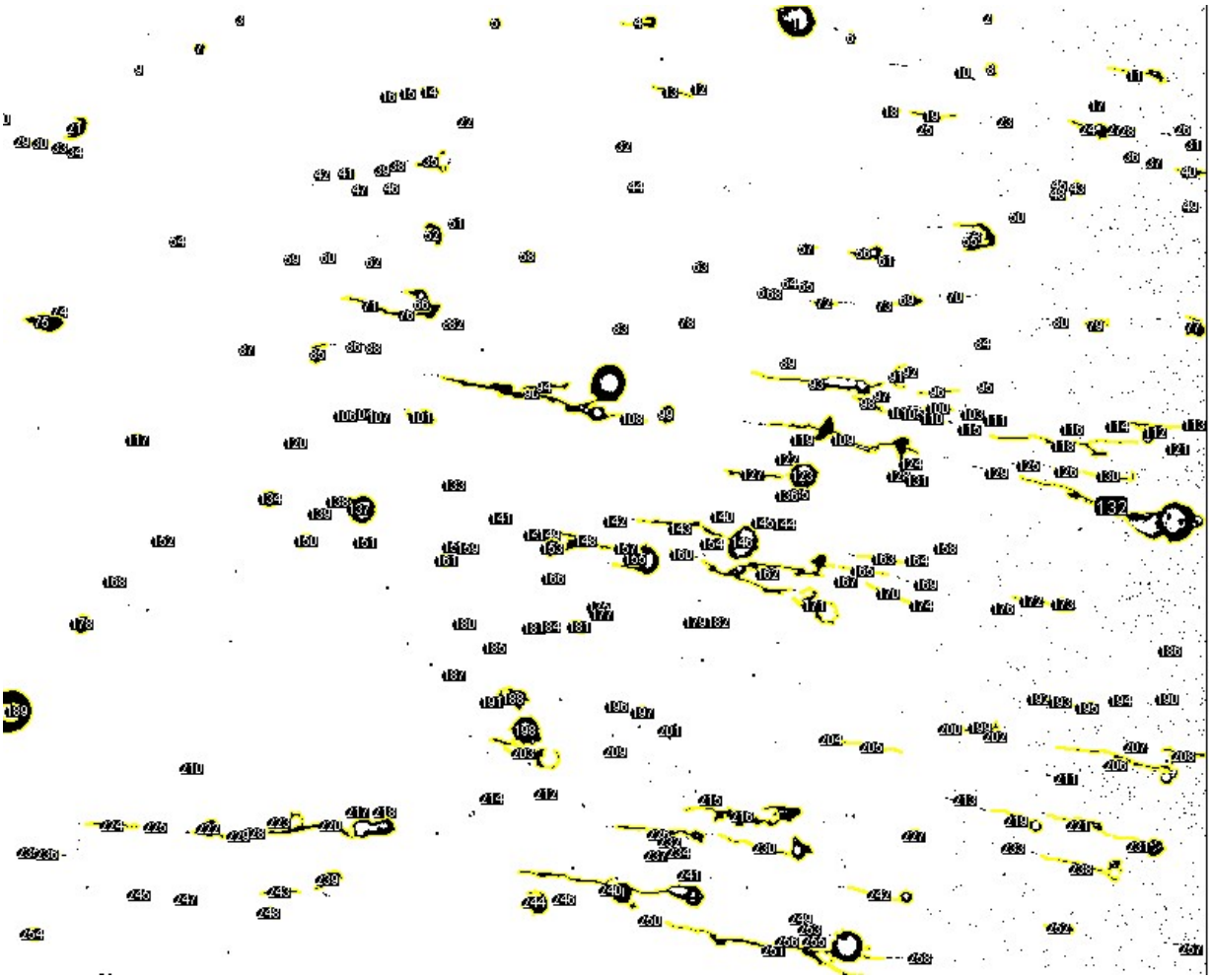

Figure A.12: Particles count images of W210 5 wt%

ceramic microsphere 10 wt%

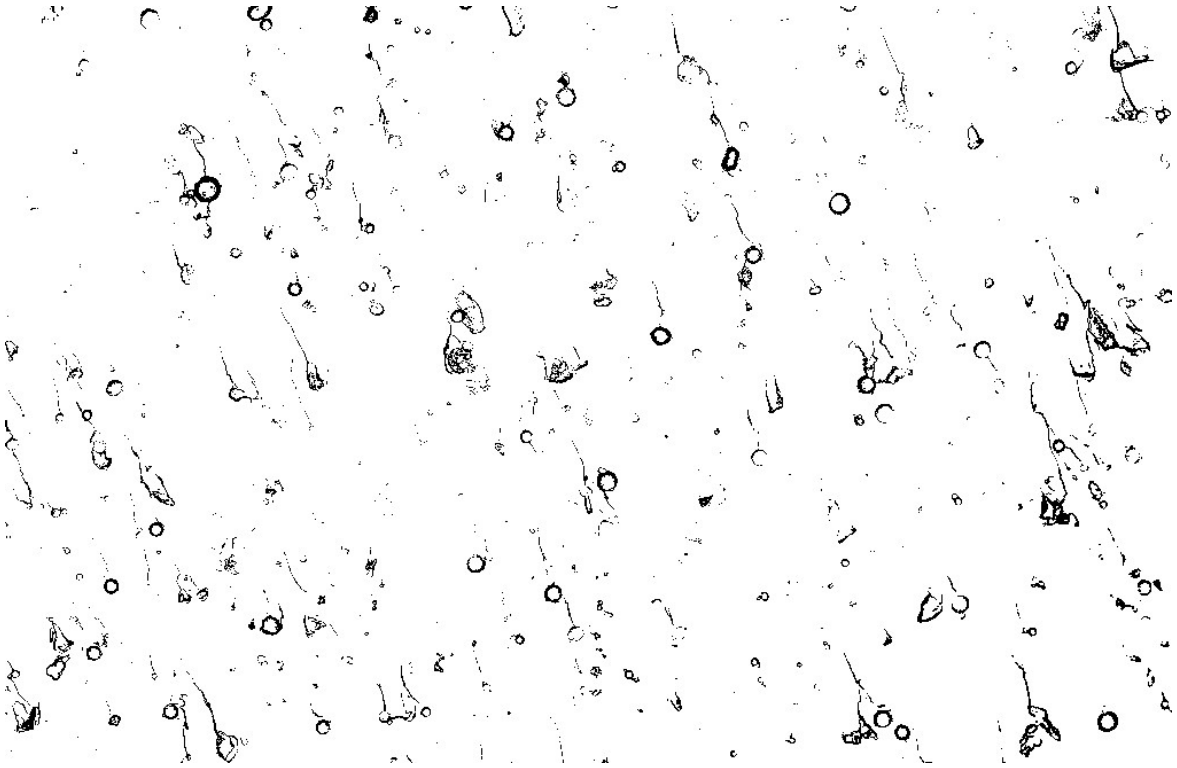

Figure A.13: Binary image of W210 10 wt%

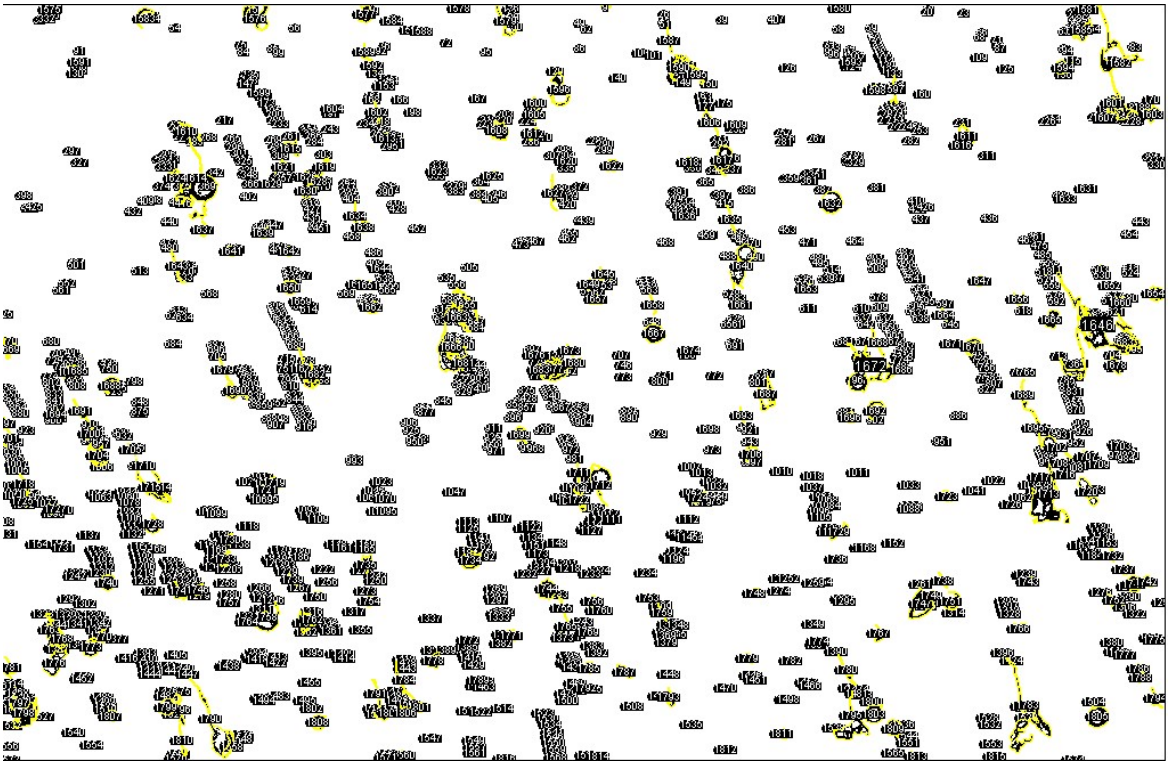

Figure A.14: Particles count images of W210 10 wt%

### A.2.4 Polyethersulfone modified epoxy

PES 2 wt%

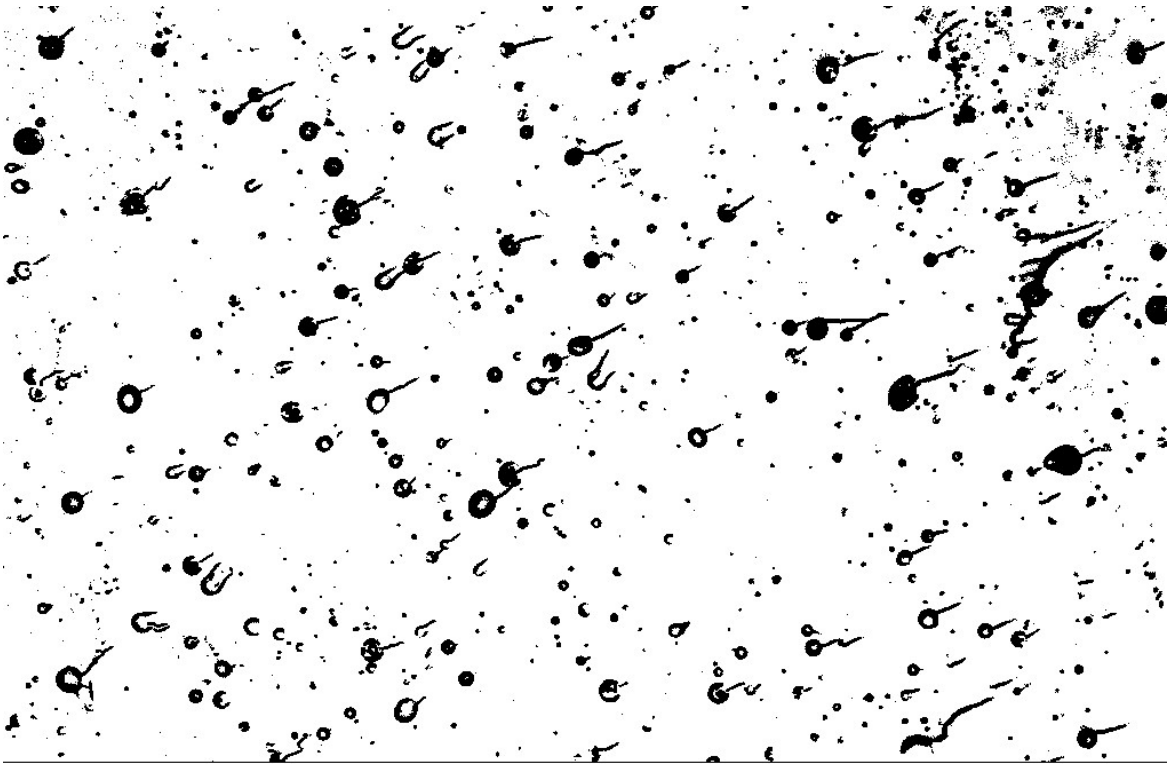

Figure A.15: Binary image of PES 2 wt%

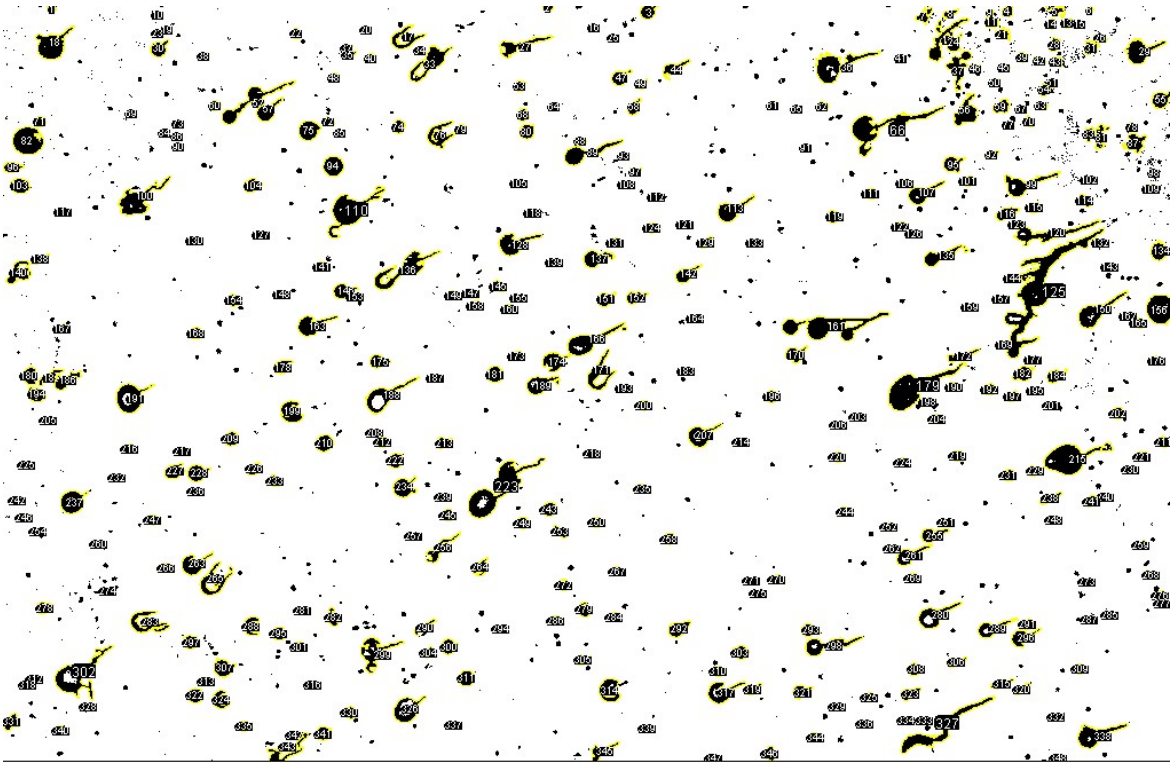

Figure A.16: Particles count images of PES 2 wt%

PES 5 wt%

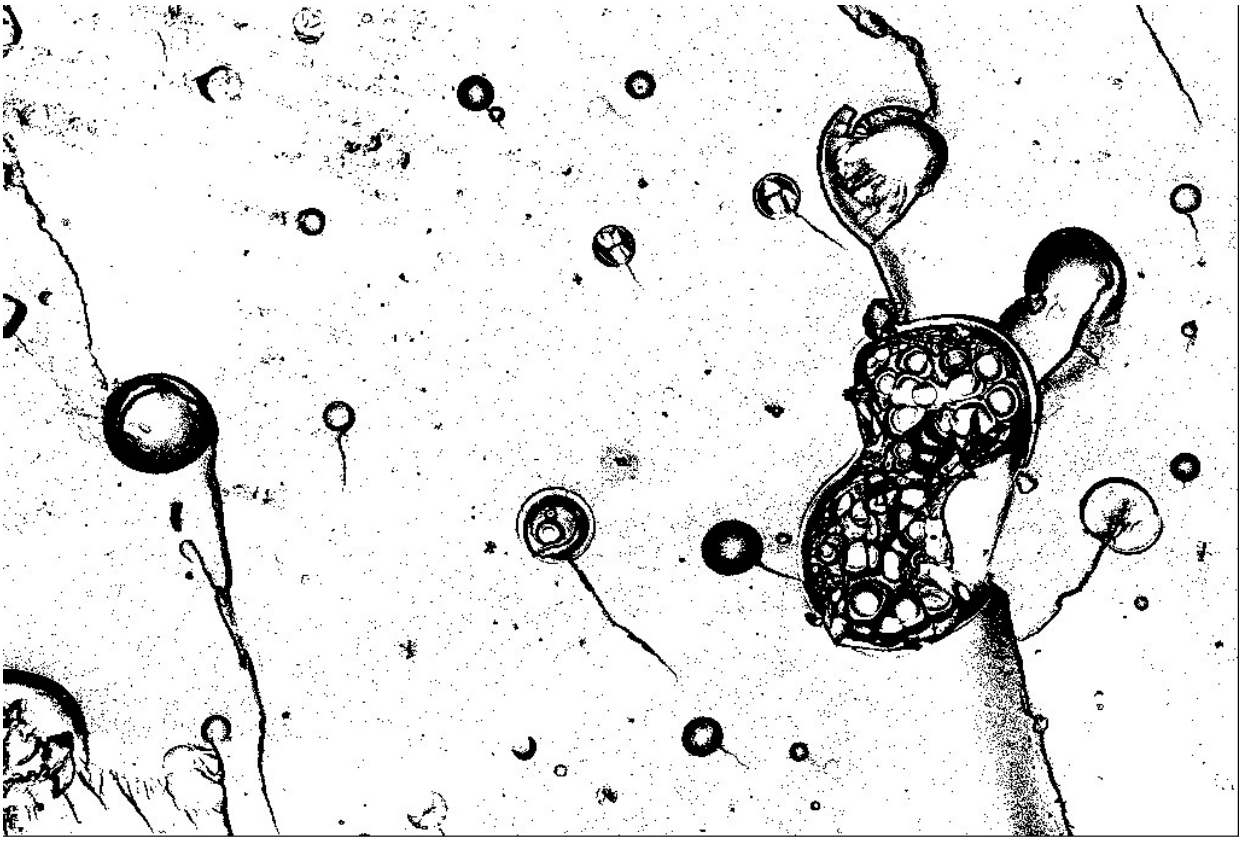

Figure A.17: Binary image of PES 5 wt%

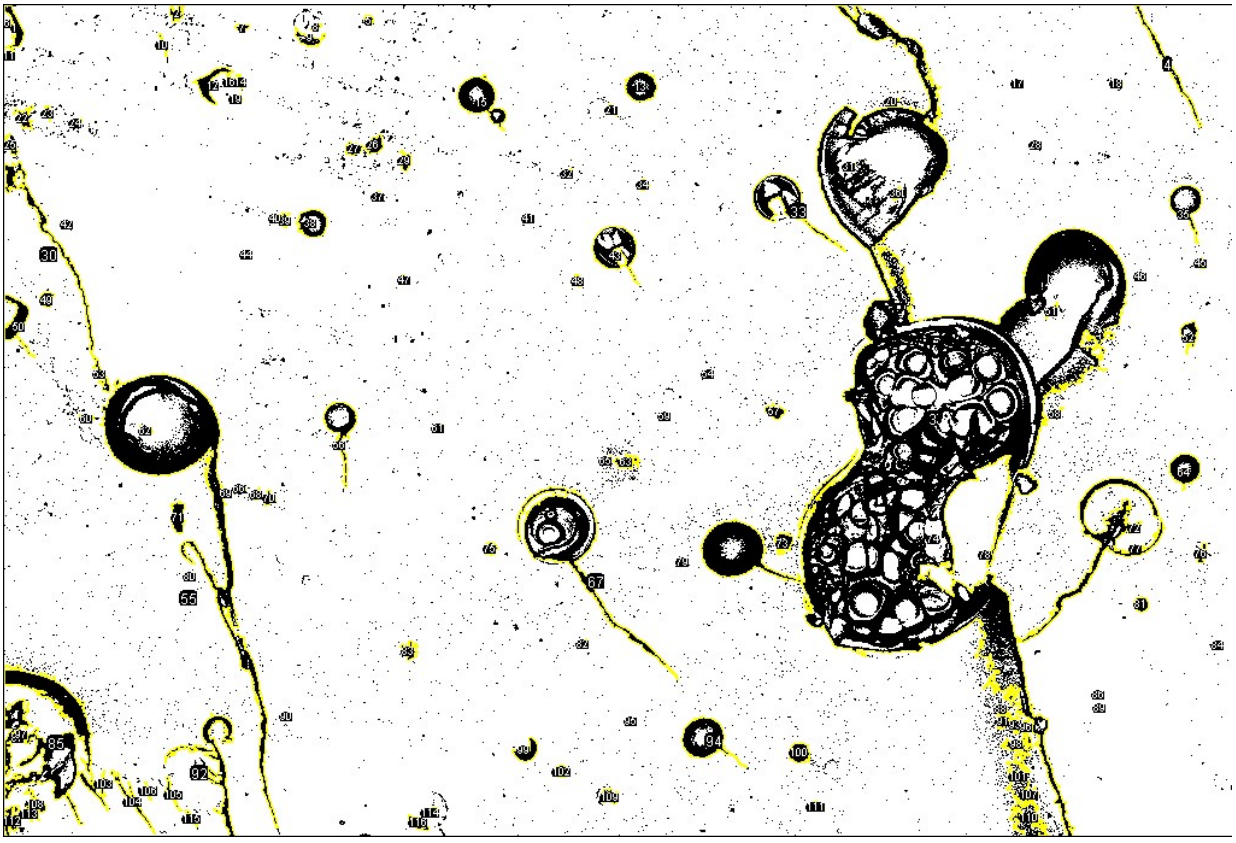

Figure A.18: Particles count images of PES 5 wt%

PES 10 wt%

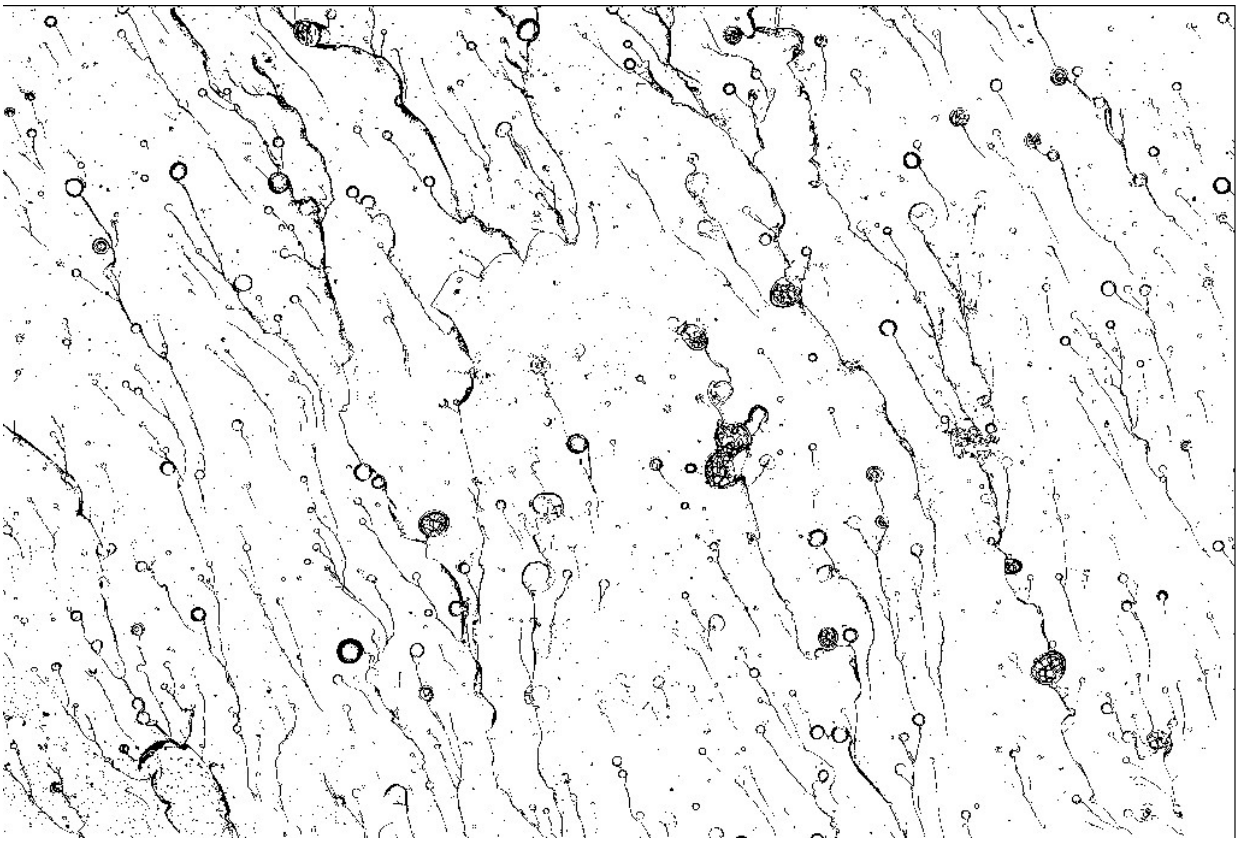

Figure A.19: Binary image of PES 10 wt%

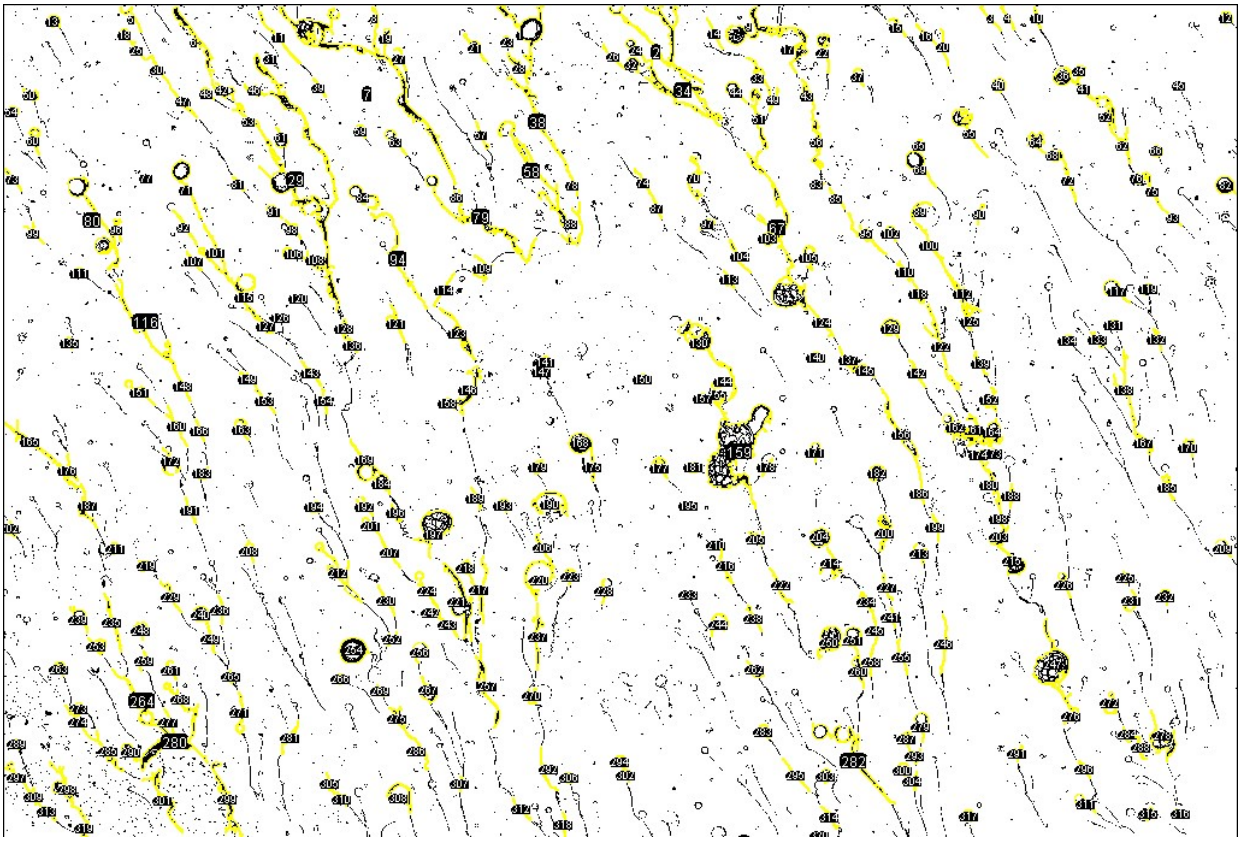

Figure A.20: Particles count images of PES 10 wt%